A NUMERICAL EVALUATION OF MULTI-DIMENSIONAL HEAT TRANSFER EFFECTS IN GREENHOUSES

BY

Sunita Kruger

Thesis submitted for the Degree of Doctor of Engineering of the University of Johannesburg

Faculty of the Engineering and the Built Environment

University of Johannesburg

Supervisor: Prof. Leon Pretorius

Co-supervisor Prof. Rudolph Laubscher

July 2015

Plagiarism Declaration

I, _____ hereby declare that this thesis is wholly my own work and has not been submitted anywhere else for academic credit by myself or another person

I understand what plagiarism implies and declare that this thesis contains my own ideas, words, phrases, arguments, graphics, figures, results and organization except where reference is explicitly made to another's work.

I understand further that any unethical academic behaviour, which includes plagiarism, is seen in a serious light by the University of Johannesburg and is punishable by disciplinary action.

Signed :_____ Date:_____

Abstract

Greenhouses are used extensively in both agricultural and horticultural industries. Cultivating crops in greenhouses is an energy-intensive process, especially as far as ventilation is concerned. The use of natural ventilation as an alternative to control the indoor climate of greenhouses has become increasingly popular. Natural ventilation in greenhouses is due to the air exchange process between the internal and external environment of the greenhouse mainly due to thermal buoyancy and wind-induced forces.

The main objective of this thesis is to determine the effect of dimensional and geometrical influences on the heat transfer characteristics of greenhouses using Computational Fluid Dynamics. This entails an investigation into the effect of geometric design changes on the thermal and flow performance of greenhouses due to buoyancy driven flow. The study also includes a numerical investigation into the effect of plant benches on the indoor climate of greenhouses.

This thesis commences with a review of the available literature, and identified areas in the research that require more attention. A background on the numerical tool used (Computational Fluid Dynamics) was given, as well as a background on the experimental methods used in this thesis. In this research study, the investigation was initiated with analysis of a simple, zero-degree roof angle cavity, which represents a square greenhouse. Results were compared to experimental results found in the literature and a good comparison was found. Confidence was established in the two-dimensional CFD model. A three-dimensional zero-degree roof angle cavity was also created and verified against data found in the literature. A good comparison between Nusselt numbers was found, and therefore confidence in the three-dimensional CFD model was also established. The three-dimensional CFD model approach was used to investigate the multi-dimensional heat transfer effects of the zero-degree greenhouse cavity. A significant difference between the two- and three-dimensional cases was observed.

The next step was to modify the zero-degree roof angle cavity, by adding an angled roof. This represented a simple, single-span greenhouse. The heat transfer in the cavity subject to various roof angles was investigated, and Nusselt-Rayleigh number relationships were established. A three-dimensional cavity of similar dimensions was investigated and compared to the two-dimensional cavity. Temperatures were found to be higher, and velocities much lower compared to the two-dimensional case. A roof ventilator was added to the one side of the greenhouse, and it was found that adding a ventilator does have a noticeable effect on the heat transfer inside the cavity. Nusselt-Rayleigh number relationships were also established for the

ventilated cases. It was also found that the type of ventilator (flap or roll-up) did not have a major effect on the heat transfer inside the cavity. Lastly, the ventilated cavity was scaled-up to represent a large greenhouse and this was qualitatively validated using a greenhouse found in the literature. Flow patterns observed compared well.

Following the validation of a single-span greenhouse model, a CFD model was created of a multi-span greenhouse and qualitatively validated against published data. Contour plots, velocity and temperature distributions at plant level were found to compare reasonably well, so that confidence was established in the two-dimensional CFD model of a full scale greenhouse. This CFD model was used to investigate natural ventilation due to buoyancy driven flow only, and compared to natural ventilation using wind and buoyancy.

A reduced-scale experimental model was created based on the large-scale multi-span greenhouse evaluated previously. The reduced-scale model was subjected to buoyancy driven flow, using plate element heaters placed on the floor of the greenhouse. Flow patterns were visualized using smoke and a green laser. The observed experimental flow patterns were recorded directly, and by using a video camera. Experimental results were found to be turbulent and unsteady. A CFD model was created based on the reduced-scale model, and flow patterns and temperatures were qualitatively compared. It was concluded that confidence has been established in the three-dimensional CFD model.

Using a similar approach for the CFD model as for the reduced-scale model, lastly a full-scale multi-span greenhouse containing peninsular arranged plant benches was investigated. It was found that the microclimate at plant level was influenced significantly by the presence of plant benches. The three-dimensional case was also compared to the two-dimensional case. It was found that the two-dimensional model overestimated the temperature difference between the inside and outside of the greenhouse. The velocities measured at plant level in the two- and three-dimensional models did not agree well either.

One of the main conclusions from this study was that the CFD models presented could be used to evaluate reduced-scale or full scale models of greenhouses. It was also found that multi-dimensional heat transfer effects were present in all the investigated cavities. Additional Nusselt – Rayleigh number relationships were deduced for specific Rayleigh number ranges for singe-span pitched roof greenhouses. The experimental results were found to be highly turbulent and unsteady, and also indicated that a reduced-scale model can be used to investigate the flow inside a full-scale greenhouse. The presence of plant benches inside a greenhouse was found to have a significant effect on the indoor climate at plant level.

This research study thus provide numerous insights into multi-dimensional heat transfer effects in cavities representing single span and multi-span greenhouses.

Acknowledgements

First of all, I would like to thank my Heavenly Father for the strength and guidance to complete this thesis.

I would also like to thank the following persons and institutions

- My husband Julius, and my two daughters Sulize and Elyssa. Specifically Julius who took care of Sulize and Elyssa when I was busy with tests or my thesis, and provided endless support, words of encouragement and patience during the past 7 years
- My parents and friends for listening and supporting my efforts
- Prof Leon Pretorius for his support, guidance and insight during my research. Also for his time, effort and encouragement. Your suggestions and consideration was greatly appreciated
- Prof Rudolph Laubscher, for support and guidance
- University of Johannesburg for providing me with funding and CFD software and University of the Witwatersrand for providing the facilities and equipment for the experimental tests
- Craig Roberson for building the Perspex reduced scale model of the greenhouse
- Michael Boer and Randall Paton who assisted with the experiments, flow visualization and capturing of the flow patterns
- Ignus Le Roux and Christiaan de Wet from Aerotherm for providing support with StarCCM+
- Rowan Rogers and Darren Grace, for conducting numerous tests, the flow visualization and video editing

In Remembrance

This thesis is dedicated to my grandfather, Frik Nel who inspired me to pursue a career in mechanical engineering.

Table of Contents

List of Figures

List of Selected Symbols

a	Total Area	m^2
A	Bounding Surface	m^2
g	Gravitational Acceleration	m/s^2
H	Height of Cavity	m
K	Mean Kinetic Energy	m^2/s^2
k	Turbulent Kinetic Energy	m^2/s^2
k	Thermal Conductivity	W/mK
L	Height of Cavity	m
i	Specific Internal Energy	kJ/kg
$\overline{n}$	Vector Normal to Surface Element dA	-
R	Universal Gas Constant or Effective Thermal Resistance	
S_i	Source Term in Energy Equation	
s	Surface Conditions	
S_{Mx}, S_{My}, S_{Mz}	Momentum Source Term in x,y and z direction	-
T	Temperature	K
t	Time	s
$\overline{U}$	Mean Vector Component	m/s
U	Mean Velocity Component in the x-direction	m/s
$\overline{u}$	Velocity Vector	m/s
$\overline{u}'$	Fluctuating Vector Component	m/s
U	Velocity component in x-direction	m/s
u'	Fluctuating Velocity Component in x-direction	m/s
V	Mean velocity Component in the y-direction	
v	Velocity Component in y-direction	m/s
v'	Fluctuating Velocity Component in y-direction	m/s
W	Mean velocity Component in the z-direction	
w	Velocity Component in z-direction	m/s
w'	Fluctuating Velocity Component in z-direction	m/s
p	Pressure	Pa
x	x-direction	
Δx	Thickness	m
y	y-direction	
y+	Wall Y+ Value	-

z	z-direction	
Greek Symbols		
α	Thermal Diffusivity	m^2/s
β	Volumetric Expansion Coefficient	1/K
Γ	Diffusion Coefficient	-
Φ	Dissipation Function	-
ϕ	General Variable for property	
ρ	Density	kg/m3
μ	Dynamic Viscosity	kg/m.s
τ	Stress	Pa
υ	Kinematic Viscosity	m^2/s
Subscripts		
∞	Free Stream Conditions	

List of Tables

CHAPTER 1

Introduction and Background

1.1 Introduction

Greenhouses are used worldwide to improve the growing conditions of crops to ensure more efficient production. Additional applications include cultivating crops out of season, and growing exotic tropical species at higher latitudes. Generally greenhouses are utilized to protect plants from various elements, such as high winds, insects and airborne diseases. They also protect plants from extreme environmental factors such as high/low temperatures and low humidity.

Due to continuous population growth and the development of new production technologies, greenhouses are not only one of the most intensive plant production systems, but also the most energy-consuming [1]. Since the Green Revolution, specifically energy consumption in agriculture, has increased drastically due to the use of diesel and electricity amongst others. To reduce the dependency of these systems on fossil fuels, renewable energy sources such as natural ventilation should be considered.

The microclimate inside greenhouses is of major importance as it directly affects the quantity and quality of crop production. A heterogeneous microclimate negatively affects crop growth and yields non-uniform production and quality. Ventilation is a vital tool for maintaining an acceptable indoor climate for optimum plant production. Two methods are currently employed to ventilate greenhouses: mechanical and natural. Natural ventilation requires less electric energy, less maintenance and is less noisy compared to mechanical systems.

The main driving forces for air flow in greenhouses are thermal buoyancy and wind-induced forces (also known as wind or stack effects) [2]. In certain instances, flow in confined greenhouses (as is the case during winter) is almost exclusively governed by buoyancy driven flow due to warm transpiring plant leaves and warm soil [3]. Because of essential coupling

between the transport properties of flow and thermal fields, buoyancy driven flow is rather complex. This is due to the fact that classical boundary layer flow theory assumes the simplifications for external flow problems (region outside the boundary layer) are unaffected by the boundary layer. When considering confined cavities with natural convection, boundary layers form adjacent to the walls, while the region outside the boundary layer is fully enclosed by the boundary layers and forms a core region. A significant complexity is imposed on the problem because of the interactions between the core and the boundary layer [4]. A confined greenhouse with a continuous crop surface can be simulated using a floor-heated dry cavity as is illustrated later in this thesis.

In the horticultural industry CFD is often used as a tool to investigate the indoor climate of greenhouses. As experimental work can become costly and cumbersome, the use of CFD has increased recently to obtain a qualitative and quantitative assessment of the environmental performance of greenhouses. CFD enables researchers to investigate the effect of various design parameters and working conditions on the indoor climate of these facilities without always building numerous expensive physical full or reduced-scale models. CFD solves the complete momentum, energy and mass transport equations, yielding a large amount of information regarding the air flow, which is difficult to obtain experimentally.

1.2 Problem Statement and Research Questions

The overall objective of this study is therefore to determine the effect of dimensional and geometrical influences on the heat transfer characteristics of greenhouses. This implies an investigation of the effect of geometric design changes on the thermal and flow performance of greenhouses with buoyancy driven flow. The main objective will be achieved by obtaining answers to the following questions in the main body of this thesis:

- What are the different greenhouse designs currently available?
- What are the various parameters influencing the indoor climate of a greenhouse?
- Does the presence of a crop influence the indoor climate of a greenhouse?
- Does the number of spans have an influence on the indoor climate of multi-span greenhouses?
- Does the presence of plant benches, and their arrangement influence the temperature and velocity profiles inside greenhouses?
- Can an in-depth study be conducted into the published literature to ascertain whether there still are certain areas in greenhouse design and indoor environment that need more investigation?

- Which numerical methodologies can be used to address fluid flow simulation in greenhouses?
- Can a zero degree roof angle single span greenhouse be evaluated against published experimental results using a Computational Fluid Dynamics model in both two and three dimensions?
- Are there differences in the thermal performance of two-dimensional versus three-dimensional square greenhouses?
- What is the effect of geometric design alterations such as roof angle and on the thermal performance of a single-span greenhouse?
- Can Nusselt-Rayleigh relationships be established for two- dimensional cavities corresponding to a single-span greenhouse?
- Are there differences in the thermal performance of two-dimensional versus three-dimensional single-span greenhouses with a non-zero roof angle?
- What will be the effect of different roof ventilator sizes and types on the thermal performance of a two-dimensional cavity?
- Are there any differences between a closed and ventilated single-span greenhouse?
- Is it possible to qualitatively validate a scaled-up cavity, using the same approach, and compare to results found in the literature by Lamrani [3].
- Is it possible to create a two-dimensional CFD model of a large, full-scale, multi-span greenhouse, and compare it to results found in the literature?
- Can a CFD model of a full-scale, multi-span greenhouse be used to investigate the differences between a combination of buoyancy and wind driven flow and buoyancy driven flow only?
- Is it possible to obtain a qualitative comparison of temperature fields and flow patterns against a CFD model be obtained using a reduced-scale model of a multi-span greenhouse?
- Can a full scale three-dimensional model be used to determine the effect of various ventilator configurations and bench arrangements on the indoor climate of the full scale greenhouse?

Taking the previously mentioned background into consideration and with the respect to the complexity of greenhouse indoor environment, this research study will systematically investigate the microclimate in a commercial greenhouse. This will be achieved by using both experimental and numerical methods to characterize the microclimate in typical greenhouse configurations.

1.3 Research Roadmap

Figure 1.1 shows the research roadmap for this research study. The research questions discussed in the previous section will be progressively addressed in the various chapters along the flow indicated in the research roadmap.

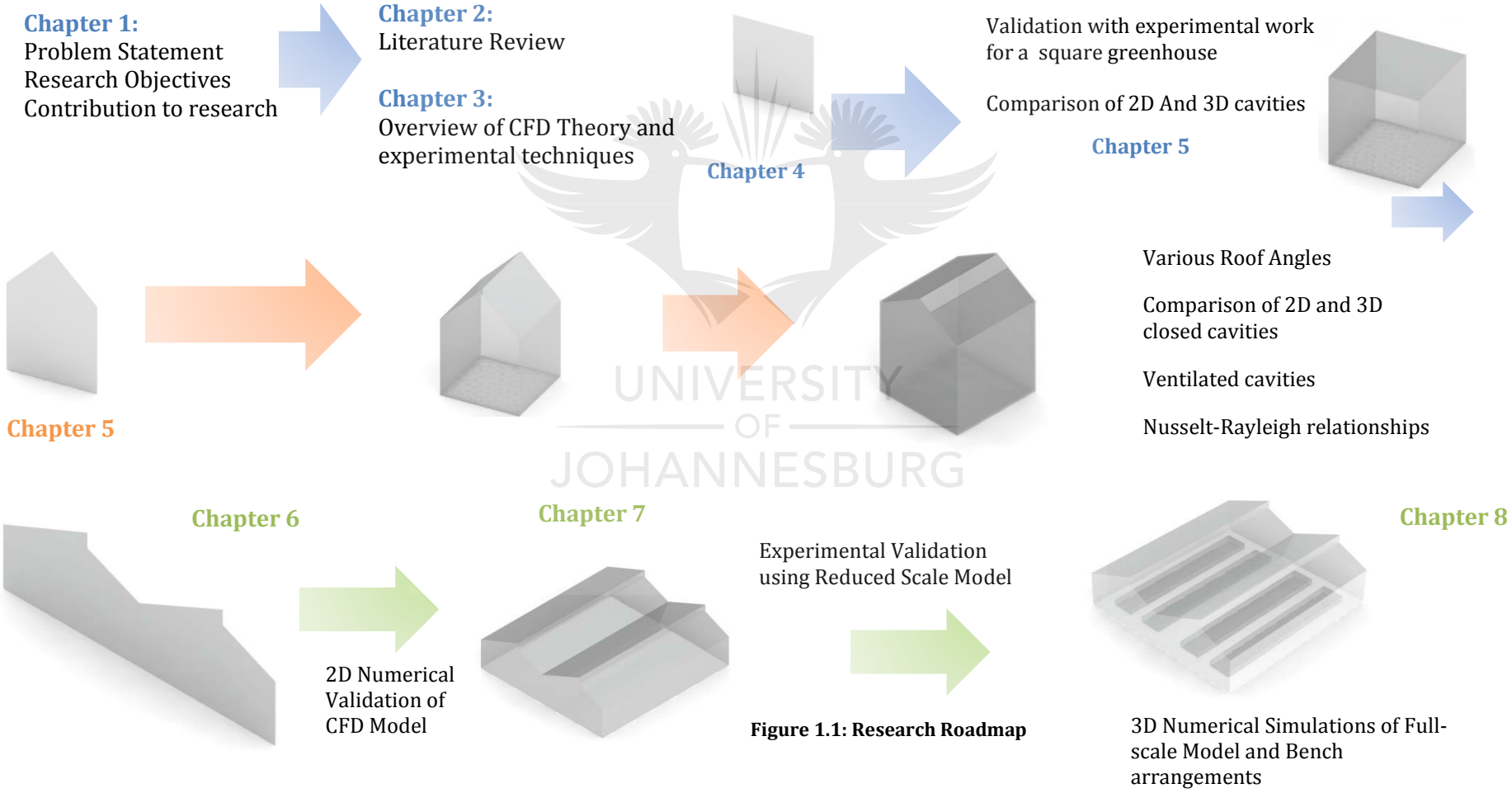

Figure 1.1: Research Roadmap

1.4 Research Contribution

In order to comprehensively understand the heat transfer mechanisms in greenhouses the heat transfer characteristics subject to various dimensional and geometric parameters must be thoroughly investigated. In this study the following topics will be addressed, leading to some research contributions:

- Nusselt-Rayleigh relationships will be derived for two -dimensional single-span zero-degree roof angle greenhouses, as well as for cavities containing various roof angles and ventilator opening sizes.
- The indoor climate of a two-dimensional single-span greenhouse is investigated and compared to a three-dimensional single-span greenhouse
- A greenhouse found in the literature will be qualitatively validated with new CFD models, and used to investigate buoyancy driven flow inside the greenhouse
- A qualitative numerical CFD validation will be obtained of the flow patterns and temperature distributions within a reduced scale model of a multi-span greenhouse subject to buoyancy driven flow.
- The influence of ventilator and bench arrangements on the indoor climate in a full-scale greenhouse will be investigated using a three-dimensional CFD model

Certain areas of this work were also based on and an extension of published work by the author during the research study resulting in this thesis [5], [6], [7], [8], [9], [10], [11], [12], [13], [14], [15], [16], [17] and [18]. This contributed to the novel knowledge generation in this thesis, and therefore some of the sections may in some aspects be similar and related to the previously mentioned publications.

1.5 Outline of Thesis

This thesis consists of 9 chapters as outlined below and referred to in the research roadmap, figure 1.1:

- **Chapter 2** is a detailed literature review discussing ventilation in greenhouses, the relevant theory and an overview of research previously done in this field
- **Chapter 3** is concerned with the theoretical background regarding Computational Fluid Dynamics, dimensional analysis of a scale models as well as an experimental background

- **Chapter 4** provides the numerical validation of a cavity representing a zero degree roof angle greenhouse. Differences in the thermal performance between a two- and three-dimensional cavity will also be investigated
- **Chapter 5** presents the results from modifying the single span, zero-degree roof greenhouse to represent a single span greenhouse with various roof angles and ventilators. This is conducted for both two and three-dimensional cavities. The two-dimensional cavity is also scaled up to represent a larger full-scale greenhouse
- A full-scale multi-span greenhouse is qualitatively validated using CFD simulation in **Chapter 6** against data found in the literature. The validated CFD model is used to investigate the effect of buoyancy driven flow as on the indoor climate of the greenhouse as well.
- **Chapter 7** contains the experimental investigation using a reduced-scale model of a full scale greenhouse. A CFD model is also created and validated using the experimental results. This again provides additional confidence in the CFD greenhouse model.
- **Chapter 8** numerically investigates a full-scale multi-span greenhouse containing peninsular arranged plant benches using the confidence gained from previous sections' CFD models for the large scale final CFD model.
- The last chapter, **Chapter 9** concludes this thesis and summarizes the research presented in this study, conclusions are drawn and recommendations made for further research
- References and Appendixes follow Chapter 9

CHAPTER 2

Literature Review

2.1 Chapter Review

This chapter discusses and summarizes relevant research in the field of greenhouse indoor climate investigations. Design aspects such as shape and ventilator configuration are discussed in section 2. Aspect of greenhouse design will be discussed in Section 2.3. The importance of temperature and velocity distributions on the microclimate is discussed in section 2.4. Numerical and experimental research on greenhouses is reviewed in section 2.5. Other aspects of greenhouses such as plant benches, crop influence and single and multi-span greenhouses are discussed in sections 2.63,2.6.4 and 2.6.5 respectively. Selected difficulties encountered when using CFD as the numerical tool is mentioned in section 2.7. Lastly, natural convection in enclosures is discussed in section 2.8. Some of the literature discussed in this chapter was adapted from papers published previously by the author for example [18]. This chapter sheds some light on the following research questions as discussed in Chapter 1:

- What are the different greenhouse designs currently available?
- What are the various parameters influencing the indoor climate of a greenhouse?
- Does the presence of a crop influence the indoor climate of a greenhouse?
- Does the number of spans have an influence on the indoor climate of multi-span greenhouses?
- Does the presence of plant benches, and their arrangement influence the temperature and velocity profiles inside greenhouses?
- Can an in-depth study be conducted into the published literature to ascertain whether there still are certain areas in greenhouse design and indoor environment that needs more investigation?

2.2 Introduction

The use of greenhouses to cultivate flowers and crops can be traced back to Roman times. It was mentioned by two agricultural writers that the Emperor Tiberius (42 BCE – 37 CE) had proto-greenhouses (specularia) constructed adjacent to his palace to grow off-season cucumbers [19] .

These structures were quite rudimentary and it was not until the 1600's that greenhouses were heated using manure and covered with glass panes in France and England. The first glass houses were constructed in the 1700's and were mainly used for cultivating melons, grapes, peaches and strawberries [20]. After World War II environmentally protected agriculture was fully established with the introduction of polyethylene as a cheaper alternative to glass.

In cold climates, greenhouses were mostly operated during autumn and from late winter to early summer. During midsummer, greenhouses were too warm, and in some regions light levels and day length were inadequate. The use of various methods, including mechanical ventilation, evaporative cooling and heating systems have been employed to extend the use of greenhouses in various climates [21].

Greenhouses protect the plants from weather extremes such as too high/low temperatures, enabling improved growing conditions. But they are also applied in other ways. For example, greenhouses are used in regions plagued by droughts to assist in a constant water supply. This also enables water to be used more efficiently [22].

The primary requirements for successful plant production are [21]:

- Favourable temperatures
- Adequate light intensity and suitable radiation spectrum
- Favourable air composition and circulation

The quality of crops in greenhouses is largely influenced by spatial variations in air velocity, temperature and humidity, which are directly influenced by fluctuations in wind flow [23]. Understanding the microclimate in the greenhouse can assist in optimizing fertilization and irrigation systems and improve control over the greenhouse environment [24]. Favourable climates for diseases, and therefore the use of pesticides can also be avoided if the indoor climate is distributed more uniformly [25]. Ventilation is of major importance, as the process is responsible for air exchange between the interior air of the greenhouse and the outside environment due wind and buoyancy effects [26].

Over the years, various aspects pertaining to greenhouse production have been researched and published [27], [28]. Popular topics include velocity and temperature distributions, pressure distributions on the roof, air exchange rates, vent configuration and wind direction to name just a few. This chapter will discuss some of the most relevant literature to the current research, as well as related topics such as plant bench arrangements, crop influence and multi-span greenhouses. The first aspect to be investigated is greenhouse designs. This will assist in determining whether and to which extent design parameters influence the indoor climate.

2.3 Greenhouse Design Aspects

The design of a greenhouse needs careful consideration, as it has a direct impact on the microclimate inside the structure. A well designed greenhouse is a major contributor to successful crop production. A number of important elements can influence the production efficiency such as the shape of the greenhouse, cover material, ventilator configuration, and roof slope.

2.3.1 Shape and Size

Greenhouses are available in various structural forms. Two basic types of greenhouses are used in industry, namely free-standing greenhouses, and gutter-connected greenhouses. The most common free-standing greenhouses are shown in Figure 2.1. When a series of some of the above mentioned greenhouses (gable or Quonset arches) are connected at gutter level, a larger greenhouse offering greater flexibility is created. Typical gutter-connected greenhouses are shown in the next figures. Figure 2.2 shows what is called a ridge-and furrow or Venlo-type greenhouse. A gothic arch gutter-connected greenhouse is shown in Figure 2.3. Detached greenhouses have certain advantages over multi-span greenhouses. It is claimed that detached greenhouses are easier to ventilate, and that light entering the greenhouse is distributed relatively uniformly [29]. Caring and maintenance are also less tiresome compared to connected structures. Multi-span greenhouses on the other hand need less land area, fewer construction materials are required, and less heat is required as there are less exposed wall surfaces. Unfortunately, the air velocity and indoor climate inside large greenhouses vary considerably, which could interfere with crop growth [30].

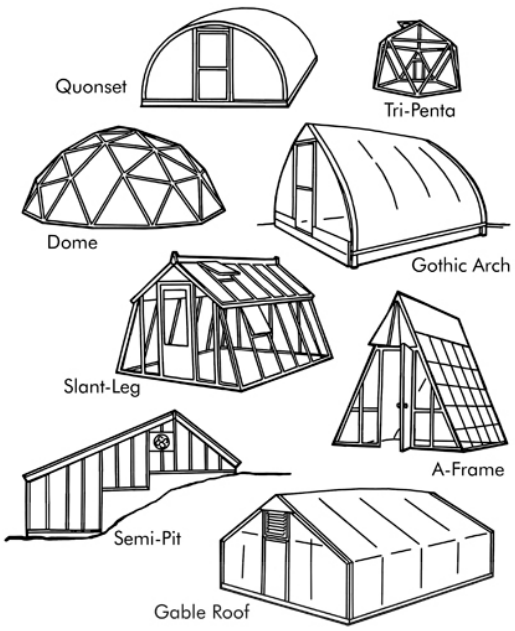

Figure 2.1: Free-standing greenhouse shapes [31]

Figure 2.2: Venlo-type gutter-connected greenhouse [31]

Figure 2.3: Gothic arch gutter connected greenhouse showing flap-type ventilators

Brugger et al [32] investigated the influence of different roof slopes and location on ventilation rate on a specific type of greenhouse, referred to as a parral greenhouse. This is a common type of greenhouse found in the Mediterranean areas, popular for its efficient water use and hydroponic growing of plants [32]. These structures are usually naturally ventilated as the cost of mechanical ventilation is unaffordable for the areas. Parral greenhouses are ventilated by sidewall and/or roof openings of the rolling cover or flap type. Excessive daytime temperatures are often found in parral greenhouses, which have a negative impact on the quality and yield of the greenhouse crops. Some design aspects of parral greenhouse were investigated. Almost no effect on the ventilation rate was found for wind velocities lower than 3m/s, but for higher velocities the effect was more visible. The authors concluded that an increased roof slope will enhance the ventilation of parral greenhouses. Ventilator openings located on the windward (opening of ventilator faces the oncoming wind) side of the roof resulted in a higher air exchange rate compared to leeward (opening of ventilator faces in the direction away from the oncoming wind) located ventilators.

2.3.2 Ventilators

Greenhouses can be equipped with various types of ventilators and in different configurations. Two types of greenhouse ventilators are commonly used in industry: roll-up type (Figure 2.4) and pivoting/flap type ventilators (Figure 2.3).

Figure 2.4: Continuous roll-up type ventilator [15]

Several authors [33], [34], [30], [35]and [36] devoted time to investigate the effects of ventilator configurations on the indoor airflow of greenhouses. The authors did not however focus on the parametric design aspects of the greenhouses or plant bench arrangements. This is also where the current research work makes a contribution.

In greenhouses with only roof ventilators, the air exchange rates per unit ground area were found to be independent of the greenhouse length [37]. Adding ventilators at opposing walls combined with roof ventilators resulted in higher exchange rates and consequently lower temperatures throughout the greenhouse. The authors concluded that sidewall ventilators play an important role in buoyancy driven flow, especially small greenhouses.

In another study by Molina-Aiz [37] the effect of two external wind speeds and vent configurations was studied for an Almeria-type greenhouse. It was found that when the roof vents were half-open and the side vents were fully open, maximum ventilation rates were numerically obtained. If the side vents were partially closed, minimum rates were predicted numerically. For an empty greenhouse, improved cooling effect may be obtained by partially opening the roof vents, and fully opening the side vents. It was also concluded that three-dimensional simulations are preferable over two-dimensional when the wind-direction is not perpendicular, as this can improve the accuracy of the CFD simulations. It should be noted that heat and vapour exchanges were not included in the simulation [37]. This will also be the case of assumptions presented in this research.

The same author [38] also attempted to optimize the vent configuration of a five-span greenhouse. This was a comprehensive study evaluating the effect of greenhouse width and spans number, vent area, location and type of vent openings, presence of insect-proof screen with different porosity and incidence of plants. The presence of insect-proof screens reduced the flow rate, with a proportional increase in temperature. It was also found that for an Almería greenhouse the flap opened towards the leeward side resulted in higher air exchange rates compared to flap opened windwards. Increasing the number of spans from 1 to 5 reduces the ventilation rate with 88% as a result of the increased width of the greenhouse.

The greenhouse microclimate and dehumidification effectiveness subject to different vent configurations was studied by Kittas and Bartzanas [39] in an arch greenhouse equipped with continuous side ventilators. Roll-up type ventilators were found to yield the maximum air velocity near the ground, with the lowest velocities observed close to the roof. The result was a decrease in temperature and humidity first near the ground, and afterwards in the remainder of the greenhouse during the dehumidification process. The exact opposite behaviour was observed for the pivoting door type ventilators, as the maximum air velocities were observed near the roof. The air temperature and humidity were decreased first near the roof during the dehumidification process.

The ventilation performance of six different greenhouses was investigated by Boulard et al [40]. The greenhouses were all equipped with either roof or side vents, or both. Results confirmed that the combination of surface area of the vent-opening and wind speed are responsible for the largest part of the air exchange rate variation. It was also noted that the presence of crop decreases the ventilation efficiency. The hypothesis that the exchange rate is linearly dependent on the wind velocity when wind effect dominates was only partially supported by the experimental data recorded. Vent design was also found to be important, as it was shown that continuous vents are more efficient compared to discontinuous vents.

Two-dimensional CFD models of 5 and 10 span parral greenhouses were used to evaluate the effect of ventilator size on the air exchange rates in a study by Baeza et al [41] A definite influence on air exchange rates was observed when increasing the widths of the ventilator openings, and air movement in the vicinity of the crop area were enhanced. The temperature gradient in relation to the outside as well as the number and size of stagnant spots were found to be reduced. Flap ventilators also proved to be more efficient compared to rolling vents. In this research study for the doctoral thesis the heat transfer at crop level is investigated in more detail, using a systematic investigation, as well as the influence of bench arrangements.

Kittas et al [42] studied the influence of wind speed on ventilation rates in a plastic tunnel equipped with continuous side ventilators. They tested various combinations of side ventilator openings under different wind velocities and directions. Air exchange rate was found to be strongly dependent on wind velocity as well as total ventilator area. Roof openings were found to be more effective than side openings, but it also depends on the type of opening if the vents are equipped with a side-mounted flap on the frame.

Experiments and a theoretical model were utilized by Teitel and Tanny [66] to investigate the transient response of the greenhouse air temperature and humidity to the opening of roof windows. Their results showed that if the roof ventilators are opened, the air temperature and humidity ratio decreases with time, and eventually approach steady-state. It was also shown that an increase in window opening height and wind speed and a decrease in solar radiation resulted in more effective ventilation. Solar radiation was excluded in this study for experimental and validation purposes.

A thorough review of the effect of ventilator configuration on the distributed climate of greenhouses was conducted by Bournet and Boulard [43]. A few important conclusions were drawn after a review of both experimental and numerical studies. It was found that sidewall ventilators alone are less efficient compared to having both roof and sidewall vents. In this case, ventilation rate strongly decreases as the number of spans increases.

It can therefore be seen that various aspects of the greenhouse structure, such as roof slope, types of roof ventilators and their location have a profound effect on the inside microclimate of greenhouses. Results from some of these studies can be used for validation purposes in this study. The next section in this chapter will discuss the indoor climate and its influence on the crop in more detail.

2.4 Indoor Climate

Environmental conditions inside a greenhouse such as temperature, humidity and carbon dioxide concentration are influenced by the air exchange between the inside and outside of the greenhouse. These parameters in turn influences crop development and production. During summer, ventilation is required to reduce temperature and remove humidity when necessary. During winter, ventilation must remove excess humidity and provide a suitable atmosphere inside the greenhouse [44]. The indoor climate inside large greenhouses varies considerably, which could interfere with crop growth as the temperature and velocity distribution directly influences the uniformity of the crop [30].

2.4.1 Temperature

Each of the intricate chemical reactions that form the basis of plant growth is influenced by the temperature to which the plant is exposed. This directly affects the rate of the reactions. Plants respond and grow optimally over a wide range of temperatures. The range is defined by three levels [29]:

- Optimum Temperature – the temperature at which plant growth is optimal
- Minimum Temperature – the temperature below which growth does take place
- Maximum Temperature – the temperature above which no growth occurs.

Plant growth and flowering are governed by leaf and root temperatures [21]. The energy balance of a roof canopy is dependent on number of factors – air temperature, relative humidity, air movement, thermal radiation exchange and convective exchange coefficients. The temperature of leaves is rather difficult to measure, and influenced by several elements. The type of heating and ventilation plays a major role; supplemental heating and the greenhouse cover (which dictates light transmittance). Misting and evaporative cooling are also factors, as well as the location of the leaves on the plant.

Night time temperatures have been found to have a profound effect on the growth of plants. Usually day temperatures are increased from 5 to 10°C above the night temperatures, depending on solar intensity [21]. In order to control plant height and development in certain crops, night temperature (NT) and day temperatures (DT) are often manipulated. Some studies have investigated the effects of DT and NT and their difference (DIF = DT-NT). Shorter crops are usually the result of a negative DIF [21].

Plants respond differently to temperatures at various growth stages. The optimum temperature for vegetative growth may not be the most favourable temperature for flower development. Research conducted [45] on the effect of moisture and temperature stress on the growth and yield quality Parameter of Phyllanthus Amarus showed that the various processes are influenced by temperatures. Phonological data revealed that days to germination, days to leaf initiation, days to flowering and days to fruiting were all affected by temperature stress imposed treatments during the experiments. Temperature also has a profound effect on the occurrence of disease in plants. The effect of temperature and light conditions on germination, development and conidiation of tomato powdery mildew on tomato plants were studied by Barbora et al [46]. It was found that that Conidia germinated across the entire range of temperatures (10 - 35°C), but germination was limited at the endpoint temperatures. The appearance of Conidiophores was delayed at temperatures slightly lower than the optimum (20-25°C) and most intense between (20-25°C).

Vertical temperature gradients in greenhouses were investigated by Zhao et al [47] under closed and naturally ventilated conditions. If mature plants were present in a closed greenhouse, large vertical gradients in temperature and humidity and temperature were observed. With young plants these gradients were negligibly small. Opening the roof vents resulted in a slight decrease in temperature as the greenhouse cools down. But when both roof and side ventilators were used, the temperature and humidity gradients were found to be somewhat larger compared to roof ventilators only. This was however not pure buoyancy driven flow as the outside wind velocity could not be ignored.

Sase et al [48], experimentally investigated the airflow and temperature distribution in a naturally ventilated greenhouse using a scale model of a greenhouse. They found that due to wind and stack effects, the airflow patterns change significantly with increasing wind velocity and wind angle. The authors also attempted a three-dimensional investigation, and it was indicated that high temperatures are seen in the windward gable-end of the greenhouse. The scale model in this current study will be subjected to buoyancy driven flow only. The effect of bench arrangements on the indoor climate will be investigated numerically. The difference between two-and three dimensional numerical models will also be studied as part of the research presented in this study.

In a study done by Ould Khaoua et al [49], the ventilation efficiency of a greenhouse was analysed by utilising two-dimensional CFD models. The influence of wind speed and roof vent configuration on airflow and temperature patterns at plant level in a compartmentalised greenhouse was investigated. They found that the ventilation rate efficiency was considerably increased by orientating the roof vents windward. Results also showed that temperature and velocity rises at crop level can be balanced by opening both windward and leeward vents. The results from this study will be used later in this investigation reported on in this thesis to evaluate a two-dimensional CFD model of a four-span Venlo-type greenhouse by comparing temperature and velocity distributions.

The distributed climate in a full-scale multi-span greenhouse was modelled and validated by Fatnassi et al [50]. They measured the distributed field of air temperature both vertically and horizontally, and used the measurements to validate a three-dimensional CFD model. Measured results showed a difference of up to 10°C between the inside and outside of the greenhouse in certain areas.

Six prototype greenhouses were evaluated in terms of cover properties, ventilation rate, and crop leaf area in a tropical greenhouse climate by Impron et al [39]. Their results indicated that the indoor air temperature was influenced predominantly by ventilation and leaf area index and

not by cover properties. The presence of a crop inside a greenhouse can be represented numerically by defining a porous region.

2.4.2 Velocity

In addition to humidity and temperature distribution at plant level, the velocity field and corresponding aerodynamic resistances are also of major importance as regards to indoor climate [43]. The convective heat exchange between the crop and interior air is dictated by air movement, which in turn influences the microclimate around the crops [26]. It directly influences the intensity of heat transfers between the air and plant canopy, as well as the intensity of water exchange between the air and the plant canopy [51]. According to ASHRAE [21] the commonly accepted air speed for plant growth is 0.5 to 0.7m/s. For carbon dioxide uptake, air speeds of 0.03 to 0.1 m/s are required across the leaf. The optimal heat exchange is found when velocities are between 0.2 and 0.7 m/s, if the air stream is vertical i.e. from bottom to the top of the plant. As plants grow, carbon dioxide is used and oxygen released through tiny pores called stomates. As a result, a high concentration of oxygen is present in the boundary layer between the leaf surface and the air, with a carbon dioxide deficit. If the air movement inside a greenhouse is insufficient, the growth rate of the plants is reduced as the amount of carbon dioxide available is inadequate [52]. The stomatal guard cells close when excessive transpiration is experienced (air speeds above 1 m/s), thereby reducing the carbon dioxide uptake and impede plant growth. Physical damage to plants may occur if air speeds above 5m/s are present. It is generally accepted that if plants in a greenhouse move noticeably due to ventilation, the air speed is excessive [21].

Lee-side ventilation-induced air movement in a large-scale multi-span Greenhouse was experimentally investigated by Wang and Deltour [53]. They found that the horizontal air movement inside the greenhouse varies linearly with height. Measurements also showed that air velocities at various locations were proportional to the external wind speed and the ventilator opening angle. It was found that for high wind speeds, air velocity inside the greenhouse was still relatively high for a zero opening angle. This was attributed to free convection due to buoyancy forces, and forced convection due to air leakage and wind forces. The turbulence investigation indicated that airflow in the horizontal plane was of low turbulence with large eddies.

A study was conducted by Teitel et al [54] on the effect of wind direction, ventilation rate, airflow patterns and temperature distributions in a multi-span greenhouse with vertical roof openings. The greenhouses were one of a set of four greenhouses. Field experiments, as well as reduced-scale experiments in a wind-tunnel were conducted and compared to a CFD study. It

was proved that wind direction does have a significant influence on flow patterns through the roof openings. All wind azimuths resulted in the flow being characterized by high velocities near the ground and the cover whereas stiller conditions were observed in the core of each span. The temperature also increased from the windward to the leeward span. The main conclusion from their study was that special consideration should be given to the orientation of the greenhouse relative to the prevailing wind. The openings where inflow is dominant should also be carefully monitored, as this may aid insects penetration into the greenhouse. They have also noted that their CFD doesn't always predict the ventilation rate correctly, as their results as well as results from several other authors were lower than the measured values. This could be attributed to the turbulence model used, as well as the fact that the heat load in real greenhouses due to solar radiation on the crop, the structural elements and greenhouse cover are not uniform as is assumed in the simulations.

The turbulent air flow inside greenhouses was extensively investigated by Boulard et al [23] and [55]. The mean and turbulent air flows were characterized for a tunnel-type greenhouse by the same author [23]. Air temperature patterns and humidity distribution were also investigated. The results indicated that a strong wind perpendicular to the tunnel axis combined with moderate temperature and humidity differences prevail significantly over the buoyancy forces. A powerful air current was observed crossing the wind tunnel between the windward and leeward vents. Air along the floor and in-between two consecutive series of openings remained stagnant. Turbulence intensity was found to increase from the centre of the tunnel towards the windward opening.

In another study by Wang et al [26] experimentally measured the air speed profiles in a greenhouse containing tomato crops using a multi-point two-dimensional sonic anemometer system. The experimental results indicated that inside air speed was linearly dependent on both the external wind speed, as well as the greenhouse ventilation flux (dependant on the combination of thermal and wind effects). If leakage ventilation is considered, air speed remained nearly unaffected, as the wind velocity and temperature effects on the greenhouse air exchange rates were minimal.

To conclude, it is seen that air velocity plays a major role in greenhouses and that an optimal range of air speeds exists. Air speeds above or below the optimal range may cause physical damage to crops, but can also hinder plant growth. This aspect of velocity ranges is also considered when qualitatively validating CFD models developed in later sections in this thesis. Another rather important factor in greenhouses is the relative humidity, which will be discussed in detail in the next section.

2.4.3 Relative Humidity

As the relative humidity will not be included in this study, only a brief discussion will be given. The rate at which plants take up water, rate of latent heat transfer and certain diseases are all dependent on the relative humidity. Relative humidities between 20 and 80% are necessary for normal plant growth, if the plants have well developed root systems. To avoid water stress conditions, a relative humidity of 40% and above is preferred [21]. Generally, transpiration increases with decrease in relative humidity. Wilting is the result of very low humidities (less than 20%) as evaporation losses are higher than the plant can replace. This occurs often when light intensities are high. Pathogenic organisms prefer high humidity; many will only germinate when the relative humidity is higher than 96%. Many also require a film of water on the leaves. Little or no air movement is also favourable for disease, as evapotranspiration from the leaves increases the relative humidity in interfoliage air. In this case, the still air surrounding the plant may be much wetter compared to the rest of the atmosphere.

From this discussion on indoor climate, it can be seen that temperature, velocity and relative humidity have all profound effects on the crops inside greenhouses. Therefore care must be taken when controlling the indoor climate and all the above factors must be considered. Many studies have been performed, both experimentally and numerically on greenhouses. This will be the focus of the next section.

2.5 Greenhouse Research – Experimental Investigations

The indoor climate of greenhouses has been investigated for several decades. Initial studies in the 1950's focused on quantitative studies to investigate the possibility of increasing the commercial viability of these structures [22].During the 1960s and 1970s the main focus was on determining the energy consumption in glasshouses, and during the 1980s and 1990s the focus shifted toward studying climate control and especially ventilation performances [56]. Amongst several experimental methods used to conduct research on greenhouses tracer gas techniques, reduced and full scale greenhouses are often used. Numerous strategically placed sensors, and energy balance methods are often used. This section pursues the objective of determining whether there are any research areas that require further detailed investigation.

2.5.1 Research in Full-Scale Greenhouses

Research in full scale greenhouses have two major purposes. Firstly, to accurately quantify the indoor climate, detailed measurements of the spatial and temporal distribution of the climatic variables are required. A few examples of research in this regard is by Shilo et al [57], Fatnassi

et al [58], Katsoulas et al [59] and Kichah et al [60]. Secondly, numerical models are often validated using results obtained from full-scale models. Although the current research presented in this thesis does not involve experiments in a full-scale greenhouse, some relevant research will be discussed in this section. The route that was taken in this study was to use a scale model of a greenhouse to validate numerical work. One reason for opting with a scale model was that it was easier to control the ambient conditions of the environment when testing. Only a limited budget was made available to conduct experimental work. The experimental work was extended numerically to a full scale greenhouse after confidence in the numerical model had been established.

The convective heat transfer coefficient on the inside and outside of the greenhouse cover was determined by Papadakis et al [61]. The method was based on the energy balance of the greenhouse cover. Results showed that at moderate wind velocities, mixed convection is the dominant convective heat transfer mechanism. Pure free convection is always found on the inside of the cover for instances when the vents are closed, i.e. the air velocity inside the greenhouse is low.

Another study by Kittas et al [62] attempted to quantify the ventilation of a glass covered greenhouse with a roof opening. Their results indicated that as wind speed increases, the effectiveness of ventilation decreases in a non-linear manner. The type of opening and the greenhouse dimension influence the calculation of the ventilation flux. If the wind was perturbed by an upwind windbreak, the ventilation effectiveness also seems to increase.

Ould Khaoua [49] investigated ventilation efficiency on a four-span Venlo-type greenhouse. Both physical experiments and some CFD were conducted. Air exchange rate was measured using nitrous oxide gas. Data were also recorded for the model boundary conditions in the CFD model. The data was also used to validate the numerical models. The study showed the numerical temperature and velocity profiles, as well as the experimental data collected inside the full-scale greenhouse that was used for the boundary conditions in the simulations. The data and results found in this paper will be used as a basis for the numerical work to be conducted later in this study. The numerical work utilizing the data in this article will include the effect of bench arrangements and differences between two and three-dimensional models.

Although full-scale experiments are quite useful, experiments in full-scale greenhouses are expensive and time-consuming. Scale models have been used traditionally together with wind tunnels to determine wind and structure interactions during the design stage of agricultural buildings [24]. As a scale model of a multi-span greenhouse is investigated in this study, the next section will deal with research done on reduced scale greenhouses.

2.5.2 Research on Scale Models

Although research on full-scale greenhouses revealed valuable insights into the ventilation and indoor climate, it is not always feasible to conduct full-scale studies. A substantial amount of sensors are required to map the climatic parameters inside greenhouses. To overcome these difficulties, scale models are traditionally used to investigate the indoor climate of greenhouse resulting from various configurations. Another advantage of using scale models is that the airflow characteristics can be controlled when testing in wind tunnels [43]. More recently, scale models have also been utilized to validate numerical models.

One of the first physical experiments on airflow in greenhouses was conducted by Businger [63]. The air circulation inside a small glasshouse was investigated and used to estimate ventilation magnitude for various ventilation strategies using a heat balance over the glasshouse.

Montero et al [64] used a 1/15 scale model replica of a greenhouse to investigate the effect of ventilator configuration on wind-driven ventilation in a single-span greenhouse. They immersed the Perspex model in a flume tank (containing a free surface) filled with water, and investigated four different ventilator configurations. Flow visualization was realized by seeding the flow with white pliolite particles. The particles were illuminated using a thin light sheet created by a silver-coated mirror and an arc lamp. Their results indicated that roof ventilation only resulted in the lowest ventilation rate, while the maximum ventilation rate was achieved with a combination of side-wall and roof openings.

Oca et al [65] studied thermal effects in a tunnel greenhouse using scale-models immersed in a water tank. Density differences due to heating of the greenhouse air were simulated by injecting salty water and black dye. Additional experiments were conducted to determine the minimum allowable value of the Reynolds number to neglect viscosity effects. They found that this method does not permit the simulation of the heat loss through the greenhouse glazing material, and can be responsible for differences between the scale model and the full scale greenhouse fluxes. This can occur if convection losses are a considerable percentage of the heat losses due to ventilation.

A reduced scale model of a confined greenhouse was used by Lamrani et al [3] to characterize the two-dimensional airflow and temperature patterns corresponding to a single cell Rayleigh-Bénard convection pattern. The greenhouse was designed to reproduce free convection generated above a plant canopy heated by solar radiation in a full-scale multi-span greenhouse. Some of the conclusions stated that for low Rayleigh numbers and during a transient regime, a flow pattern can be observed which briefly takes the form of two counter rotating cells. For

higher Rayleigh numbers in the permanent regime, a more stable convective mode was observed, with a single roll occupying the entire volume. A single cell was observed for steady and turbulent flows. The authors proposed that the Nusselt correlation found in the investigation can be used to calculate the exchange coefficients in greenhouses without crops or with a low crop under moderate solar radiation. The previous mentioned study was extended by investigating the effect of roof ventilators on the natural ventilation in the same greenhouse by Boulard et al [66]. The results from this investigation can useful for validating numerical models to some extent later in this study.

A one-tenth scale model was created by Montero et al and immersed in a water tank [64]. Buoyancy driven flow was simulated by adding a salty solution to the water through the floor of the model. The flow was visualized inside the scale model, and stagnant regions where heat accumulated were identified. The effect of insect proof screens was also investigated, and the importance of roof and sidewall combinations was emphasized, especially when insect-proof screens were used.

Munoz et al [67] used both a full scale and reduced scale model to determine and model the air exchange rate of greenhouses with insect-proof screens. Experimental tests were carried out in a multi-span tunnel greenhouse, while a 1:3 scale model was used to calculate discharge coefficients.

This section has demonstrated the usefulness of scale models in the investigation of greenhouses. The current study will also utilize a reduced scale model to validate a numerical model of a greenhouse. The next section will discuss the use of numerical models in greenhouse investigations in more detail.

2.6 Greenhouse Research - Numerical Studies

With recent advances in computing power and data space, Computational Fluid Dynamics (CFD) has become a popular numerical method for characterizing the climate distribution inside greenhouses. A major advantage of using CFD is that it enables the investigation of useful parametric studies on for example large scale buildings without the need for physical alterations to the greenhouse. CFD also yields a detailed description of the various flow parameters, thus avoiding the use of intrusive measuring equipment. CFD also solves the complete momentum, energy and mass transport equations, resulting in a fairly large amount of information on the flow field. Achieving this with experimental work would be extremely costly and time-consuming. The success of using CFD however depends on the correct physical modelling of the problem, for example the definition of the boundary conditions. Some studies

addressing various aspects of greenhouses using numerical modelling will be discussed in this section. Although numerous studies have been conducted previously, there is still room for improvement, as well as various aspects that can be investigated using numerical models. Examples are heat transfer characteristics, differences between two and three-dimensional models of greenhouses, the influence of bench arrangements, as well as an integrated focus on parametric CFD studies aiming at improving the thermal design of complex geometrical greenhouses.

2.6.1 Buoyancy driven flow

The main driving forces for air flow in greenhouses are thermal buoyancy and wind-induced forces (also known as wind or stack effects) [2]. Pressure gradients are caused by heterogeneous temperature and humidity distributions induced by buoyancy forces [43]. Flow in confined greenhouses (as is the case during winter) is almost exclusively governed by buoyancy driven flow due to warm transpiring plant leaves and warm soil [3] . A situation often encountered in greenhouses is where the largest part of the incident solar radiation is absorbed close to the soil level. This represents the case for a young crop or a very tall greenhouse. This gives rise to the well-known Rayleigh-Bénard convection, as the lower portion of the greenhouse (soil) is warmer than the roof slopes and the walls. Rayleigh-Bénard convection of cavities similar to greenhouses will be investigated in this study, in order to evaluate the thermal performance of these structures.

Simulating buoyancy driven flows using CFD has its challenges. When simulating buoyancy driven flow in ventilated cavities, the domain size, inlet position, cavity size and heat distribution all influence the predicted heat transfer coefficient and heat transfer rate [68]. Simulation accuracy depends on the size of the computational domain. Natural ventilation in large buildings, containing multiple inlets and outlets should contain a computational domain larger than the physical size of the building adding to the complexity of the CFD simulation.

Buoyancy driven flow is often considered as a rather difficult situation for greenhouse cooling. Experiments have shown that a wind velocity higher than 2m/s dominates the ventilation process, and the influence of temperature differences can be ignored [69]. But for cases with a low wind velocity (smaller than 0.5m/s) thermally driven ventilation is significant.

The internal convective flows inside a closed greenhouse generated by buoyancy forces were for example studied by Tadj et al [70] in a tunnel greenhouse containing a crop and heating pipes. The indoor climate was studied using CFD for three different locations of the heating pipes. The same energy output was modelled and results showed that there was no significant difference in mean air temperature for the three heat pipe positions.

Mistriotis et al [71] analysed the efficiency of natural ventilation in single and multi-span greenhouses at low wind speeds, when air temperature differences constituted the main driving force. Various ventilator configurations were investigated using computational fluid dynamics. The models included realistic representations of heat sources and boundary conditions. The significance of roof and side-wall ventilators was confirmed using the results of this study.

In a study by Baeza et al [27] the role of sidewall vents on buoyancy driven natural ventilation containing insect screens was investigated using CFD. They investigated the effect of distance between opposing sidewall vents, as well as the presence of insect screens. Sidewall vents were found to be important in buoyancy driven flow cases, but of critical importance in smaller greenhouses(less number of spans). They recommended that large greenhouses be constructed relatively narrow to fully utilize sidewall vents. It was also found that when insect screens are used in combined ventilation; the air exchange rate was reduced, much more compared to wind-driven ventilation only.

As can be seen, several authors addressed buoyancy driven flow in greenhouses. In this current study, the course followed will be to first analyse the buoyancy driven flow in single span greenhouse, then gradually increasing the complexity of the problem to include a multi-span greenhouse. The next section will focus on situations were wind is the only driving force present.

2.6.2 Wind Driven Ventilation

The wind effect dominates ventilation for wind velocities higher than about 2m/s [69]. It was shown in previous research that ventilation resulting from wind exhibits three-dimensional behaviour [72].

Wind-driven ventilation was studied by Campen and Bot using three-dimensional Computational Fluid Dynamics (CFD) [72]. They also investigated the influence of two types of roof openings. Their results confirmed the linear relationship between ventilation rate and wind speed for a specific wind direction. They determined that a variation in wind direction of only 10° could increase ventilation up to 50% in certain cases. On average, the rollup window configuration was found to induce higher ventilation rates compared to the flap types (Refer to section 2.3.2)

A numerical investigation was conducted by Shklayer et al [73] to investigate the three-dimensional isothermal flow patterns and mass fluxes in a pitched-roof greenhouse. Both the standard k-epsilon and RSM turbulence models were used in the validation with experimental results. The standard k-epsilon gave adequate results for the pressure coefficients on the

glasshouse, and this model was used to calculate all the results. Results showed that for a wind blowing parallel to the ridge, the flow consists of two vortexes rotating in opposite directions that transport air mass in through the vents and deliver it to the windward half of the interior. For winds blowing at 15-75 degrees to the ridge direction, spiral type flow was observed. Ventilation rate was also found to be less reactive to wind direction varying from 45 to 90 degrees compared to a change from 0 to 45 degrees. The three-dimensional CFD greenhouse model in this research study also includes plant benches.

Natural ventilation due to wind forces only in twin-span greenhouse with continuous roof openings was studied by Haxaire [74]. Measurements were taken inside a full-scale greenhouse, and CFD was used to simulate the forced convective patterns. The presence of plants was modelled using a porous medium. It was found that climatic heterogeneity (non-uniformity) increased with height, and that the south side was colder and dryer compared to the north side of the greenhouse (northern hemisphere).

Majdoubi et al [75] investigated experimentally and numerically the airflow and microclimatic patterns in a one-hectare Canary type greenhouse. After validating their 3D CFD model with experimental results, it was used for exploring the inside air temperature, humidity fields, plant microclimates and transpiration. For a wind direction perpendicular to the side and roof openings, it was found that insect screens reduced the air velocity inside significantly, while the inside temperature and humidity increased, especially close to the crop canopy. It was found that for a low wind speed of 1.3m/s, the outside wind dictated the inside air flow direction. The temperature and humidity induced buoyancy forces create air loops which tend to improve the indoor climatic conditions and improved the rate of heat and water vapour evacuation.

Ventilation efficiency of a multi-span greenhouse was numerically investigated using CFD by Lee et al [76]. They considered various structural greenhouse types. Their results indicated that ventilation rates are strongly affected by the wind direction. A wind parallel to the ventilators was found not be beneficial and produced a low ventilation rate. The Venlo-type greenhouse was found to have the lowest ventilation rate.

Boulard et al [77] used three-dimensional CFD to investigate the climate and fungal spore transfer in a rose greenhouse. Their results showed that that in the absence of sporulation within the greenhouse, the air exchange mechanisms between the inside and outside of the greenhouse are vital for determining the inside transport and distribution of the fungus and the distribution of the inside climate. High ventilation rates during daytime are advantageous for inoculums deposition, as well as proximity to the windward vent openings. High air humidity promoting the development of the mould is met during the night.

In a study by Wang et al [78], the microclimate inside a typical plastic greenhouse was investigated using three-dimensional CFD models. A radiation model was included, as well as a fractal permeability model to simulate the crop. Good agreement was found between the experimental and numerical results. They also found that airflow patterns, temperature and humidity profiles were different from those found in a sawtooth Mediterranean-type greenhouse.

Bartzanas et al [33] investigated the effect of vent arrangement on windward ventilation of a tunnel greenhouse using CFD. A numerical model was constructed and validated against experimental data collected in an identical greenhouse. The CFD model was modified to investigate the influence of four different vent arrangements on the natural ventilation. The results indicated that for evaluating the performance of various ventilation systems, the best criterion is not necessarily the highest obtainable ventilation rate. Other criteria that should be taken into consideration as well are air velocities and corresponding aerodynamic resistance in the region covered by the crop and air temperature differences between the inside and outside of the greenhouse. These criteria led to the conclusion that a combination of roof and side openings provides an appropriate solution for ventilation.

A systematic ventilation analysis using CFD has been carried out by the same authors [79]. The length of a Mediteranean-type greenhouse was varied and the influence on the ventilation was examined numerically after validation with experimental results. Comparison of the numerical results with full-scale and wind-tunnel results showed good comparison when a two-scale k-Ɛ turbulence model was used. The results indicated that ventilation seems to be more efficient for shorter greenhouses compared to longer ones up to 50 meters. The conclusions can unfortunately not be generalized, as it concerns only the above-mentioned type of greenhouse. An important conclusion regarding greenhouse design was drawn – ventilation efficiency can be improved by internal separating walls of a greenhouse where only a single roof ventilator is open.

The previously discussed studies indicate that numerical models can be used to investigate wind driven ventilated greenhouses successfully. Three-dimensional CFD models were used successfully to investigate the indoor climate of a greenhouse. In this research study, the three-dimensional CFD model is used to investigate the effects of plant benches on the indoor climate on the indoor climate of a large Venlo-type greenhouse. The next section discusses the influence of internal obstructions typically found in greenhouses.

2.6.3 Plant Benches and Partitions

An important factor in commercial greenhouse is the efficient utilization of the space within the greenhouses, which is based on the maximum amount of growing area achieved [80]. Floors as well as plant benches are commonly used. Floors are advantageous in some cases, especially when used in conjunction with ground floor heating systems. In order to achieve even water distribution the cement must be laid exactly level.

Various raised bench arrangements are frequently used in multi-span greenhouses, such as longitudinal and peninsular arrangements. Movable plant benches are [79] also gaining popularity as they can increase the usage efficiency up to 90%. But these plant benches cannot be used in a retail setting, or where frequent access to the plants is required.

Each type of arrangement has its advantages and disadvantages however. For example, the peninsular bench layout results in a greater growing area compared to longitudinal, but routine tasks such as watering become cumbersome with the longitudinal arrangement [80]. A disadvantage of growing plants directly on the floor is additional strain on employees as they have to work in an awkward position.

Airflow was modelled through perforated plant benches in a study by Jacobsen and Nielsen [81]. It was found that plant shape and leaf area index (LAI) have minimal influence on the vertical ventilation flow of a perforated bench. In another study by Sethi and Dubey, the space inside a small greenhouse is optimised by developing a multi-rack tray system [82]. The authors developed a thermal model that can assist in predicting the soil, plant and room air temperature as a function of location and time of the year.

To the author's knowledge, not too many studies on naturally ventilated greenhouses included the effects of plant benches. The study conducted by Ould Khaoua [49] included plant benches, but the effects of the plants were ignored as they were quite young. The study was done using two-dimensional CFD, therefore the 3D effect of the plant benches was not taken into account. There is scope for more detailed research in this area, such as using three-dimensional CFD to determine the influence on the indoor climate, as is done in this study.

A few studies included the presence of a crop in their investigations; this is discussed in the next section.

2.6.4 Crop Influence

Natural ventilation results in air movement and directly influences convective heat exchange between the vegetation and the interior air (microclimate) inside a greenhouse. Studies have

shown that coupling between air temperature and humidity is affected by the combination between ventilation rate and the mechanisms involved in transpiration [58]. The local climate inside greenhouses is characterized by large temperature gradients, water vapour concentrations and leaf boundary layer velocities [58]. In a literature review conducted by Bournet and Boulard [43] it was found that crops placed in perpendicular rows to the airflow significantly reduced ventilation.

A simple model was developed by Fatnassi et al [58] to determine the inside air speed, ventilation and crop transpiration rates. The model was based on parameters obtained experimentally - temperature, humidity and radiation. Although reasonable agreement was found between the efficiency coefficients for ventilation and previously published results, the model has its limitations. It is only applicable in summer and in greenhouses with a mature crop, with a small temperature difference between the inside and outside.

Reichrath et al [83] conducted a CFD study on a glasshouse containing a tomato crop, and attempted to construct a model of the tomato crop canopy, and its influence on the glasshouse environment. They specifically investigated CO_2 dispersal, ventilation rate and temperature distribution. A simple, representative model of a commercial multi-span Venlo-type glasshouse containing a tomato crop was developed. The results showed good agreement with available data. Some unrealistic results were found at the boundaries of the model, and it was concluded that the boundary conditions of the representative part needed a more detailed investigation.

Air speed inside a greenhouse containing a tomato crop was found to be highly correlated to the external wind speed for a maximum roof opening angle, but little correlation was found for a minimum roof opening angle [26].

This section indicates the significant influence a crop presence can have on natural ventilation. The next section will focus on studies investigating larger, multi-span greenhouses.

2.6.5 Single and Multi-span Greenhouses

Depending on the application, greenhouses can either be single or multi-span. Multi-span greenhouses are often used in large plant production facilities. Detached greenhouses have certain advantages over multi-span greenhouses. It is claimed that detached greenhouses are easier to ventilate, and that light entering the greenhouse is distributed relatively uniformly [29]. Caring and maintenance are also less tiresome compared to connected structures. Multi-span greenhouses on the other hand need less land area, fewer construction materials are required, and less heat is required as there are less exposed wall surfaces. Unfortunately, the air velocity and indoor climate inside large greenhouses vary considerably, which could interfere

with crop growth [30]. Multi-span greenhouses were also found to have a reduction in ventilation rate – Molina-Aiz [38] found that increasing the number of spans from 1 to 5 reduces the ventilation rate with 88% as a result of the increased width of the greenhouse. Tunnel greenhouses were investigated by Munoz et al [67] and Baeza et al [27], an Almeria-type greenhouse was studied by Molina-Aiz et al [84].

Lee-side ventilation-induced air movement was experimentally investigated by Wang et al [53] in a large 12 span Venlo-type greenhouse. It was concluded that horizontal air velocities at various locations were proportional to the external wind speed and the opening angle. It was also found that the airflow in the horizontal plane was of low turbulence with large eddies. Reichrath et al [85] conducted CFD simulations in order to validate the pressure distributions on the roof of both a 52 span and 7 span Venlo-type glasshouse. Each glasshouse simulation was conducted using both the standard k-epsilon turbulence model and the RNG turbulence model. They found acceptable agreement between the predictions and the experimental results. The authors concluded that the current approach as described in the paper was acceptable for simulating pressure and airflow around a large commercial greenhouse, and that the ventilation process could also be modelled.

Ventilation efficiencies of naturally ventilated multi-span greenhouses located in Korea were investigated by Lee et al [86]. The tracer gas decay method has been used to quantify the ventilation efficiency, and CFD to visualize the flow patterns. Their initial results showed that of the four types of multi-span greenhouses investigated, wind direction have a smaller influence on the ventilation rate in Quonset-arch greenhouse. The Venlo-type greenhouses containing individual roof vents were also less influenced compared to a Venlo-type greenhouse containing continuous roof vents.

In this study, one of the objectives is to study a multi-span greenhouse containing two spans both experimentally using a reduced scale model as well as numerically.

2.7 Challenges Encountered in CFD Studies

Previous CFD studies on greenhouses have been limited by assumptions made and inadequate modelling techniques [24]. But with recent developments in computer technology it is now possible to conduct full three-dimensional studies. Since most commercial codes are designed for robustness and not particularly for accuracy, it is imperative that the solutions be tested for accuracy. A challenge often encountered in buoyancy-driven flows in enclosures is the inherent unsteady behaviour which causes convergence problems when steady RANS calculations are

used. This is particularly observed when higher-order convection schemes and fine meshes are used [87]. A few other challenging aspects to be taken into consideration when using CFD to create a numerical model are discussed in the next sections.

2.7.1 Turbulence Modelling

Previous studies have indicated the turbulent nature of natural ventilation flows in greenhouses [23]. Turbulent flow has an influence on plant growth, and therefore careful modelling of the fluctuating component of the flow is necessary. CFD could be useful in the design of the ventilator openings (size, position and shape) to ensure smooth mixing of outdoor air with indoor air especially at crop level. Thus deciding on the correct turbulence model is of particular importance. Three turbulence models (the standard k-ε model, the renormalisation group (RNG) model and the realizable k- ε model) were tested by Roy et al [88] for natural ventilation in a tunnel type greenhouse. The RNG model resulted in more homogenous climatic conditions in the tunnel compared to the other two turbulence models. The accuracy of the same three models was tested by Nebbali et al [89]. They compared experimental and numerical values for temperature and humidity, and found that all three models performed satisfactory. The standard k-epsilon model was found to give the lowest error value compared to the two other models mentioned by Nebbali.

2.7.2 Y+ Criterion of Turbulence Models

Another important parameter to consider is the near wall modelling assumptions for each turbulence model. For each RANS turbulence model, the y+ criterion must be observed to ensure proper modelling of the flow in the boundary layer. In order to ensure that the y+ criterion is observed, the mesh in the boundary layer must be adjusted otherwise significant errors may result. The low-Reynolds number approach for example, is valid throughout the boundary layer, including the viscous sublayer [90]. Therefore a sufficiently fine mesh is required, which can be computationally expensive for large Reynolds numbers.

2.7.3 Mesh Independent Solutions

Unstructured and hybrid meshes make efficient solutions possible in cases where complex geometries are involved. Increased computing power also enables users to apply local mesh refinement more efficiently, which captures flow features without creating distorted cells as those created in structured meshes [24]. To design a suitable quality CFD model, mesh refinement is a requirement to ensure a grid independent solution can be obtained (or at least as close as possible). It is therefore necessary to monitor the solution progress and residual errors.

2.8 Natural Convection in Enclosures

Natural convection is the dominant mechanism in numerous engineering applications and naturally occurring processes, and has been a topic of considerable interest over the past few decades. Examples of applications are pollution, materials processing, solar receivers, energy storage systems, grain storage and the design and construction of indoor environments such as buildings and greenhouses. Specifically, natural convection in dry, floor heated cavities has direct application in numerous processes such as boilers and large-scale geophysical phenomena [3]. As Rayleigh-Bénard convection was investigated in previous studies and heat transfer characteristics in greenhouses are included in the objectives, natural convection will be briefly reviewed in this section.

Convection can be divided into two basic processes – forced convection where the motion of the fluid arises from an external agent (fan, wind, motion of heated object) and natural convection that occurs if no external agent exists to induce the flow, the flow arises "naturally" from the effect of a density difference (due to a temperature/concentration difference in a body force field such as gravity) [91]. The flow in the last mentioned process is due to buoyancy forces produced by density differences. The flow in natural convection is the result of an interaction of the density difference with the body force in the field – which is gravitation in this case.

Crop production in greenhouses is mainly influenced by photosynthesis and transpiration. These two processes are governed by radiative and convective transfers. The processes involved are rather complicated since both free and forced convection modes may be present. In greenhouses, convective exchange occurs between the cover, soil, vegetation and the interior air. Convective exchanges occur also between the cover and the exterior air. A combination of forced convection (due to, wind pressure) and free convection (due to buoyancy) governs the heat transfer process. When a greenhouse is well ventilated, forced convection is the dominant mode, while in closed greenhouses free convection is the dominant process [56].

The scientific literature concerned with convective and ventilation transfers in greenhouses were reviewed in a two part paper by Roy et al [56]. They summarized the relevant literature where a simplified scheme was used by assuming the greenhouse climate is homogenous. The convective transfers include heat and mass transfers between the air and solid surfaces (walls, roofs and leaves) as well as air, heat, water vapour and tracer gas transfers to or from the inside air. The second part of the study [92] reviewed the scientific literature relative to convection and ventilation processes in greenhouses involving studies of distributed climates.

The complexity involved in the analytical and experimental study of natural convection is due to the flow being intrinsically linked and dependent on the temperature and/or concentration fields. At the onset of natural ventilation the motion is unknown and needs to be determined from heat and mass transfer processes, which are in turn linked to fluid flow mechanisms. Compared to forced convection, velocity and pressure differences encountered are usually much smaller [91]. Another difficulty when dealing specifically with natural convection in enclosed spaces is the boundary layers forming near the walls, which encloses the external region. This enclosed region forms a core region which is partially or fully encircled by the boundary layers. The core region is dependent on the boundary layer, which in turn is influenced by the core. A significant complexity is imposed on the problem because of the interactions between the core and the boundary layer [4]. It is often found that several global core flows and flow subregions exist (cell and layers) which are embedded in the core.

Numerous studies have been published on natural convection in enclosures of various shapes and sizes, and different boundary conditions. Studies on square and rectangular enclosures are of particular interest as the core design basis of the greenhouses considered can be found in the square and rectangle. Some of the relevant research will be discussed in the following section, specifically research pertaining to Rayleigh-Bénard convection, which is the classic problem of thermally driven convection in enclosures heated from below and cooled from above.

2.8.1 Square and cubical cavities

Square cavities are of prime importance in certain applications, and have therefore been investigated quite often as seen in the literature [93], [94], [95], [96] [97]. Studies focusing on natural convection in square cavities heated from below are of particular interest in this study.

Basak et al [4] studied the effects of thermal boundary conditions on natural convection flows within a square cavity using a penalty Finite Element Method. The floor was subjected to uniform and non-uniform heating. They studied cases over a wide range of Rayleigh and Prandtl numbers. It was found that increased heat transfer rates at the center of the bottom wall were produced with non-uniform heating compared to uniform heating. It was also shown by average Nusselt numbers that overall lower heat transfer rates were obtained for the non-uniform heating case.

A thorough study consisting of both experimental and numerical work was performed by Baïri [98]. A square cavity at various inclination angles and Rayleigh numbers was investigated. Results were found to agree reasonably well with results published in the literature. For all values of the Rayleigh number investigated, it was found that the inclination of the cavity played a major role in the convective exchanges. Another author [99] investigated tilted square

cavities. They found that in general the mean Nusselt number increases with increasing Rayleigh number for all inclination angles that were examined, and increases with increasing Prandtl number for the same Rayleigh number. It was also found that with increasing inclination angle, the Nusselt number decreases significantly for all Rayleigh and Prandtl numbers.

Leong et al [100] attempted a physically-realizable experiment in a laboratory to be used for CFD validation. A cubical air-filled cavity with one pair of opposing faces at different temperatures, the remaining faces with a linear variation from the hot all to the cold wall. The cavity was tilted at various angles and Nusselt numbers were measured and found to be within an average deviation of 0.3% when compared to the CFD code used.

A three-dimensional numerical investigation on tilted Rayleigh-Bénard convection has been completed by Crunkleton and Anderson [101]. Their results indicated even a small tilting of the cavity could mask the critical Rayleigh number transition in low Prandtl number fluids.

2.8.2 Rectangular Cavities

Natural convection in shallow enclosures has been studied extensively due to its importance in fundamental fluid mechanics and heat transfer. Flow visualization of the roll patterns in Rayleigh-Bénard convection was performed by Lir and Lin [102]. Baïri et al [103] conducted both experiments and numerical simulations in a tilted parallelepipedic cavity for large Rayleigh numbers. Relatively good agreement was found between the numerical results and the measurements taken.

Corcione [104] numerically studied natural convection in rectangular enclosures heated from below and cooled from above. Several different thermal boundary conditions were applied at the sidewalls. Some of their main conclusions were that the heat transfer rate increases as each adiabatic sidewall is replaced by a cooled/heated sidewall. For each geometrical configuration investigated they found it is characterized by a specific Rayleigh number over which the heat transfer rate from any heated/cooled sidewall is independent of the boundary conditions assumed at the opposite wall.

In a paper by Zaman et al [105], a two-dimensional rectangular enclosure with two discrete heat sources from below was studied. As the Rayleigh number increased, it was found that the flow rate increased in both clockwise and anticlockwise directions. The local heat transfer rate from the heat sources increased as well. A slight difference in heat transfer rate from the two sources was observed at higher Rayleigh numbers.

Said et al [106] studied turbulent natural convection in an inclined rectangular enclosure. They utilized the low-Reynolds number k-epsilon model to model turbulence. The effect of angle of inclination, Rayleigh number and number of partitions was studied. It was found that the standard k-epsilon model with wall functions yielded higher heat transfer predictions, while the low-Reynolds extension of this model agreed well with experimental results. The average Nusselt number was significantly reduced when a single partition was inserted, and decreases with the addition of more partitions. They also determined an optimum angle of inclination for the highest Nusselt number.

2.8.3 Open Cavities

Cavities open to the atmosphere have many applications in engineering. Some examples are solar chimneys, double facades, Trombe walls and ventilated greenhouses containing roof and/or side ventilators. These cavities are often used in buildings for passive heating and natural ventilation. Many studies utilized either or both numerical and experimental techniques to investigate the heat transfer in open cavities [107], [108]. A greenhouse containing roof and/or side vents can be approximated as a cavity open to the atmosphere containing buoyancy-induced flow.

Fontana et al [109] for example investigated a two-dimensional partially open square cavity containing an internal heat source. The thermal and fluid dynamics were found to be severely influenced by the presence of the heat source, the opening size and temperature difference between the vertical walls. When the flow is mainly controlled by the heat source, large secondary circulations were found inside the cavity. When the temperature difference controls the natural ventilation, the size of the secondary circulation is negligibly small compared to the main circulation.

The effect of opening ratio on the convective loss was investigated for cubical, spherical and hemispherical cavity shapes by Prakash et al [110]. It was found that the natural convection loss increases with the increase in cavity wall temperature. An increase in cavity inclination resulted in a decrease in loss. The hemispherical open cavity with opening ratios of 0.5 and 0.25 has the highest natural convection loss compared to the other cavities.

The transient characteristics inside an open-ended cavity were thoroughly researched by Vafai and Ettefagh [111]. It was concluded that the oscillations of central vortex inside the cavity is directly responsible for the periodic oscillations in the Nusselt number. The frequency of the oscillations for the Nusselt number and the central vortex were found to be equal. It was established that the frequency of the oscillations of the central vortex was directly related to the Rayleigh number.

Polat and Bilgen [112] investigated laminar natural convection in inclined shallow cavities containing an opening. The side facing the opening was heated by a constant heat flux. Volumetric flow rate was found to be increasing as the aspect ratio and Rayleigh number. As the Rayleigh number increased, the heat transfer for a specific aspect ratio exhibited asymptotic behaviour. For shallow cavities, the transition is delayed at higher Rayleigh numbers.

The parametric ranges of the applicability of the Bejan similarity solution for an open cavity was evaluated by Boetcher and Sparrow [113] . One of the main objectives of the study was to determine the validity of an existent similarity solution. Within the parametric ranges investigated, the authors could not obtain any conditions for which the similarity model was valid. They have also investigated the extension of the solution domain into the external space adjacent to the cavity opening, the boundary conditions applied at the surfaces of the solution domain, and lastly the mesh density. Numerical results indicated that the highest Nusselt number values were found in the vicinity of the channel opening.

2.8.4 Partitioned Cavities

Greenhouses are often compartmentalized to create different environments inside the same greenhouse if different types of plants are cultivated. Natural convection in partitioned enclosures with localized heating from below was investigated by Ntibarufata et al [114] . It was found that natural convection dominated heat transfer when the length of the heat source is increased and positioned more to the centre of the enclosure. For a given Rayleigh number they concluded that heat transfer was minimally influenced by the position of the partition and its length. Lastly results showed that for a given condition, for a smaller aspect ratio, heat transfer is improved.

Cavities containing partitions were addressed by a few authors. Alamiri et al [115] focused on buoyancy-induced flow in a partially divided square enclosure. The enclosure contained an isothermal heater protruding from the bottom surface. Height, width and location of the heater were varied to study their effect on flow patterns and heat transfer. A significant effect on the flow patterns, temperature fields and heat transfer was observed. In particular it was noticed that heater height, width and location increased the average Nusselt number. A partitioned cavity with differentially heated vertical and conducting horizontal walls was investigated by Ampofo [116]. Local and average Nusselt numbers were found to be decreasing, therefore reducing the heat transfer along the hot wall for the particular partitions investigated.

2.9 Conclusion

The literature review highlighted the complexity of the mechanisms involved in naturally ventilated greenhouses, especially situations where buoyancy driven flow are present. The literature reviewed indicated the use of various experimental methods for investigating the indoor climate of greenhouses. It was shown that the use of scale models can also be quite beneficial to obtain information about the microclimate and flow patterns inside these structures. Although rectangular and square enclosures have been a popular research topic, there are none or very few published on enclosures similar to a greenhouse structure.

CFD is a useful tool to investigate various aspects of greenhouses. The effect of size and shape, orientation, ventilator positions and opening angle on the distributed climate inside greenhouses has been investigated using CFD. Some caution should be observed however when creating the CFD the model, as certain criteria have to be met depending on the turbulence model. A mesh independence study is also a necessity. In this research study, the use of the standard k-epsilon low-Reynolds number turbulence model will also be investigated, as the studies investigated by the most authors used only the standard k-epsilon turbulence model.

A few articles have been identified that will be used as a basis for the CFD models developed in this study. Various authors presented results for natural convection in a square or cubical enclosure. A study by Baïri [98] will be used as a basis for the natural convection studies, and results for a three-dimensional cube by Küreckci [117] will be used to validate natural convection in a cube. A scaled-up greenhouse was investigated by Lamrani [3], and will be used to qualitatively validate a two-dimensional cavity representing a single-span greenhouse. Results obtained by Ould Khaoua et al [49] will be used for the validation of the final full-scale multi-span greenhouse CFD model that is developed in this thesis. These specific articles provide useful data that can be used to systematically analyse the greenhouse commencing with a simple square cavity, and gradually increasing the complexity to a full-scale multi-span greenhouse.

The next chapter provides the theoretical background required to analyse the heat transfer characteristics and utilize the CFD software that is also commercially available. A general background pertaining to CFD will be given, and the relevant theory will be discussed. A background on experimental methods used in this research study will also be given.

CHAPTER 3

Background on Numerical CFD and Experimental Methods

3.1 Chapter Review

The previous chapter summarized significant aspects of greenhouse design, the indoor climate and important research published in the last few decades. Some research gaps were identified from the literature review including aspects of experimental and numerical simulation of greenhouses and design aspects thereof. As this investigation will therefore be both numerical and experimental, this chapter establishes the fundamental background required for the investigation techniques used in this thesis. A brief background on Computational Fluid Dynamics as well as the relevant theory will be given. Finally reduced-scale modelling and flow visualization will also be presented to the extent to which it is deemed necessary for confirmation of aspects of the numerical modelling. The discussion in this chapter attempts to determine which numerical methodologies are available for fluid flow simulations specifically for use in thermal designs of greenhouses.

3.2 Introduction to Computational Fluid Dynamics (CFD)

3.2.1 Brief History of CFD

The use of Computational Fluid Dynamics has become a significant element in professional engineering practice, applied in various different branches of engineering disciplines. One of the most challenging problems in science and engineering is the task of obtaining solutions to the governing equations of fluid mechanics. This task was becoming less tedious and cumbersome due to advances in computer technology and the availability of increasing computing power since the early 1960's. CFD techniques have been integrated by the aerospace industry into the design, research and manufacturing of the aircraft and jet engines since the 1960's. Commercial software became available on the market in the early 1970's, establishing CFD as an important component as regards to engineering practice in industrial, defence and environmental organizations [118]. One of the first engineering problems attempted with the application of CFD methods was the simulation of transonic flows based on the solution of the non-linear

potential equation [119]. The first two-dimensional and three-dimensional Euler equations were solved during the early 1970's and 1980's. Currently CFD is extensively utilized in basic and applied research, design of engineering equipment, and the calculation of environmental and geophysical phenomena [118], such as for example in studies on turbidity currents by Nasr-Azadani [120], Some recent areas of applications of CFD software (specifically STARCCM+) include electronics, electric machines, marine engineering, oil and gas industry, building services and life sciences [121].

3.2.2 Governing Equations

The term "Fluid Dynamics" can be defined as the interactive motion of a large amount of individual particles [122]. In this case, the fluid consists of a large amount of molecules or atoms, leading to the assumption that the fluid can be regarded as a continuum.

The dynamic behaviour of a fluid is governed by the following conservation laws of physics:

- Conservation of Mass
- Conservation of Momentum
- Conservation of Energy

If a certain flow quantity is conserved, it implies that its total variation inside an arbitrary volume can be expressed as the net effect of the amount of the quantity being transported across the boundary of the volume, internal forces and sources and external forces acting on the volume [122]. Conservation of momentum or Newton's second law of motion implies the rate of change of momentum equals the sum of the forces on a fluid particle. Conservation of Energy is based on the first law of Thermodynamics, which states that the rate of change of energy is equal to the sum of the rate of heat addition to and the rate of work done on a fluid particle. The governing equations for the flow of a compressible Newtonian Fluids are shown in Table 3.1 [123].

Table 3.1: Governing Equations of the Flow of a Compressible Newtonian Fluid [123]

Continuity	$\frac{\partial \rho}{\partial t} + \mathrm{div}(\rho \bar{u}) = 0$	3-**1**
x-momentum	$\frac{\partial (\rho u)}{\partial t} + \mathrm{div}(pu\bar{u}) = -\frac{dp}{dx} + \mathrm{div}(\mu \mathrm{grad} u) + S_{Mx}$	3-2
y-momentum	$\frac{\partial (\rho v)}{\partial t} + \mathrm{div}(pv\bar{u}) = -\frac{dp}{dy} + \mathrm{div}(\mu \mathrm{grad} v) + S_{My}$	3-3
z-momentum	$\frac{\partial (\rho uw)}{\partial t} + \mathrm{div}(pw\bar{u}) = -\frac{dp}{dz} + \mathrm{div}(\mu \mathrm{grad} w) + S_{Mz}$	3-4
Energy	$\frac{\partial (\rho i)}{\partial t} + \mathrm{div}(\rho i\bar{u}) = -p\,\mathrm{div}\bar{u} + \mathrm{div}(k\,\mathrm{grad}\,T) + \Phi + S_i$	3-5
Equations of State	$p = p(\rho, T)$ and $i = i(\rho, T)$ e.g. perfect gas $p = \rho RT$ and $i = C_V T$	3-6

If a general variable φ is introduced, the conservative form of all fluid flow equations can usually be written as shown in Equation 3.7:

$$\frac{d(\rho\phi)}{dt} + \mathrm{div}(\rho\phi\bar{u}) = \mathrm{div}(\Gamma \mathrm{grad}\phi) + S_\phi \qquad 3\text{-}7$$

Equation 3-7 is called the transport equation for property φ. This equation emphasizes the various transport processes: the first term on the left-hand side is the rate of change term, while the second term is the convective term. The first term on the right-hand side is the diffusive term (Γ= diffusion coefficient) and the last term is the source term. Equation 3-7 can also be made to represent the internal energy equation by changing ϕ into T or vice versa, using the equation of state [123]. By setting φ = *1*,*u*,*v*,*w* or T and h_0, and selecting appropriate values for the diffusion coefficient and the source terms, the continuity, momentum and energy equations result.

The integration of equation 3.7 over a three-dimensional control volume (CV) is a crucial step in the finite volume method:

$$\frac{d}{dt}\int_{CV} \rho\phi dV + \int_A \mathrm{div}(\rho\phi\bar{u}) dV = \int_{CV} (\Gamma \mathrm{div}\phi) dV + \int_{CV} S_\phi dV \qquad 3\text{-}8$$

Applying Gauss's Divergence Theorem [123], equation 3-8 can be written as shown in equation 3-9:

$$\frac{d}{dt}\int_{CV}\rho\phi dV+\int_{A}\bar{n}.(\rho\phi\bar{u})dA=\int_{A}\bar{n}.(\Gamma\,\mathrm{grad}\,\phi)dA+\int_{CV}S_{\phi}dV \qquad 3\text{-}9$$

The first term on the left hand side indicates the rate of change of the total amount of fluid property φ in the control volume. The product in the second term expresses the flux component of the property φ due to fluid flow along the outward vector **n**, therefore the second term on the left hand side is the convective term, i.e. the net rate of decrease of fluid property φ of the fluid element due to convection. The first term on the right is the diffusive term and associated with a flux into the element. This term represents the net rate of increase of fluid property φ of the fluid element due to diffusion. The last term represents the rate of increase of property φ due to sources inside the fluid element [123].

3.2.3 Discretization Methods

It is nearly impossible to solve the previous mentioned equations or integral form thereof using exact analytical numerical methods for general cases. The spatial discretization of the Navier-Stokes equations is the numerical approximation of the convective and viscous fluxes and the source term [122]. This aids in providing a road to approximate numerical solutions to the transport equations. Anderson [124] defines discretization as "discretization is the process by which a closed-form mathematical expression, such as a function or a differential or integral equation involving functions, all of which are viewed as having an infinite continuum of values throughout some domain, is approximated by analogous (but different) expressions which prescribe values at only a finite number of discrete points or volumes in the domain". Spatial discretization can be subdivided into the following categories: *finite difference, finite volume and finite element* [119].

Finite Difference

One of the first methods applied to obtaining numerical solutions of differential equations was first used by Euler around 1768 [122]. This method is directly applied to the differential form of the governing equations, and describes the unknowns φ of the flow problem using point samples at the node points of a grid, consisting of co-ordinate lines. The finite difference approximations of derivatives of φ in terms of point samples of φ at each grid points are generated using truncated Taylor series expansions [123]. The method has the advantage that it is simple, and it is possible to obtain higher-order approximations relatively easy, enabling high-order accuracy of the spatial discretization. As the method requires a structured grid, a

disadvantage is the range of application. It can also not generally be applied directly in body-fitted coordinates – the governing equations are first transformed into the Cartesian coordinate system. Therefore the Finite Difference method tends to be applied only to rather simple geometries [122].

Finite Volume Method

The Finite Volume Method employs the integral formulation of the Navier-Stokes/Euler equations. This method was first used for the simulation of 2D inviscid flows [125]. The physical space is divided into a number of arbitrary control volumes. The first step is to perform the integration of the governing equations of fluid flow over all the non-overlapping control volumes. Mass, momentum and energy are automatically conserved since it is based on the direct discretization of the conservation laws. An important advantage is that the spatial discretization is carried out directly in the physical space to eliminate problems with transformation between coordinate systems [122]. The software used in this research study is based on the finite volume method.

Finite Element Method

The Finite element method is another numerical technique used to solve partial differential equations. The first step in the Finite Element Method is to subdivide the physical space into triangular (in 2-D) or tetrahedral (in 3-D) elements which form a grid. Complex geometries are handled with relative ease, as the grid itself doesn't have to be structured [126]. Simple piece-wise functions such as linear or quadratic functions are used to describe the local variations of unknown flow variables φ. The exact solution of φ satisfies the governing equations accurately. Substituting the piece-wise approximating functions for φ, it will not satisfy the equation exactly and a residual is defined to measure the errors [123]. The errors or residuals are then minimized by multiplying them by a set of weighting functions and integrating. A set of algebraic equations is obtained for the unknown coefficients of the approximating functions. The Finite Element Method was originally developed for structural analysis [127]. About a decade later the method was used for the numerical solution of field equations in continuous media [122]. In the early 1990's, the method became popular for solving the Euler and Navier-Stokes equations.

Spectral Methods

This method is not always generally used in practice, but a superior choice compared to the above mentioned methods in certain situations such as flow induced vibrations, strained two-dimensional wake flow and transition in rotor-stator cavity flow [123].

The unknowns are approximated using truncated Fourier Series or series of Chebyshev polynomials. Whereas the Finite Element and Finite Difference approaches are only valid locally, this approximation is valid throughout the whole computational domain [123]. The geometric flexibility of the Finite Element method is combined with the high-order spatial accuracy and rapid convergence of spectral schemes. The main disadvantage of this method is the high numerical effort compared to the previously mentioned methods [122].

Gridless Method

This method uses only clouds of points for the spatial discretization, and doesn't require the points to be connected to form a grid. It is based on the differential form of the governing equations, written in the Cartesian coordinate system. Using a specified number of neighbours surrounding a particular point, least-squares reconstruction is used to calculate gradients of the flow variables. The key advantage of the gridless method is its flexibility in solving flows involving complex structures, and locating the clouds of points where appropriate. It is however unclear whether conservation of mass, momentum and energy is actually guaranteed [122].

3.3 Solution Algorithms

One of the main steps involved in obtaining a numerical solution using CFD, is the construction of the overall calculation sequence. This procedure is used to solve the resulting set of algebraic equations.

The velocity field in fluid flow problems is generally not known, and must be calculated from the appropriate governing equations. The magnitude and direction of the local velocity field are directly linked to the convection of a scalar variable φ. The velocity field develops as part of the overall solution process. To illustrate this, consider the governing equations for two-dimensional laminar steady flow [123]:

$$\frac{\partial}{\partial x}(\rho uu)+\frac{\partial}{\partial y}(\rho vu)=\frac{\partial}{\partial x}\left(\mu\frac{\partial u}{\partial x}\right)+\frac{\partial}{\partial y}\left(\mu\frac{\partial u}{\partial y}\right)-\frac{dp}{dx}+S_u \qquad 3\text{-}10$$

$$\frac{\partial}{\partial x}(\rho uv)+\frac{\partial}{\partial y}(\rho vv)=\frac{\partial}{\partial x}\left(\mu\frac{\partial v}{\partial x}\right)+\frac{\partial}{\partial y}\left(\mu\frac{\partial v}{\partial y}\right)-\frac{dp}{dy}+S_v \qquad 3\text{-}11$$

$$\frac{\partial}{\partial x}(\rho u)+\frac{\partial}{\partial y}(\rho v)=0 \qquad 3\text{-}12$$

Solving equations 3-10 to 3-12 yields two new difficulties:

1. Non-linear quantities are included in the convective terms of the momentum equation
2. All the equations are essentially coupled since every velocity component appears in each momentum equation as well as the continuity equation. Pressure also appears in both momentum equations, but no other equation is presented for pressure [123].

This situation is typically applicable in buoyancy flow inside large cavities like greenhouses.

Before a numerical method can be formulated containing the velocity components and the pressure, the above mentioned difficulties must be addressed. The displaced or "staggered" grid is one method used to resolve the previously mentioned issues. The method is based on the notion that the velocity components can be arranged on grids that are different to those used for all the other variables. This method will solve the abovementioned problem.

The most widely-used solution algorithm for finite volume pressure based methods is the SIMPLE (Semi-Implicit Method for Pressure-Linked Equations) algorithm [128]. This is an iterative solution strategy which can eliminate both the previously mentioned problems. This method has been used as the basis for numerous methods as well as the SIMPLE procedure [129], which will be discussed next.

THE SIMPLE Algorithm

This is fundamentally a guess-and-correct procedure that was initially developed for the pressure calculation on the staggered grid arrangement by Patankar and Spalding [130]. Consider a typical node P(i,j) shown in Figure 3.1 with its surrounding control volume whose faces are located at e,w,n and s. This figure depicts the staggered grid arrangement – pressure and other scalars are stored/defined at the node P. But vectors are stored at the cell faces.

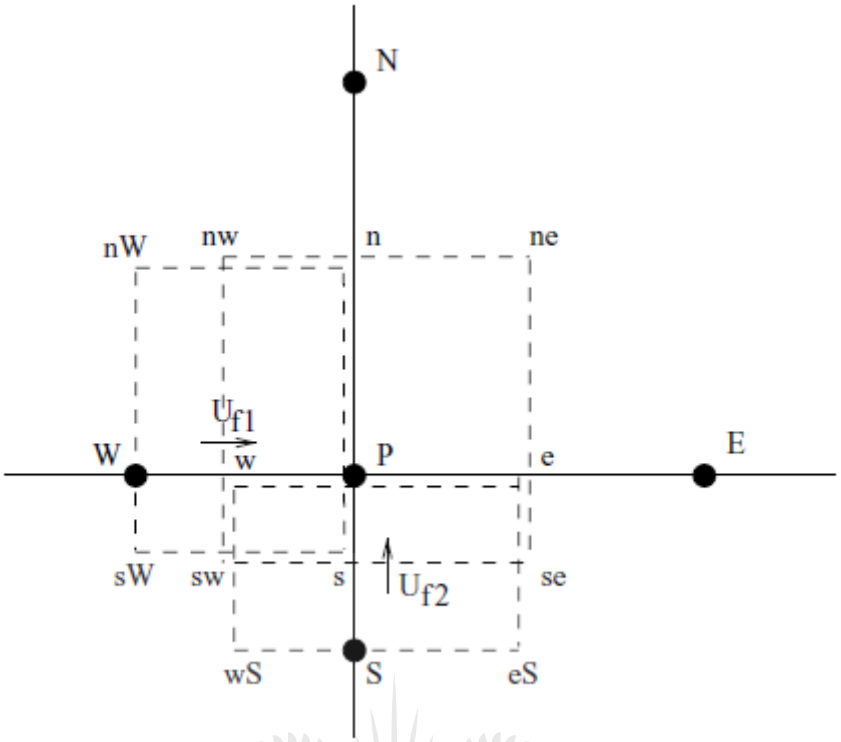

Figure 3.1: Staggered grid [118]

The basics steps in the approximate solution procedure or algorithm are as follows [118]**:**

1) An initial pressure field p* is guessed
2) The guessed pressure field is used to solve the discretized momentum equations to obtain the velocity components u* and v*
3) The SIMPLE method requires the conservation of mass for the control volume of a cell. The guessed pressure and velocity component field will in general not satisfy mass conservation over the cell control volume
4) To satisfy mass conservation over the control volume surrounding node P, a mass-conserving pressure-correction equation is derived
5) The calculated pressure correction p' is then used to correct the guessed pressure and velocities.

A complete description of the method and equations can be found in [131] and [123]. To model segregated flow, the SIMPLE solver algorithm is used to control the solution update by StarCCM+ [132], the software that is used in the research presented in this thesis.

Patankar improved the SIMPLE method by developing the SIMPLER (SIMPLE Revised) method. In StarCCM+, when the segregated solver is used, the solution update for the segregated flow model is controlled according to the SIMPLE algorithm.

3.4 Turbulence Modelling

Most or many flows encountered in nature and engineering are turbulent. The theoretical analysis of turbulence is perhaps one of the most fundamental problems of Computational Fluid Dynamics. Turbulence is by definition random and chaotic, leading to some major difficulties when solving for fluid flows [119]. Taylor and Von Karman [133] defined turbulence in 1937 as follows:

> "Turbulence is an irregular motion which in general makes its appearance in fluids, gaseous or liquid, when they flow past solid surfaces or even when neighbouring streams of the same fluid flow past or over one another"

Major aspects of turbulence are that a number of different length and time scales are usually involved at a high Reynolds number, it is fully three-dimensional and time-dependent. In contrast to laminar flow, turbulent flow is irregular and intermittent [133]. Some characteristics of turbulent flows are the following [134]:

- Randomness

Turbulent flow seems to be characterized by irregular, chaotic and unpredictable behaviour and consists of a range of various eddy sizes (scales). The largest eddies are of the same order as the flow geometry, while the smallest eddies are by viscous forces (stresses) dissipated into internal energy [135].

- Nonlinearity

Turbulent flows are highly non-linear which serves two purposes. Firstly it is responsible for exceeding a critical value of any relevant nonlinearity parameter (Reynolds number, Rayleigh number, inverse Richardson number). When the stability criteria are exceeded, the state becomes unstable, progresses to more complicated disturbances and eventually becomes chaotic. Turbulent flows are also responsible for vortex stretching, which is a major process by which vorticity is maintained in three-dimensional vortex flows [134].

- Diffusivity

Turbulent flows are characterized by a rapid diffusion of momentum and heat, caused by macroscopic mixing of fluid particles. This implies that for increasing turbulence, the spreading rates of boundary layers and jets for example also increase. An increase in turbulence increases momentum exchange in for example boundary layers, and could reduce/delay boundary layer

separation at bluff bodies. Wall friction is also increased by increasing diffusivity internal flows [135].

- Vorticity

Vorticity is defined as a vector field that yields a microscopic measure of the rotation at any point in a fluid [136]. High levels of fluctuating vorticity are present in turbulent flows. Visible structures in turbulent flow are termed "eddies". A large range of eddy sizes are found in turbulent flows [134].

- Dissipation

Due to the dissipative nature of turbulent flows, kinetic energy in the small eddies are transformed into internal energy. Therefore the energy transfer occurs on increasingly smaller scales, i.e. the smaller eddies extract their energy from slightly larger eddies, the larger eddies extract their energy from even larger eddies, and the largest eddies obtain their energy from the mean flow [135]. Therefore a continuous supply of energy is required by turbulent flows to make up for the viscous losses [134].

3.4.1 Types of Turbulence Models

A substantial amount of research effort has been and still is dedicated to developing numerical models which will accurately capture turbulence effects. Turbulence models are generally divided into five classes [119]:

- Algebraic
- One-equation
- Multiple-equation
- Second-order closures (Reynolds Stress Models)
- Large-Eddy Simulation (LES)

The first three models mentioned above are collectively known as the "*first order closures*" and are based mostly on the eddy-viscosity hypotheses. Figure 3.2 shows an overview of the various classes of turbulence models, which are sorted according to their decreasing level of complexity.

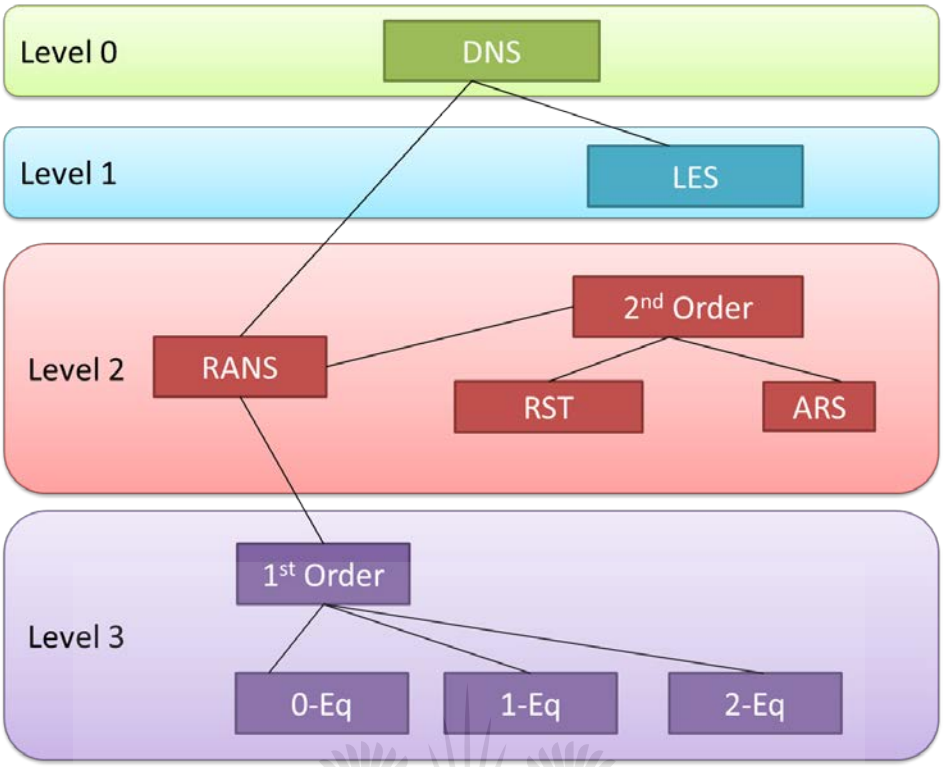

Figure 3.2: Hierarchy of turbulence models [119]

Abbreviations:

- DNS – Direct Numerical Simulation
- LES – Large Eddy Simulation
- RANS – Reynolds-Averaged Navier-Stokes
- 1-st Order – first order closures
- 2nd Order – second order closures
- RST – Reynolds-Stress Transport models
- ARS –Algebraic Reynolds-Stress models
- 0-,1-,2-Eq – zero –(algebraic) one, two-equation models

None of the above turbulence models are capable of predicting all kinds of turbulence flows. Some models fail at predicting separated flows, while it can predict attached boundary layer flow flawlessly [119]. The three main categories are discussed in more detail in the next section.

Turbulence models for RANS Equations (Reynolds-averaged Navier-Stokes Equations)

The focus is on the mean flow and turbulence effects on the mean flow properties. The Navier-Stokes equations are time averaged prior to the application of numerical methods. Due the interactions between various turbulent fluctuations, additional terms appear in the time-averaged (or Reynolds averaged) flow equations. Classical turbulence models are utilized to

model these terms: the most well-known model being the k-epsilon and Reynolds Stress model. This approach is the most common due to relatively modest computing resources required for reasonably accurate results [123]. One disadvantage of the models is that due to the averaging procedure, no detailed information is available about turbulent structures [119].

The RANS models can be divided into first- and second order closures. The Reynolds-stress Transport (RST) model is one of the second-order closure models, which are the most complex but flexible of the models. This method solves modelled transport equations for the Reynolds-stress tensor, and is capable of capturing the influence of streamline curvature or system rotation on the turbulent flow [119]. Another approach is the Algebraic Reynolds-Stress (ARS) models. They are a combination of the lower level models and the RST models. Only two transport equations are employed. This approach can predict rotational turbulent flows and secondary flows in channels with accuracy close to the RST models.

Due to the numerical stiffness of the RST and non-linearity of the ARS equations, first-order closures are more commonly employed in practice. First-order closures express the Reynolds stresses as a single scalar value, called the *turbulent eddy viscosity.* A linear relationship is assumed between the turbulent shear stress and the mean strain rate. First-order closures are subdivided into zero-, one-, and multiple-equation models (based on the number of transport equations utilized). In this research study, the two-equation k-epsilon model of Launder and Spalding was used [137] due the turbulent nature of flows in greenhouses [28]. The turbulent nature of flows in greenhouses considered is also shown in the experimental section of the thesis.

LES (Large Eddy Simulation)

This intermediate method simulates the larger scales of turbulence that are set by the geometry or specific flow conditions. The unsteady Navier-Stokes equations are space filtered prior to the computations to include the larger eddies and ignore the smaller eddies. A sub-grid scale model is used to account for the influence of the neglected smaller unresolved eddies on the resolved flow (mean flow plus large eddies). As the equations to be solved are unsteady, computer resources required are large [123].

DNS (Direct Numerical Simulation)

DNS is ranked as being the most computationally intensive numerical solution of turbulence [133]. The mean flow as well as all the turbulent velocity fluctuations is computed. Spatial grids are used to solve the unsteady Navier-Stokes equations. These grids are extremely fine to ensure that the Kolmogorov length scales are resolved, combined with sufficiently small time-steps to capture the period of the fastest fluctuations [123].

The RANS turbulence models together with the standard k-epsilon and low-Reynolds k-epsilon turbulence models were utilized in this study, therefore the next section will give a brief background on the applicable theory. For a more detailed description, please refer to Versteeg and Malalasekera [123].

3.4.2 Reynolds-Averaged Navier-Stokes Equations for Incompressible Flow

The instantaneous continuity and Navier-Stokes equations in Cartesian coordinates for an incompressible flow with constant viscosity are written as follows: [123]:

Table 3.2: Instantaneous Continuity and Navier-Stokes Equations

Continuity	$\operatorname{div} \bar{u} = 0$	3-**13**
z-component	$\frac{\partial u}{\partial t} + div(u\bar{u})) = -\frac{1}{\rho}\frac{\partial p}{\partial x} + \nu\, div(grad(u))$	3-14
y-component	$\frac{\partial u}{\partial t} + div(v\bar{u})) = -\frac{1}{\rho}\frac{\partial p}{\partial x} + \nu\, div(grad(v))$	3-15
z-component	$\frac{\partial u}{\partial t} + div(w\bar{u})) = -\frac{1}{\rho}\frac{\partial p}{\partial x} + \nu\, div(grad(w))$	3-16

The equations in Table 3.2 are the governing equations for turbulent flow. The effects of the fluctuations on the mean flow must be investigated using Reynolds Decomposition. The flow variables (u,v and w) and the pressure p are replaced by the sum of a mean and fluctuating component:

$$\bar{u} = \overline{U} + \bar{u}' \qquad u = U + u' \qquad u = V + v' \qquad w = W + w' \qquad p = P + p' \qquad 3\text{-}17$$

Taking the time average and applying the rules which govern time averages of fluctuating properties, the continuity for the main flow is presented:

$$\operatorname{div} \overline{U} = 0 \qquad 3\text{-}18$$

The time averages of the individual terms (See Versteeg [123]) is substituted into the instantaneous Navier-stokes equations to give the time-averaged x,y and z-momentum equations as shown in Table 3.3:

Table 3.3: Time Averaged Momentum Equations

x-component	$\frac{\partial U}{\partial t}+div\left(U\overline{U}\right)+div\left(\overline{u'\overline{u}'}\right)=-\frac{1}{\rho}\frac{\partial p}{\partial x}+\nu\, div\left(grad\left(U\right)\right)$	**3**-19
y-component	$\frac{\partial V}{\partial t}+div\left(V\overline{U}\right)+div\left(\overline{v'\overline{u}'}\right)=-\frac{1}{\rho}\frac{\partial p}{\partial x}+\nu\, div\left(grad\left(V\right)\right)$	3-20
z-component	$\frac{\partial V}{\partial t}+div\left(W\overline{U}\right)+div\left(\overline{w'\overline{u}'}\right)=-\frac{1}{\rho}\frac{\partial p}{\partial x}+\nu\, div\left(grad\left(W\right)\right)$	3-21

The time-averaging process introduced new terms (third term on the left) for each equation. These terms are associated with convective momentum transfer due to turbulent eddies, and involve products of fluctuating velocities. They are additional turbulent stresses on the mean velocity components, U,V and W.

x: $$\frac{\partial U}{\partial t}+div\left(U\overline{U}\right)=-\frac{1}{\rho}\frac{\partial p}{\partial x}+\nu\, div\left(grad\left(U\right)\right)+\frac{1}{\rho}\left[\frac{\partial\left(-\rho\overline{u'^2}\right)}{\partial x}+\frac{\partial\left(-\rho\overline{u'v'}\right)}{\partial y}+\frac{\partial\left(-\rho\overline{u'w'}\right)}{\partial z}\right] \quad 3\text{-}22$$

y: $$\frac{\partial V}{\partial t}+div\left(V\overline{U}\right)=-\frac{1}{\rho}\frac{\partial p}{\partial x}+\nu\, div\left(grad\left(V\right)\right)+\frac{1}{\rho}\left[\frac{\partial\left(-\rho\overline{u'v'}\right)}{\partial x}+\frac{\partial\left(-\rho\overline{v'^2}\right)}{\partial y}+\frac{\partial\left(-\rho\overline{v'w'}\right)}{\partial z}\right] \quad 3\text{-}23$$

z: $$\frac{\partial W}{\partial t}+div\left(W\overline{U}\right)=-\frac{1}{\rho}\frac{\partial p}{\partial x}+\nu\, div\left(grad\left(W\right)\right)+\frac{1}{\rho}\left[\frac{\partial\left(-\rho\overline{u'w'}\right)}{\partial x}+\frac{\partial\left(-\rho\overline{v'w'}\right)}{\partial y}+\frac{\partial\left(-\rho\overline{w'^2}\right)}{\partial z}\right] \quad 3\text{-}24$$

Equations 3-22 to 3-24 are called the Reynolds-averaged Navier-Stokes equations [123]. The extra terms result from six additional stresses (three normal and three shear stresses) called the Reynolds stresses:

$$\tau_{xx}=-\rho\overline{u'^2} \qquad \tau_{yy}=-\rho\overline{v'^2} \qquad \tau_{zz}=-\rho\overline{w'^2} \quad 3\text{-}25$$

$$\tau_{xy}=\tau_{yx}=-\rho\overline{u'v'} \qquad \tau_{xz}=\tau_{zx}=-\rho\overline{u'w'} \qquad \tau_{yz}=\tau_{zy}=-\rho\overline{v'w'}$$

The variances of the x-,y- and z-velocity fluctuations are included in the normal stresses. The second moments associated with correlations between different velocity components are contained within the shear stresses. Turbulent stresses are usually very large compared to the viscous stresses in a turbulent flow.

If a transport equation for an arbitrary scalar quantity, for example, temperature is derived, similar additional turbulent transport terms arise:

$$\frac{\partial \Phi}{\partial t} + div\left(\Phi \overline{U}\right) = -\frac{1}{\rho} div\left(\Gamma_{\Phi} grad\Phi\right) + \left[-\frac{\partial \overline{u'\varphi'}}{\partial x} - \frac{\partial \overline{v'\varphi'}}{\partial y} - \frac{\partial \overline{w'\varphi'}}{\partial z} + S_{\Phi} \right] \quad 3\text{-}26$$

3.5 K-epsilon Turbulence Model

To calculate turbulent flows with the RANS equations mentioned previously, turbulence models must be developed to predict the Reynolds stresses and the scalar transport terms, and close the system of mean flow transport equations. Generally, RANS turbulence models are classified according to the number of additional transport equations required to solve in addition to the RANS flow equations. The k-epsilon model has two additional transport equations, and is one of the most widely used turbulence models. It is presumed in this model that an analogy exists between the action of viscous stresses and Reynolds stresses on the mean flow. The model focuses on the mechanisms affecting the turbulent kinetic energy.

The time-average governing equation for the mean kinetic energy (k) is given by [123]:

$$\frac{\partial(\rho K)}{\partial t} + div\left(\rho K \overline{U}\right) = div\left(-\rho \overline{U} + 2\mu \overline{U} S_{ij} - \rho \overline{U} \overline{u_i' u_j'} - 2\mu S_{ij}.S_{ij} + \rho \overline{u_i' u_j'}.S_{ij} \right) \quad 3\text{-}27$$

This equation is obtained by multiplying the x-component Reynolds equation by U, y-component by V and z-component by W. Simplifying the results leads to equation 3-27.

If each instantaneous Navier-Stokes equation is multiplied by the appropriate fluctuating velocity components, as well as a repeat of this process on equations 3-22 - 3-24, some substantial algebra and simplification, the equation for the turbulent kinetic energy *k* is obtained [123]:

$$\frac{\partial(\rho k)}{\partial t} + div\left(\rho k \overline{U}\right) = div\left(-\overline{\rho' \overline{u}'} + 2\mu \overline{\overline{u}' s_{ij}} - \rho \frac{1}{2} \overline{u_i' . u_i' u_j'} - 2\mu \overline{s_{ij}.s_{ij}} - \rho \overline{u'_i u'_j}.S_{ij} \right) \quad 3\text{-}28$$

The commercial software used for the numerical models in this research study has seven k-epsilon models available:

- Standard k-Epsilon
- Standard Two-Layer k-epsilon
- Standard low-Reynolds number
- Realizable k-epsilon
- Realizable Two-Layer k-epsilon
- Abe-Kondoh-Nagano low-Reynolds number
- V2F low-Reynolds number

The k-epsilon models are generally suitable for industrial-type applications, with or without heat transfer. A good compromise between robustness, computational cost and accuracy is provided. The models are also capable of handling complex recirculation. When coarse meshes are used, the Standard k-Epsilon and Realizable k-Epsilon can be used. In general, the Realizable model yields better results compared to the Standard model [132]. The Two-Layer models (Standard and Realizable) is the most flexible, and gives good results for fine and intermediate meshes, and can be used with high Reynolds number meshes. When natural convection flows are investigated, the Standard low-Reynolds number model, Abe-Kondoh-Nagano low-Reynolds number model and V2F low-Reynolds number model are all suitable [132].

Research by Norton et al [24] indicated that the quality of the numerical solution depends on the chosen turbulence model. A study by Nebbali et al [89] found the standard k-epsilon model to give the lowest error value compared to the two other models (RNG and realizable k-epsilon). In a study by Henkes et al [138] it was mentioned that various low-Reynolds number models predicted wall heat transfer the closest to the experimental values. The low-Reynolds number has additional damping functions which allow it to be applied to the viscous boundary layer adjacent to the walls, and is recommended for use in natural convection problems. Since previous research indicates the turbulent nature of flow in greenhouses [28], a turbulence model was used in the numerical CFD simulations , in this research specifically the k-epsilon standard low-Reynolds number turbulence model was used which is discussed in the next sections.

3.5.1 Low-Re Number Turbulence Models

The previous models have some shortcomings when integrating the viscous sublayer, and additional viscous damping is required to predict accurate values of certain constants. The low-Reynolds number turbulence models can be used to solve the viscous sublayer. Damping functions are applied to some or all of the coefficients in the model. The function of the damping functions is to modulate the coefficients as functions of turbulence Reynolds number, usually also incorporating the wall distance [132]. The Standard low-Reynolds number k-epsilon is the turbulence model utilized in this study when natural convection is investigated. This model has identical coefficients to the standard k-epsilon model, but damping functions are provided in order to apply the model to the viscous-affected regions near walls. More details on the model such as coefficients can be found in the StarCCM+ User Manual [132] as well as in Wilcox [139].

This section discussed the numerical background required for this study. The next section will focus on the background pertaining to the experimental background of this research.

3.6 Experimental Background

In order to establish confidence in a more complex numerical model of a greenhouse, a reduced-scale model of a greenhouse will be tested in this research. The results will be used to qualitatively validate the complex numerical model based on the same full-scale greenhouse. This section discusses the relevant background required for scale model testing and flow visualization. It is essential that the fundamental similarity laws that are relevant to the study be correctly established and implemented during the experimental investigation. The result of this section relates to the general 3D Navier-stokes equations as discussed in section 3.2.2, where in this section for illustration purposes a number of assumptions have been made - steady state and laminar flow with the aim of presenting the important dimensionless numbers required during experimental testing.

3.6.1 Reduced-Scale Modelling

Full-scale experiments on buildings are often expensive, time-consuming and cumbersome. To overcome these difficulties, reduced-scale models are often used to allow testing in a laboratory, with the objective of determining the properties at full scale [140]. Recently scale modelling has also been used in applications were the building is not related to a full scale building, but are used for validating mathematical models [141]. The second application doesn't require flow similarity, but the selecting the correct measurement techniques can be a challenge.

Reduced-scale models are used extensively for evaluating ventilation performance and to predict air movement and temperature distribution. It has been established that reasonable accuracy for convective heat transfer in buildings can be achieved using these reduced-scale models [142]. An advantage of using scale models is the fact that they are relatively inexpensive to build and to modify. The reduced space requirement is also major advantage – as long as the scale of the model is carefully selected to maintain similarity between the full-scale prototype building and reduced-scale model. In this study, buoyancy driven natural ventilation in a greenhouse will be investigated experimentally using a scale model. This type of natural ventilation is more complex and difficult to model as there are several parameters that are dependent and interdependent on the ventilation driving force.

3.6.2 Dimensional Analysis and Similitude

The objective of utilizing a scale model in experimental testing is to essentially replicate the behaviour of the full scale prototype. In order to obtain valid test results, similarity between the reduced-scale and full-scale prototype building must be established as far as possible. When experimental data is available for a class in a set of dynamically similar flows, the flow

properties of the other can be predicted [134]. But in order for this to be valid, certain relevant non-dimensional parameters should be equal, depending on the nature of the problem. The non-dimensional parameters can be derived in two ways – using the governing differential equations, or by performing a dimensional analysis on the variables involved. To validate the scale model used in this research study for application in greenhouses, the velocity distribution, airflow patterns and temperature distribution should be similar. There are three main criteria required for similarity between a reduced-scale model and prototype:

Geometric Similarity

Geometric similarity between two systems is met when the ratio of all significant dimensions is similar for each system. This is usually the easiest of the similarity requirements to meet. When applied to buildings, this must be met at least in the depth and height of the model, with adequate width to prevent constricted airflow, as natural ventilation in buildings are a three-dimensional problem [140]. Dimensions of all surfaces and openings such as windows and doors must be reduced by the same scaling factor in all three dimensions x, y and z. If geometric similarity is not met, the flow patterns and temperature distributions within the space are influenced.

Kinematic and Dynamic Similarity

This type of similarity is found when in geometric similar systems, the ratios of the fluid velocities and accelerations are equal [143]. Meeting this requirement will ensure that the streamlines and flow patterns are similar in the model and prototype [140]. The ratios of all the forces causing the fluid motion are normally required to be equal.

Thermal Similarity

Thermal similarity is only achievable when all three heat transfer modes by conduction, convection and radiation in the model and prototype are identical, in addition to geometric and kinematic similarities. It can be shown that to achieve thermal similarity, the Peclet numbers must be equal [143].

3.6.3 Boundary Conditions

Similarity of the boundary conditions must be met in addition to the equality of the dimensionless numbers (Reynolds, Prandtl and Archimedes) which is required for kinematic and thermal similarity. This will ensure that the velocity and temperature fields between the model and prototype are similar.

Similarity of the boundary conditions is achieved when there is similarity of the geometric, hydrodynamic and thermal conditions at the solid boundaries of the model and the prototype. If

the prototype is scaled down accurately, then geometric similarity is achieved. Hydrodynamic similarity is automatically met for instances where the room is enclosed by solid walls. It is seen that the first two are relatively easily attained, but meeting the thermal similarity condition has its challenges. To attain complete thermal similarity, all the heat transfers in the prototype must be known in order to scale them appropriately in the model [144]. It was shown by Awbi [143] that field temperature similarity is also required in addition to the Peclet numbers being equal for convective heat transfer.

It was therefore concluded by Awbi [143] that for internal flow which is mainly convective, values of the Prandtl, Reynolds and Archimedes numbers must be equal in the model and prototype. The Peclet number is the product of the Prandtl and Reynolds numbers. Nevrala [144] found that it was nearly impossible to achieve equal Prandtl numbers for two different fluids and also satisfy other modelling parameters. This explains why air is still used for modelling non-isothermal flows in enclosures. The requirements for Reynolds number equality are quite different from the Archimedes number equality requirements, and therefore it is impossible to achieve both equalities simultaneously in a model study [143].

3.6.4 Governing Equations

Momentum and energy transfer in free convection originates from the related conservation principles as previously stated in section 3.2.2. Buoyancy forces play an important part, as well as inertia, viscous forces and energy transfer by advection and diffusion [145]. The differential forms of the continuity, momentum and energy equations can be used to developed useful dimensionless parameters, which are valuable tools for flow analysis. If a laminar boundary layer is for illustration purposes considered which is driven by buoyancy forces, with gravity acting in the negative x direction, the x-momentum equation reduces to the boundary layer equation with the body force per unit volume (-ρg) as shown in equation 3-29:

$$u\frac{\partial u}{\partial x}+v\frac{\partial u}{\partial y}=-\frac{1}{\rho}\frac{\partial p}{\partial x}-g+\nu\frac{\partial^2 u}{\partial y^2} \qquad 3\text{-}29$$

If there is no body force in the y-direction, $\delta p/\delta y = 0$ from the y-momentum equation. Therefore the x-pressure gradient at any point in the boundary layer must be equal to the pressure gradient in the quiescent region outside the boundary layer. But $u=v=0$ in this region, therefore equation 3-29 reduces to:

$$\frac{\partial p}{\partial x}=-\rho_\infty g \qquad 3\text{-}30$$

If this expression is substituted into the derived x-momentum equation, the following expression (Equation 3-31) is obtained [145]:

$$u\frac{\partial u}{\partial x}+v\frac{\partial u}{\partial y}=-\frac{g}{\rho}\left(\rho_{\infty}-\rho\right)+v\frac{\partial^{2}u}{\partial y^{2}} \qquad 3\text{-}31$$

This equation must apply at every point in the free convection boundary layer. The buoyancy force is given by the first term on the right in equation 3-31. Because of the density being variable, flow is established.

The governing equations for natural convection are of substantial complexity, since they are coupled, elliptic, partial differential equations [91]. The variation of density with temperature is problematic when solving these equations, therefore approximations are often used [91]. The Boussinesq approximation is often used to simplify these equations. Two aspects are important:

1) The density variation in the continuity equation is neglected
2) The density difference (results in the flow) is approximated as a pure temperature effect, implying that the effect of pressure on the density is neglected.

If the flow accelerations are small compared to gravitational acceleration, the density difference can be approximated as:

$$\rho_{\infty}-\rho=\rho\beta\left(T-T_{\infty}\right) \qquad 3\text{-}32$$

Where β is the volumetric thermal expansion coefficient, which provides a measure of the amount of which the density changes due to a change in temperature at constant pressure [145]:

$$\beta=-\frac{1}{\rho}\left(\frac{\partial\rho}{\partial T}\right)_{p}\approx\frac{1}{\rho}\frac{\rho_{\infty}-\rho}{T_{\infty}-T} \qquad 3\text{-}33$$

This approximation is used extensively in natural convection, but is only valid if $\beta\left(T-T_{\infty}\right)$ is much smaller than 1 – it is valid for small temperature differences if β remains unchanged. Substituting the approximated density difference into the x-momentum equation, it becomes evident how the buoyancy force responsible for the flow is related to the temperature difference:

$$u\frac{\partial u}{\partial x}+v\frac{\partial u}{\partial y}=-g\beta\left(T-T_{\infty}\right)+v\frac{\partial^{2}u}{\partial y^{2}} \qquad 3\text{-}34$$

To complete the set of governing equations, the conservation of mass and energy equation is added [145]:

Conservation of mass: $$\frac{\partial u}{\partial x}+\frac{\partial u}{\partial y}=0 \qquad 3\text{-}35$$

Energy equation: $$u\frac{\partial T}{\partial x}+v\frac{\partial T}{\partial y}=\alpha\frac{\partial^2 T}{\partial y^2} \qquad 3\text{-}36$$

Viscous dissipation [145] is typically neglected in the energy equation, which is a valid assumption as it is small for the low velocities associated with natural convection. The buoyancy term in Equation 3-34 complicates matters somewhat, as the solution to the momentum equation is now dependent on knowledge of the temperature T, and therefore the solution to the energy equation. The previous mentioned three equations (3-34 - 3-36) are hence coupled and must be solved simultaneously [145] as also generally stated in Section 3.2.2.

3.6.5 Important Dimensionless Numbers

The dimensionless parameters that govern free convective flow and heat transfer may be obtained by non-dimensionalizing the governing equations using the following expressions:

$$x^*\equiv\frac{x}{L} \qquad y^*\equiv\frac{y}{L} \qquad u^*\equiv\frac{u}{u_0} \qquad v^*\equiv\frac{v}{u_0} \qquad T^*\equiv\frac{T-T_\infty}{T_s-T_\infty} \qquad 3\text{-}37$$

L is a characteristic length, and u_0 an arbitrary reference velocity [145]. The x-momentum (Eq. 3-29) and energy equations (3-36) then become:

$$u^*\frac{\partial u^*}{\partial x^*}+v^*\frac{\partial u^*}{\partial y^*}=\left[\frac{g\beta(T_s-T_\infty)L}{u_0^2}\right]T^*+\frac{1}{\mathrm{Re}_L}\frac{\partial^2 u^*}{\partial y^{*2}} \qquad 3\text{-}38$$

$$u^*\frac{\partial T^*}{\partial x^*}+v^*\frac{\partial T^*}{\partial y^*}=\frac{1}{\mathrm{Re}_L\,\mathrm{Pr}}\frac{\partial^2 T^*}{\partial y^{*2}} \qquad 3\text{-}39$$

The buoyancy force gives rise to the expression in brackets in the first term on the right in equation 3-38. To simplify the equation, the reference velocity is usually specified as:

$$u_0^2=g\beta L(T_s-T_\infty) \qquad 3\text{-}40$$

If the resulting equation is then multiplied by the dimensionless temperature T*, it yields unity. The Reynolds number Re_L then becomes:

$$\mathrm{Re}_L=\frac{u_0 L}{\nu}=\sqrt{\frac{g\beta(T_s-T_\infty)L^3}{\nu^2}} \qquad 3\text{-}41$$

This yields another important dimensionless number called the Grashof number [145], often defined as the square of the Reynolds number Re_L:

$$Gr_L = \frac{g\beta(T_s - T_\infty)L^3}{\nu^2} \quad 3\text{-}42$$

The Grashof number indicates the ratio of the buoyancy force to the viscous force acting on a fluid [145]. The Grashof number is similar to the Reynolds number in forced convection - large values of Gr imply small viscous effects in the momentum equation [91] .

In natural convection, no free stream velocity is present, and therefore the buoyancy velocity is defined as [91] by approximating air as an ideal gas:

$$u_b = \sqrt{g\beta L(T_s - T_\infty)} \quad 3\text{-}43$$

The Prandtl number is measure of the rate of spread due to momentum changes in the flow compared to the effect of temperature differences [146]. It essentially gives a comparison between momentum and thermal diffusion and is defined as [145]:

$$\Pr \equiv \frac{\nu}{\alpha} \quad 3\text{-}44$$

When the scale model is tested in air, the Prandlt number remains the same for both scale model and prototype. In free convection, hydrodynamic instabilities may occur. This implies that disturbances in the flow may be heightened and leads to transition from laminar to turbulent flow. The relative magnitude of the buoyancy and viscous forces in the fluid dictates the transition. Transition in free convection can be represented by the Rayleigh Number, which is the product of the Grashof and Prandtl numbers. For vertical plates, the Rayleigh numbers is given by equation 3-45 [145]:

$$Ra = Gr \cdot \Pr = \frac{g\beta(T_s - T_\infty)x^3}{\nu\alpha} \quad 3\text{-}45$$

As already mentioned, there are some limitations to this approach in meeting all the similarity requirements and a compromise must be found between a practical scale model and meeting the objectives of the study. For example, reducing the scale by a factor of 10 will result in an increase of velocity by a factor of 10 to keep the Reynolds number, and a temperature difference of 1000 to retain the Archimedes number [140]. It is therefore nearly impossible to match all of the dimensionless parameters. This problem can solved if the flow is fully developed turbulent flow, then the Archimedes number becomes the most relevant dimensionless number to match [140]. If the Reynolds number is sufficiently high, a change in Reynolds number will no longer affect the majority structure of turbulence, and dynamic similarity can be achieved [147]. After

meeting the critical Reynolds number ($Re > 2.3 \times 10^3$) condition for both model and prototype, it is deemed sufficient to achieve critical values of Grashof number when air is the working fluid [140]. Some research [148] proposes a critical value of Grashof number for transition to turbulent flow in range of 10^6 to 10^9 (based on experimental work), if the height of the room is used as characteristic length. A critical Rayleigh number of 2×10^7 is proposed by Hagstrom [149] when modelling natural convection of a plume under forced ventilation conditions, resulting in turbulent convection flows.

It is generally suggested that accurate modelling can only be achieved for problems in Fluid Dynamics when the Prandtl, Reynolds and Grashof numbers are identical, but this constraint leads to the conclusion that only a 1:1 scale model can be used to model convective heat transfer accurately. Metais and Eckert [150] demonstrated that accurate modelling of the Reynolds and Grashof numbers are not critical in defining a general flow pattern. Their investigation suggested that for sufficiently large values of the Reynolds number, the influence of the viscous and buoyancy terms in the momentum equations are negligible. Actual buildings are characterized by turbulent flow, since $Re \approx 10^5$ and $Gr \approx 10^9$ [142].

The type of convection often encountered in greenhouses, and also considered in this research study is natural convection. As a reduced-scale model will be used it is vital to take note of the previous mentioned problems encountered when dealing with natural convection. It is therefore concluded that achieving full similarity will not be possible, although reasonable assumptions based on previous research can be made.

3.7 Flow Visualization

Flow visualization is an important tool used to investigate and understand certain properties of a flow field. As the motion of most fluids is invisible to the human eye during direct observation, various techniques have been developed allowing the visualization of the flow field. A method employed frequently is flow visualization using tracer material. The addition of tracer material ensures that sufficient light is scattered for direct observation of the flow. Common tracers are dye used in liquids, and smoke in the flow of a gas, for example air.

Flow visualization using smoke and dye is one of the oldest techniques, dating back to the time of Leonardo Da Vinci [151]. The technique has various advantages – it is inexpensive and simple to implement, and may provide substantial information for the flow field under investigation [151]. The term “smoke” can also refer to steam, vapour, aerosols, and mist in this context [152]. It is important that the following criteria are met when using smoke:

1) The smoke particles must be small enough so that their motion reflects the motion of the flow under investigation
2) The flow field must not be significantly affected
3) The particles must retain high reflective properties
4) It must be nontoxic

It is required to use a neutrally buoyant tracer material to ensure minimum difference in the motion of the fluid and the tracer. A two-phase fluid is generated with the addition and dispersion of a tracer material. In the experimental setup, the motion that is observed is the motion of the dispersed phase [152]. By ensuring a minimum difference between the two phases, the fluid and tracer can be regarded to form a continuum. The method and placement of the tracer in the flow is quite important as it influences what will be visible in the experiment.

The smoke used for visualization can be generated by numerous sources – burning tobacco, wood, wheat straw, or by vaporizing wheat straw. The requirement of neutral buoyancy cannot be fulfilled by these substances since the densities of the tracer materials are order of magnitude larger than the density of air. But the particles have diameters less than 1μm, therefore buoyance effects are negligible for a first-order approximation.

Many methods exist to generate the "smoke" required. Smoke generators are based on the vaporization of hydrocarbon oils, particularly kerosene. Steam combined with a cooling agent is sometimes used in closed-circuit wind tunnels. Another popular chemical method that produces a dense, white mist is the reaction of titanium tetrachloride $TiCl_4$ with water [152]. A white mist (TiO_2), the result of the chemical reaction, is released which is of high optical reflectivity. Hydrochloric acid fumes are also released and are toxic; therefore experiments should be conducted in a well-ventilated area.

Another method which was also employed as a first attempt in this research study, is the use of neutrally buoyant, helium-filled soap bubbles. The bubbles are generated quite quickly – in the order of 15 000 per minute. The helium allows the bubbles to follow any air motion over a range of speeds, from 0 to approximately 60m/s [153]. The size of the bubbles can be varied, and are durable – they have been used to visualize flow through axial fans and centrifugal blowers [154]. Figure 3.3 shows the setup of the helium bubble generator, as well as flow visualization through a desktop fan and around a model jeep. Unfortunately due to the low velocities in the scale-mode of the greenhouse, this technique was unsuccessful, as smoke proved to be much more effective in visualization of the flow patterns.

(a)

(b)

(c)

Figure 3.3: a) Helium bubble generator b)Flow through a desk fan c) Flow around a model jeep [155]

3.8 Illumination and Recording

An important aspect of flow visualization is the source of illumination. The appropriate source, duration and form illumination must be evaluated for the experiment. For simple flow visualization techniques, front light illumination with ordinary lights or spot lights might be sufficient. If information on the flow velocity is required, time control of the source is required. The most common method used to obtain information on flow structures within a flow field is by using a light sheet [152]. In this current greenhouse research a laser is used as the light source and expanded using a cylinder lens or a glass rod. A plane is defined in the flow field by expanding a laser beam to form the light sheet required. To capture the flow structures, a camera is placed orthogonal to the direction of the light sheet, along the normal to the plane formed by the light sheet.

Recording the air flow patterns and direct visualization of velocity profiles in air flows is a rather difficult task, due to the higher degree of diffusion of possible tracers such as smoke. The type of camera and light source position can affect the observed cross-section and image quality [140].

3.9 Conclusion

This chapter gave a brief but relevant only overview of Computational Fluid Dynamics (CFD) and the experimental background required for the experimental tests in this research study. Turbulence modelling was discussed, as well as the specific turbulence model used in the simulations. The details and mathematical analysis of CFD were not discussed in full detail, as this is widely discussed in the literature. But appropriate detail was shown to be able to appreciate and understand the fundamentals of the choices made in the numerical approximations used in this research study of the specific greenhouses concerned. A reduced-scale model of a greenhouse will be investigated experimentally, and therefore a summary of reduced-scale modelling and dimensional analysis was also given. The governing equations were identified and non-dimensionalized in order to facilitate the dimensional analysis for the full-scale and prototype models. The most important dimensionless numbers that were identified was the Reynolds, Grashof and Rayleigh numbers. Lastly aspects of flow visualization were discussed. The next chapter applies CFD in novel investigations to the natural convection in various cavities, as this is often encountered in greenhouses.

CHAPTER 4

Numerical Modelling and Validation for Square Cavities as Approximation for Greenhouses

4.1 Chapter Review

In this chapter, the numerical simulation research commences with the validation of a few fundamental geometries used as the building blocks for the final numerical models of the greenhouse. The purpose of the numerical work in this chapter is to commence the investigation by studying the fundamental or basic geometry contained in a greenhouse, namely a square filled with air. This chapter firstly attempts to establish whether a zero degree roof angle single span greenhouse CFD model can be evaluated against published experimental results using a Computational Fluid Dynamics model in both two and three dimensions. This chapter addresses the following research questions:

- Can a zero degree roof angle single span greenhouse be evaluated against published experimental results using a Computational Fluid Dynamics model in both two and three dimensions?
- Are there differences in the thermal performance of two-dimensional versus three-dimensional square greenhouses?

4.2 Introduction

During mid-season and sunny winters greenhouses are usually fully closed, with buoyancy effects due to warm soil and transpiring leaves the only driving forces present. This situation corresponds to the classic Rayleigh-Bénard convection where a cavity is heated from below and cooled from above. The thermal situation in a closed greenhouse containing a continuous crop canopy surface can be approximated by natural convection in a dry, floor heated cavity [3]. As a starting point to the parametric evaluation of multi-dimensional heat transfer in greenhouses, a square cavity representing a greenhouse with a zero degree roof angle was numerically

investigated and validated in this research using results from experiments by Baïri [98]. Once the two-dimensional investigation had been concluded, a three-dimensional case for a zero-degree greenhouse was numerically studied and verified. The three-dimensional case was compared to an experimental investigation conducted on natural convection in a cubical enclosure by Kürekcį and Őzcan [156].

4.3 Two-dimensional Numerical Model – Square Greenhouse

The initial CFD model of a square cavity considered in this research was based on the cavity studied experimentally and numerically by Baïri [98] shown in Figure 4.1. The bottom and top walls in the current CFD model as initial basis for a greenhouse were heated and cooled respectively, generating the buoyant flow in the cavity, while the vertical walls were adiabatic. This is similar to one of the cases investigated by Baïri [98]. The top wall was assigned a temperature of T_c=15°C, and the temperature on the bottom wall, T_H, was adjusted to achieve different values of the Rayleigh number (Ra). The flow field was assumed to be steady, and the fluid (air) incompressible. All CFD analyses in this research considered in this section were done for the two-dimensional cases only.

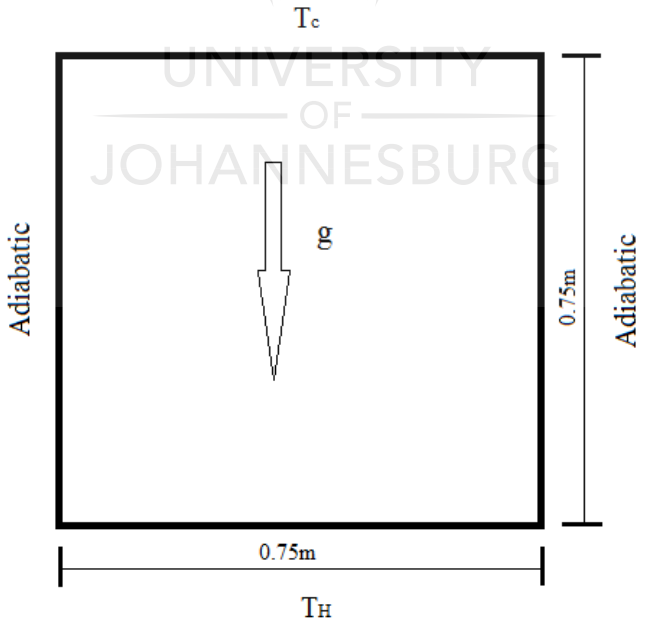

Figure 4.1: Dimensions of square greenhouse as modelled

The Rayleigh number was calculated using $\Delta T = T_h - T_c$ associated with the distance L between the two active walls and the following equation:

$$Ra = \frac{g\beta L^3 \Delta T}{\nu\alpha} \qquad 4\text{-}1$$

The properties of air used in the model were calculated using the average temperature between the hot and cold wall (T_{ave}) for each case. Table 4.1 shows the relevant parameters used to calculate the Rayleigh numbers associated with the temperature differences that were investigated.

Table 4.1: Calculation of Rayleigh Numbers

Height	**Units**	**0.75 (m)**							
T_{floor}	K	293.25	298.25	308.25	318.25	328.25	338.25	348.25	358.25
T_{roof}	K	288.25	288.25	288.25	288.25	288.25	288.25	288.25	288.25
ΔT	°C	5	10	20	30	40	50	60	70
T_f	K	290.75	293.25	298.25	303.25	308.25	313.25	318.25	323.25
β	1/K	3.44E-03	3.41E-03	3.35E-03	3.30E-03	3.24E-03	3.19E-03	3.14E-03	3.09E-03
α	m^2/s	2.13E-05	2.16E-05	2.23E-05	2.30E-05	2.37E-05	2.45E-05	2.52E-05	2.59E-05
υ	m^2/s	1.51E-05	1.53E-05	1.57E-05	1.62E-05	1.67E-05	1.72E-05	1.77E-05	1.82E-05
Ra	-	2.22E+08	4.27E+08	7.92E+08	1.10E+09	1.35E+09	1.57E+09	1.75E+09	1.90E+09
Nu	-	41.80	52.78	65.29	72.90	78.01	81.61	84.29	86.36

The boundary conditions as applied in the CFD model are summarized in Table 4.2.

Table 4.2: Boundary Conditions

Boundary	**Type**	**Thermal Specification**
Bottom Wall (Floor)	Wall Type (no-slip)	Isothermal
Top Wall (Roof)	Wall Type (no-slip)	Isothermal
Left Wall	Wall Type (no-slip)	Adiabatic
Right Wall	Wall Type (no-slip)	Adiabatic

4.3.1 Mesh

The square cavity was meshed for CFD purposes using the polyhedral meshing model included in the StarCCM+ software. The main advantage of using polyhedral cells instead of tetrahedral cells is that a polyhedral mesh contains approximately 5 times fewer cells than an equivalent tetrahedral mesh for a given surface. This meshing model utilizes an arbitrary polyhedral cell shape to assemble the core mesh. A special dualization scheme is used to create the polyhedral mesh based on an underlying tetrahedral mesh automatically created in the process [132].

As turbulent flow in a square cavity with natural convection is characterized by a thin boundary layer containing relatively large flow gradients, a large number of cells are required in this region. The advancing prism layer meshing model [132] was used to generate these cells in order to adequately capture boundary layer, turbulence effects and heat transfer near the wall boundaries. This specific meshing model was chosen instead of the standard prism layer meshing model as it has the ability to generate thicker and more uniform cell layers compared to the standard prism layer meshing model. Firstly a subsurface is generated at the specified prism layer thickness value, effectively "shrinking" the starting surface. The core mesh is then built using the subsurface. The cell faces are lastly extruded from the numerical core mesh to the original starting surface to construct the prism layer mesh. Four different base sizes were tested to determine mesh independence. These meshes are shown in Figure 4.2.

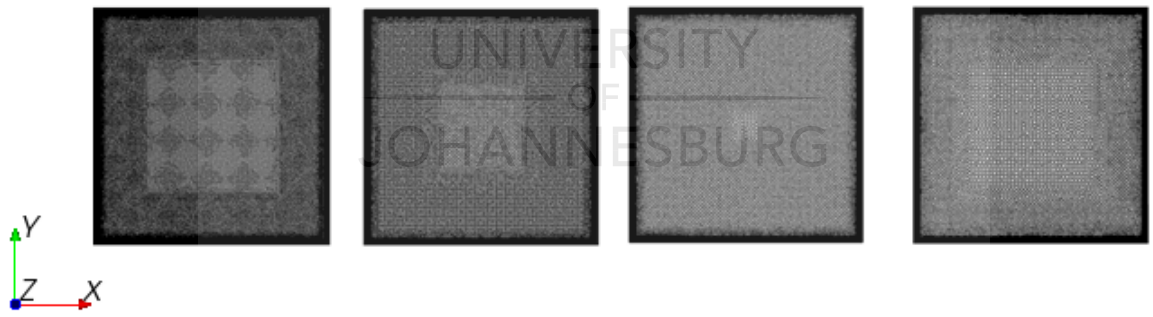

Figure 4.2: Four different mesh base sizes - a) 0.008m b) 0.012m c) 0.016m and d) 0.02m

The maximum simulated x- and y-velocity components in the CFD domain were monitored, and the average Nusselt number on the hot wall was calculated for each base size and are shown in Table 4.3. The number of polyhedral cells generated for each base size is plotted in Figure 4.3.

Table 4.3: Mesh sensitivity analysis (Ra = 1.35 x 10^9)

Base Size (m)	# of Cells	U_{max}	V_{max}	Nu_{ave}
0.008	139370	0.295	0.333	78.938
0.010	97188	0.294	0.333	78.834
0.014	65471	0.294	0.333	78.865
0.016	57996	0.294	0.333	78.860
0.018	39677	0.295	0.334	78.637
0.025	28570	0.294	0.333	78.606
0.030	24469	0.294	0.333	78.597

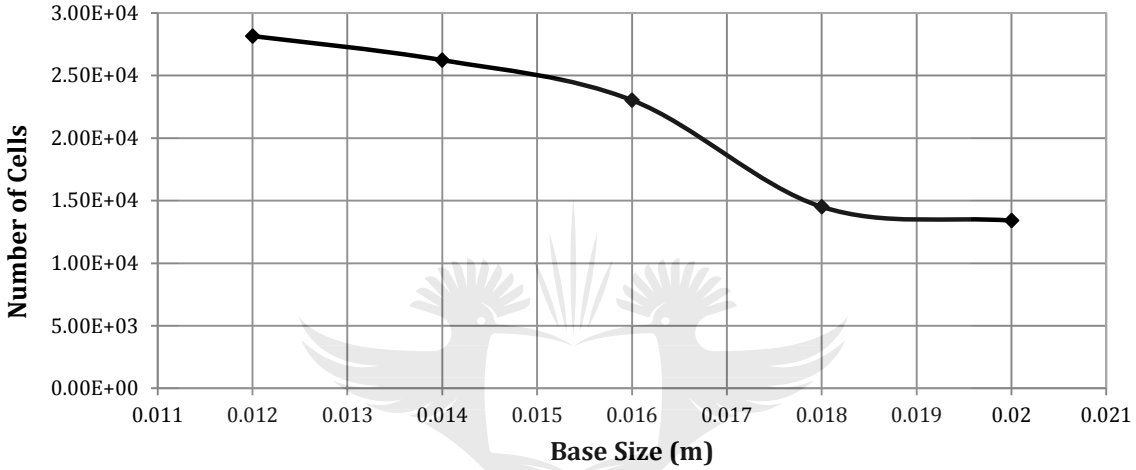

Figure 4.3: Number of cells vs base size (m)

Figure 4.4 shows the base size versus the average Nusselt Number on the hot wall. Taking simulation time and available resources into account, it was decided to use a base of 0.016m for all the simulations in this section. The difference between the values is less than 1% , therefore it can be concluded that the results are independent of the cell size.

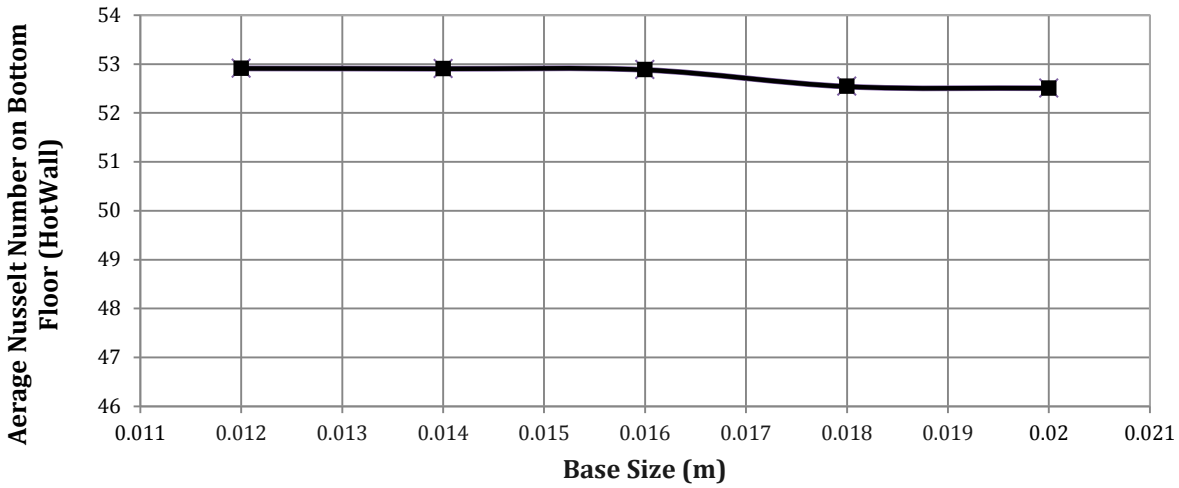

Figure 4.4: Base size vs average Nusselt number on hot wall

The final mesh settings used in this model are shown in Table 4.4. Based on computer simulation time and the results from the monitored values, a base size of 0.016m was chosen. The simulation converged after approximately 5 000 iterations for a base size of 0.018m, and the 0.016m base size, but only after 8 000 iterations for a base size of 0.014m. The difference between the two average Nusselt Numbers for 0.016m and 0.018m was approximately 0.65%. Decreasing the base size further did not have any significant influence on the average Nusselt number calculated on the hot wall. The motivation for the prism layer thickness and number of cells will be explained in the next section. All the other values shown in Table 4.4 were left as specified by default in the CFD program. The Surface Growth rate control determines the rate at which face edge sizes vary from one face to its neighbour [132]. If the value is decreased, a surface mesh with more faces is generated. The value specified for density controls the overall density of the mesh everywhere in the bulk volume. The growth factor is used to control the mesh density of the core mesh by altering the rate at which cells grow from coarse to fine areas. The mesh on the boundaries was also refined to ensure that cells with a high aspect ratio (if the height for example of the cell is much higher compared to the width) did not occur in the boundary layer adjacent to the walls.

Table 4.4: Mesh Parameters

Property	Value
Base Size (m)	0.016
Number of Prism Layers	20
Prism Layer Stretching	1.5
Prism Layer Thickness (m)	0.022
Surface Growth Rate	1.3
Surface Size (Tet/Poly Density)	
Density	1.0
Growth Factor	1.0
Blending Factor	1.0
Local Custom Surface Size	
Relative Minimum Size	10% of Base Size
Relative Target Size	50% of Base Size

4.3.2 Physics Setup

In StarCCM+ a physics continuum must be defined, which is interpreted as a collection of models that represents the substance (solid or fluid) being simulated [132].

The following models were used in the CFD software to model the physics for the fluid in the square:

- Ideal Gas
- K-Epsilon Turbulence
- Low y+ Wall Treatment
- Reynolds-Averaged Navier-Stokes
- Segregated Flow - Segregated Fluid Temperature
- Standard K-Epsilon Low-Re
- Steady
- Two Dimensional
- Gravity

The solution update for the segregated flow model is controlled according to the SIMPLE algorithm [123] that was discussed previously. The segregated fluid temperature model was chosen as a companion to the segregated flow model. This model solves the total energy equation with temperature as the solved variable. The equation of state is then used to calculate enthalpy. The model is appropriate for simulations that do not involve combustion [132].

Since only the flow in the turbulent regime will be investigated, the k-epsilon turbulence model was activated. Accurately predicting turbulent buoyant flows are difficult to achieve, and have been successful in only a few cases as illustrated in [157]. This is due to the complexity of the

numerical simulation of boundary layers adjacent to the walls, as well as the uncertainty of the general turbulence models for turbulent natural convection [157]. Two turbulence models were tested for the initial case considered here, namely the RANS k-epsilon realizable two-layer model, and the k-epsilon Standard low-Reynolds Number turbulence model. In a study by Henkes et al [158] it was mentioned that various low-Reynolds number models predicted wall heat transfer the closest to the experimental values. The Low-Reynolds number has additional damping functions which allow it to be applied to the viscous boundary layer adjacent to the walls, and is recommended for use in natural convection problems.

The low Y+ wall treatment was used in conjunction with the low-Reynolds number turbulence model. It is assumed by this wall treatment that the viscous sublayer is resolved, and wall laws are unnecessary. This wall treatment can however be used only with a fine enough mesh. An initial simulation was done to determine whether the near wall spacing is appropriate for the simulation, i.e. whether the amount of prism layers created on the walls was sufficient. Ten prism layers were initially specified in the mesh setup, with a thickness of 0.01m. The dimensionless Wall Y+ was defined as follows [132]:

$$y^+ = \frac{yu^*}{\nu} \qquad 4\text{-}2$$

Where y is the normal distance from the wall to the wall cell-centroid, u^* is a reference velocity and ν the kinematic viscosity. The dimensionless Wall Y+ values were plotted as a scalar on the wall boundaries of the cavity. They were found to be overall less than 1 for the chosen mesh base size, which implies that the prism layer thickness and amount of prism layer cells are adequate for the chosen turbulence model. If values of Y+ significantly exceed 1, substantial errors may result. A typical Wall Y+ obtained during CFD analysis of the square cavity is shown in Figure 4.5. The turbulence parameters for the simulations in this chapter are shown in Table 4.5.

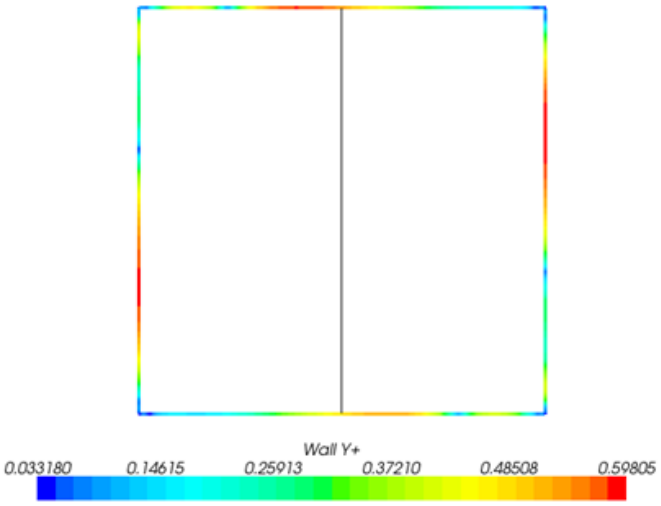

Figure 4.5: Wall Y+ values on wall boundaries

Table 4.5: Turbulence Parameters

Under Relaxation Factor	**0.8**
Convergence Tolerance	0.1
Epsilon	0.0
Turbulent Viscosity (Under Relaxation Factor)	1.0

4.3.3 Results - Square Greenhouse

The essential CFD results for the numerical two-dimensional square greenhouse scale model are presented here in the form of vector and scalar contour plots. In order to assess the convective contribution of the heat exchange within the cavity, the surface average Nusselt number (ratio of convective to conductive heat transfer across a boundary) was calculated for the floor of the cavity. The Nusselt number is given by equation 4-3:

$$Nu = \frac{hL}{k} \qquad 4\text{-}3$$

The surface averaged Nusselt number on the hot floor across all the cells was calculated from the CFD results and compared to results found in the literature as shown in Figure 4.6. A custom user function was written in StarCCM+ which calculated the Nusselt Number for each cell on the hot wall using the boundary heat flux. The syntax can be seen in equation 4-4:

$$(abs(\$BoundaryHeatFlux)/\Delta T) * L/k \qquad 4\text{-}4$$

The equation essentially takes the absolute value of the boundary heat flux ($ implies it is a scalar function in StarCCM+), divides it by the temperature difference, multiplies the answer by

the height of the cavity and lastly divides by the thermal conductivity of the air. The surface averaged Nusselt number was calculated as follows using the scalar-based report function in the software, where the surface averaged Nusselt number was calculated for the hot wall (cavity floor) as shown in equation 4-5:

$$\text{Surface Averaged Nusselt Number} = \frac{1}{a}\int Nu\ da = \frac{\sum_f Nu_f A_f}{\sum_f A_f} \qquad 4\text{-}5$$

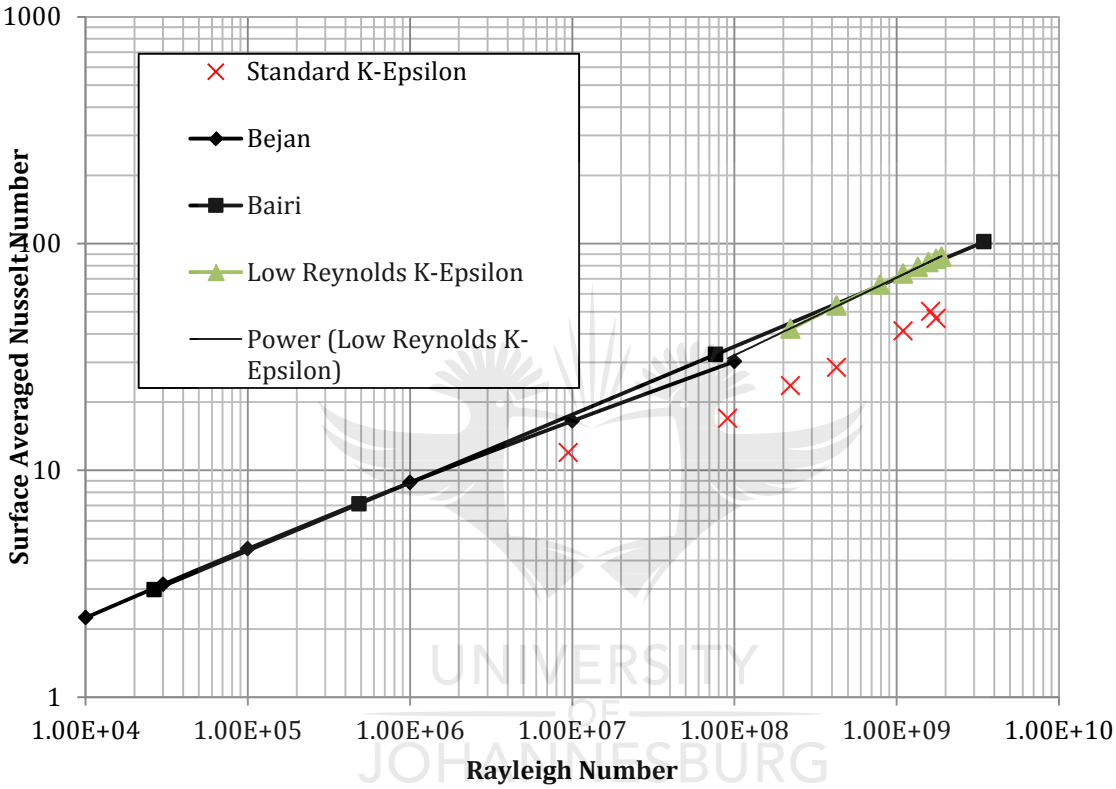

Figure 4.6: Average Nusselt number along the hot wall vs Rayleigh number

The graph in Figure 4.6 shows the numerical results for the Nusselt number when applying both the standard realizable k-epsilon turbulence model as well as the LRN k-epsilon turbulence model. Simulations applying the standard realizable k-epsilon turbulence model indicate a relatively large discrepancy when compared to experimental results, as well as the numerical results using the standard low-Reynolds number k-epsilon turbulence model. This is in essential in agreement with results published by Baïri [98]. The Nusselt-Rayleigh relationship that best fit the curve was found to be:

$$Nu = 0.0589 Ra^{0.3422} \qquad 4\text{-}6$$

Overall, a relatively good agreement was found between the numerical and experimental results when using the low-Reynolds number k-epsilon turbulence model in Figure 4.6. This creates additional confidence to use the model to investigate complementary cases under similar assumptions.

The temperature distributions at mid-height of the cavity are shown in more detail in Figure 4.7. It should be noted here that the temperature plots are all horizontal at the two vertical walls, as they are specified as adiabatic, it is just not clear from the Excel plots shown here. For all Rayleigh numbers, the same trend is followed – in the centre of the cavity a uniform core region temperature distribution is found which is different from the temperature distribution in the boundary layer near the adiabatic walls. The section of the cavity at mid-height containing a uniform distribution (less than 1% variance) is approximately the same for each Rayleigh number (from abou1.2m to 0.62m). The temperature difference at the adiabatic walls to the core region becomes more noticeable as the Rayleigh number increases. The temperature difference from the wall to the uniform temperature is relatively small for the Ra = 2.22 x 10^8 case (from 17.2 to 17.6° C) compared to temperature difference of about 5°C for the Ra = 1.90 x 10^9 case. All the cases except the lowest temperature of 5 for the highest temperature difference of 70°C exhibits a decrease from the wall to the uniform temperature distribution. It can be seen from Figure 4.9 that the Ra = 2.22 x 10^8 (ΔT = 5°C) is the only case with a counter-clockwise rotating cell. This can be attributed to numerical influences.

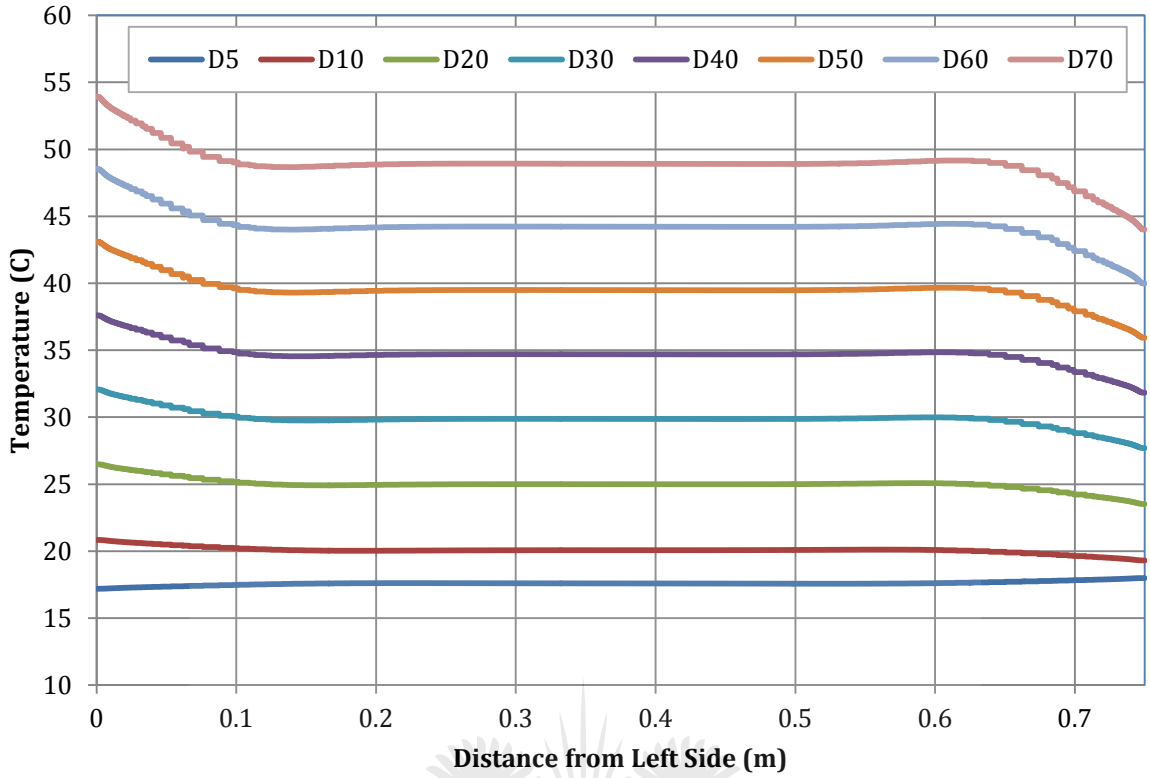

Figure 4.7: Temperature distribution at mid-height

The CFD results of velocity and temperature contour plots for each case (ΔT = 5°C to 70°C as indicated in Table 4.1) are shown in Figure 4.8 and Figure 4.9 In each case a single dominant convective flow cell forms in the cavity, all in the same direction, except for the lowest temperature difference. In this case the cell rotates clockwise compared to the other cases which all rotate counter-clockwise. This is probably indicative of local numerical influences. Two smaller rotating flow cells can be seen in opposing corners for each case. The centre remains stagnant, while the maximum velocity is seen next to the vertical adiabatic walls, and the top and bottom isothermal walls. The maximum velocity also increases as the temperature difference between the floor and roof of the cavity increases. From the temperature contour plots it is evident that the centre of the cavity contains a relatively uniform temperature distribution compared to the boundary layers forming against the walls of the cavity. The thermal boundary layer becomes progressively smaller as the temperature difference in the cavity increases as seen in the temperature contour plot in Figure 4.9. The term "D5" refers to a temperature difference between the top and bottom of the cavity of 5°C, D10 refers to a 10°C difference and so forth.

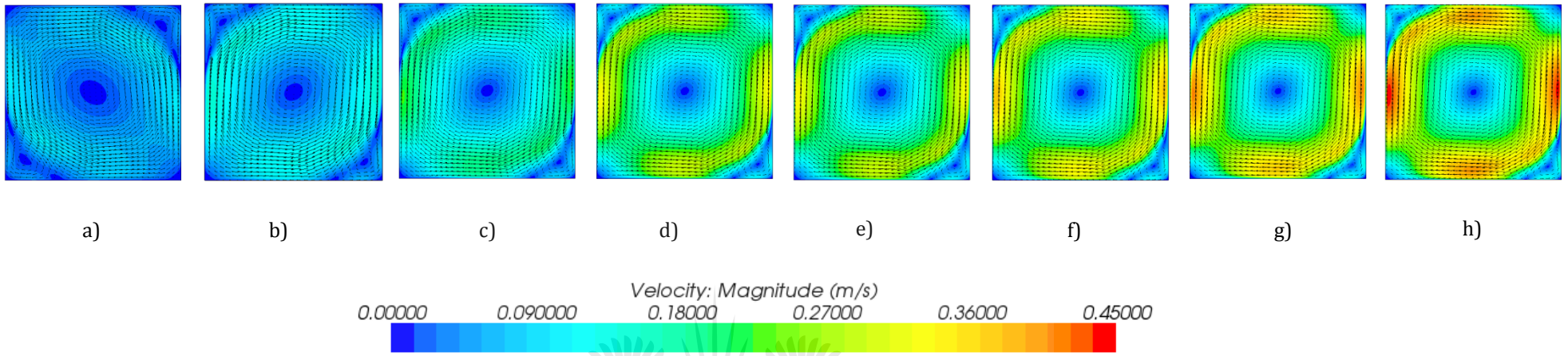

Figure 4.8: Vectors and velocity contour plots

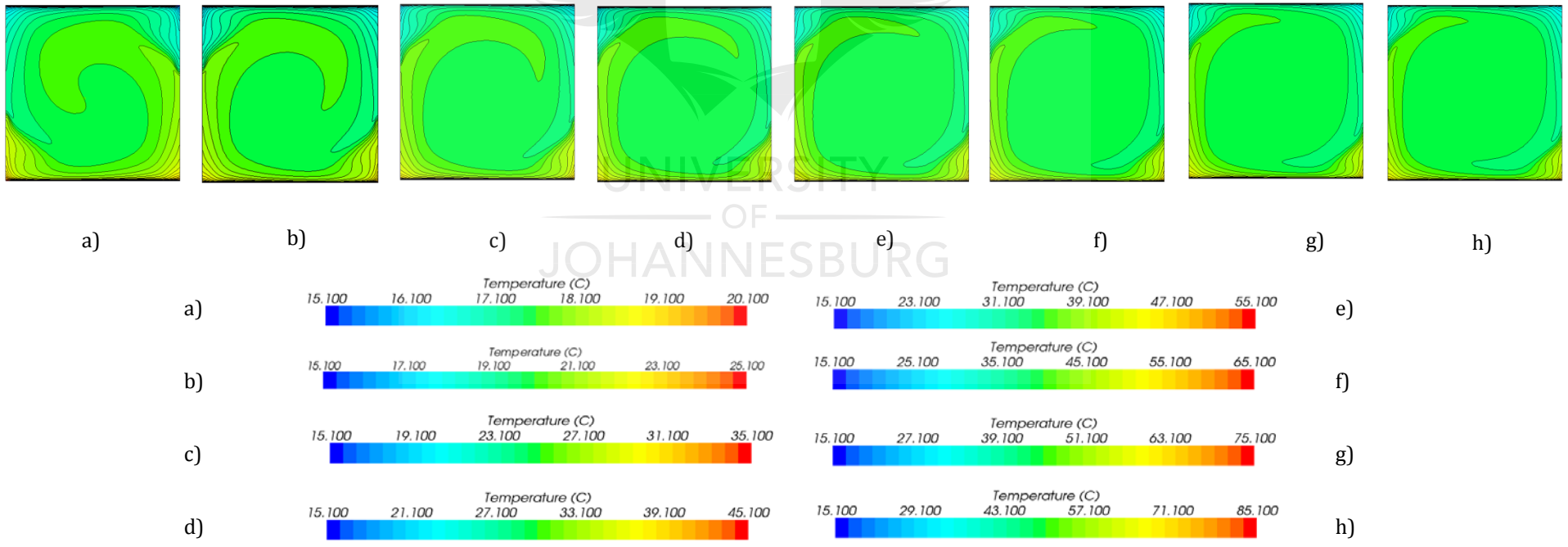

Figure 4.9: Temperature contour plots

The boundary heat flux distribution for the hot wall (floor region) is shown in Figure 4.10. The same trend is observed in all the cases, except for the lowest temperature difference, where the maximum boundary heat flux is towards the left of the cavity. This can be correlated to the direction of the convective cell, as seen in Figure 4.9. The increase from the minimum boundary heat flux to the maximum for the remainder of the cases (ΔT 10 - 70°C) becomes more pronounced as the temperature difference, and therefore Rayleigh number increases in the cavity. This can be due to the velocity that increases in the bottom right corner for these cases, as shown in the contour plot from Figure 4.9.

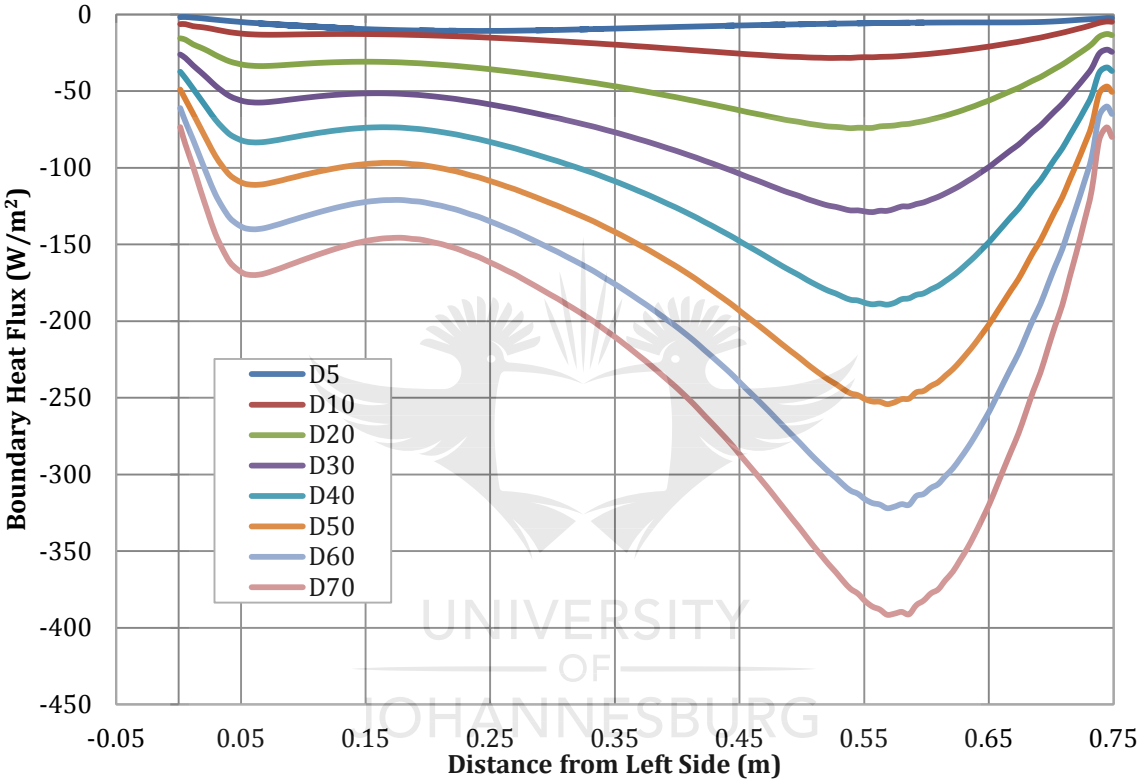

Figure 4.10: Boundary heat flux distribution

The absolute velocity distribution at mid-height is shown in Figure 4.11. Once again, all the curves are characterized by the same trend – a high gradient next to the adiabatic walls, with almost no movement in the centre of the cavity. It can be seen however that the velocity gradient adjacent to the adiabatic walls increases with Rayleigh number. It is also noticed that the gradient of the increase in velocity from the centre towards the walls increases as the Rayleigh number increases.

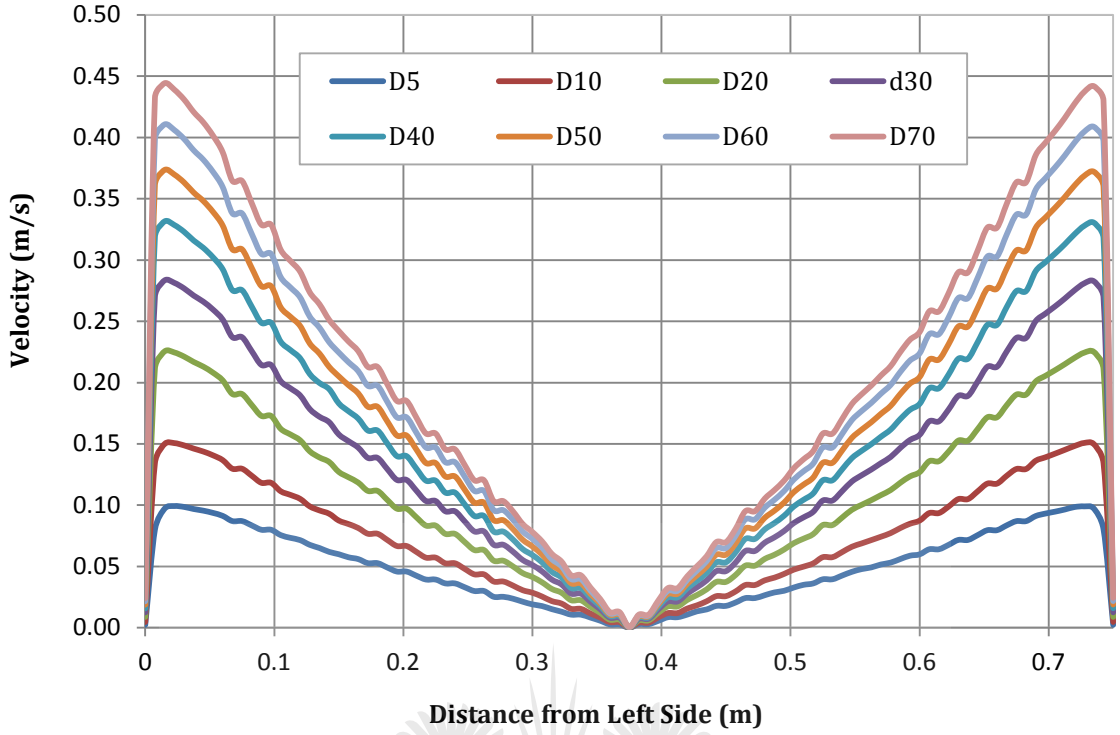

Figure 4.11: Velocity distribution at mid-height

The next subsection addresses the question of the thermal effect of a third dimension in the square model greenhouse.

4.4 Three-Dimensional Square Greenhouse

From the Rayleigh-Nusselt relationships calculated from the results in the previous section, confidence in the two-dimensional CFD model was established. In this section, the numerical greenhouse scale model has been extended to a three-dimensional square or a cubical cavity. The results were firstly compared to experimental results for a 200mm cube found in the literature by Küreckci and Özcan [156], who investigated the natural convection of a cubical cavity both experimentally and numerically. This is again done to increase confidence in the current CFD models for the greenhouse. The investigation will then be expanded further to a cubical cavity of 0.75m and the heat transfer will be investigated for the various Rayleigh numbers previously mentioned. This will enable the comparison of the two-and three-dimensional cavities, to ascertain the influence of a third dimension on temperature and velocity distributions.

4.4.1 Numerical Model

The cubical enclosure numerically modelled has dimensions of 200mm x 200mm x 200mm to be able to compare to Kürekci et al [156].One vertical wall of the cavity was specified a constant temperature of 69°C, while the cold wall was kept at a constant temperature of 41°C. The remainder of the cube walls were adiabatic. The details of the experimental setup to which the current model can be compared can be found in [156]. A schematic diagram considered for CFD modelling of the cubical enclosure is shown in Figure 4.12. The gravitational vector is in the negative y-direction in the CFD model. The CFD model was run in the laminar regime to be able to compare to previously published results.

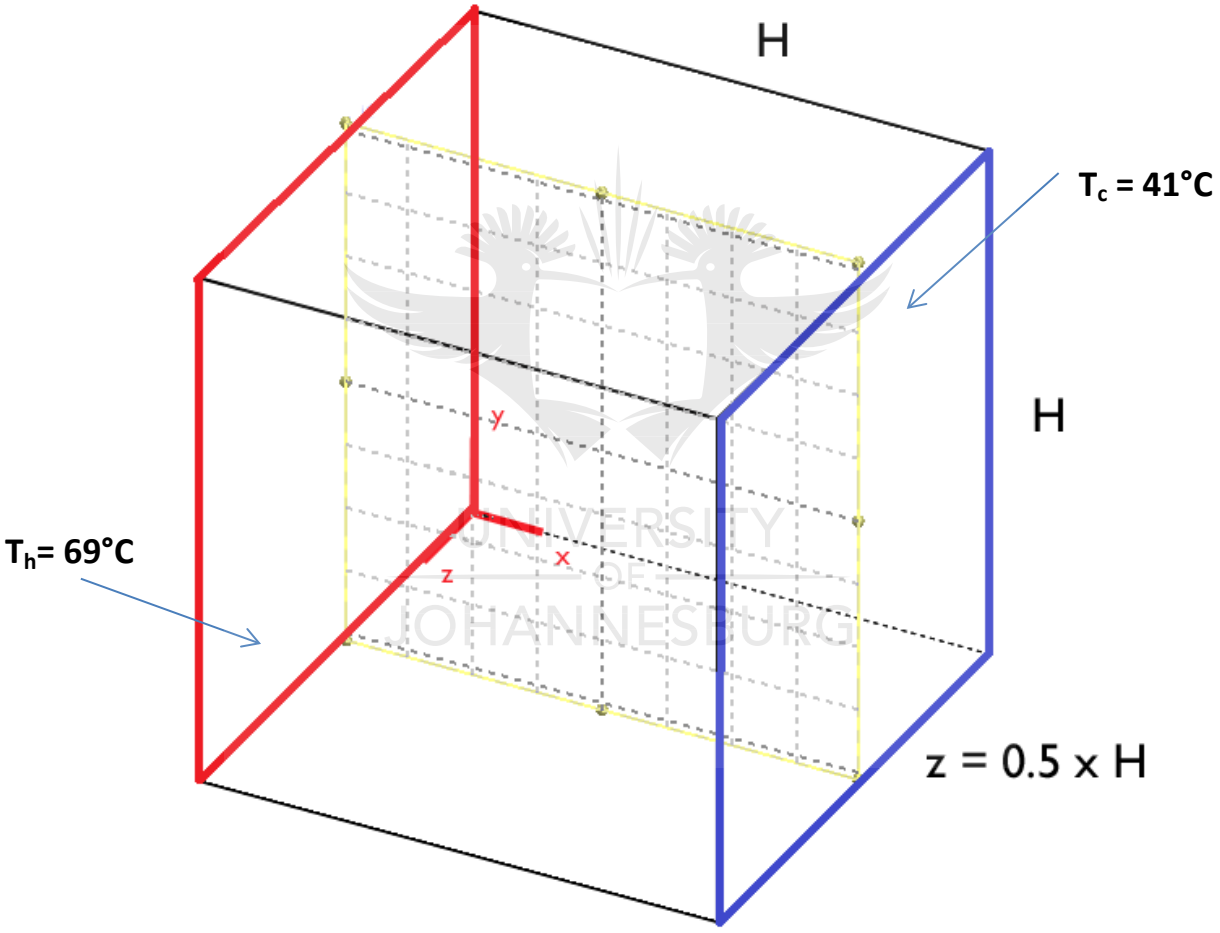

Figure 4.12: Schematic of cubical enclosure considered for the CFD model

To monitor numerical CFD accuracy, a mesh sensitivity analysis was once again conducted. Variables such as temperature, velocity and surface average Nusselt number were monitored. As mentioned by Dol et al [159], three-dimensional high-Reynold number flow is rather complex, and requires a fine mesh in the regions adjacent to the solid walls, therefore 20 prism layers were once again selected, with a combined thickness of 0.02m. A base size of 0.003m was

chosen as the temperature no longer varied with a decreasing mesh size. The rest of the mesh parameters are shown in Table 4.6. The blending factor, which is responsible for the transition in mesh density between the volumetric cell size and the surface mesh size, was left at the default value of 1.0. The boundary conditions are summarized in Table 4.7, and the turbulence parameters in Table 4.8 The essential CFD results from the mesh sensitivity analysis are plotted in Figure 4.13.

Table 4.6: Mesh settings for cubical enclosure

Property	Value
Base Size (m)	0.003
Number of Prism Layers	20
Prism Layer Stretching	1.5
Prism Layer Thickness (m)	0.02
Surface Growth Rate	1.3
Surface Size (Tet/Poly Density)	
Density	1.0
Growth Factor	1.0
Blending Factor	1.0

Table 4.7: Boundary conditions

Boundary	Type	Thermal Specification	Value [°C]
Front Wall	Wall (no-slip)	Adiabatic	-
Back Wall	Wall (no-slip)	Adiabatic	-
Top Wall	Wall (no-slip)	Adiabatic	-
Bottom Wall	Wall (no-slip)	Adiabatic	-
Right Wall	Wall (no-slip)	Isothermal	41
Left Wall	Wall (no-slip)	Isothermal	69

Table 4.8: Turbulence parameters

Under Relaxation Factor	0.8
Convergence Tolerance	0.1
Epsilon	0.0
Turbulent Viscosity (Under Relaxation Factor)	1.0

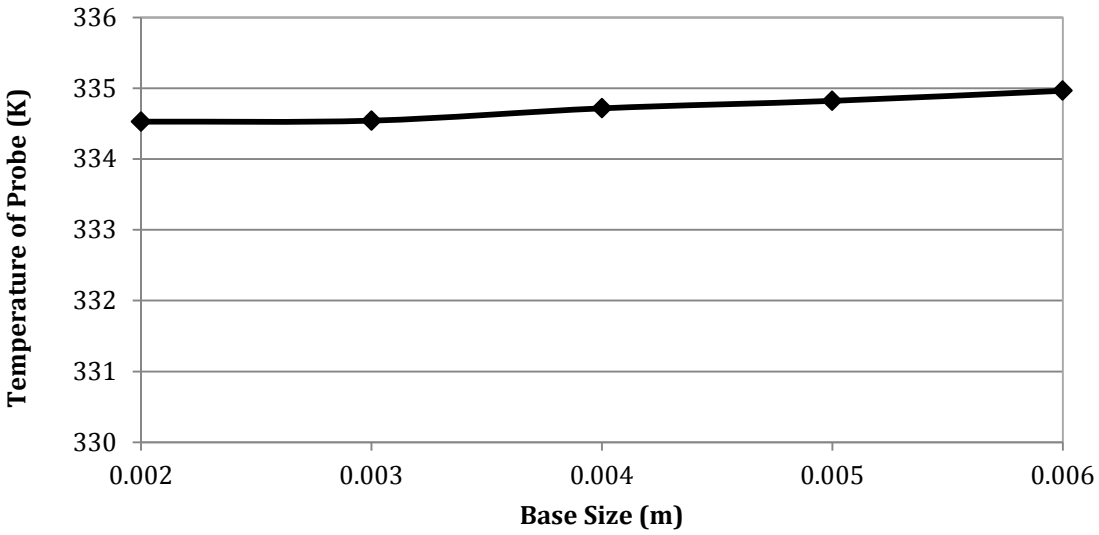

Figure 4.13: Mesh sensitivity study for cubical enclosure

A custom user function was written which calculated the Nusselt Number for each cell on the hot wall using the boundary heat flux. The syntax can be seen in equation 4-7:

$$(abs(\$BoundaryHeatFlux)/28)*0.2/0.0283831 \quad \text{4-7}$$

This equation calculated the Nusselt number for each cell by dividing the absolute value of the boundary heat flux by the temperature difference (28°C), multiplying by the height of the cavity (0.2m), and dividing by the thermal conductivity of the air. The surface averaged Nusselt number was calculated as follows using the scalar-based report function in the software, where the surface averaged Nusselt number was calculated for the hot wall as shown in equation 4-8:

$$\text{Surface Averaged Nusselt Number} = \frac{1}{a}\int Nu\ da = \frac{\sum_f Nu_f A_f}{\sum_f A_f} \quad \text{4-8}$$

The numerical results obtained for the current 3D square scale model are compared to results obtained in the literature [117]. A difference of 5.04% was found between the numerical obtained Surface Averaged Nusselt number and the Nusselt number found by Kürekci [117] as shown in Table 4.9. Therefore additional confidence has again been established in the current three-dimensional CFD model of a cubical enclosure.

4.4.2 Results - Temperature Field

The numerically computed contour plot for temperatures in the cubical enclosure at midplane is shown in Figure 4.14. High gradients are visible near the hot and cold walls respectively. A constant core temperature across the width of the cavity for various heights can be seen. An increase in temperature is also visible from the bottom to the top of the cavity. This is similar to

what was found by Kürekci [117]. The variation of the temperature with respect to the x-direction at the centre of the cavity (z/H = 0.5) is shown in Figure 4.15. When compared to the temperature variation for computed by Kürekci (Figure 4.16), the results agree reasonably well.

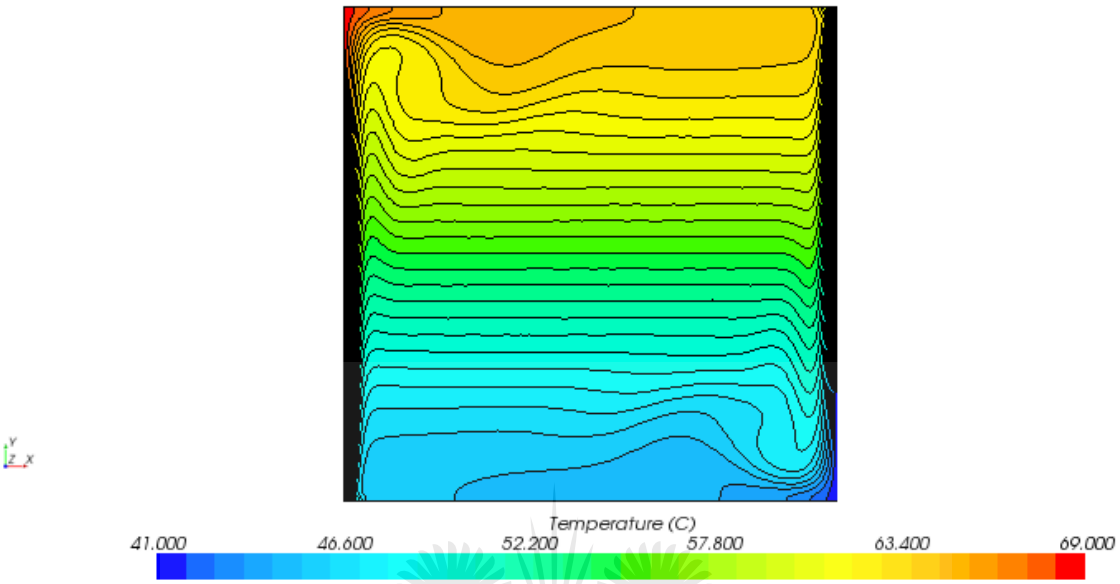

Figure 4.14: Numerical temperature contour plot

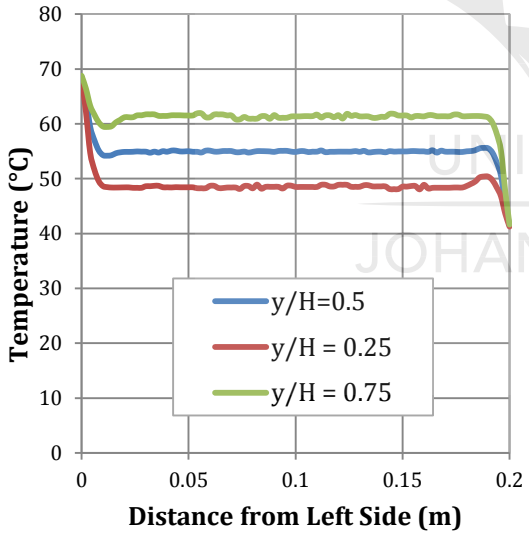

Figure 4.15: Current Numerical temperature variation with x/H (at z/H = 0.5)

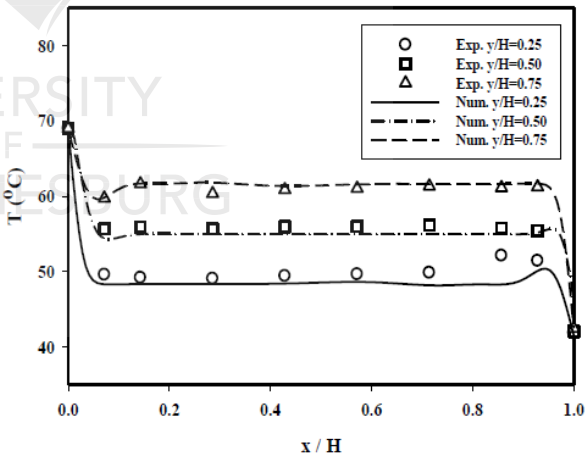

Figure 4.16: Experimental and numerical temperature variation with x/H at z/H=0.5 [117]

4.4.3 Results – Velocity Field

Figures 4.17 and 4.18 compare the numerically calculated vertical velocity profiles with the results obtained by Kürekci [156]. Large velocity gradients are found adjacent to the isothermal walls, with a stagnant area from about 0.025m to 0.175m. This was found for all three heights

(y/H = 0.25,0.5, and 0.75). The numerical results in this case also overestimate the velocity close to the walls, which was also found for the numerical case y/H in the published research.

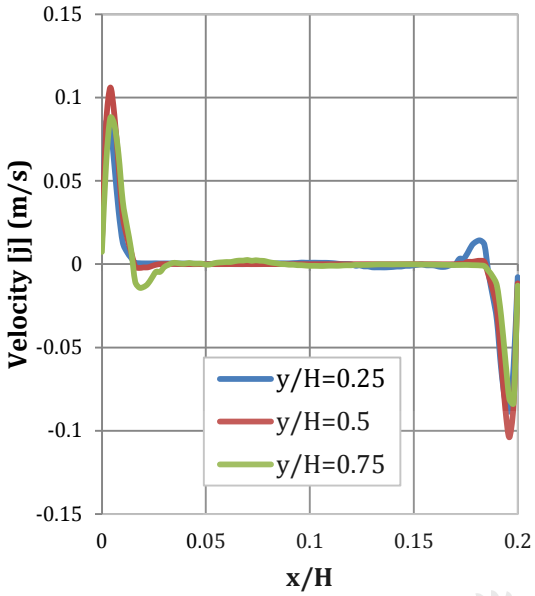

Figure 4.17: Current Numerical vertical velocity profile

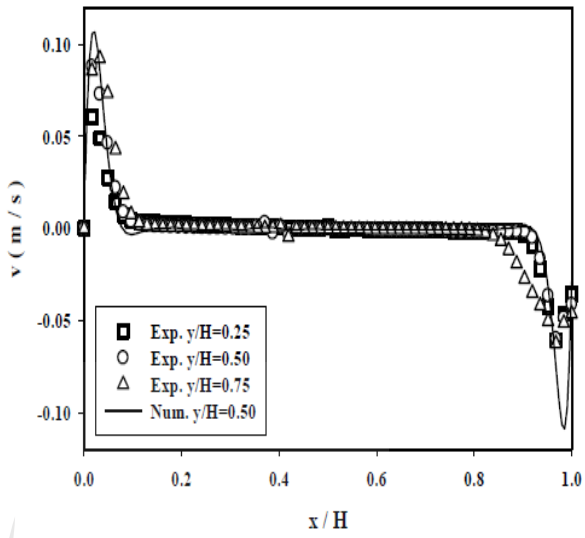

Figure 4.18: Experimental and numerical vertical velocity profile with x/H at z/H=0.5 [137]

4.4.4 Results – Nusselt Number

The Surface Averaged hot wall Nusselt number was once again calculated using the same custom user field function as mentioned before. Table 4.9 compares the results calculated from the current CFD results with studies found in the literature [95], [98], [100], [160] and [117]. From the table it can be seen that a maximum difference of 9% was found when compared to work done by Leong and Hollands [100], while the minimum difference is found to be 1.64% when compared with the work conducted by Dixit and Babu [95].

Table 4.9: Calculated Nusselt numbers

	Present Work	Dixit and Babu [95]	Baïri [161]	Leong and Hollands [100]	Bilgen [160]	Kürekci [156]
Nusselt Number	17.07	16.79	16.073	15.549	16.629	16.21
% Deviation	-	1.64	5.84	8.91	2.58	5.04

4.5 Comparison between 2D and 3D Case

Confidence has thus been established in the three-dimensional numerical CFD model. This same approach can be used to model the original 0.75m greenhouse with zero degree roof angle as a three-dimensional cube, and the results can then be compared to the two-dimensional case. A three-dimensional model of a 0.75m x 0.75m cube as scale model of the greenhouse was created in the numerical CFD program. The top and bottom walls were specified as 15.1°C and 55.1°C (Ra = 1.35×10^9) respectively. The sidewalls were all specified as adiabatic (Table 4.11). The base size, number of prism layer and prism layer thickness were all kept the same as in the two-dimensional case. The mesh and orientation are shown in Figure 4.19, and the mesh parameters are summarized in Table 4.10.

Table 4.10: Mesh Properties for 0.75m Cube

Property	Value
Base Size (m)	0.016
Number of Prism Layers	20
Prism Layer Stretching	1.1
Prism Layer Thickness (m)	0.022
Surface Growth Rate	1.3
Surface Size (Tet/Poly Density)	
Density	1.0
Growth Factor	1.0
Blending Factor	1.0
Surface Size	
Relative Minimum Size	25%
Relative Target Size	100%

Table 4.11: Boundary conditions

Boundary	Type	Thermal Specification	Value [°C]
Front Wall	Wall	Adiabatic	-
Back Wall	Wall	Adiabatic	-
Right Wall	Wall	Adiabatic	-
Left Wall	Wall	Adiabatic	-
Top Wall (Roof)	Wall	Isothermal	15.1
Bottom Wall (Floor)	Wall	Isothermal	55.1

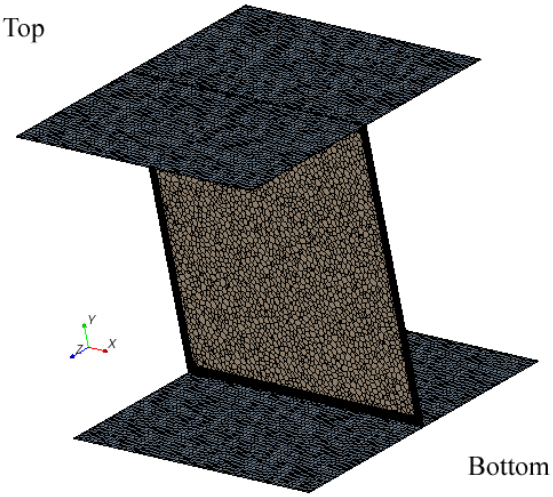

Figure 4.19: Mesh for 0.75m x 0.75m cube

The low-Reynolds number standard k-epsilon turbulence model was used, and the parameters are shown in Table 4.12. Gravity was specified in the negative y-direction.

Table 4.12: Turbulence Parameters for 0.75m Cube

Under Relaxation Factor	**0.8**
Convergence Tolerance	0.1
Epsilon	0.0
Turbulent Viscosity (Under Relaxation Factor)	1.0

The temperature contour plots for the two cases are compared in Figure 4.20. For the three-dimensional case, the contour plot was taken in the z/H = 0.5 plane. The temperature contours for the two-dimensional case tends to be more circular, whereas the contours for the three-dimensional case tend to be slightly more of square shape. This is also visible in the velocity vector plots (Figure 4.21). The vector plot for the two-dimensional case also shows two secondary convective cells in the top left and bottom right corners. This is not present in the three-dimensional case. The temperature difference through the boundary layer to the uniform core region for the three-dimensional case is not as steep as for the two-dimensional case, which is visible in the temperature distribution plot (Figure 4.22). The centre of the cavity is at the same temperature for both cases. As far as velocity distribution in the centre of the cavity is concerned, quite a significant difference is noticed between the two-and three-dimensional case. Both cases exhibit the same trend of reaching a maximum adjacent to the walls, and decreasing towards the centre. The maximum velocity reached in the two-dimensional case is 0.33 m/s whereas a velocity of 0.22 m/s is reached in the three-dimensional case. This amounts to a difference of approximately 33% as calculated in the following equation:

$$\frac{x_{max} - x_{min}}{x_{max}} = \frac{0.33 - 0.22}{0.33} \times 100 = 33.33\% \qquad 4\text{-}9$$

All future differences in this thesis will be calculated using this equation.

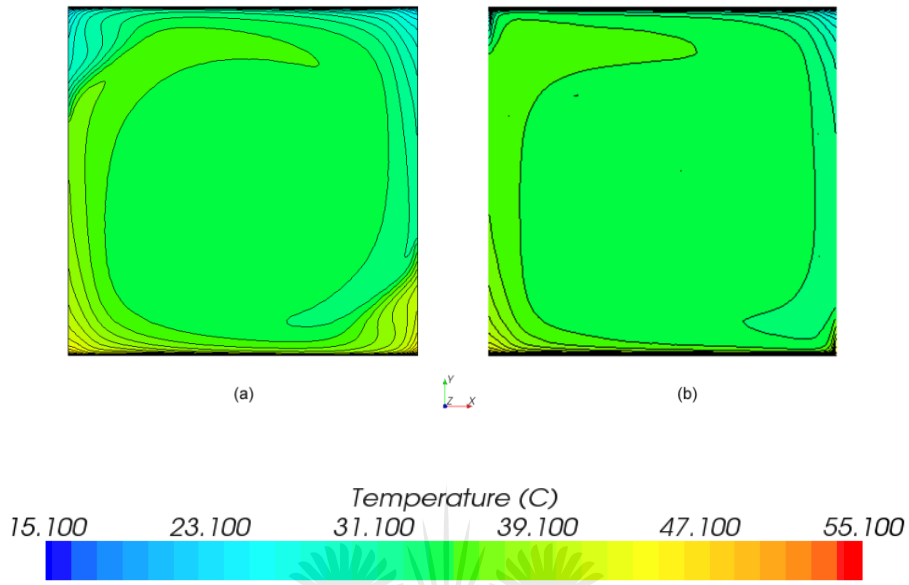

Figure 4.20: Temperature contour plot comparison for (a) Two-dimensional case (b) Three-dimensional case (z/H=0.5)

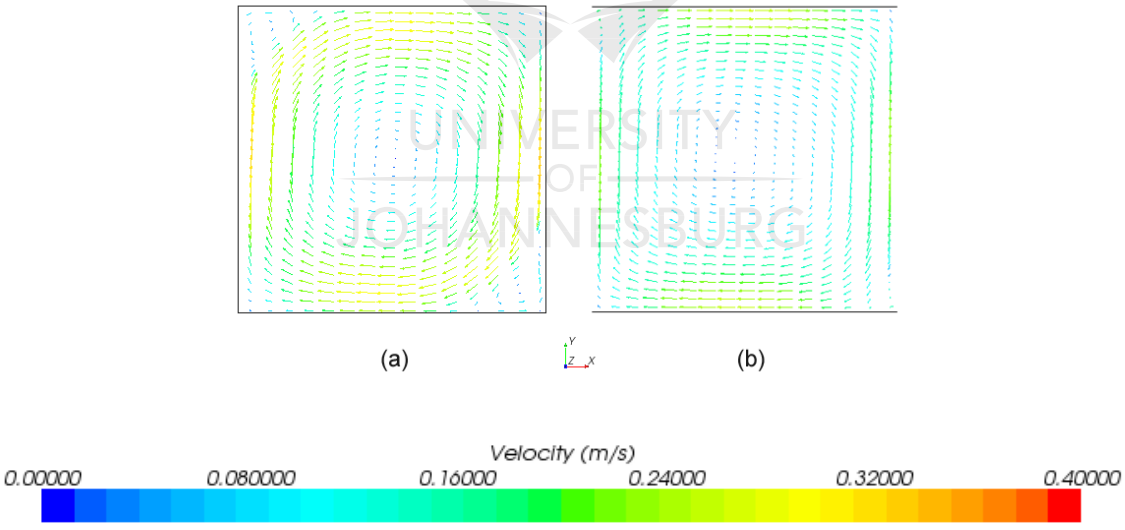

Figure 4.21: Vector plot comparison for (a) Two-dimensional case (b) Three-dimensional case (z/H=0.5)

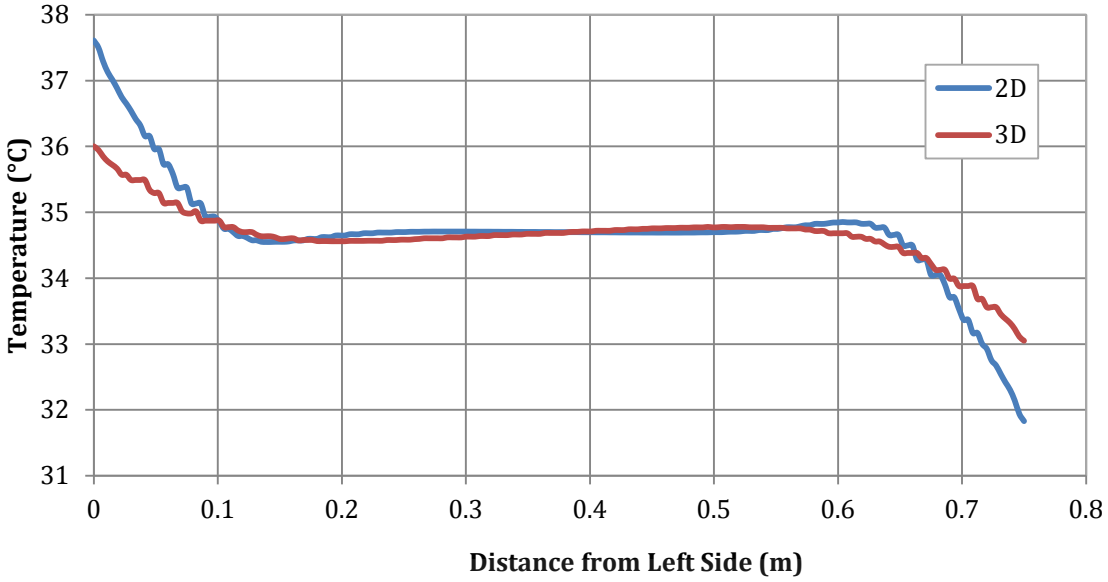

Figure 4.22: Comparison of temperature distribution in the centre of the cavity

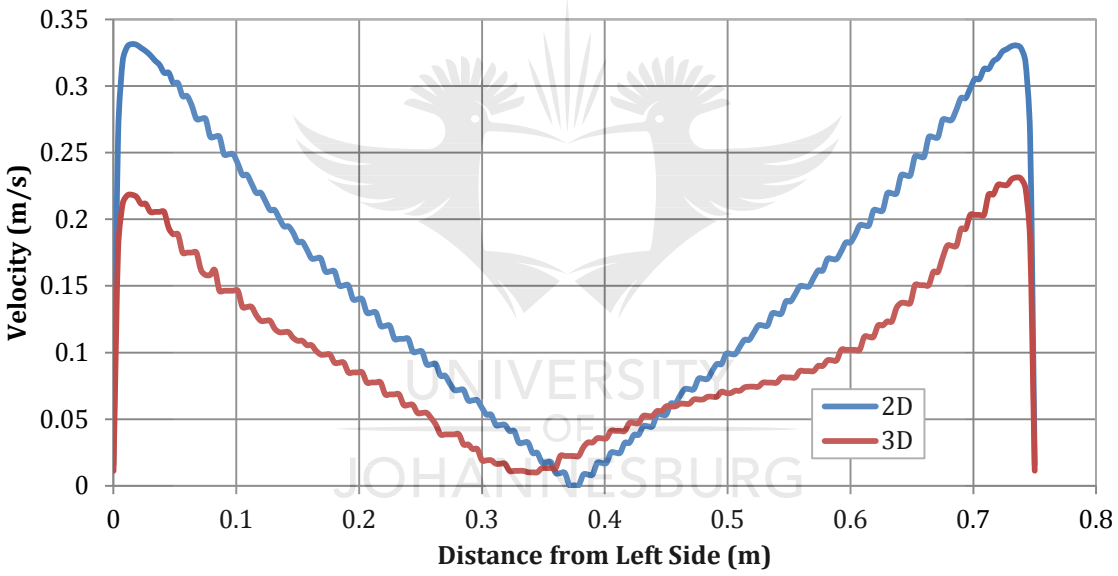

Figure 4.23: Comparison of velocity distribution in the centre of the cavity

The Nusselt number distribution is shown in the 3D surface plot in Figure 4.24. The maximum Nusselt number is visible towards the front right corner. The average Nusselt number was calculated to be **77.3.** The Nusselt number for the two-dimensional case was **78.7,** which amounts to a difference of 1.8%.

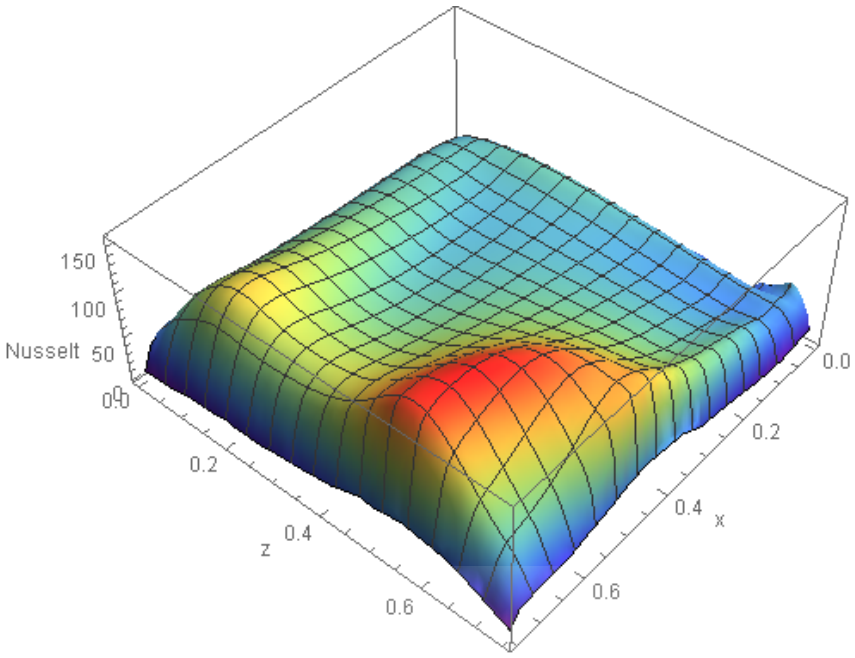

Figure 4.24: Nusselt Number distribution on the floor of the cube

4.6 Conclusion

In this chapter, the objective was to numerically validate a greenhouse scale model with a zero degree roof angle (square) against data found in the literature for both two and three dimensional cavities. The heat transfer, temperature and velocity fields driven by buoyancy forces were investigated for both cases. The numerical CFD results were compared to those found in the literature, and a reasonably good comparison was found for both the two- and three-dimensional cavities. An extended three-dimensional model heated from below and cooled from above was constructed using a similar numerical approach to the validated three-dimensional case. Results found that there is a significant difference between the two- and three-dimensional models, most noticeable in the regions adjacent to the vertical walls. Temperature differences through the boundary layer to the core region are steeper and velocities are higher for the two-dimensional case. These two and three-dimensional CFD models can now be utilized in the next chapter to determine the influence of geometric design changes on the thermal performance of numerical scale models of a single span pitch roof greenhouse.

CHAPTER 5

Design Effects in a Single-span Greenhouse Model

5.1 Chapter Review

The previous chapter established confidence in the numerical models created for a single span, zero degree roof angle greenhouse in two and three dimensions. This chapter aims to develop the numerical model one step further by modifying the roof of the cavity to represent a single-span pitched-roof greenhouse. This numerical model will be used in this chapter to answer the research questions set out in chapter 1:

- What is the effect of geometric design alterations such as roof angle on the thermal performance of a single-span greenhouse?
- Is it possible to deduce Nusselt-Rayleigh relationships for a two dimensional single-span greenhouse cavity?
- Are there differences in the thermal performance of two-dimensional versus three-dimensional single-span greenhouses with a non-zero roof angle?
- What will be the effect of different roof ventilator sizes and types on the thermal performance of a two-dimensional cavity?
- Are there any differences between a closed and ventilated single-span greenhouse?
- Is it possible to qualitatively validate a scaled-up cavity, using the same approach, and compare to results found in the literature by Lamrani [3].

5.2 Modified Square – Single-span Greenhouse (2D)

To meet the above-mentioned objectives set out as research questions, the following steps will be taken:

- The CFD model geometry presented in Chapter 4 will be modified to represent a two-dimensional mono-span closed greenhouse with various roof angles (10, 30, 45 and 60

degrees respectively). The effect of these modifications on the indoor climate will be investigated in detail.

- A three-dimensional case of a pitched-roof greenhouse will be investigated and compared to the same case in two-dimensions.
- The roof geometry of the original two-dimensional mono-span greenhouse will be modified to include a roll-up type roof ventilator. The effect of opening size on the heat transfer inside the cavity will be investigated.

Since confidence has been established in the numerical model for the zero-degree roof angle greenhouse in the previous chapter, the previous numerical model will be adjusted accordingly. The natural convection inside a single-span greenhouse cavity for various Rayleigh numbers will be investigated in detail using Computational Fluid Dynamics to establish Nusselt-Rayleigh relationships. Various roof geometries were simulated and analysed.

5.2.1 Numerical Model

The roof of the original square greenhouse model discussed in the previous chapter was modified to have an angle of 10, 30, 45 and 60 degrees respectively as shown in Figure 5.1.

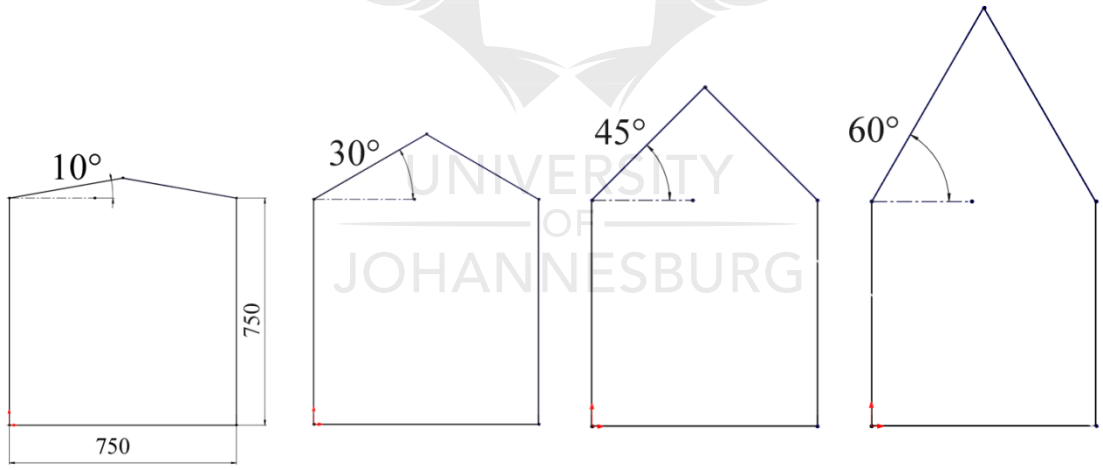

Figure 5.1: Modified square greenhouse scale model

The modified roof was still defined as the cold wall, while the floor of the cavity the hot wall. The Rayleigh number was again based on the height of the walls (which corresponded to the distance between the hot and cold wall in the previous section). The Rayleigh number (as calculated in equation 4-1) was varied by adjusting the floor temperature as shown in Table 5.1 (similar to the procedure followed in chapter 4).

Table 5.1: Temperature differences and associated Rayleigh numbers

Height	**0.75m**							
$\mathbf{T_{floor}}$	20.1	25.1	35.1	45.1	55.1	65.1	75.1	85.1
$\mathbf{T_{roof}}$	15.1	15.1	15.1	15.1	15.1	15.1	15.1	15.1
ΔT	5	10	20	30	40	50	60	70
$\mathbf{T_f}$	290.75	293.25	298.25	303.25	308.25	313.25	318.25	323.25
β	3.44E-03	3.41E-03	3.35E-03	3.30E-03	3.24E-03	3.19E-03	3.14E-03	3.09E-03
α	2.13E-05	2.16E-05	2.23E-05	2.30E-05	2.37E-05	2.45E-05	2.52E-05	2.59E-05
υ	1.51E-05	1.53E-05	1.57E-05	1.62E-05	1.67E-05	1.72E-05	1.77E-05	1.82E-05
Ra	2.22E+08	4.27E+08	7.92E+08	1.10E+09	1.35E+09	1.57E+09	1.75E+09	1.90E+09

5.2.2 Mesh and Physics Setup

The mesh size and parameters were kept the same as for the square greenhouse (refer to Table 5.2), a typical mesh and prism layer mesh is shown in Figure 5.2. The physics setup was kept exactly the same as mentioned in chapter 4, implying that turbulent flow was again assumed in the CFD models. The meshing parameters are summarized in Table 5.2, and the turbulence parameters in Table 5.3. Gravity was chosen to be in the negative y-direction. The boundary conditions are summarized in Table 5.4.

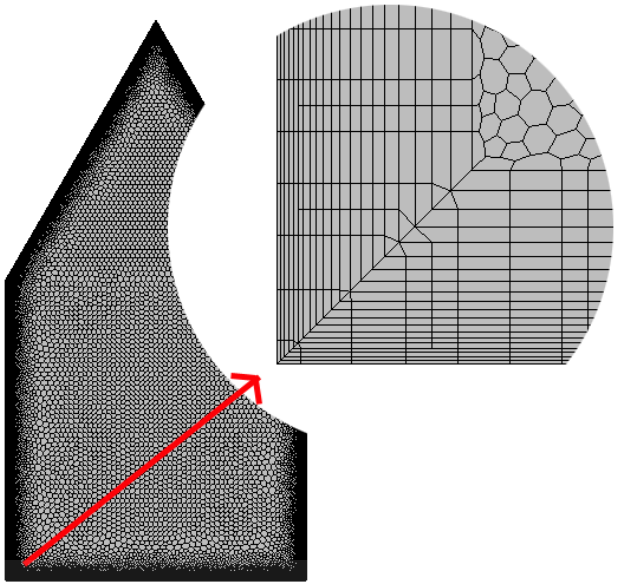

Figure 5.2: Typical mesh for modified cavity

Table 5.2: Mesh properties of single-span pitch roof greenhouse

Property	Value
Base Size (m)	0.016
Number of Prism Layers	20
Prism Layer Stretching	1.5
Prism Layer Thickness (m)	0.022
Surface Growth Rate	1.3
Surface Size (Tet/Poly Density)	
Density	1.0
Growth Factor	1.0
Blending Factor	1.0
Local Custom Surface Size	
Relative Minimum Size	10% of Base Size
Relative Target Size	50% of Base Size

Table 5.3: Turbulence parameters for single-span pitch roof greenhouse

Under Relaxation Factor	**0.8**
Convergence Tolerance	0.1
Epsilon	0.0
Turbulent Viscosity (Under Relaxation Factor)	1.0

Table 5.4: Boundary conditions

Boundary	Type	Thermal Specification
Left Wall	Wall	Adiabatic
Right Wall	Wall	Adiabatic
Bottom Wall (Floor)	Wall	Isothermal
Top Wall (Roof)	Wall	Isothermal

5.2.3 Results

The results for the modified square to approximate a single span greenhouse scale model are presented in this section. Figure 5.3 to Figure 5.18 compare the temperature and velocity contour plots for the various roof angles for each Rayleigh number. All of the cases except two yielded steady state results. For the two unsteady cases (60 Degree roof angle, $\Delta T = 5°C$, 45 Degree roof angle, $\Delta T = 10°C$) the average of the varying surface average Nusselt number was taken for the Nusselt-Rayleigh plots. All the plots (velocity vector and velocity contour plots) are characterized by a large, dominating convective loop, and a smaller loop rotating in the opposite direction in one of the bottom corners. The 60 degree roof angle cavity also contains another large convective loop, rotating in the ridge of the roof. Thermal boundary layers are confined to the walls for all cases, and large thermal boundary layers are noticed at the top corner (ridge of the roof) of the roofs for the 10,30,45 and 60 degrees roof angle greenhouses. As the roof angle increases, the thermal boundary layer adjacent to the roof thickens. For the non-zero roof angle cavities, the thermal boundary layer at the bottom of the cavity adjacent to the hot wall is quite large, and reduces in size as the Rayleigh number increases, meaning that the inner core increases.

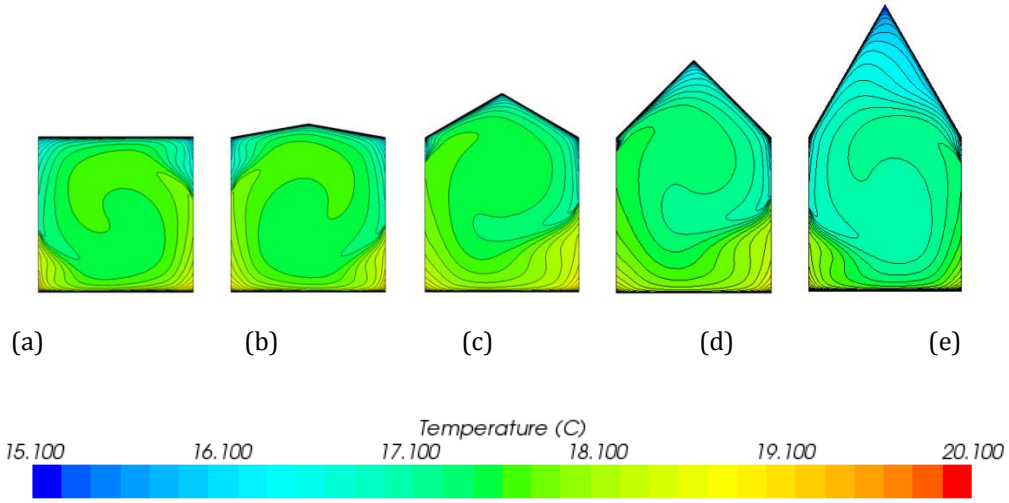

Figure 5.3: Isotherms for ΔT = 5°C (Ra = 2.22 x 10^8) for various roof angles a) 0 degrees b)10 degrees c) 30 degrees d) 45degrees and e) 60 degrees

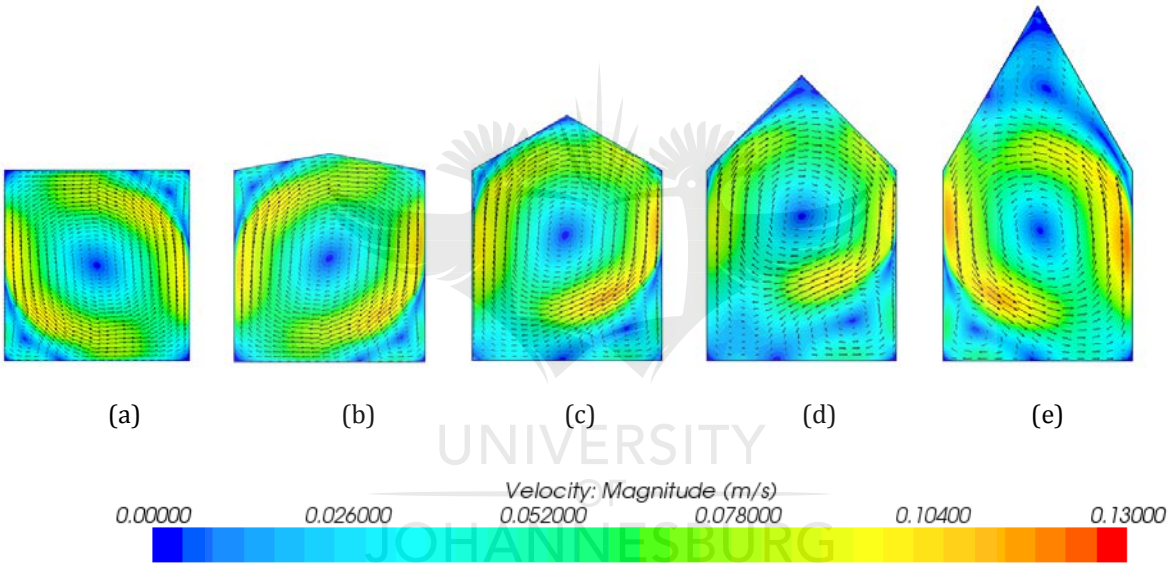

Figure 5.4: Vectors and velocity contour plots for ΔT = 5°c (Ra = 2.22 x 10^8) for various roof angles a) 0 degrees b)10 degrees c) 30 degrees d) 45 degrees and e) 60 degrees

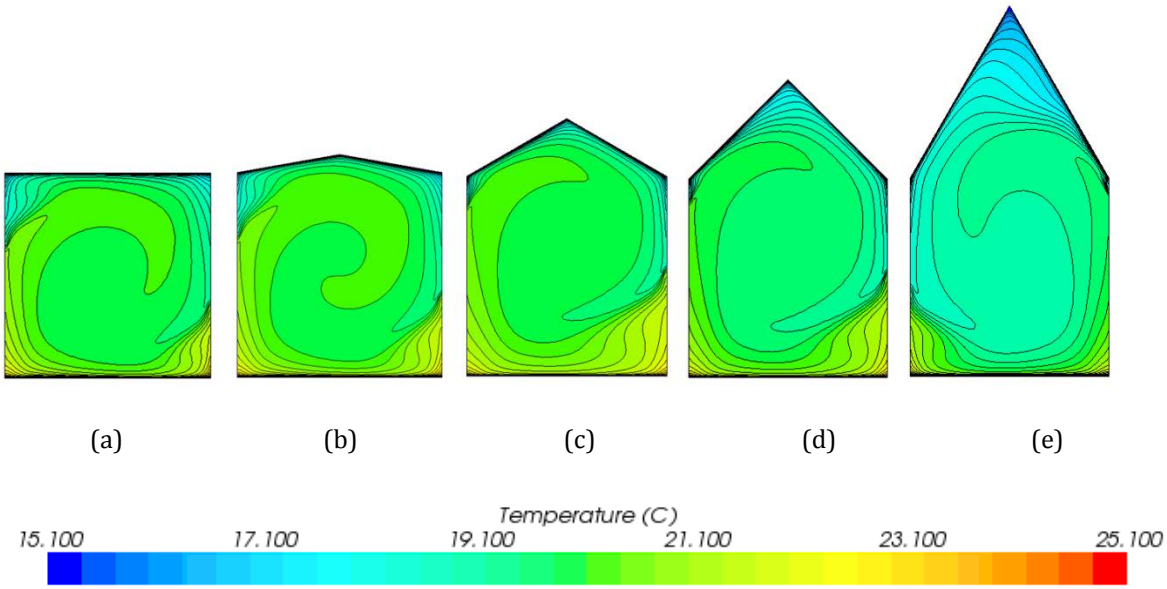

Figure 5.5: Isotherms for ΔT = 10°C (Ra = 4.27 x 10^8) for various roof angles a) 0 degrees b)10 degrees c) 30 degrees d) 45 degrees and e) 60 degrees

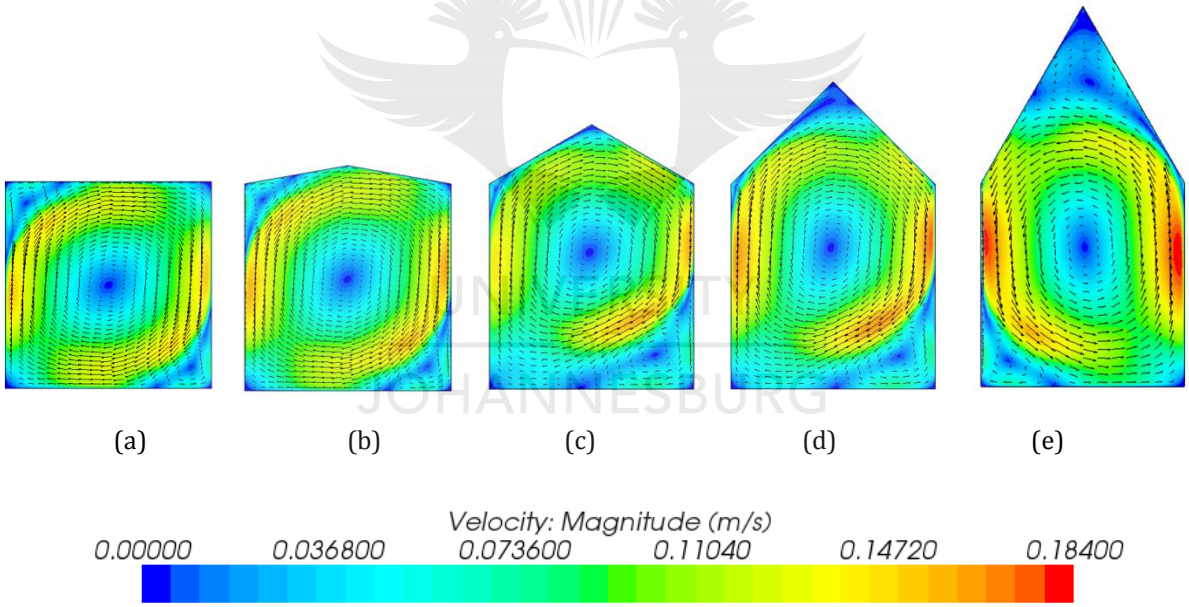

Figure 5.6: Vectors and velocity contour plots for ΔT = 10°C (Ra = 4.27 x 10^8) for various roof angles a) 0 degrees b)10 degrees c) 30 degrees d) 45 degrees and e) 60 degrees

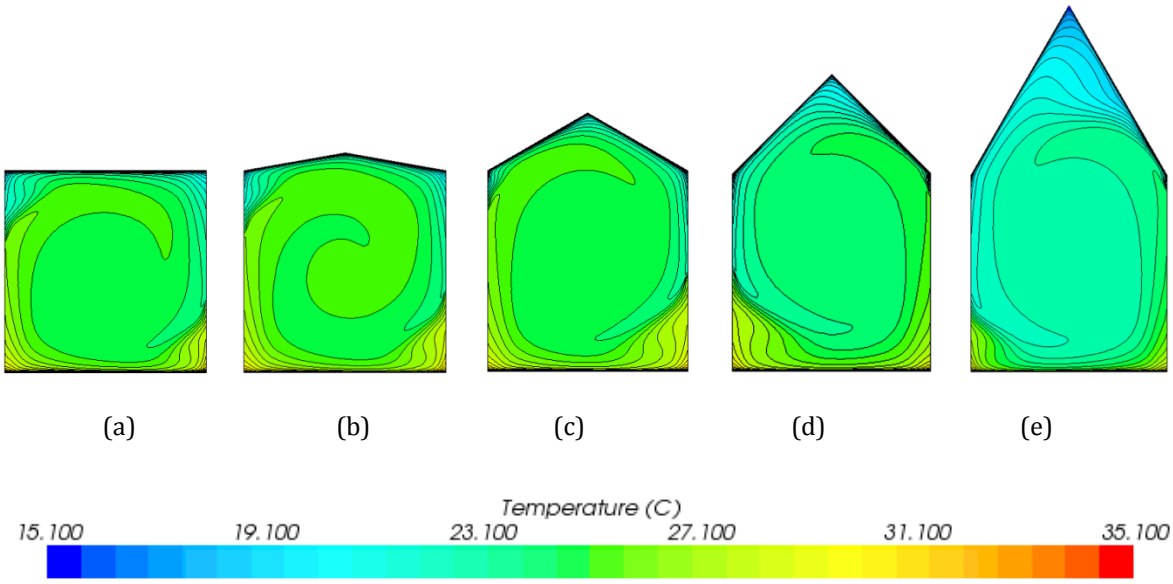

Figure 5.7: Isotherms for ΔT = 20°C (Ra = 7.92 x 10^{8}) for various Roof Angles a) 0 degrees b)10 degrees c) 30 degrees d) 45 degrees and e) 60 degrees

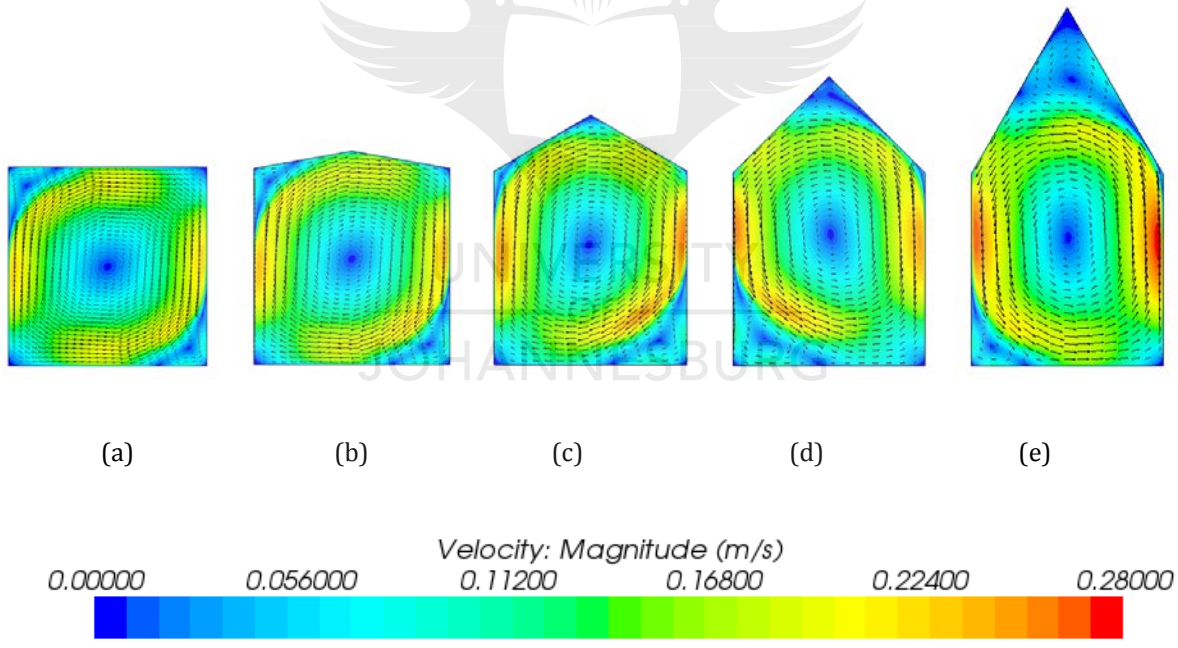

Figure 5.8: Vectors and Velocity Contour Plots for ΔT = 20°C (Ra = 7.92 x 10^{8}) for various Roof Angles a) 0 degrees b)10 degrees c) 30 degrees d) 45 degrees and e) 60 degrees

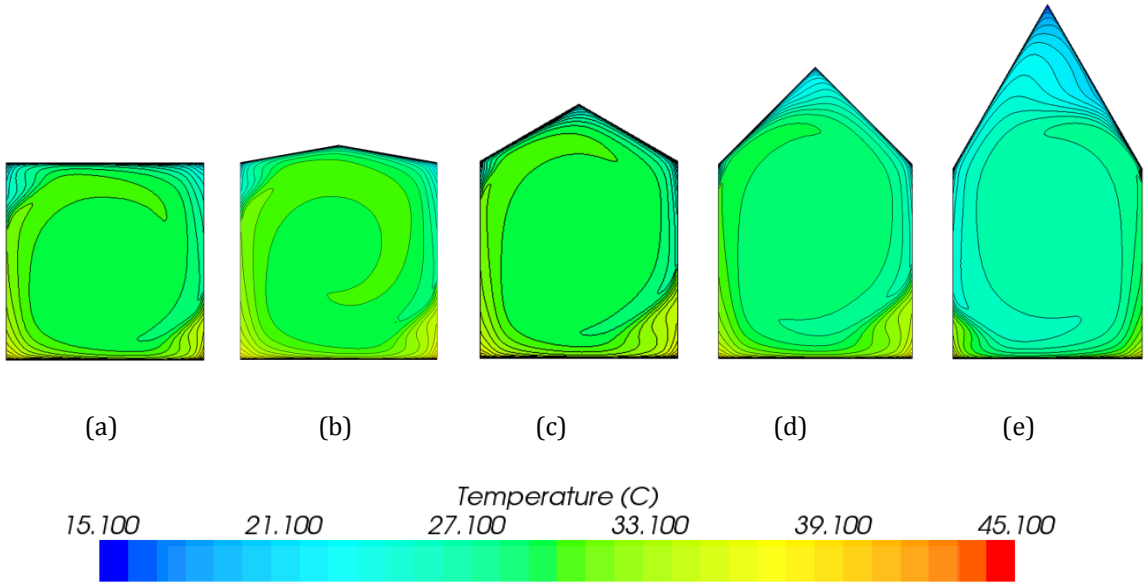

Figure 5.9: Isotherms for ΔT = 30°C (Ra = 1.10 x 10^9) for various Roof Angles a) 0 degrees b)10 degrees c) 30 degrees d) 45 degrees and e) 60 degrees

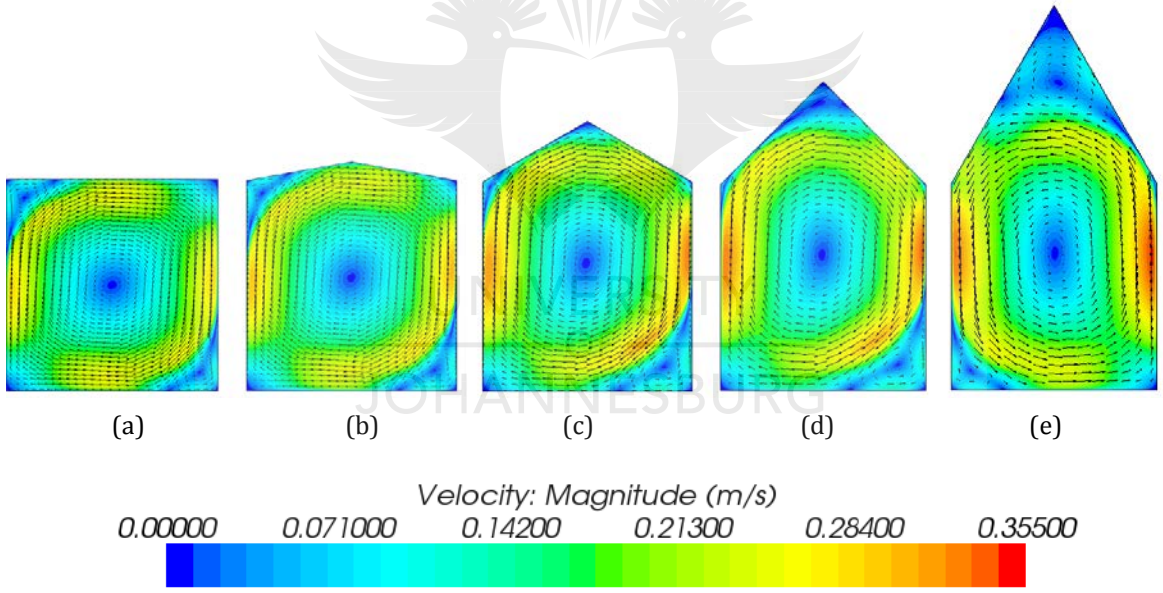

Figure 5.10: Vectors and Velocity Contour Plots for ΔT = 30°C (Ra = 1.10 x 10^9) for various Roof Angles a) 0 degrees b)10 degrees c) 30 degrees d) 45 degrees and e) 60 degrees

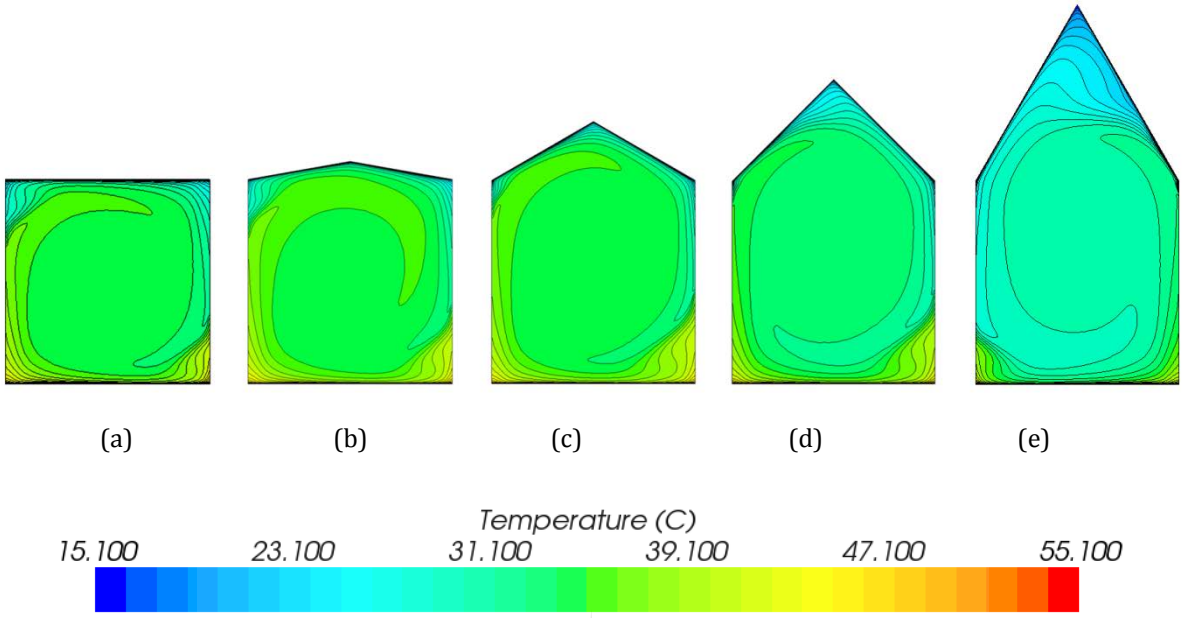

Figure 5.11: Isotherms for ΔT = 40°C (Ra = 1.35 x 10^9) for various Roof Angles a) 0 degrees b)10 degrees c) 30 degrees d) 45 degrees and e) 60 degrees

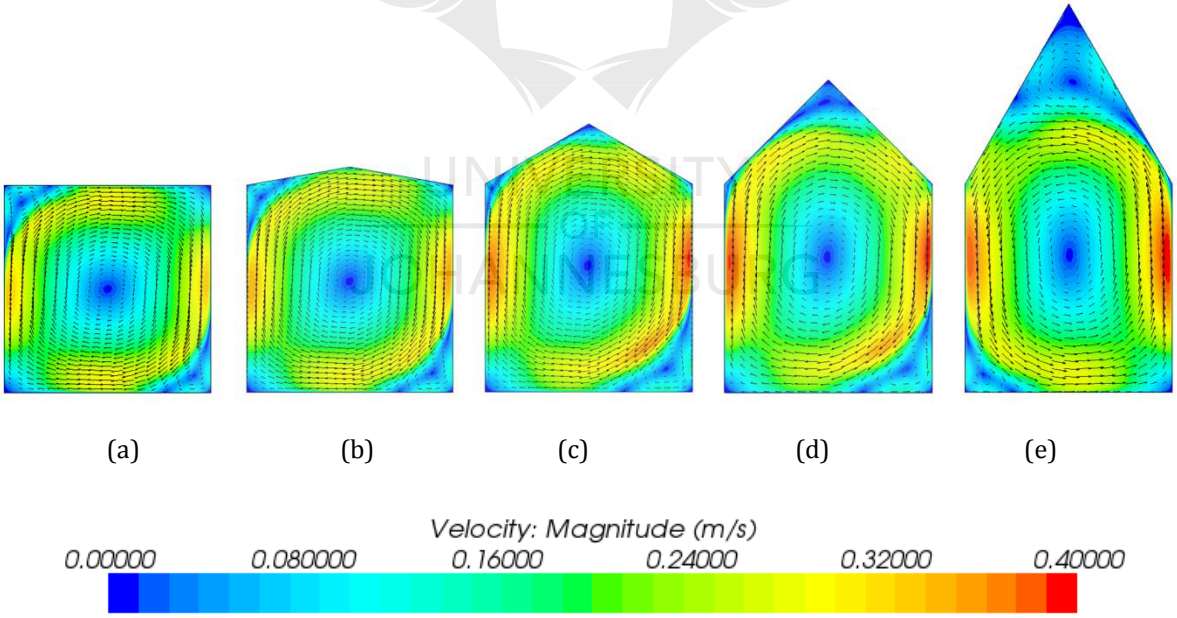

Figure 5.12: Vectors and Velocity Contour Plots for ΔT = 40°C (Ra = 1.35 x 10^9) for various Roof Angles a) 0 degrees b)10 degrees c) 30 degrees d) 45 degrees and e) 60 degrees

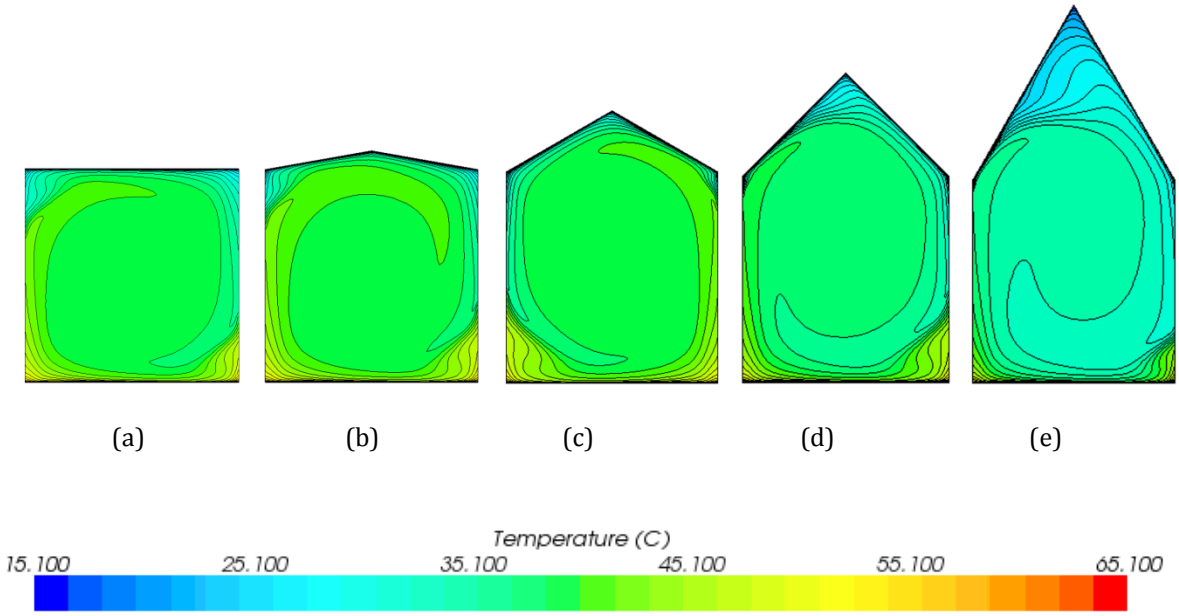

Figure 5.13: Isotherms for ΔT = 50°C (Ra = 1.57 x 10^9) for various roof angles a) 0 degrees b)10 degrees c) 30 degrees d) 45 degrees and e) 60 degrees

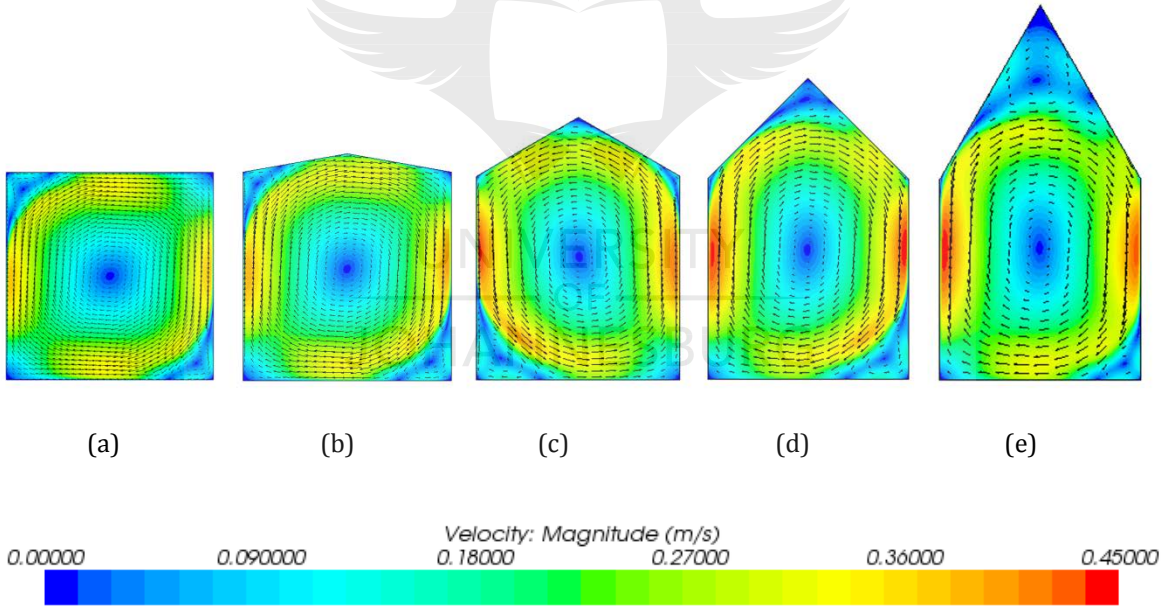

Figure 5.14: Vectors and Velocity Contour Plots for ΔT = 50°C (Ra = 1.57 x 10^9) for various Roof Angles a) 0 degrees b)10 degrees c) 30 degrees d) 45 degrees and e) 60 degrees

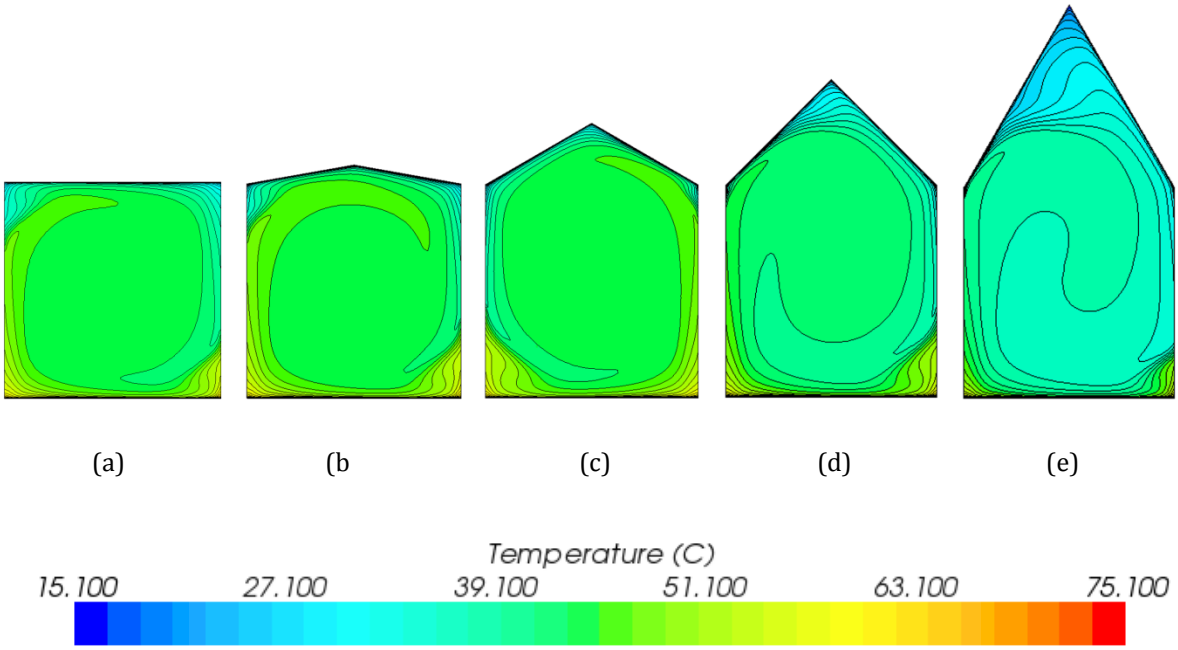

Figure 5.15: Isotherms for ΔT = 60°C (Ra = 1.75 x 10^9) for various roof angles a) 0 degrees b)10 degrees c) 30 degrees d) 45 degrees and e) 60 degrees

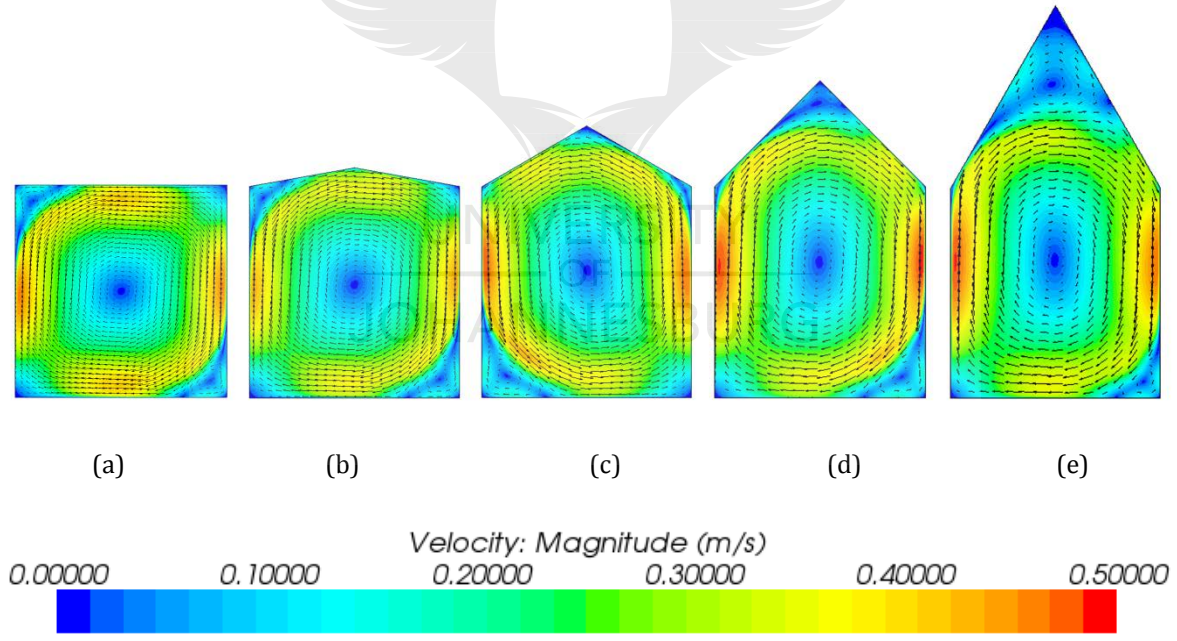

Figure 5.16: Vectors and Velocity Contour Plots for ΔT = 60°C (Ra = 1.75 x 10^9) for various roof angles a) 0 degrees b)10 degrees c) 30 degrees d) 45 degrees and e) 60 degrees

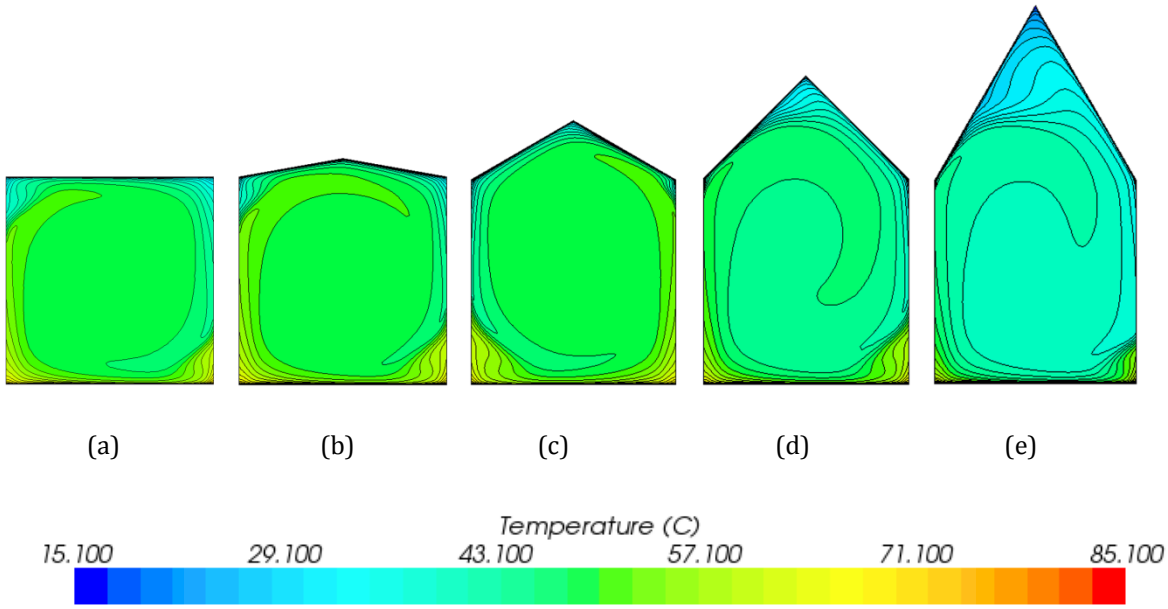

Figure 5.17: Isotherms for ΔT = 70°C (Ra = 1.9 x 10^9) for various Roof Angles a) 0 degrees b)10 degrees c) 30 degrees d) 45 degrees and e) 60 degrees

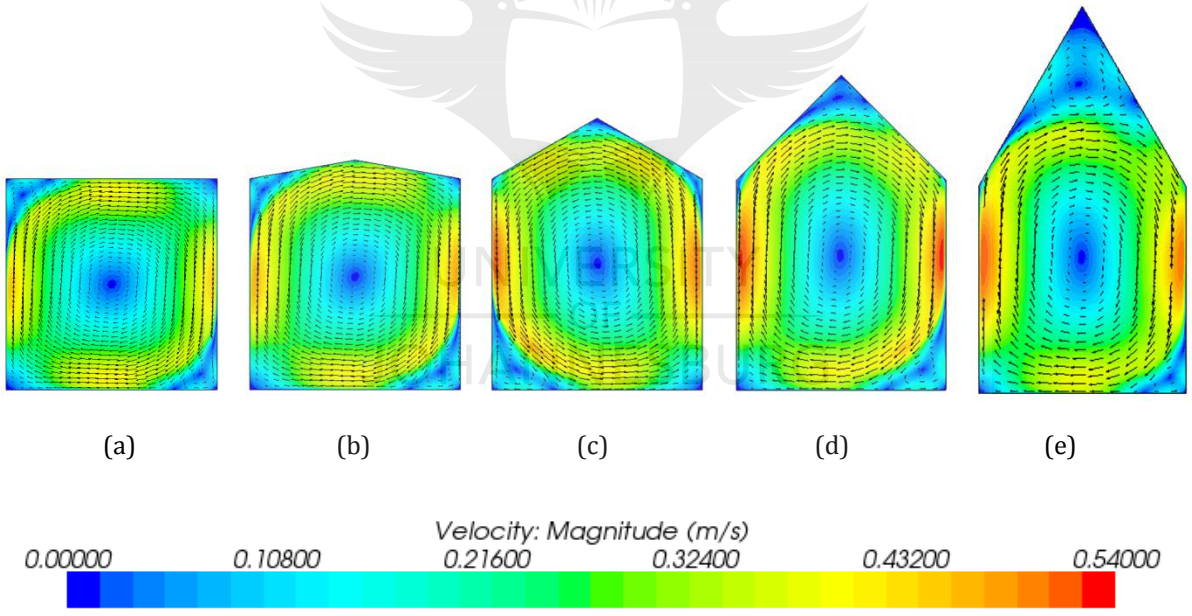

Figure 5.18: Vectors and Velocity Contour Plots for ΔT = 70°C (Ra = 1.9 x 10^9) for various Roof Angles a) 0 degrees b)10 degrees c) 30 degrees d) 45 degrees and e) 60 degrees

A summary of the direction of the various convective cells in each case is shown in Table 5.5 and Table 5.6 respectively. For all the 10 degree roof angle cases, all the dominating flow cells were in the clockwise direction, with two smaller cells in the top left and bottom right corners. This is similar to the zero-degree roof greenhouse validated in the previous chapter. Although the top left convective cell was noticeably smaller than the bottom right cell for the 10 degree roof angle

cavity. For a temperature difference of 5 to 40 degrees °C (Ra = 2.22 x 10^8 to Ra = 1.35 x 10^9), the dominating cell moves clockwise for the 30 degree roof angle cavity, with a smaller counter-clockwise rotating cell in the bottom right corner. For a temperature difference of 50 – 70 (Ra = 1.57 x 10^9 to R = 1.9 x 10^9) degrees, the directions of the loops reverses, and the smaller cell is located in the bottom left corner. For a roof angle of 45 degrees, only a temperature difference of 10 and 20 degrees Celsius (Ra = 4.27 x 10^8 and Ra = 7.92 x 10^8) yields a counter-clockwise dominating flow cell with the smaller cell rotating clockwise in the bottom left corner. For a roof angle of 60 degrees, an additional smaller cell is noticed in the corner of the roof. A temperature difference of 5 to 40 degrees creates a counter-clockwise convective loop with a smaller counter-clockwise rotating cell rotating in the bottom left corner.

Table 5.5: Summary of Convective Cells for Roof Angles of 10 and 30 Degrees

	Roof Angle					
	10			30		
ΔT	**Large Cell**	**Small Cell**	**Position of Small Cells**	**Large Cell**	**Small Cell**	**Position of Small Cells**
5	C	CC	TLBR	C	CC	BR
10	C	CC	TLBR	C	CC	BR
20	C	CC	TLBR	C	CC	BR
30	C	CC	TLBR	C	CC	BR
40	C	CC	TLBR	C	CC	BR
50	C	CC	TLBR	CC	clock	BL
60	C	CC	TLBR	CC	clock	BL
70	C	CC	TLBR	CC	clock	BL

Legend:

C	**Clockwise**
CC	Counter-Clockwise
TLBR	Top-Left-Bottom-Right
BR	Bottom Right
BL	Bottom Left

Table 5.6: Summary of Convective Cells for Roof Angles of 45 and 60 Degrees

	Roof Angle						
	45			60			
ΔT	**Large Cell**	**Small Cell**	**Position of Small Cells**	**Large Cell**	**Small Cell**	**Position of Small Cells**	**Roof**
5	C	CC	BR	CC	C	BL	C
10	CC	C	BL	CC	C	BL	C
20	CC	C	BL	CC	C	BL	C
30	C	CC	BR	CC	C	BL	C
40	C	CC	BR	CC	C	BL	C
50	C	CC	BR	C	CC	BR	CC
60	C	CC	BR	C	CC	BR	CC
70	C	CC	BR	C	CC	BR	CC

5.2.4 Nusselt Number Distribution

The Nusselt number distribution for each roof angle is shown in Figure 5.19 to Figure 5.22 as a function of temperature difference. As expected, the Nusselt number distribution increases overall with Rayleigh number for all roof angles. Figure 5.19 plots the Nusselt number distribution on the hot wall (floor) of the cavity for a 10 degree roof angle, all the cases exhibit a similar trend. A first maximum is reached towards the right side of the cavity, with a second smaller maximum noticed on the left side of the cavity. A small convective loop is present in the right bottom corner, and therefore contributes to the convective heat transfer.

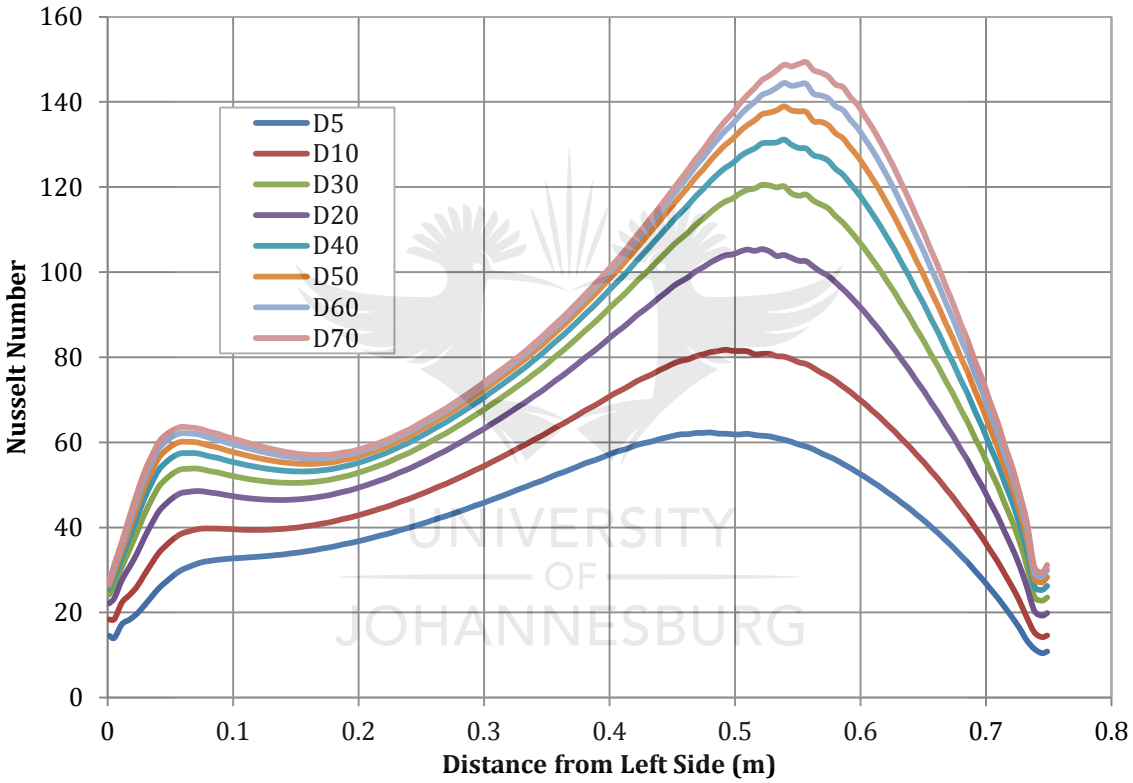

Figure 5.19: Nusselt Number Distribution on Hot Wall (Floor) of 10 Degree Roof Angle Greenhouse

Figure 5.20 shows the Nusselt number distribution for the case of a 30 degree roof angle. The maximum for the first 5 cases (Ra = 2.22 x 10^8 to 1.35 x 10^9) is reached towards the right side of the cavity, and for the last three cases (Ra = 1.57 x 10^9 to 1.9 x 10^9) towards the left side of the cavity. The maximum heat transfer occurs on the side where a small secondary cell rotates in the bottom corner in each case. The rapid change in Nusselt number in the region 0 to 0.1m is due to a stagnant section in the corner, and then an increase to the main convective cell moving adjacent the hot wall/bottom of the cavity. The Nusselt number distribution for the first two

cases (Ra = 2.22 x 10^8 and Ra = 4.27 x 10^8) is noticeably different from the other cases. If the vector plots are investigated closely (refer to Figure 5.4 and Figure 5.6), one notices that the secondary cell is almost as large as half the bottom wall. The size of the cell diminishes slightly with increasing Rayleigh number.

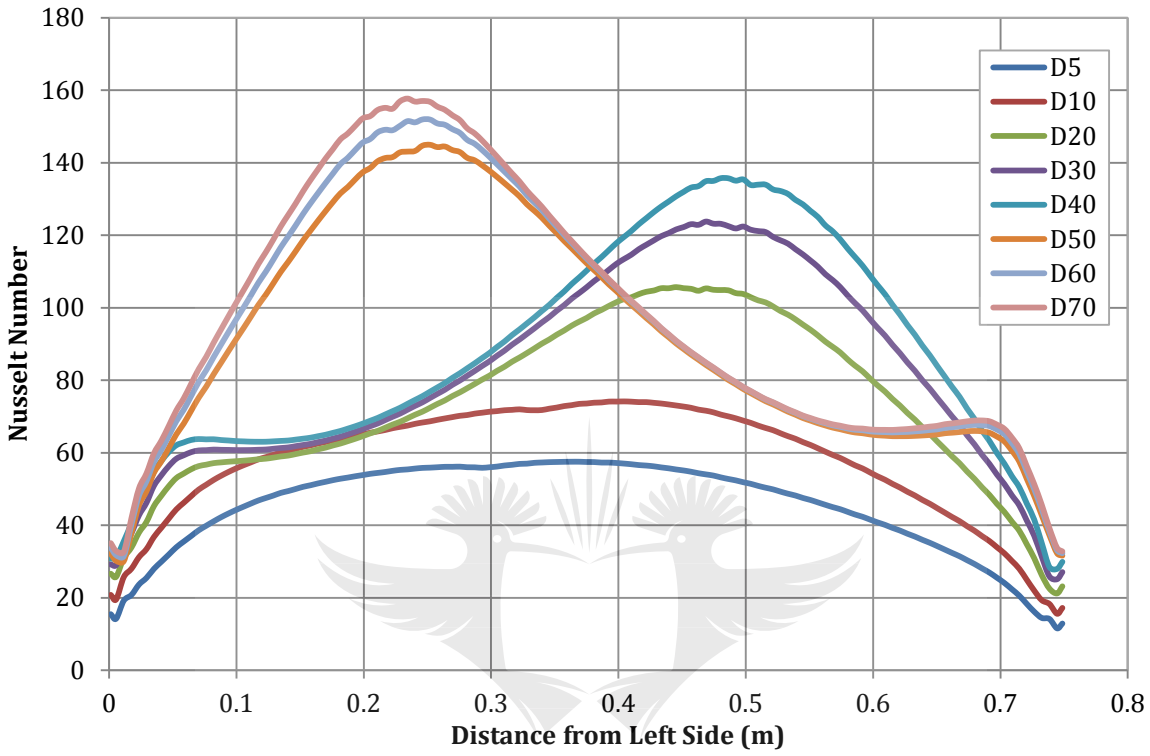

Figure 5.20: Nusselt Number Distribution on Hot Wall (Floor) of 30 Degree Roof Angle Greenhouse

The variation of the Nusselt number distribution with Rayleigh number for a roof angle of 45 degrees is shown in Figure 5.21. The three lowest Rayleigh numbers (Ra = 2.22 x 10^8, 4.27 x 10^8 and 7.92 x 10^8) reveals the same trend. A maximum is reached around 0.3m from the left side of the cavity for each case. The very slight dip that is noticed in these curves may be due to the formation of a large secondary cell in the corner. For the case of Ra = 2.22 x 10^8 and 4.27 x 10^8, the large cell (almost half the cavity width) forms in the bottom right hand corner, while the cell moves to the left hand corner for Ra = 7.92 x 10^8. The last five cases also display the same trend as far as the curve is concerned – a local maximum is reached close to the left wall, with a large gradient noticed from the wall to approximately 0.5m. This may be due to the stagnant region in the bottom left corner. Another local maximum is reached in the region of 0.6m from the left wall.

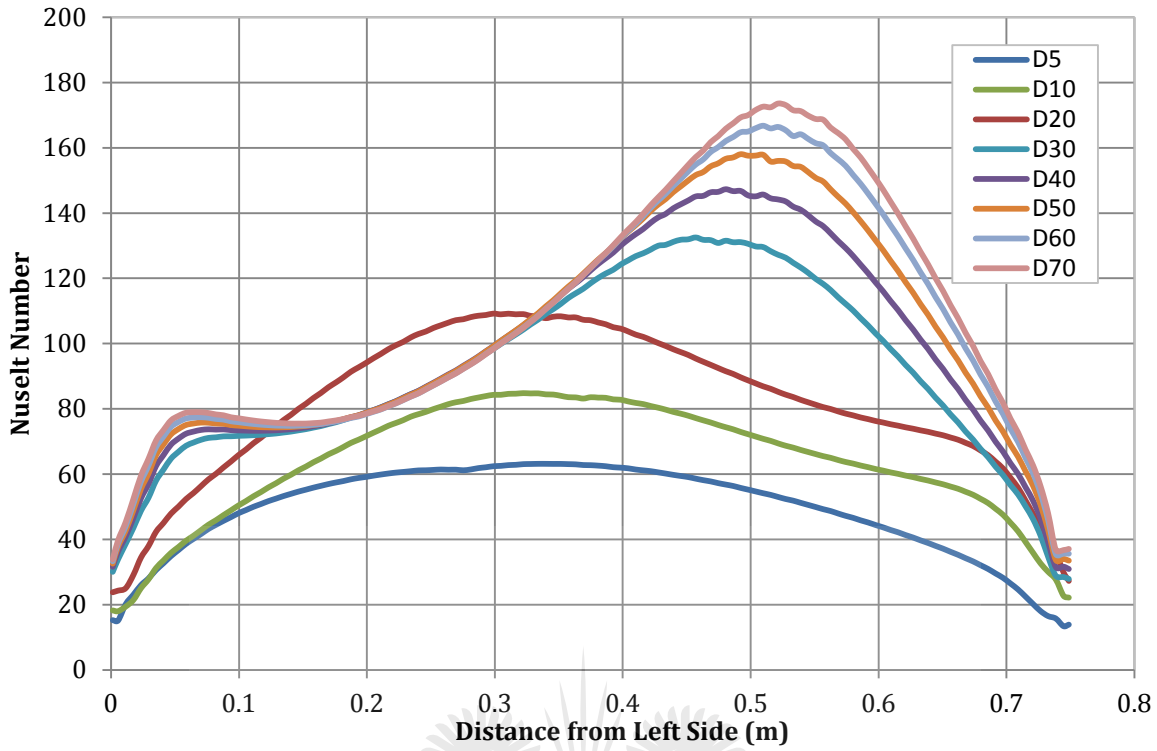

Figure 5.21: Nusselt Number Distribution on Hot Wall (Floor) of 45 Degree Roof Angle Greenhouse

Lastly, Figure 5.22 plots the Nusselt Number distribution on the floor of the cavity for a roof angle of 60 Degrees for various Rayleigh numbers. The graph legend shows the corresponding temperature differences. For this roof angle, the five lowest Rayleigh numbers corresponding to a temperature difference of 5,10,20,30 and 40°C display similar behaviour. All consist of a local maximum on the left half of the cavity, with a smaller convective cell forming in the bottom left corner. The size of the cell increases as the Rayleigh number decreases. A large gradient is noticed in the right corner, due to the stagnant region in the corner. The highest three Rayleigh numbers corresponding to 50,60 and 70°C degrees difference between the bottom and top wall is distributed in an opposite fashion. The maximum is reached towards the right adiabatic wall, with a steep gradient in the left corner. The smaller convective cell rotates in the bottom right corner for these three cases.

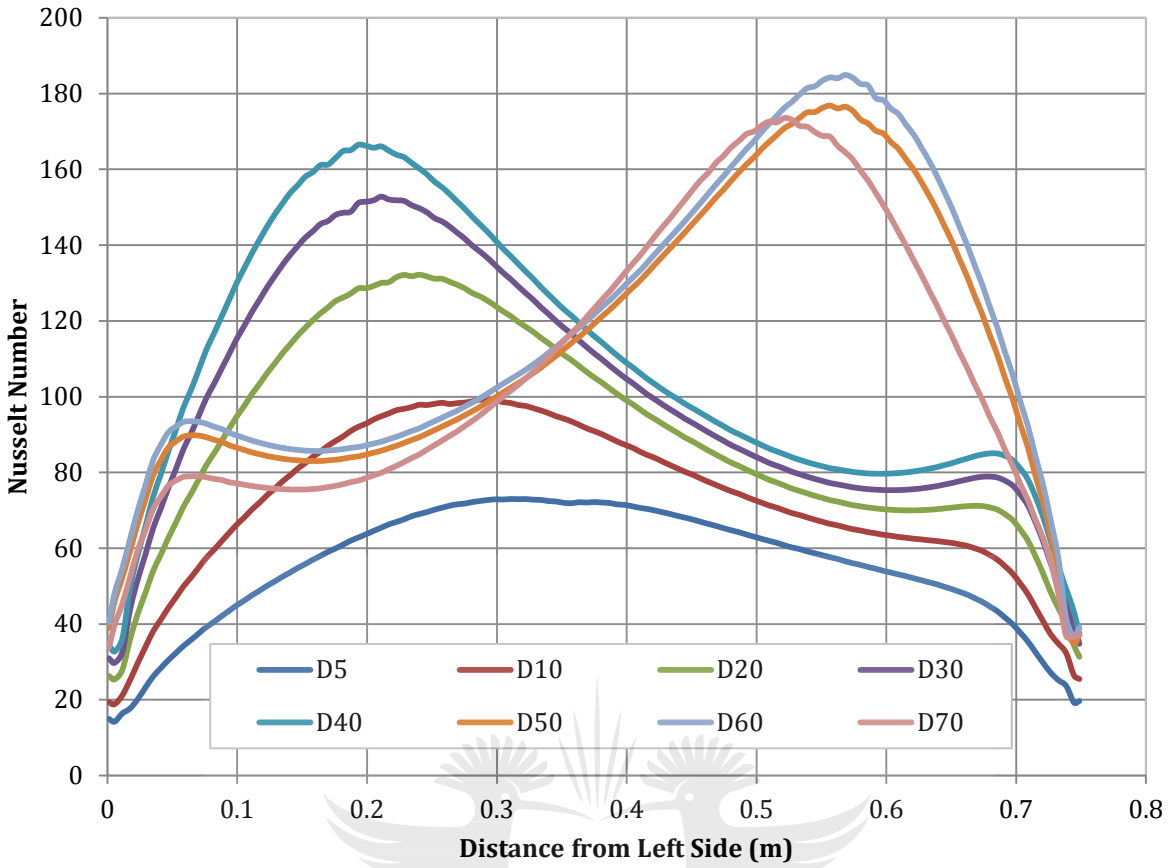

Figure 5.22: Nusselt Number Distribution on Hot Wall (Floor) of 60 Degree Roof Angle Greenhouse

The temperature distribution for the various Rayleigh numbers as a function of roof angle is plotted next in Figures 5.23 to 5.26 respectively. The graphs look quite similar, therefore only the most significant graphs will be discussed. From Figure 5.23 it can be seen that for the lowest Rayleigh number (Ra = 2.22 x 10^8) overall the 10 degree roof angle has the highest temperature distribution, whereas the 60 degree roof angle exhibits the lowest temperature difference in general. There is almost no difference in temperature distribution if the zero and 10 degree roof angle distributions are compared. As the Rayleigh number increases to 4.27 x 10^8 as shown in Figure 5.24, the effect becomes slightly more pronounced, and it can be seen that the temperature distribution for the 60 degree roof angle is the lowest – almost 1°C lower compared to the zero and 10 degree roof angles. There is also a small difference in the core region temperature distribution if the zero and 10 degree roof angle cases are compared. As the Rayleigh number increases, the effect on the temperature distribution at mid-height becomes more significant. For the case of Ra = 1.9 x 10^9 (Figure 5.25), the temperature in the centre of the cavity (from 0.1 to about 0.6m) is approximately 3 degrees lower for the 45 degree case compared to the 30 degree roof angle case. The temperature difference in the centre of the

cavity is approximately 7 degrees lower for the 60 degree roof angle case compared to the 30 degree roof angle case. The temperature differences due to the thermal boundary layer in the vicinity of the walls depend on the direction of the main convective cell for each case. Right next to each vertical wall, one notices a small part of the isotherm being orthogonal to the wall, this is due to the adiabatic boundary condition specified for the vertical walls.

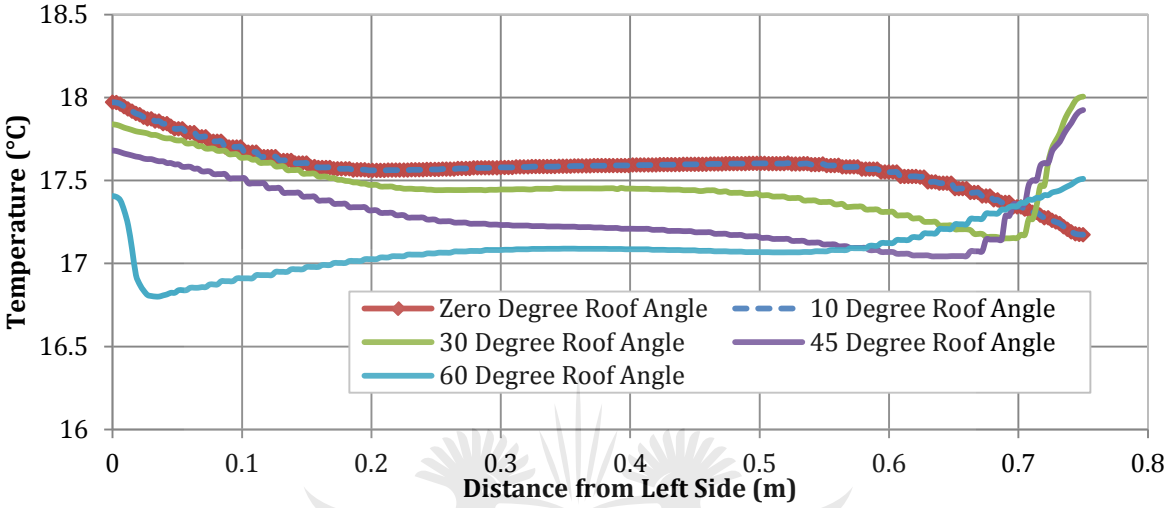

Figure 5.23: Horizontal Temperature Distribution at mid-height of the Cavity for Ra = 2.22 x 10^8 (ΔT = 5°)

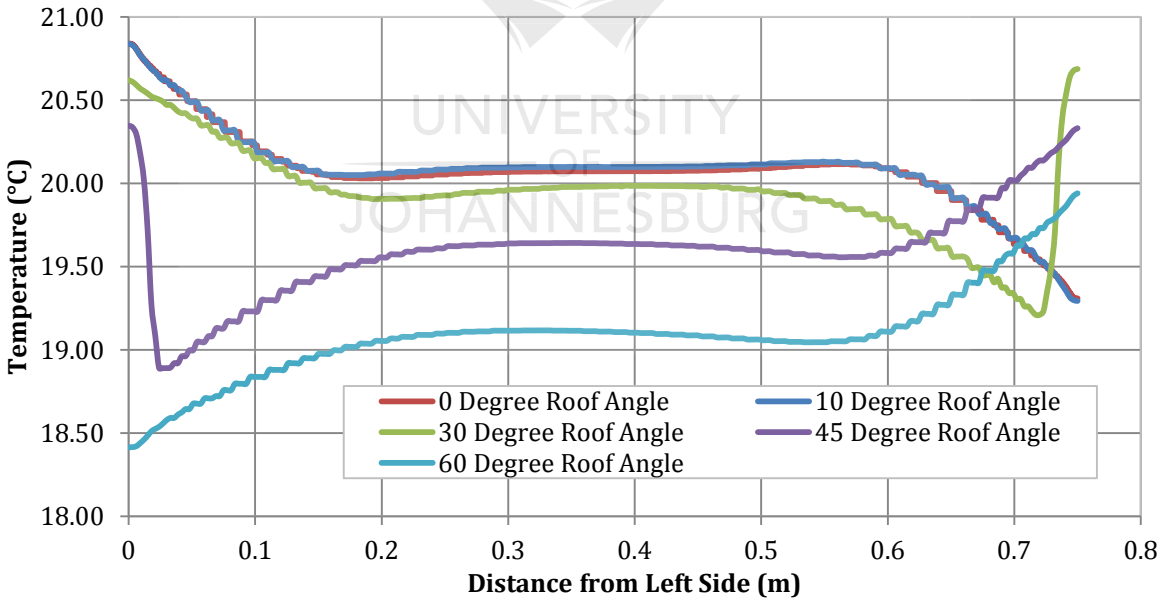

Figure 5.24: Horizontal Temperature Distribution at mid-height of the Cavity for Ra = 4.27 x 10^8 (ΔT = 10°C)

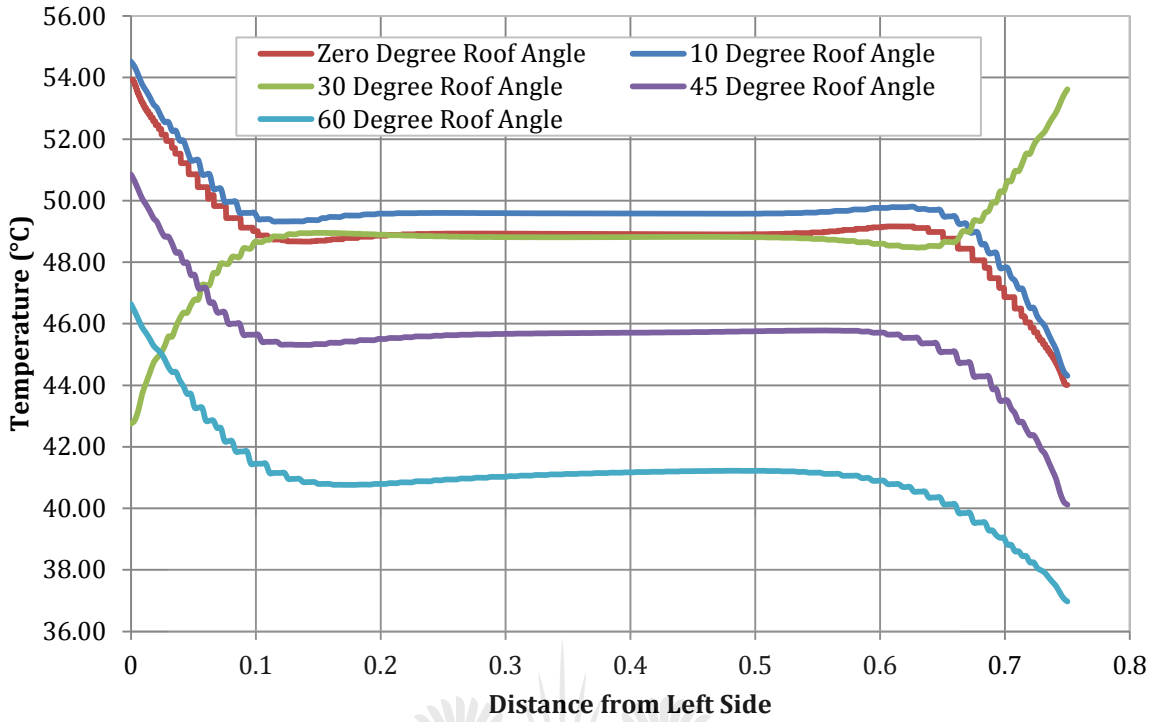

Figure 5.25: Horizontal Temperature Distribution at mid-height of the Cavity for Ra = 1.9 x 10^9 (ΔT = 70°C)

Figures 5.26 to 5.29 compare the velocity distribution at mid-height for 5 different roof angles and various Rayleigh numbers. The little steps that are visible in the graph, are due to the number of points chosen in the line probe in the CFD software. Each probe point in the numerical program returns a value for the specific property chosen from the cell it intersects. Certain cells in the numerical grid has more than a single point traversing the cell, therefore a number of points with the same value are generated. The zero and 10 degree roof angle velocity distributions were quite similar for all the cases. The velocity rises sharply to a maximum in the vicinity of the adiabatic walls, then decreases towards zero in the centre of the cavity for the zero and 10 degree roof angles. The velocity is slightly higher than zero for the 30, 45 and 60 degree cases. The lowest Rayleigh number (ΔT = 5°C) shows an almost symmetrical velocity distribution for a zero and 10 degree roof greenhouse, but not for 30,45 and 60 degree roof angles. This behaviour is attributed to the large secondary cell that forms in the bottom right corner for the last three roof angles. For the rest of the Rayleigh numbers, the velocity distributions are more symmetrical compared to Ra = 2.22 x 10^8. As expected, the overall velocity distribution increased with increasing Rayleigh number.

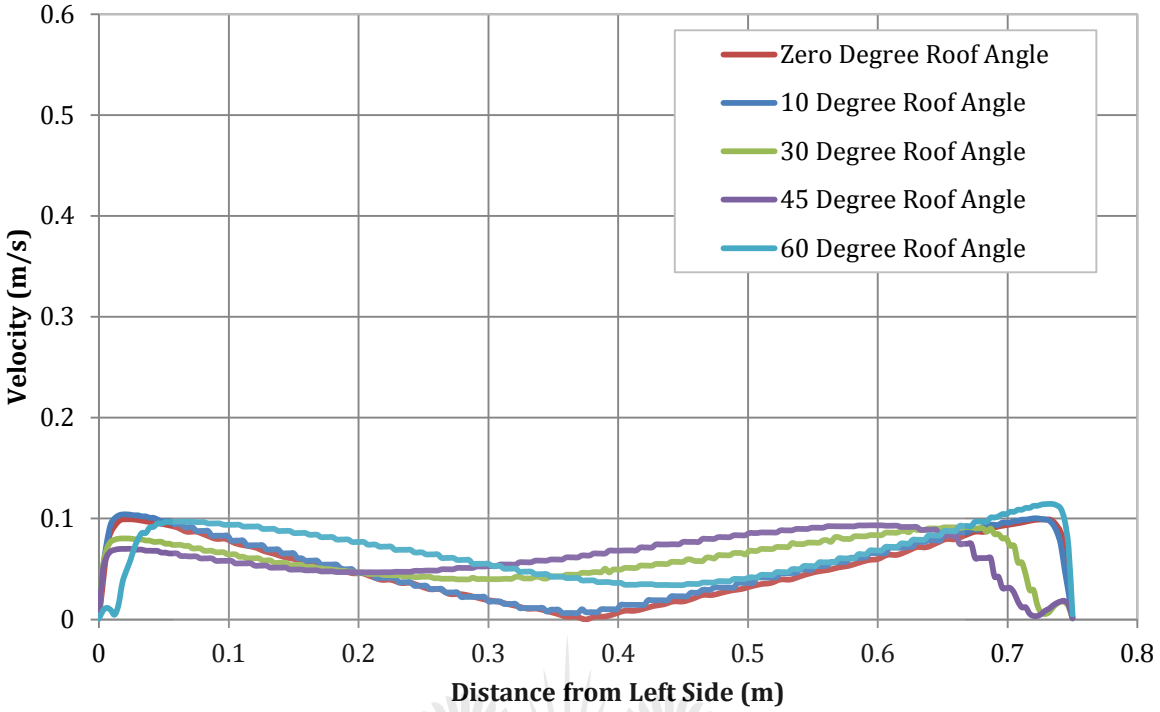

Figure 5.26: Horizontal Velocity Distribution at mid-height of the Cavity for Ra = 2.22 x 10^8 (ΔT = 5°C)

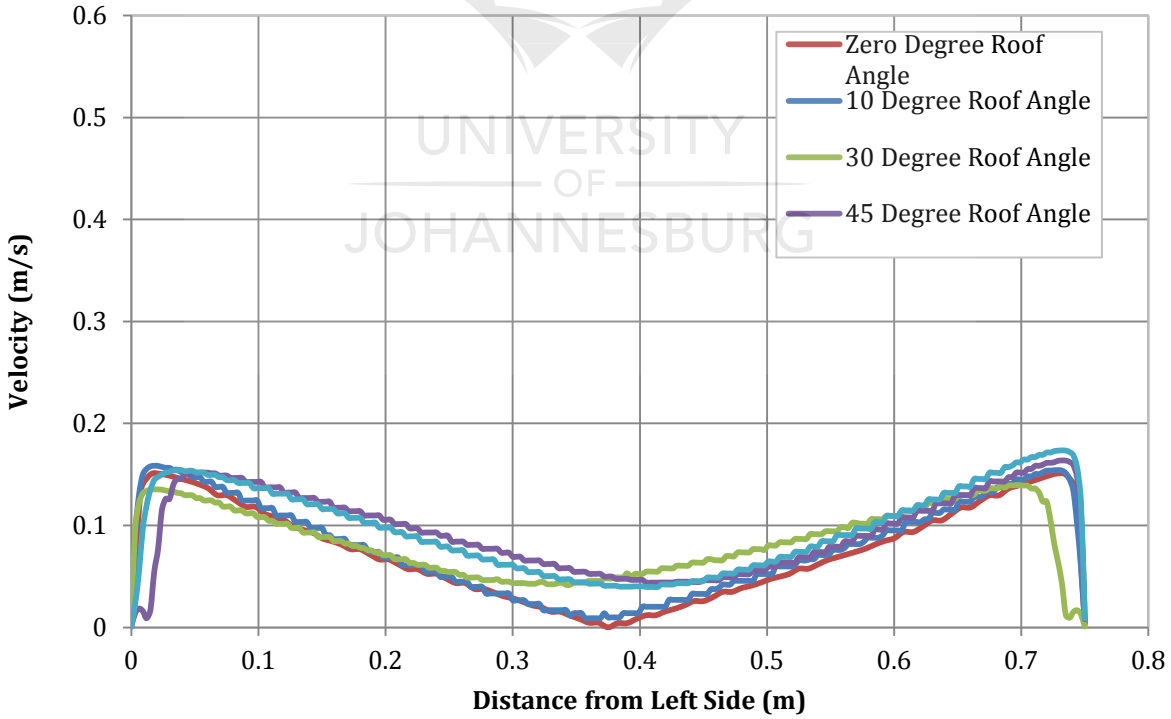

Figure 5.27: Horizontal Velocity Distribution at mid-height of the Cavity for Ra = 4.27 x 10^8 (ΔT = 10°C)

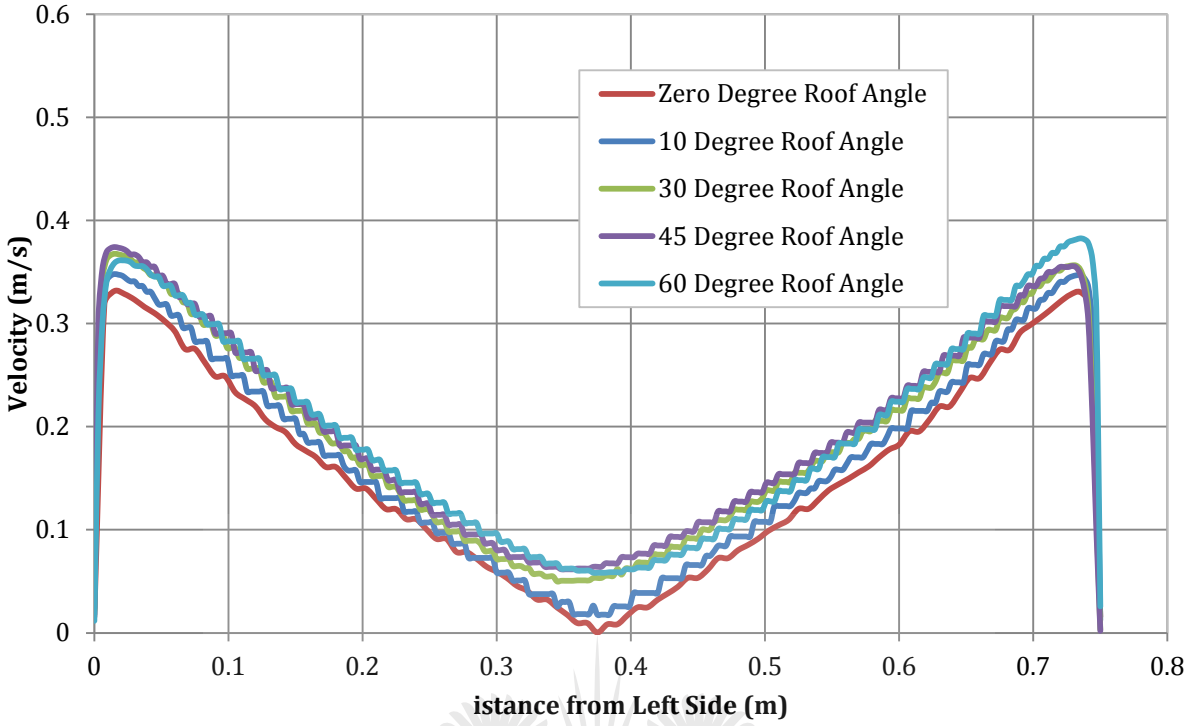

Figure 5.28: Horizontal Velocity Distribution at mid-height of the cavity for Ra = 1.35 x 10^9 (ΔT = 40°C)

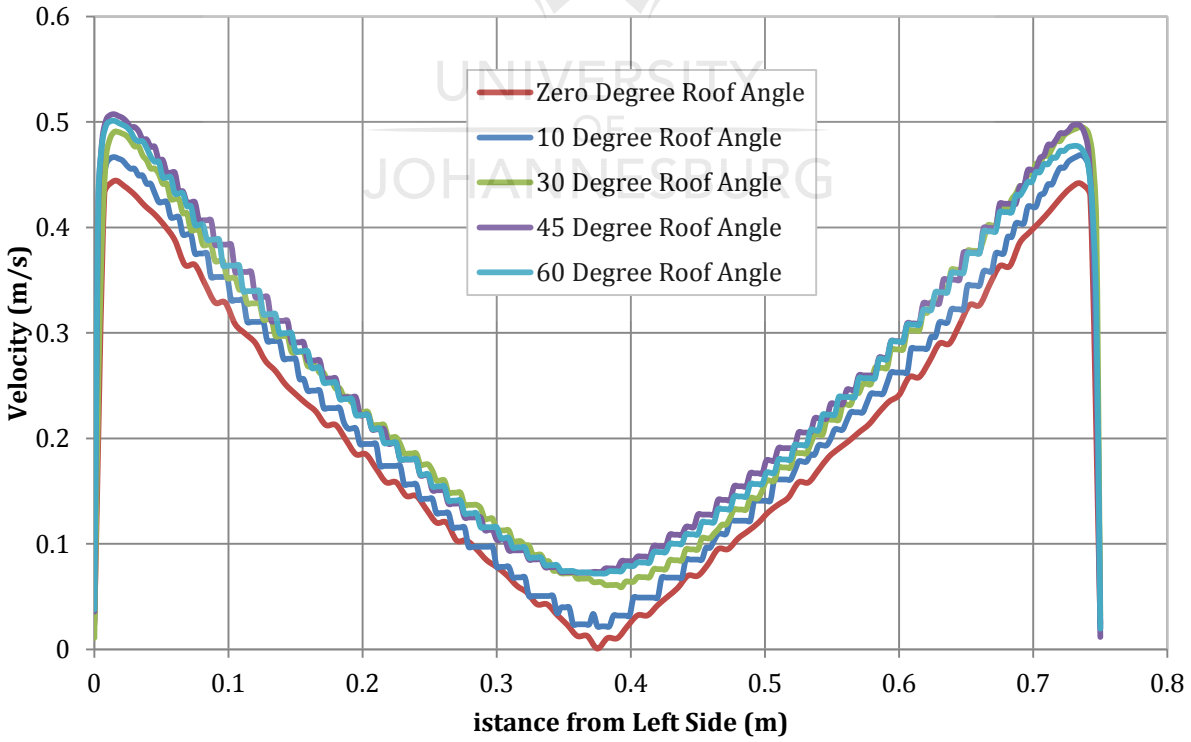

Figure 5.29: Horizontal Velocity Distribution at mid-height of the cavity for Ra = 1.9 x 10^9 (ΔT = 70°C)

The variation of average Nusselt number on the hot wall with roof angle is shown in Figure 5.30. The average Nusselt number on the hot wall increases Rayleigh number as expected, but also with roof angle.

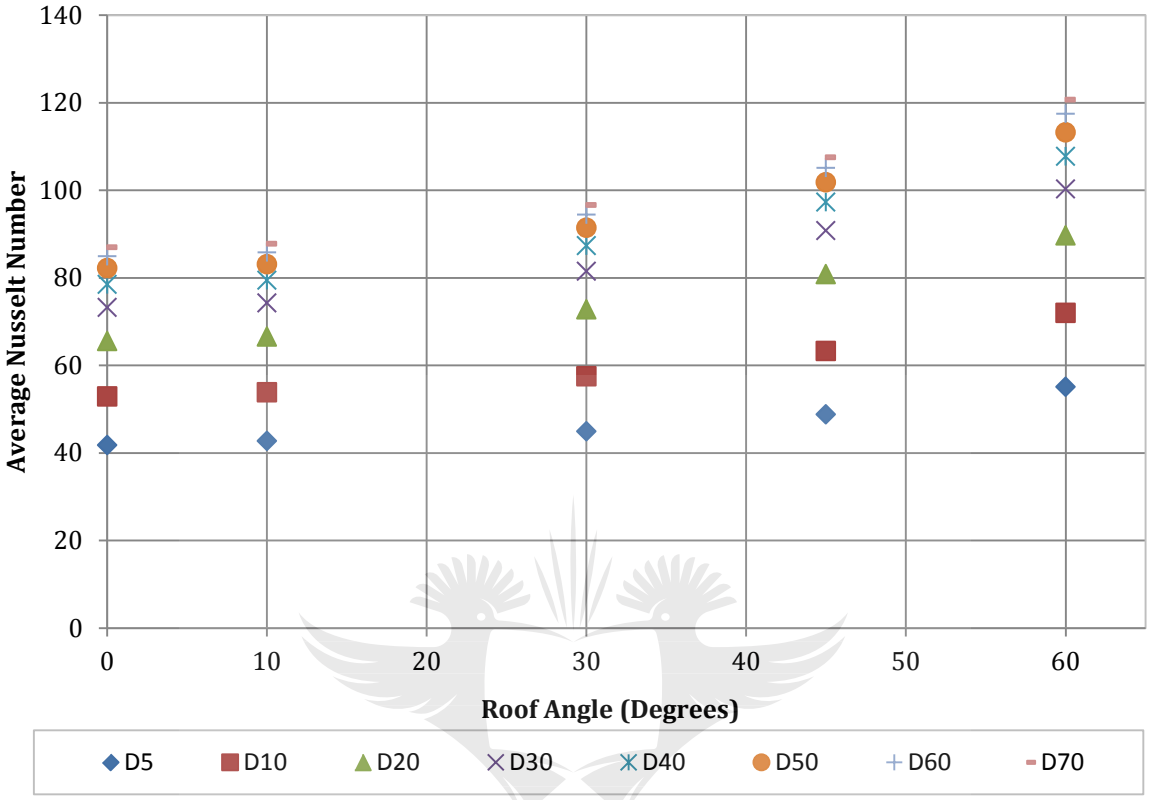

Figure 5.30: Variation of Average Nusselt Number with roof angle

The overall effect of the roof angles on the heat transfer is shown in Figure 5.31, where the distributions of the average Nusselt number on bottom wall, are plotted versus the logarithmic Rayleigh number. The plot also indicates that for all Rayleigh numbers the average heat transfer at the hot wall increases with roof angle.

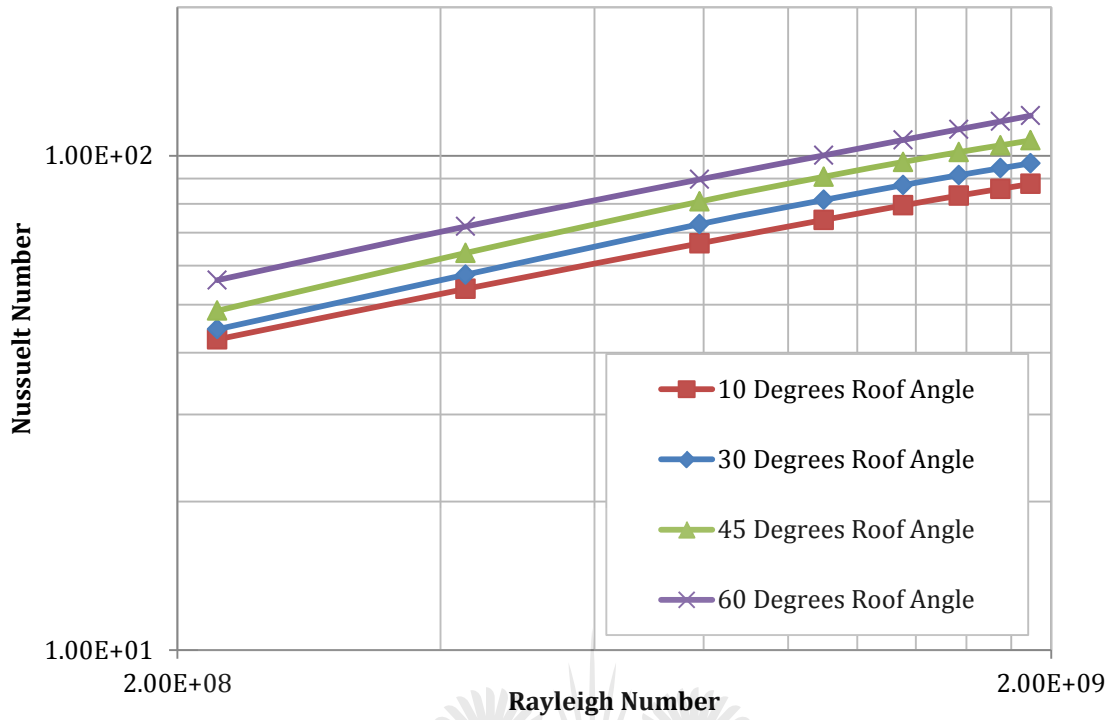

Figure 5.31: Average Nusselt vs Rayleigh Numbers for the Hot Wall

Nusselt-Rayleigh relationships that best fit the curves have been deduced from these plots and are tabulated in Table 5.7.

Table 5.7: Approximate Nusselt-Rayleigh Relationships determined from CFD

Roof Angle	Nusselt-Rayleigh Relationship
10°	$Nu = 0.0646Ra^{0.3381}$
30°	$Nu = 0.0436Ra^{0.3613}$
45°	$Nu = 0.0405Ra^{0.3699}$
60°	$Nu = 0.061Ra^{0.3556}$

This section dealt with two-dimensional single span greenhouses scale models only. The next section investigates a three-dimensional cavity of the same dimensions, to establish whether there is any difference in the heat transfer characteristics.

5.3 Modified Square – Single-span Greenhouse (3D)

This section in this chapter addresses the three-dimensional heat transfer effects. A two-dimensional and three-dimensional single span greenhouse of the same dimensions as the previous cavity is compared. An intermediate temperature difference of 40°C (Ra = 1.35 x 10^9) was selected between the floor and the roof of the cavity with a 45 Degree roof angle. To enable a comparison between the two and three-dimensional greenhouse scale models, the CFD model in this section was similar to the CFD model of the scale greenhouse in the previous section. The low-Reynolds k-epsilon turbulence model was used and gravity was modelled in the negative y-direction. The mesh parameters are shown in Table 5.8, the boundary conditions in Table 5.9, and the turbulence parameters in Table 5.10.

Table 5.8: Mesh parameters for 3D 45 degree roof angle greenhouse scale model

Property	Value
Base Size (m)	0.03
Number of Prism Layers	20
Prism Layer Stretching	1.1
Prism Layer Thickness (m)	0.022
Surface Growth Rate	1.3
Surface Size (Tet/Poly Density)	
Density	1.0
Growth Factor	1.0
Blending Factor	1.0
Surface Size	
Relative Minimum Size	25%
Relative Target Size	100%

Table 5.9: Boundary conditions

Boundary	Type	Thermal Specification
Left Wall	Wall	Adiabatic
Right Wall	Wall	Adiabatic
Front Wall	Wall	Adiabatic
Back Wall	Wall	Adiabatic
Bottom Wall (Floor)	Wall	Isothermal
Top Wall (Roof)	Wall	Isothermal

Table 5.10: Turbulence parameters

Under Relaxation Factor	**0.8**
Convergence Tolerance	0.1
Epsilon	0.0
Turbulent Viscosity (Under Relaxation Factor)	1.0

A plane section of the temperature contour plot in the middle (z/H = 0.5) of the three-dimensional cavity is compared to the two-dimensional temperature contour plot in Figure 5.32. The three dimensional nature of the flow in the three-dimensional cavity is clearly visible, illustrating a non-uniform temperature distribution throughout. The two-dimensional cavity shows a large section in the centre of the greenhouse consisting of a uniform temperature distribution, with the thermal boundary layers confined to the walls.

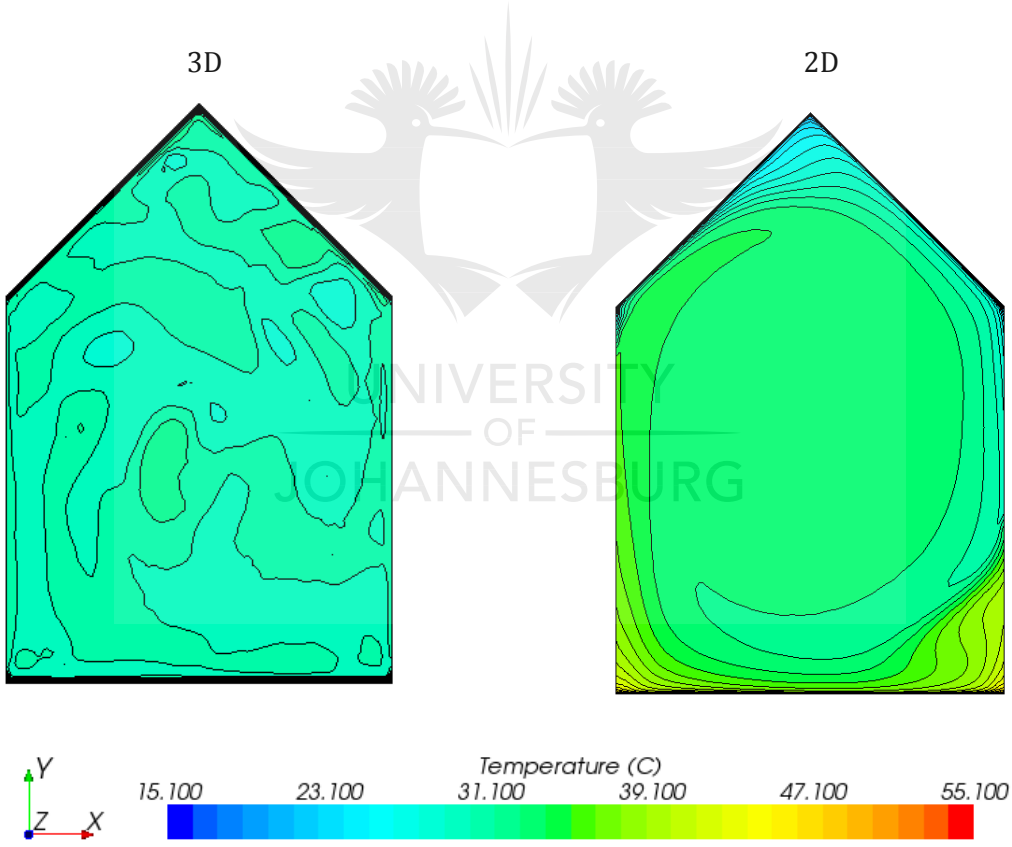

Figure 5.32: Comparison between 3D and 2D Temperature Contour Plots for Ra = 1.35 x 10^9

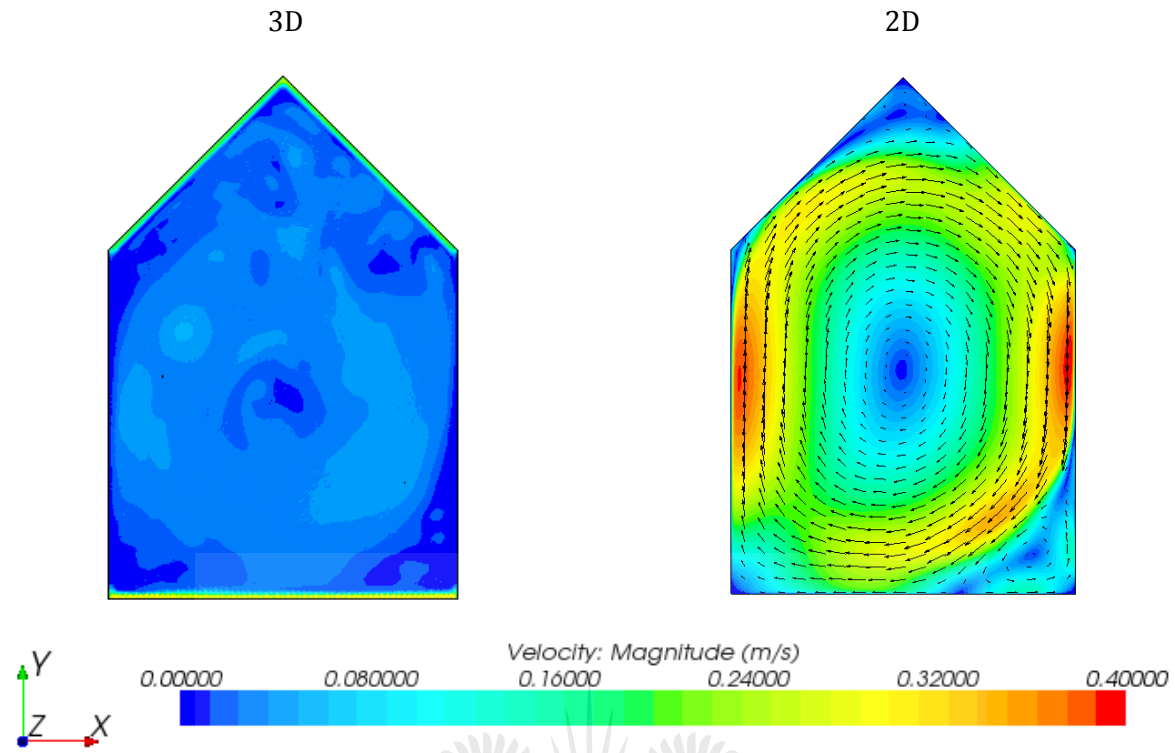

Figure 5.33: Comparison between 3D and 2D Velocity Contour and Vector Plot at z/H = 0.5 for Ra = 1.35 x 10^9

As far as velocity distribution is concerned, the essential differences can be seen in Figure 5.33. The velocity in the entire section is relatively homogenous for the three-dimensional model. This is compared to a clear, single dominating convective cell rotating in the two-dimensional cavity, combined with a smaller cell in the bottom right corner. One has to remember that the convective cell may form in three dimensions in the three-dimensional case, resulting in the possibility that a convective cell may not be so clearly visible in a two-dimensional section of the three-dimensional model. The highest velocity is visible adjacent to the adiabatic walls for the 2D case, whereas velocities of the same magnitude is noticed adjacent to the isothermal walls for the three-dimensional case. Thin velocity boundary layers are also visible in the 3D case. To enable a clearer view of the vectors, the velocity magnitude has been superimposed on the 2D wireframe vectors themselves, and is shown in Figure 5.34 for the three-dimensional case. A distinctive clockwise rotating cell is noticeable as in the two-dimensional case, with a smaller cell in the bottom right corner.

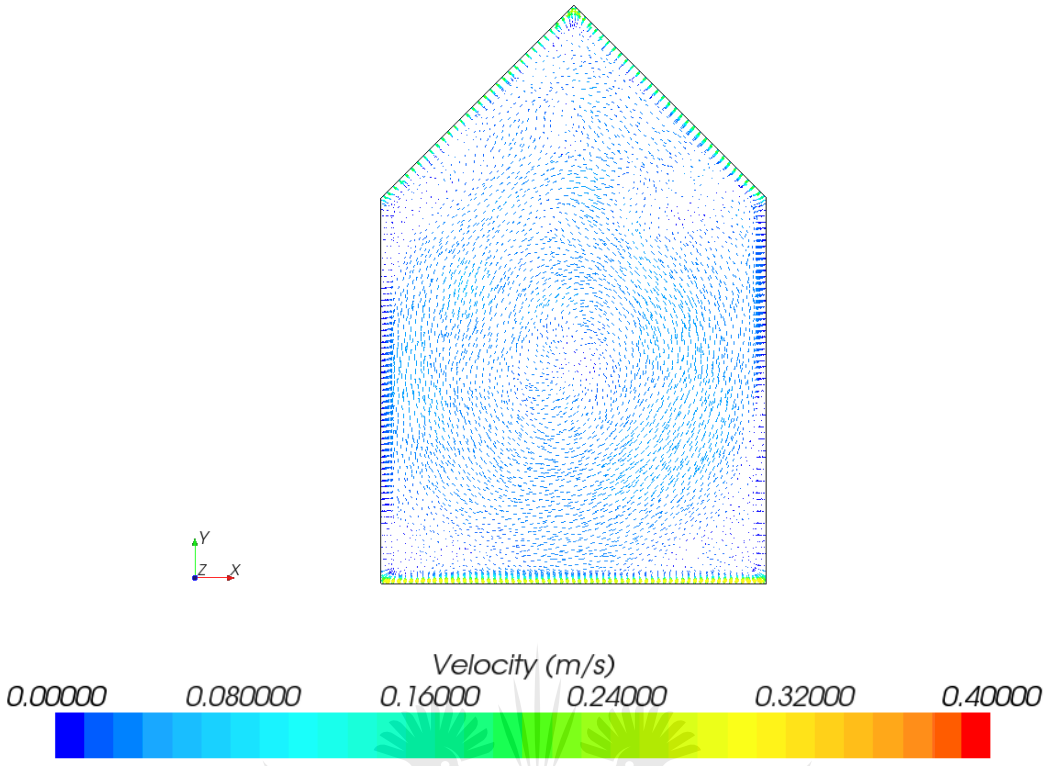

Figure 5.34: 2D Wireframe Vector Plot at z/H = 0.5 for the 3D case

A longitudinal section through the ridge of the roof (x/H=0.5) shows the temperature and velocity contour plot respectively in Figure 5.35 and Figure 5.36. The front of the cavity is warmer compared to the back. The entire is cavity is divided into vertical layers with a homogenous temperature from top to bottom. When the velocity plot is investigated, it seems as if the velocity is higher in the top corner at the back compared to the rest of the cavity. Due to the higher velocity, the air is cooler in this region.

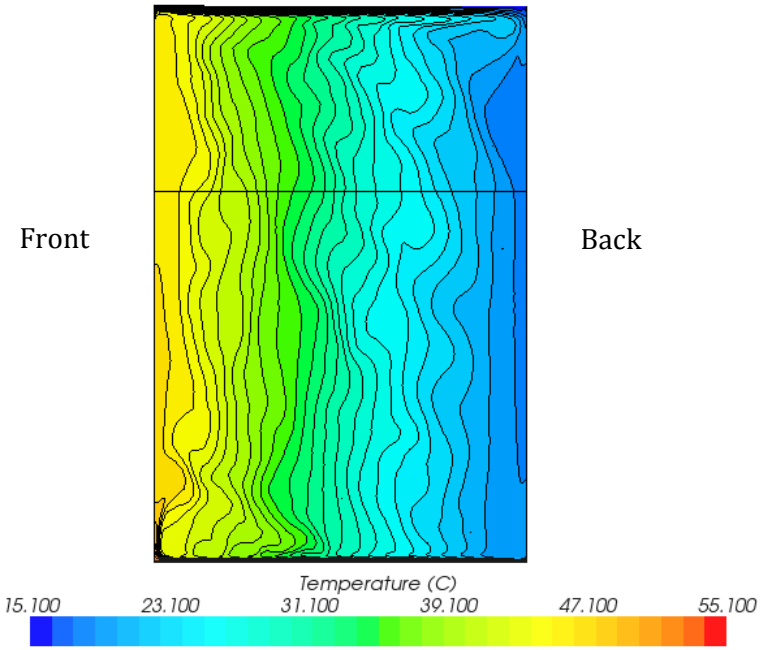

Figure 5.35: Temperature Contour Plot for x/H = 0.5

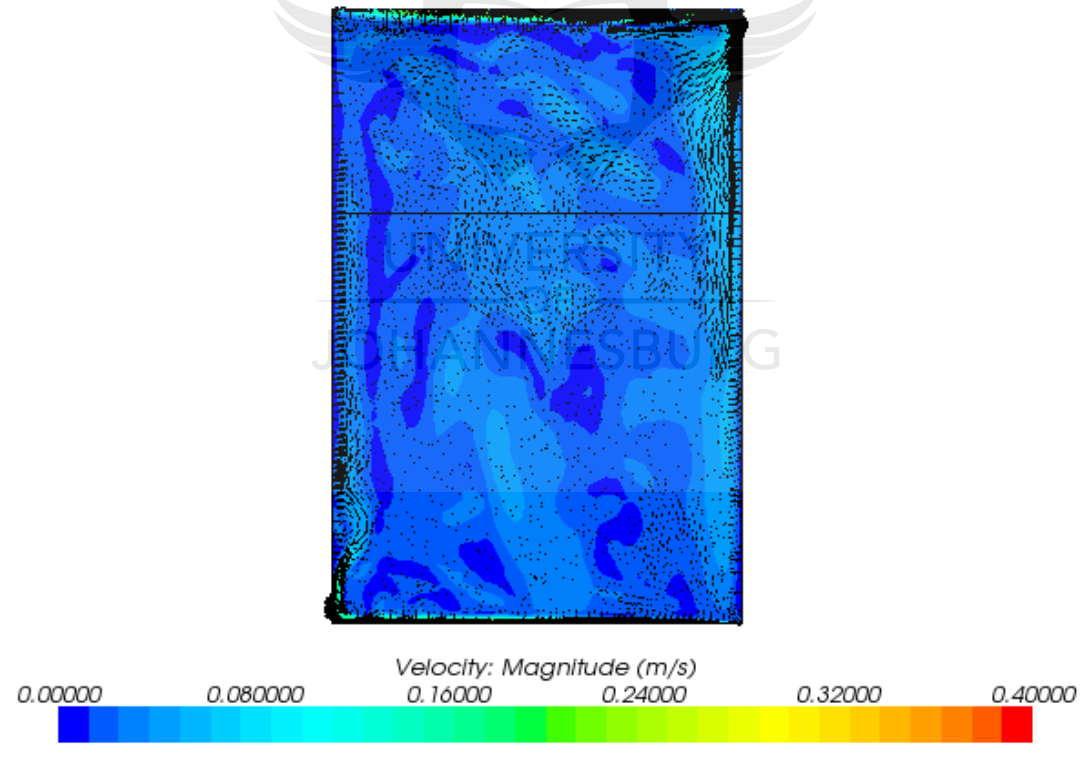

Figure 5.36: Velocity Contour and Vector Plot for x/H = 0.5

Three line-probes were inserted at three different heights at z/H = 0.5 in the CFD software models as shown in Figure 5.37**.** In order to further determine whether there are any difference between the 2D and 3D case, the temperature plots for the three different heights are shown in

Figure 5.38. Superimposed on these plots is the temperature distribution at the same three levels for the two-dimensional case. The two-dimensional curves are visibly smoother, while the curves for the three-dimensional case vary with more than 5 degrees in some cases. There is also a large overall temperature gradient visible from 0.65m towards the right wall for the lowest level for the 2D case. Overall the temperature for the three-dimensional cavity is slightly higher. This can be attributed to the lower velocity at all three sections, as seen in Figure 5.39. The difference in velocity distribution is also quite noticeable. The three-dimensional case exhibits a lower velocity, generally smaller than 0.05m/s. The two-dimensional case contains large velocity gradients in the vicinity of the adiabatic wall, which is not present in the three-dimensional case.

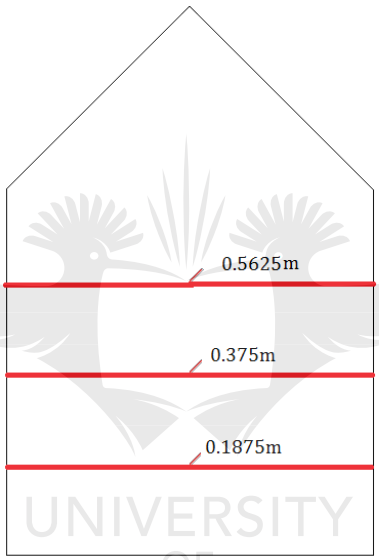

Figure 5.37: Line-probe positions

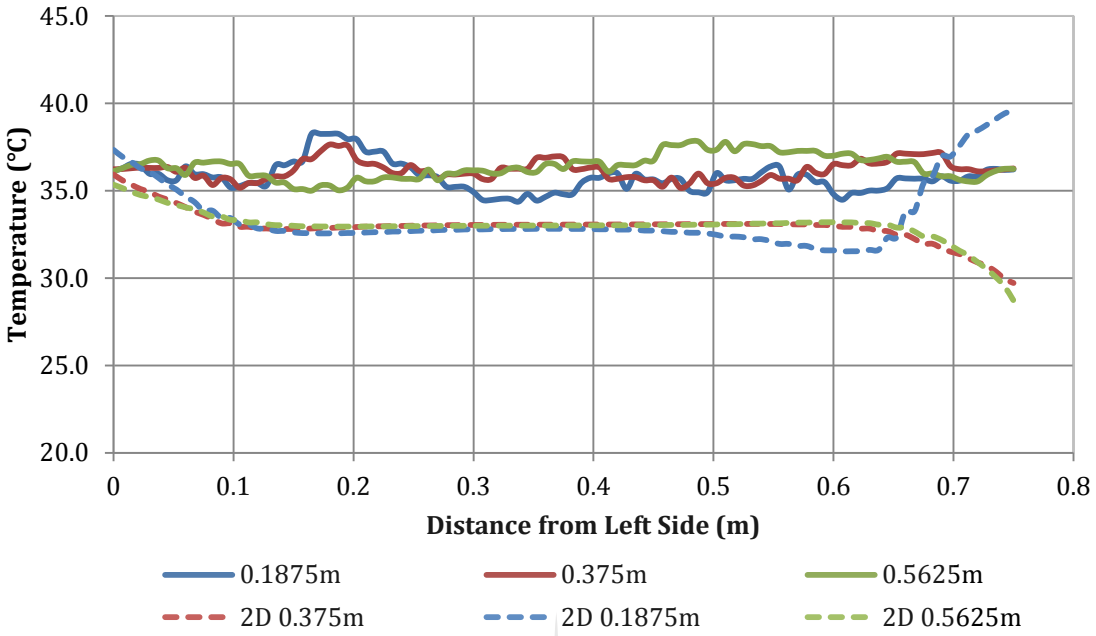

Figure 5.38: Temperature Distribution at different heights at z/H = 0.5

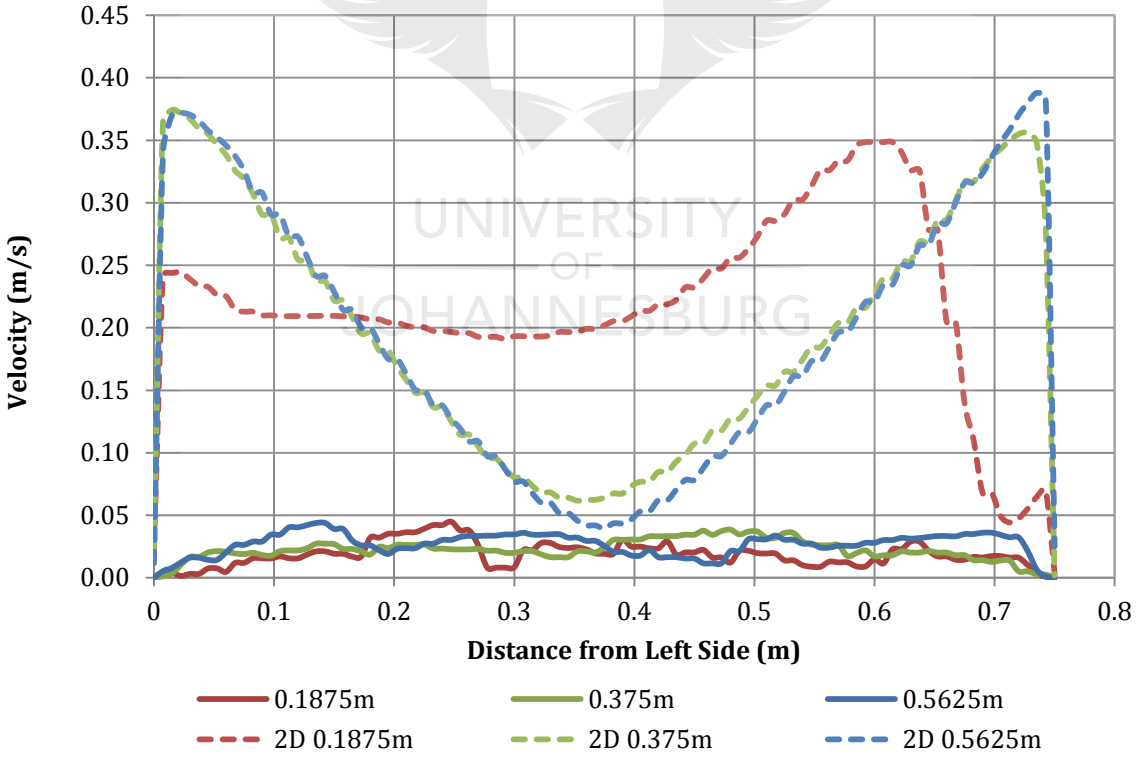

Figure 5.39 : Velocity Distribution at different heights at z/H = 0.5

The surface averaged Nusselt Numbers were calculated for the floors of the 2D and 3D models. In the three-dimensional case, the surface averaged Nusselt number was calculated for entire hot floor of the cavity. For the three-dimensional case, the Nusselt number was found to be Nu = **67.25,** while for the two-dimensional case, the Nusselt number was calculated as Nu **= 97.25.** This amounts to a difference of 31%. The distribution of the Nusselt number on the floor of the three-dimensional scale model of the greenhouse is shown in Figure 5.40. The highest Nusselt numbers (approximately Nu = 192) is found at the back of the cavity adjacent to the back vertical wall. The Nusselt numbers decrease across the width of the cavity towards the front wall, where the lowest Nusselt numbers are observed.

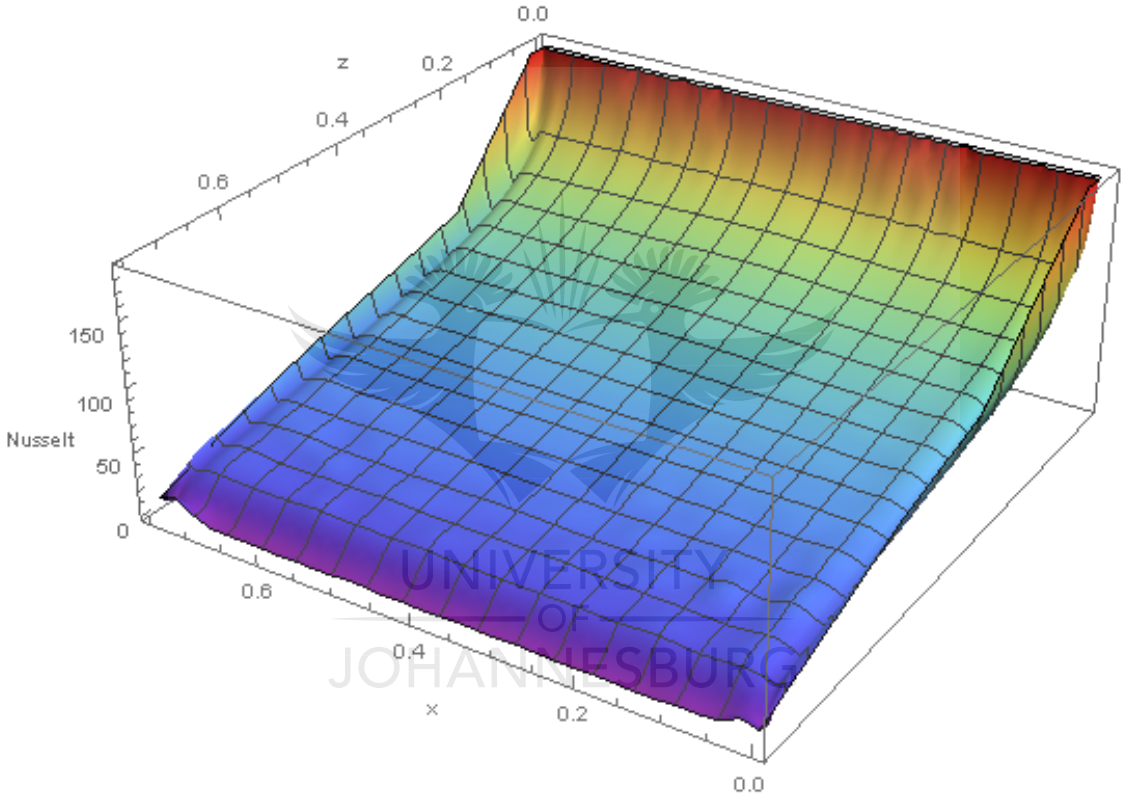

Figure 5.40: Nusselt number distribution on floor of 3D greenhouse scale model

The differences can be explained by the presence of the three-dimensional effects, which cannot be accounted for by the two-dimensional numerical model. In order to investigate the three-dimensional effects in more detail, an isosurface plot was constructed as shown in Figure 5.41 . An isosurface is a graphical tool available in the software which enables the visualization of a constant value scalar function. The temperature stratification is clearly visible as layers of decreasing temperature from the front of the cavity towards the back of the cavity.

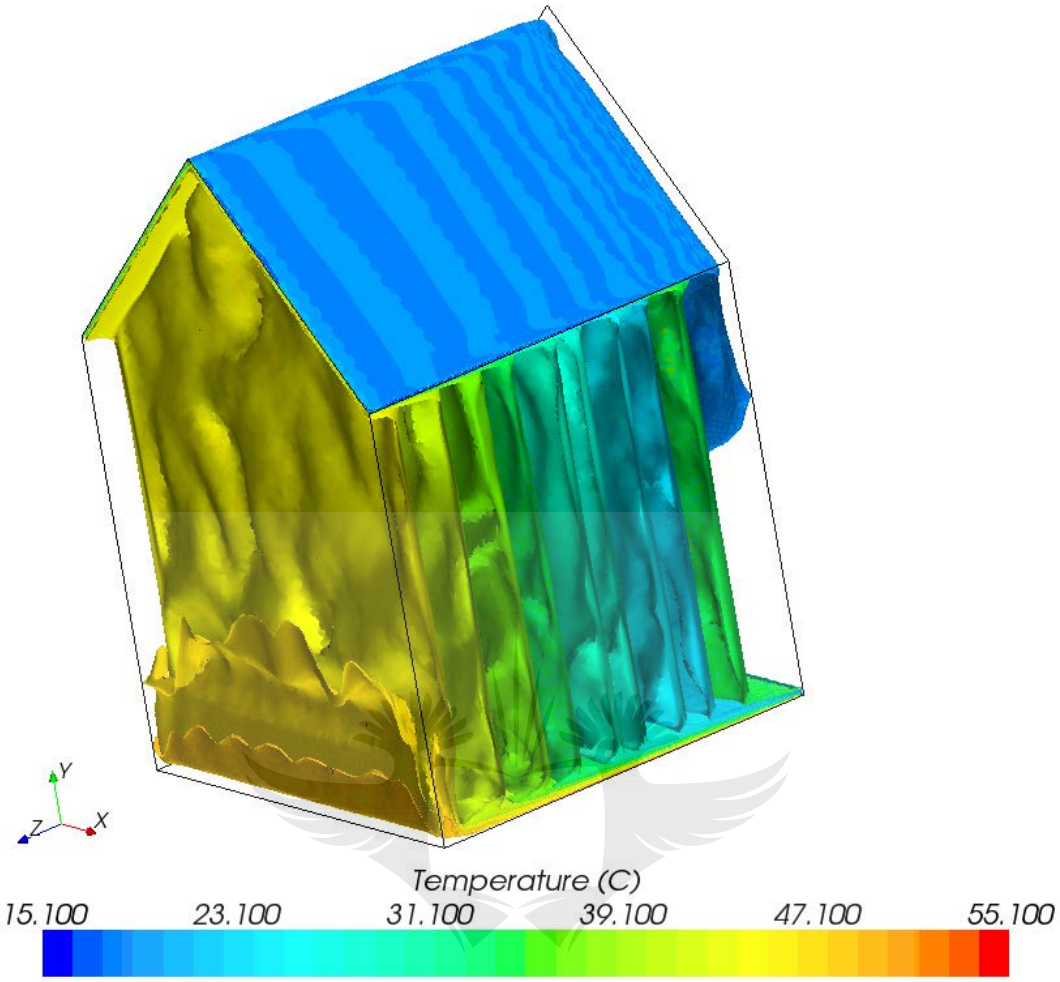

Figure 5.41: Isosurface Plot

To further investigate the effects of the three-dimensional geometry, animations were utilized that was available in the software. Shown in Figure 5.42 is vectors superimposed on a temperature scalar plot for x/H=0.5. When the plot was animated, it could be observed that the warmer fluid moves upward against the front of the cavity, while the colder fluid moves downward. The centre of the cavity, away from the walls is characterized by various smaller convective cells, which are also responsible for the three-dimensional effects as seen in the isosurface plot. The highest velocities are found in the upper right and bottom left corner, and adjacent to the floor and roof of the cavity.

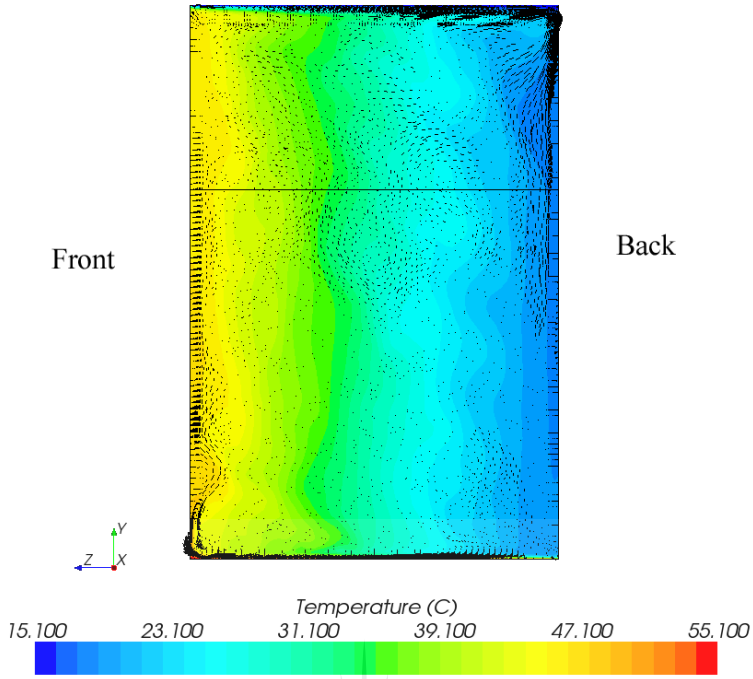

Figure 5.42: Temperature Contour Plot with Vectors

5.4 Ventilated Greenhouse Cavity

5.4.1 Numerical Method

In order to investigate the convection in the ventilated cavity, the previously discussed 2D numerical model was modified to represent a single-span greenhouse scale model containing a roll-up vent on the right side of the roof. The effect of opening size (S/4, S/2 and 3S/4) were studied (Figure 5.43). As the focus of this investigation was not the heat transfer through the walls to the outside of the environment of the greenhouse, the greenhouse walls were modelled as an empty cavity or void with no contribution to the flow domain. The boundary conditions are summarized in Table 5.11 and shown schematically in Figure 5.44. The ventilator is placed in the right side of the roof, and evaluated for three roll-up ventilator sizes, namely S/4, S/2 and 3S/4, where S is the length of the roof on one side.

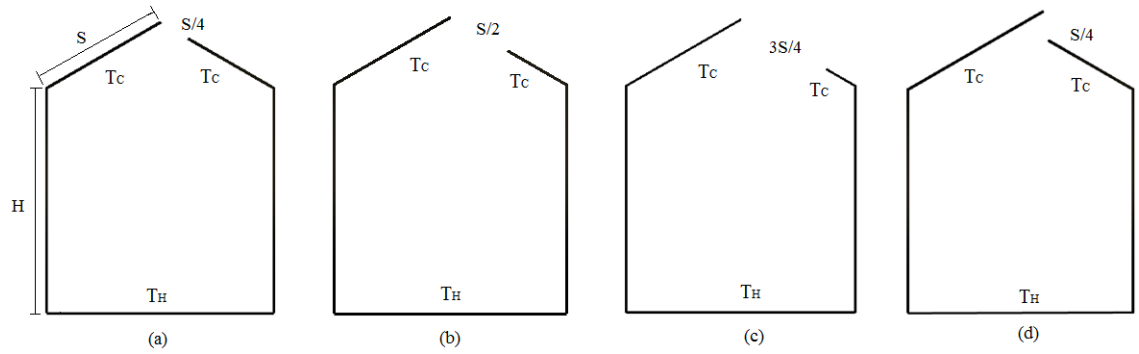

Figure 5.43: Schematic Diagram of Cavities Investigated

Table 5.11: Boundary Conditions for Ventilated Greenhouse (with reference to Figure 5.44)

Boundary Name	***Boundary Type***	***Value***
Greenhouse Walls (Inside)	Wall (no-slip)	-
Top Wall (Roof)	Isothermal	15.1°C
Bottom Wall (Floor)	Isothermal	Depends on Rayleigh Number
Right Wall	Adiabatic	-
Left Wall	Adiabatic	-
Left and Right side of Computational Domain	Velocity Inlet	0.001 m/s
Top of Computational Domain	Combined Symmetry Plane and Pressure Boundary	-

A large computational domain (12m high, 8m on each side of cavity) was created around the ventilated cavity, to ensure minimal influence of the control volume boundary conditions (Figure 5.44). The left and right side of the cavity was specified as velocity inlets, with low values of 0.001m/s and an inlet temperature of 5°C. The choice was made to establish a flow field initially which will force the flow out at the top of the domain. The top boundary consisted of a symmetry plane with a small pressure boundary in the middle, approximately the size of the width of the cavity. The size of the pressure boundary was kept to a minimum to avoid reversed flow back into the domain. The flow field was considered to be steady, with all the thermophysical properties kept constant. The cavity inner-walls were designated as the hot wall (floor of the cavity) and cold wall (roof of the cavity). The temperature of the roof/cold wall was kept constant at 15.1°C, while the temperature of the hot wall (floor of the greenhouse) was varied to yield different Rayleigh numbers as shown in Table 5.1. The vertical walls of the greenhouse scale model were kept adiabatic, and the low-Reynolds number turbulence model was used.

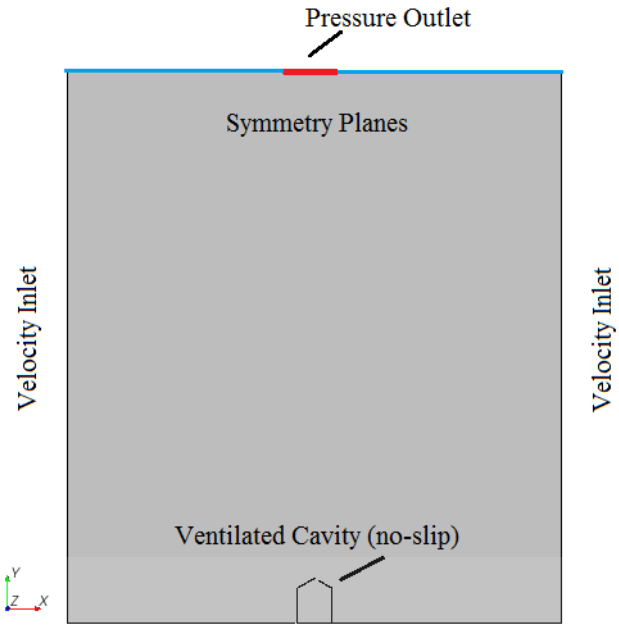

Figure 5.44: Schematic Layout of Boundary Conditions used in Numerical Simulations

A second grid independence test was conducted to determine the number of polyhedral cells required for a grid-independent solution. The results are shown in Figure 5.47. The surface-averaged Nusselt number was monitored as in the previous sections, and it was found that only from a base size of 0.44m and above was a small influence noticed. Taking the available hardware and time to research a converged solution into consideration, a base size of 0.44m was chosen for the ventilated cavity mesh. The rest of the mesh parameters where left as discussed previously in section 5.2.2, with the prism layer disabled for the outside ground boundary. The surface size on the inside adiabatic walls were set to a minimum of 10% and a target value 50% of the chosen base size. A control volume of a relative size of 6% was created around the greenhouse. The final mesh showing the boundary layer mesh around the greenhouse walls can be seen in Figure 5.45, with the mesh refinement visible around the greenhouse in Figure 5.46. The final mesh parameters are shown in Table 5.12.

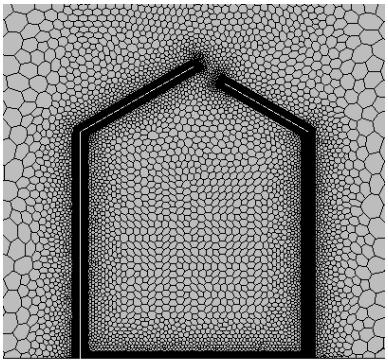

Figure 5.45: Mesh and prism layers

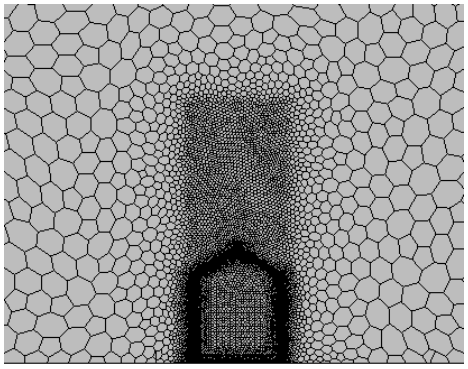

Figure 5.46: Mesh refinement around greenhouse

Table 5.12: Mesh parameters

Property	Value
Base Size (m)	0.44
Number of Prism Layers	20
Prism Layer Stretching	1.1
Prism Layer Thickness (m)	0.022
Surface Growth Rate	1.3
Surface Size (Tet/Poly Density)	
Density	1.0
Growth Factor	1.0
Blending Factor	1.0
Surface Size	
Relative Minimum Size	10%
Relative Target Size	50%

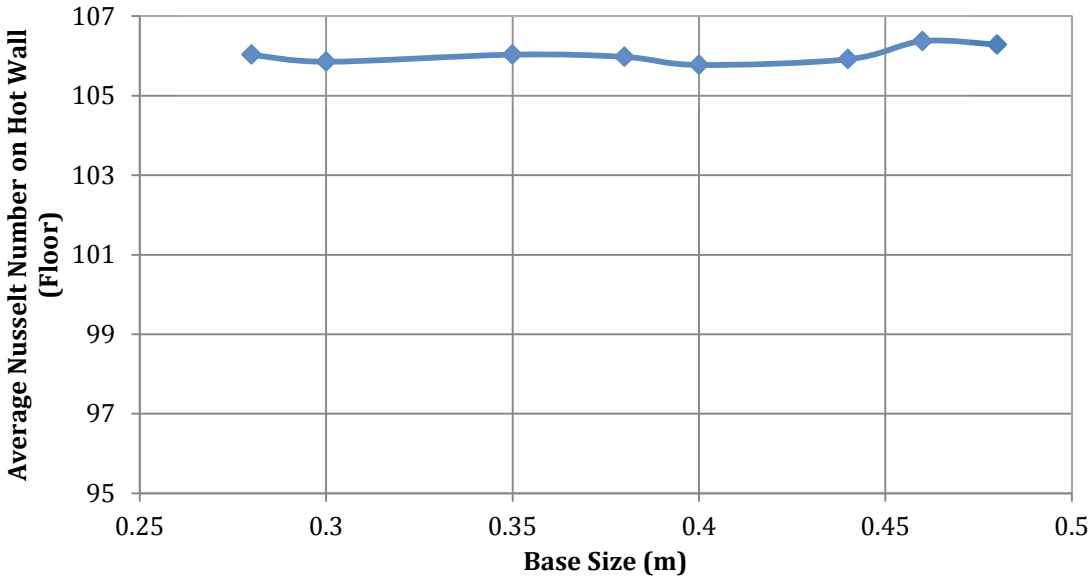

Figure 5.47: Mesh Sensitivity Analysis for Ventilated Cavity

5.4.2 Results – Ventilated Cavity

The numerical computed CFD results for the 2D ventilated cavities are presented here in the form of scalar and vector plots. The heat transfer along the hot wall/floor, temperature and velocity fields are examined for the three different opening sizes and flap type ventilator in the right side of the roof. The isotherms and streamlines in the next figures represent the flow structure and thermal field. The isotherms and velocity vectors for each opening size are compared in Figure 5.48 to Figure 5.63 for the various Rayleigh numbers. Each case is characterised by a large, single rotating convective cell in the centre of the cavity, and a smaller rotating cell (opposite direction to large cell) in the bottom left corner. The size of the cell is reduced slightly as the opening size increases. When the temperature contour plots are considered, it is noticed that the cavity containing the smallest size opening (S/4) has a higher temperature compared to the larger opening sizes. This is due to the due the smaller opening permitting less mixing with the cold outside air (which was specified as 5°C). The temperature distribution in the cavity is characterized by a uniform temperature distribution in the core region (except for Ra = 2.22 x 10^8), with temperature differences noticeable through the boundary layer from the hot floor and cold roof areas. A temperature gradient progressing from the opening downwards adjacent to the left side of the roof is also visible in each case, with the gradient increasing as the opening size increases.

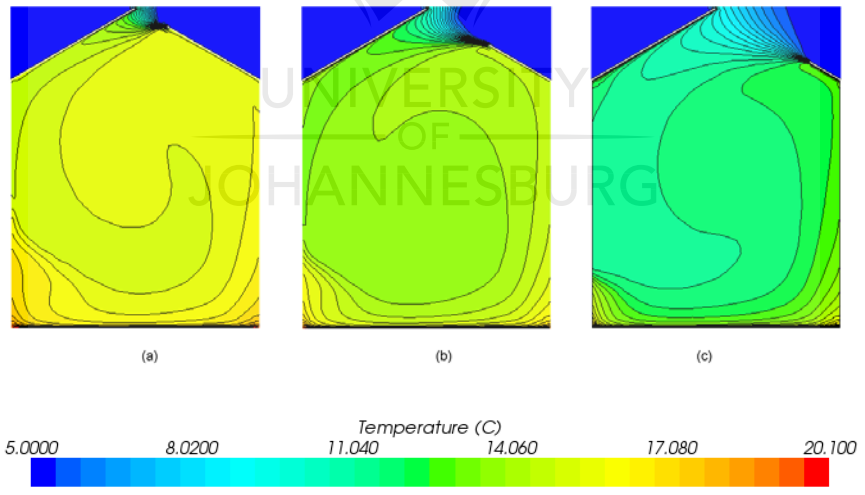

Figure 5.48: Temperature Contour Plots for ΔT = 5°C (2.22 x 10^8) for a) S/4, b) S/2 c) 3S/4

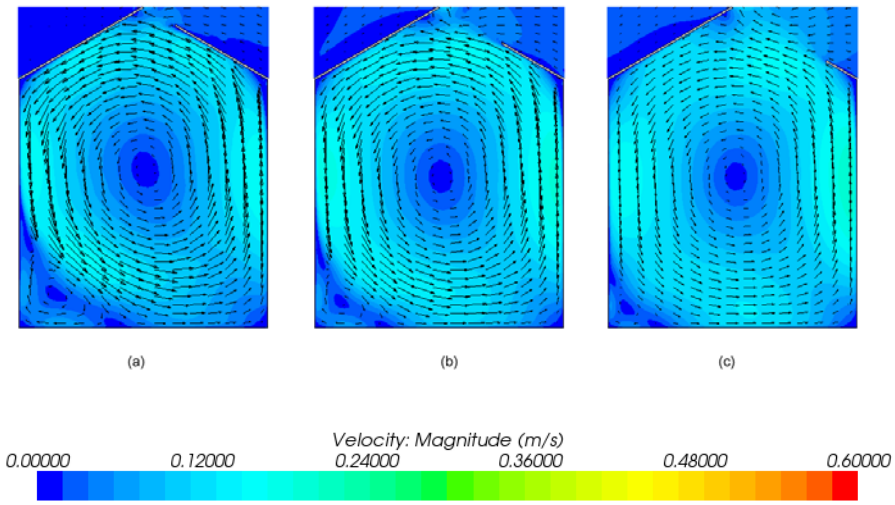

Figure 5.49: Vector and Velocity Contour Plots for ΔT = 5°C (2.22 x 10^8) for a) S/4, b) S/2 c) 3S/4

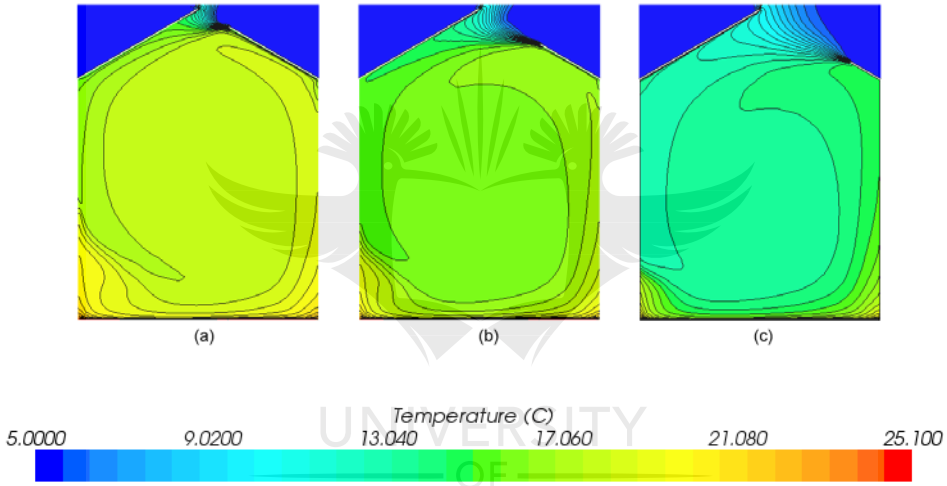

Figure 5.50: Temperature Contour Plots for ΔT = 10°C (4.27 x 10^8) for a) S/4, b) S/2 c) 3S/4

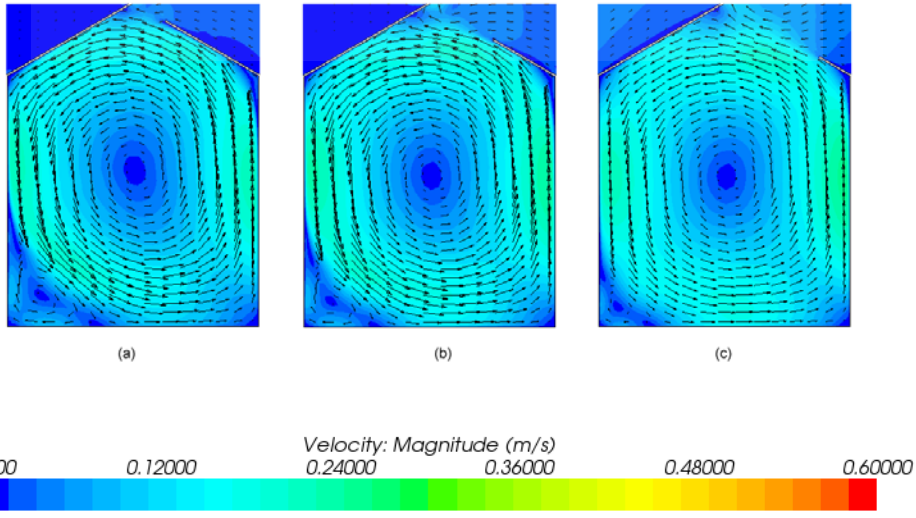

Figure 5.51: Vector and Velocity Contour Plots for ΔT = 10°C (4.27 x 10^8) for a) S/4, b) S/2 c) 3S/4

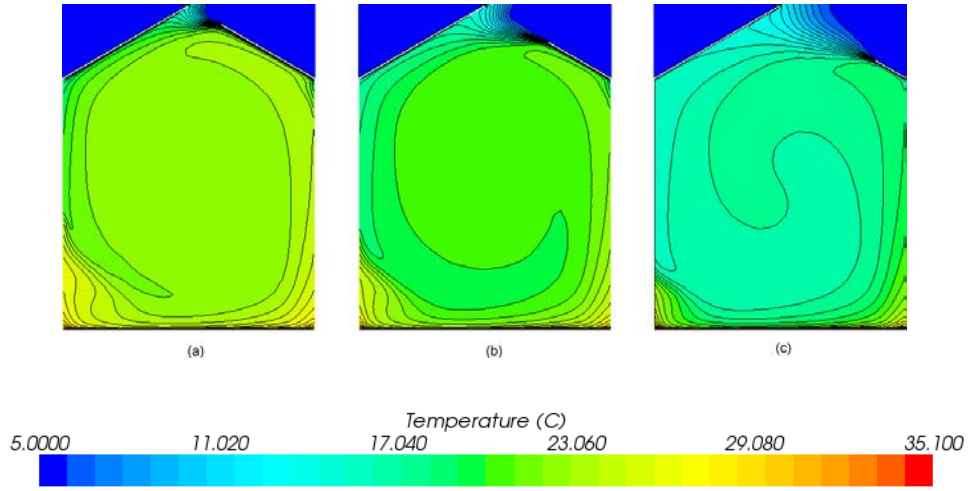

Figure 5.52: Temperature Contour Plots for ΔT = 20°C (7.92 x 10^8) for a) S/4, b) S/2 c) 3S/4

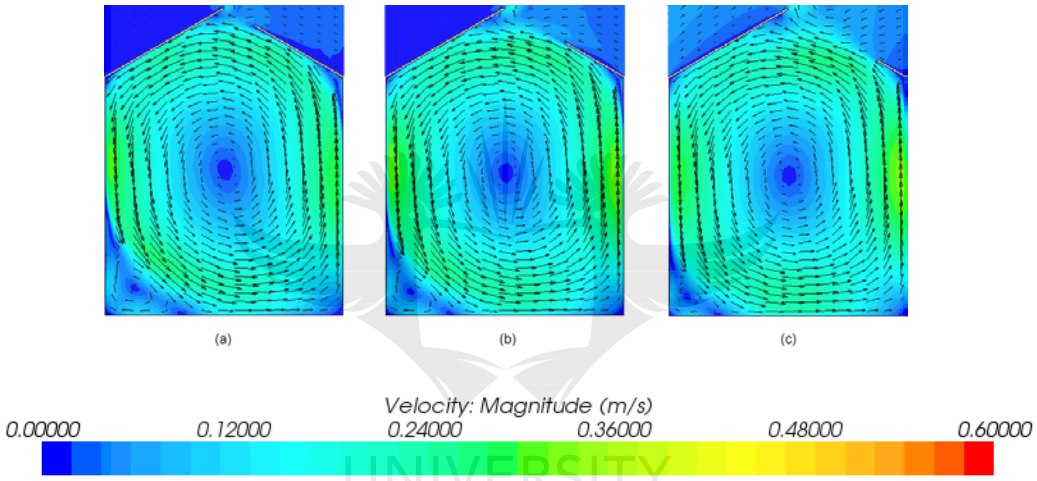

Figure 5.53: Vector and Velocity Contour Plots for ΔT = 20°C (7.92 x 10^8) for a) S/4, b) S/2 c) 3S/4

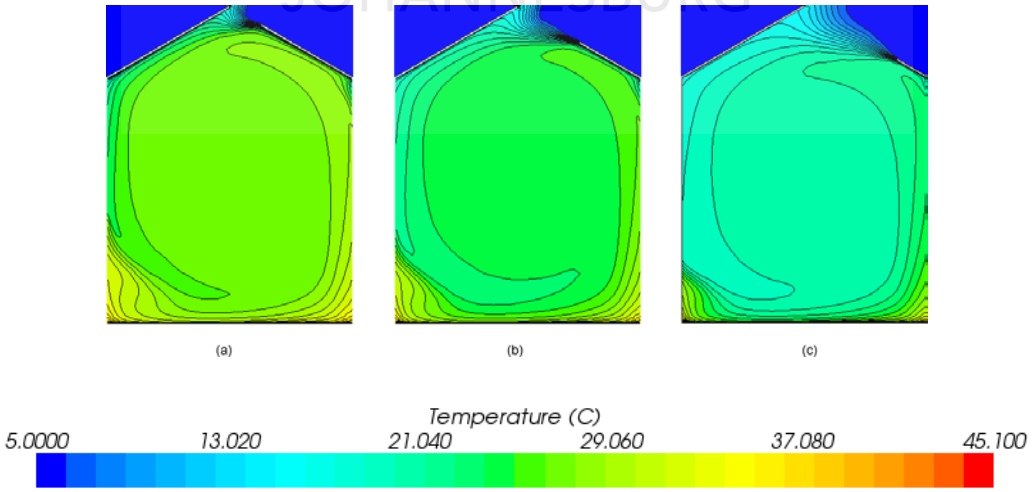

Figure 5.54: Temperature Contour Plots for ΔT = 30°C (1.1 x 10^9) for a) S/4, b) S/2 c) 3S/4

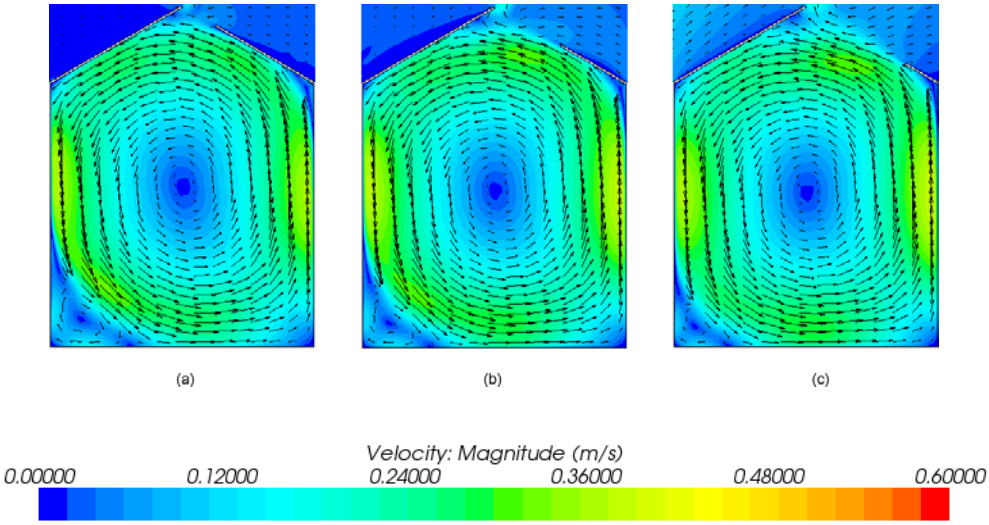

Figure 5.55: Vector and Velocity Contour Plots for ΔT = 30°C (1.1 x 10^9) for a) S/4, b) S/2 c) 3S/4

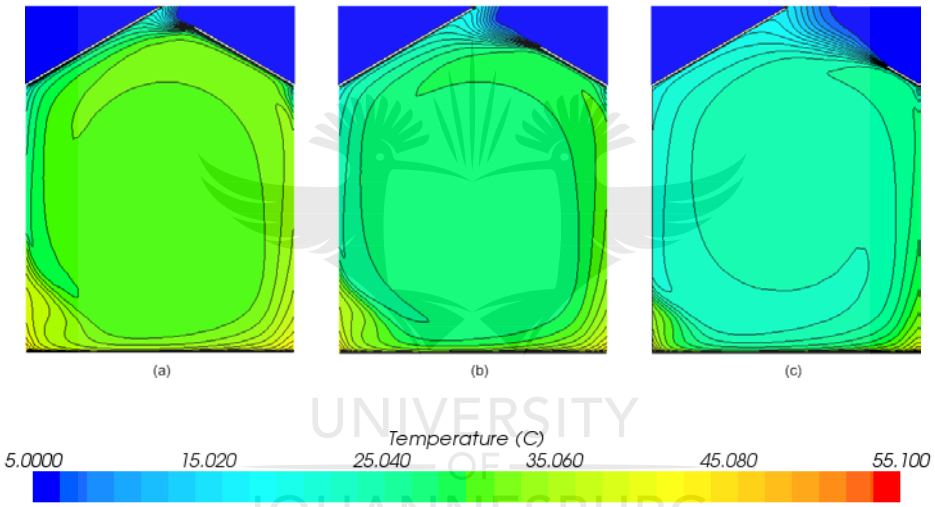

Figure 5.56: Temperature Contour Plots for ΔT = 40°C (1.35 x 10^9) for a) S/4, b) S/2 c) 3S/4

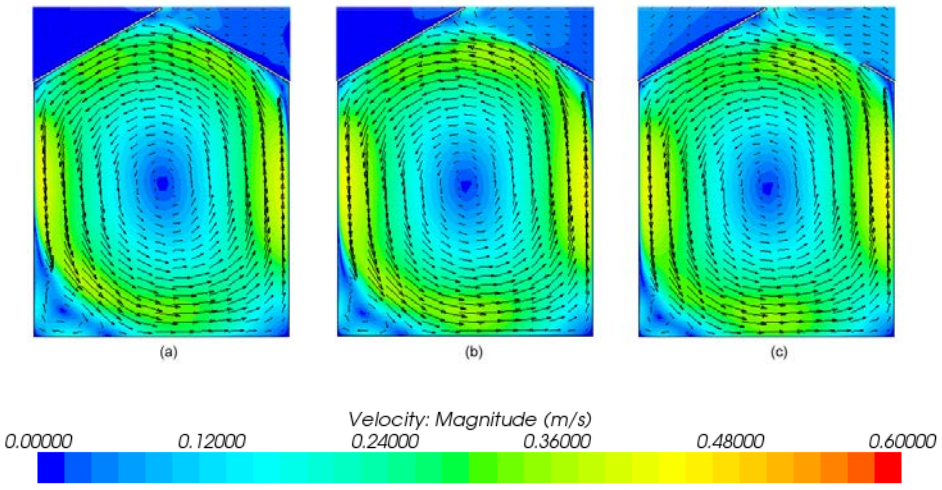

Figure 5.57: Vector and Velocity Contour Plots for ΔT = 40°C (1.35 x 10^9) for a) S/4, b) S/2 c) 3S/4

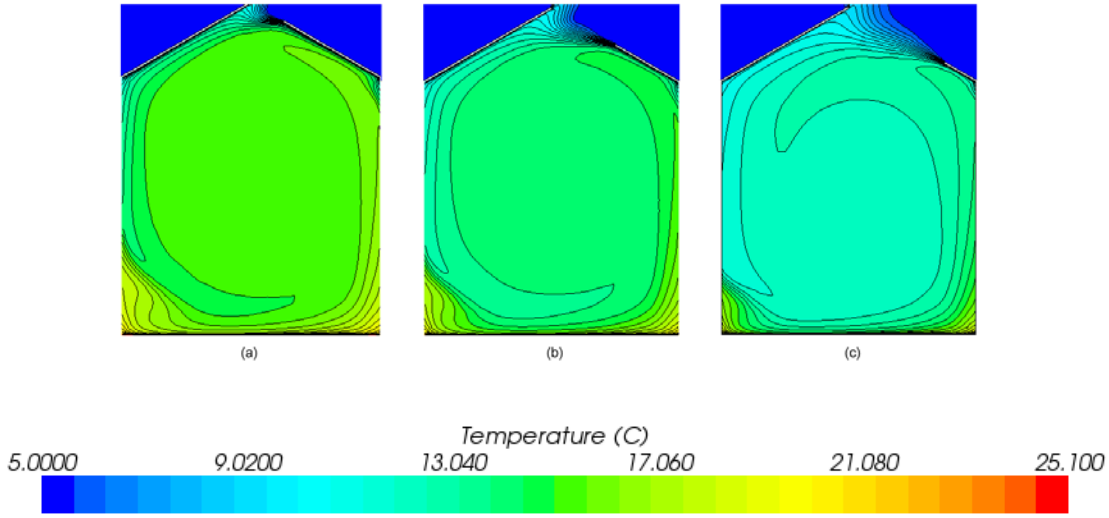

Figure 5.58: Temperature Contour Plots for ΔT = 50°C (1.57 x 10⁹) for a) S/4, b) S/2 c) 3S/4

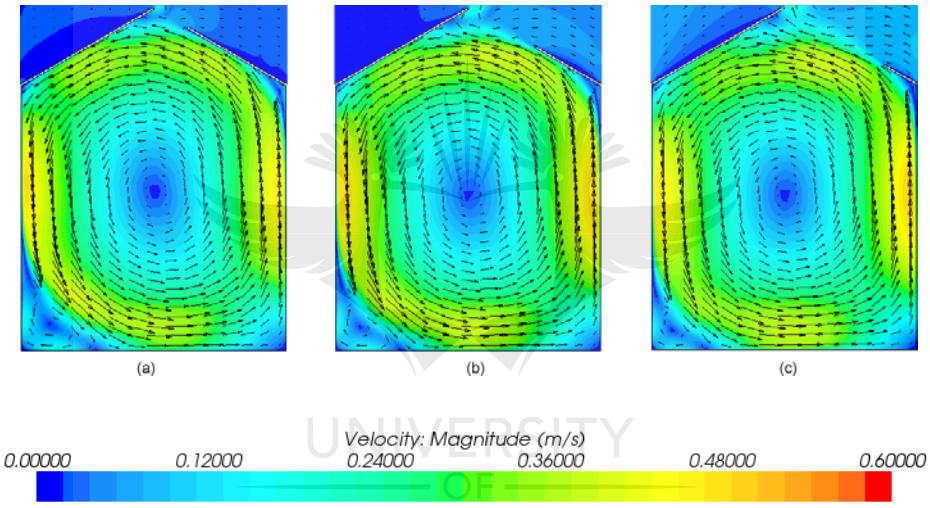

Figure 5.59: Vector and Velocity Contour Plots for ΔT = 50°C (1.57 x 10⁹) for a) S/4, b) S/2 c) 3S/4

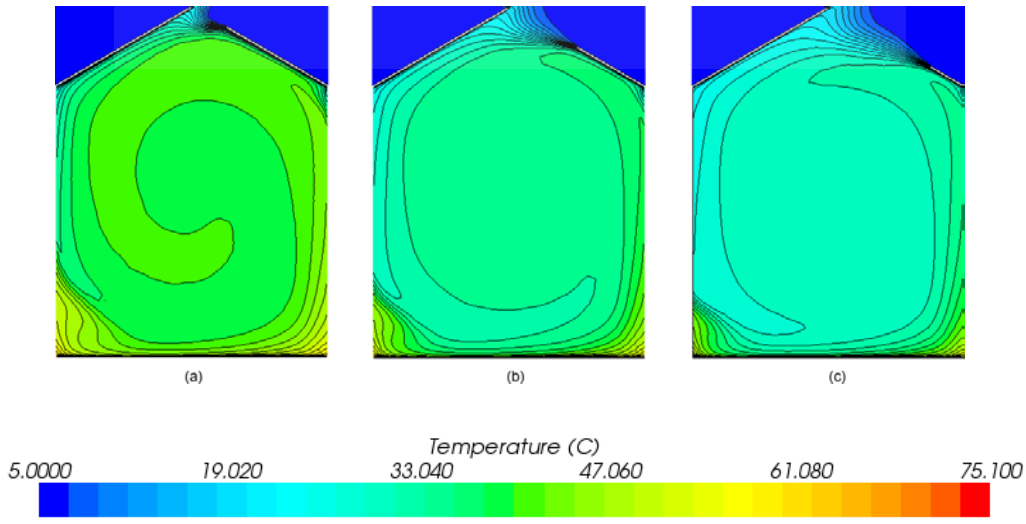

Figure 5.60: Temperature Contour Plots for ΔT = 60°C (1.75 x 10⁹) for a) S/4, b) S/2 c) 3S/4

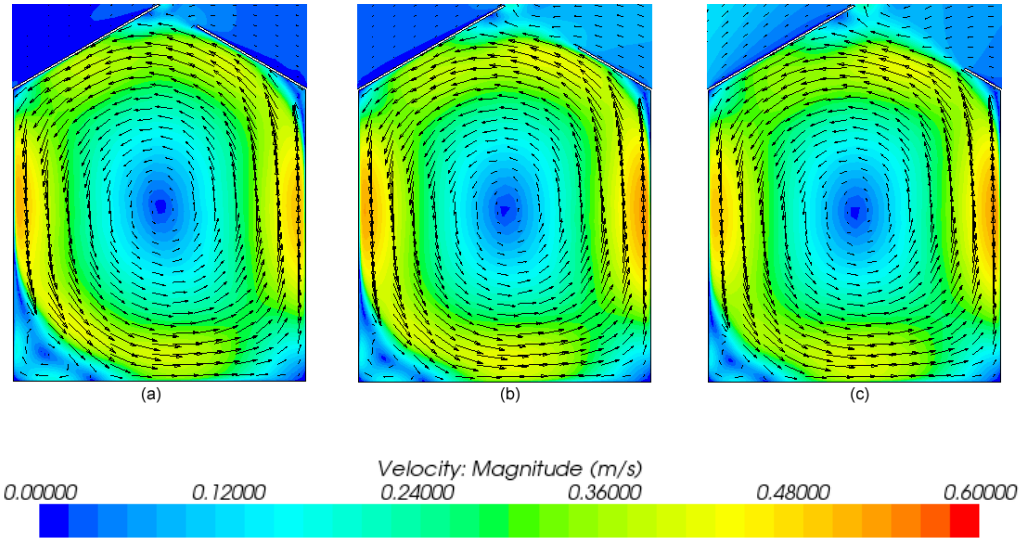

Figure 5.61: Vector and Velocity Contour Plots for ΔT = 60°C (1.75 x 10^9) for a) S/4, b) S/2 c) 3S/4

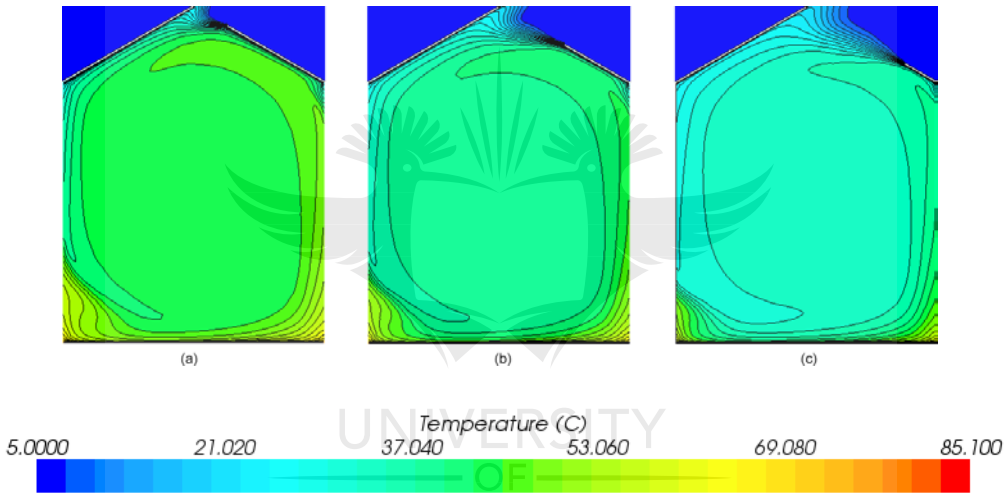

Figure 5.62: Temperature Contour Plots for ΔT = 70°C (1.9 x 10^9) for a) S/4, b) S/2 c) 3S/4

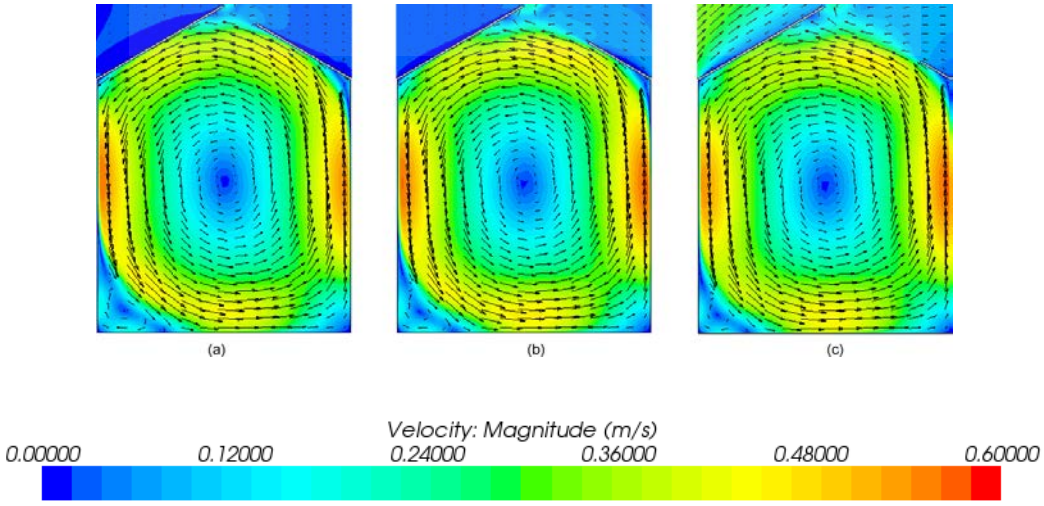

Figure 5.63: Vector and Velocity Contour Plots for ΔT = 70°C (1.9 x 10^9) for a) S/4, b) S/2 c) 3S/4

The different Nusselt number distributions for the various opening sizes are compared next for various Rayleigh numbers. The same trend is followed by the Nusselt number distributions for all the opening sizes and Rayleigh numbers. A local maximum is reached on the left side of the cavity, which is also where the secondary convective cell is formed. For each case a second local maximum forms towards the right side of the cavity. In each case an increase in overall Nusselt number distribution is noticed as the opening size increases.

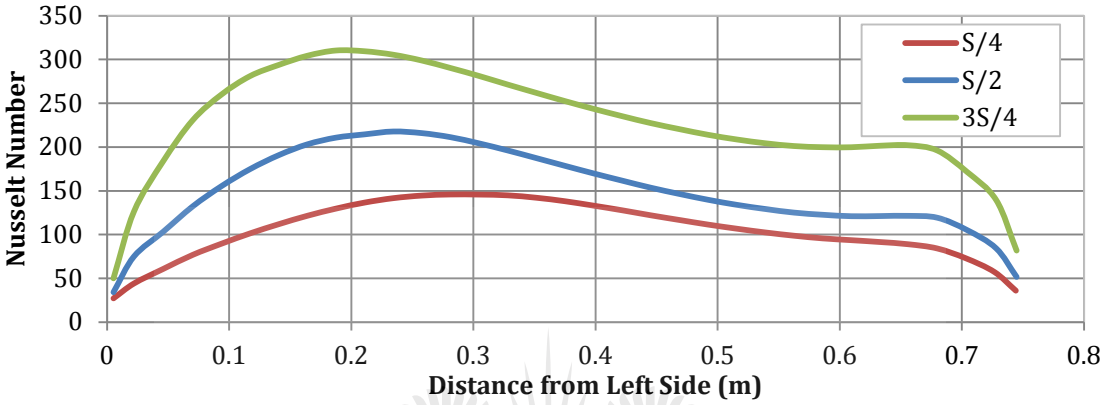

Figure 5.64: Nusselt Number Distribution on the Hot Wall (Floor) for ΔT = 5°C (Ra = 2.22 x 10^8)

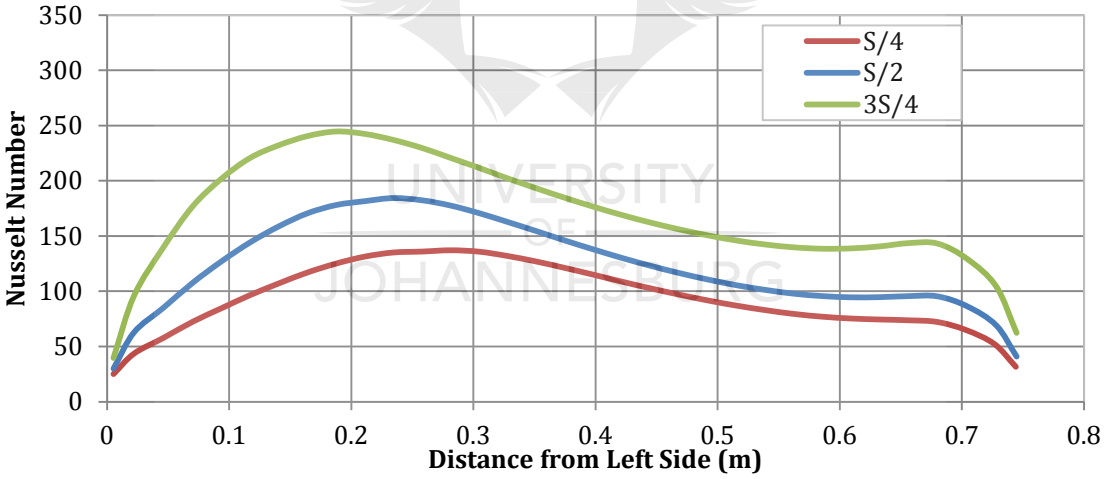

Figure 5.65: Nusselt Number Distribution on the Hot Wall (Floor) for ΔT = 10°C (Ra = 4.27 x 10^8)

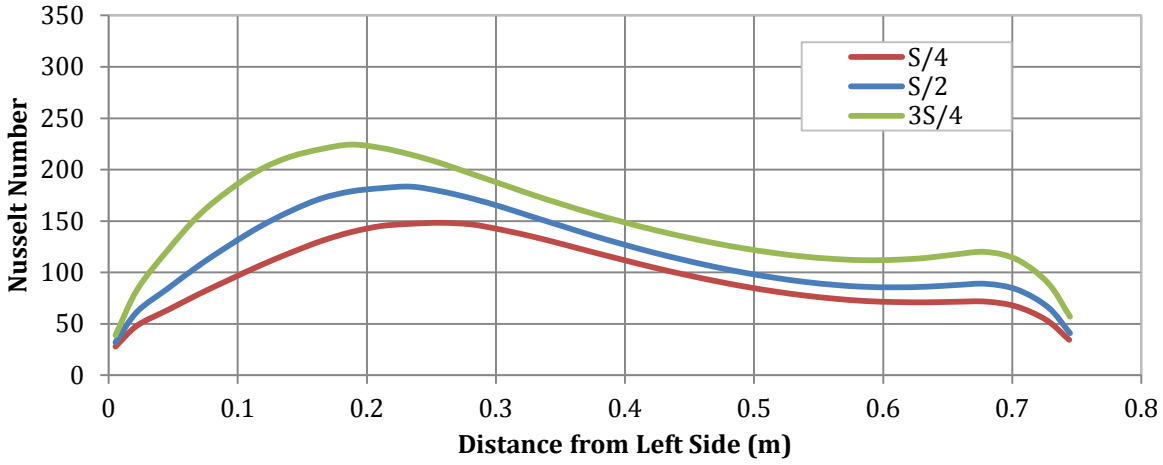

Figure 5.66: Nusselt Number Distribution on the Hot Wall (Floor) for ΔT = 20°C (Ra = 7.92 x 10^8)

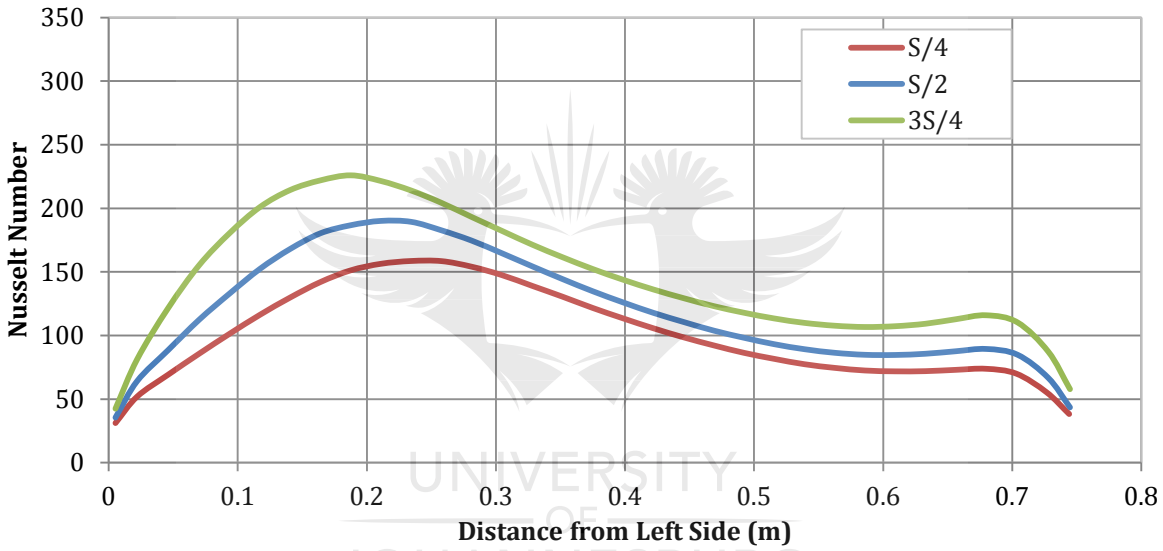

Figure 5.67: Nusselt Number Distribution on the Hot Wall (Floor) for ΔT = 30°C (Ra = 1.1 x 10^9)

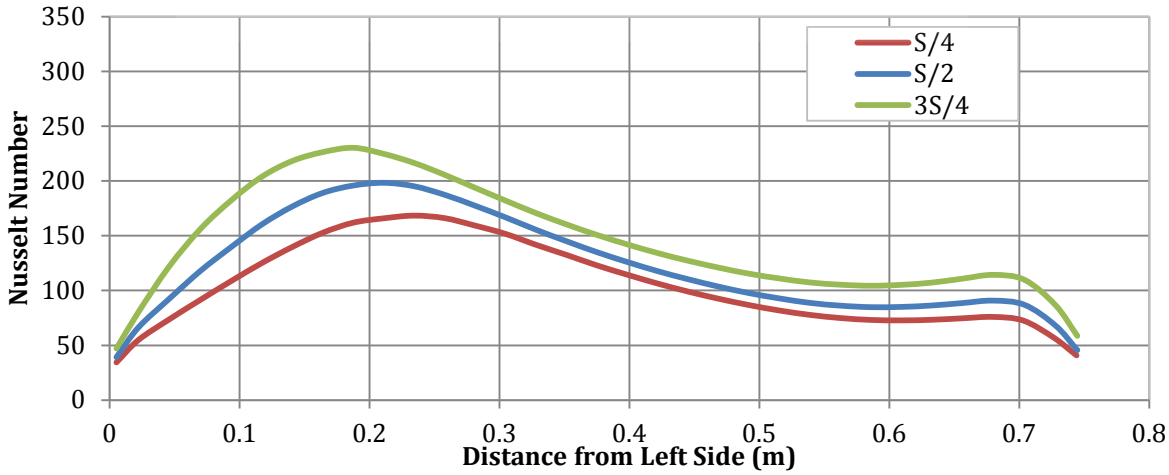

Figure 5.68: Nusselt Number Distribution on the Hot Wall (Floor) for ΔT = 40°C (Ra = 1.35 x 10^9)

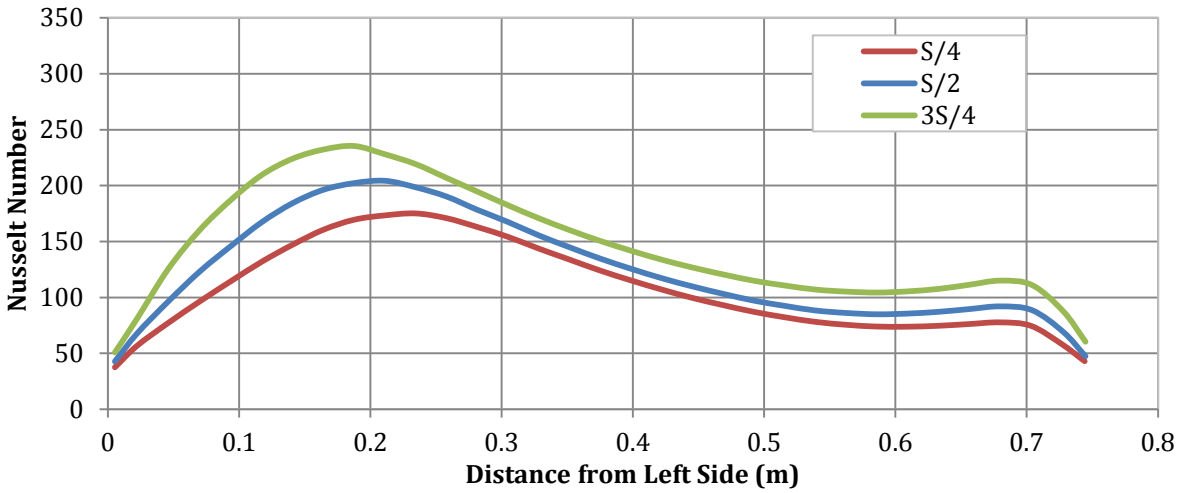

Figure 5.69: Nusselt Number Distribution on the Hot Wall (Floor) for ΔT = 50°C (Ra = 1.57 x 10^9)

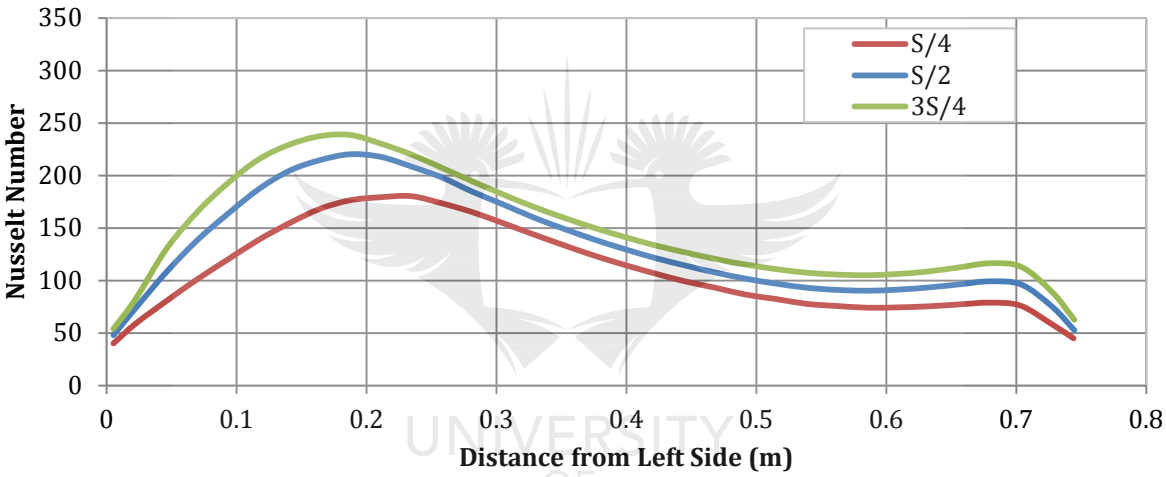

Figure 5.70: Nusselt Number Distribution on the Hot Wall (Floor) for ΔT = 60°C (Ra = 1.75 x 10^9)

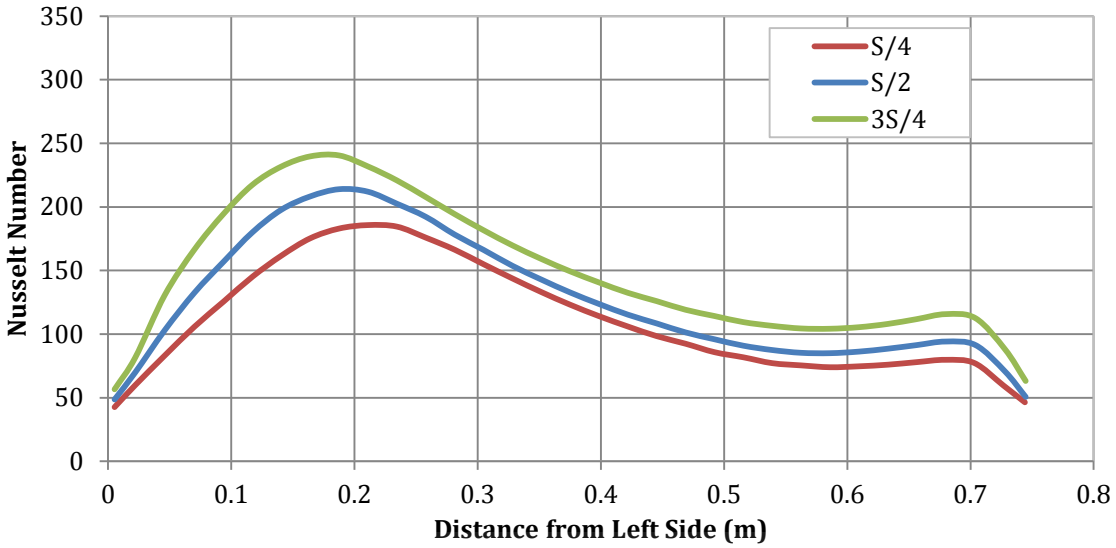

Figure 5.71: Nusselt Number Distribution on the Hot Wall (Floor) for ΔT = 70°C (Ra = 1.9 x 10^9)

Similar to the Nusselt number distributions, it was found that the temperature distributions through the centre of the cavity (at y/H=0.5) all follow a similar trend for all Rayleigh numbers. A typical plot for Ra = 2.22 x 10^8 is shown in Figure 5.72, which corresponds to a temperature difference of 5°C between the floor and the roof. As seen in the temperature contour plots, the cavity with a smaller opening size has the highest temperature distribution. This is similar for all the Rayleigh numbers, but only ΔT = 40°C and 70°C are shown here (See Figure 5.73 and Figure 5.74). The difference in overall temperature distribution increases with increase in temperature difference between the floor and the roof.

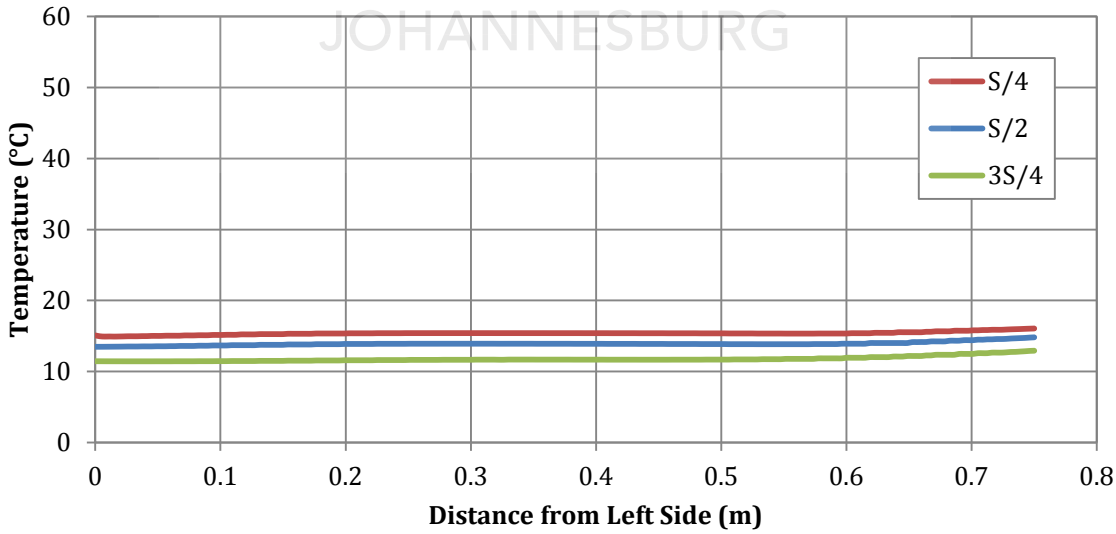

Figure 5.72: Temperature Distribution for ΔT = 5°C (Ra = 2.22 x 10^8)

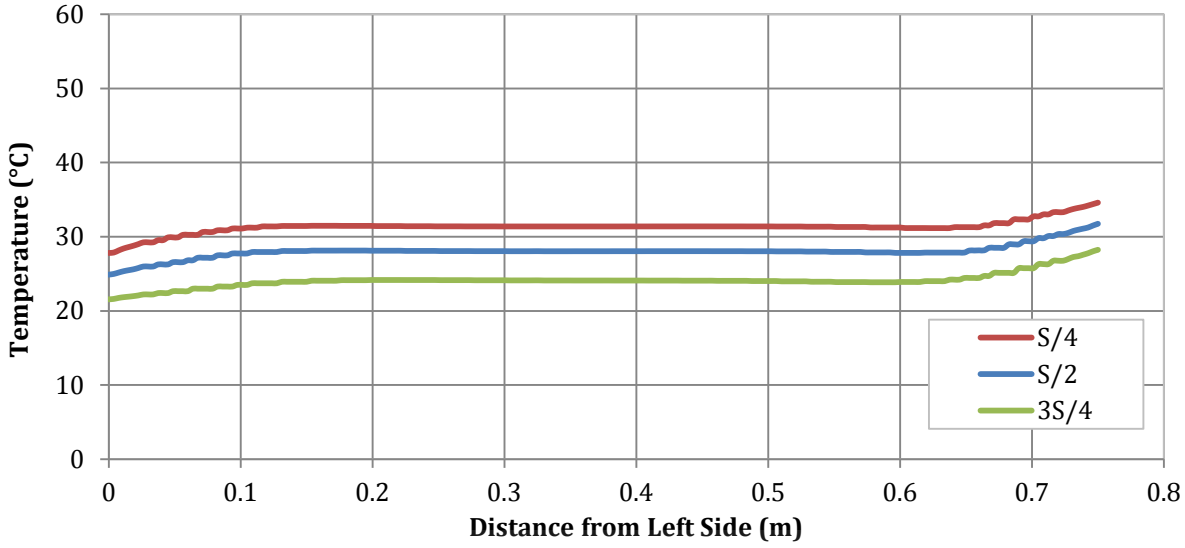

Figure 5.73: Temperature Distribution for ΔT = 40°C (Ra = 1.35 x 10^9)

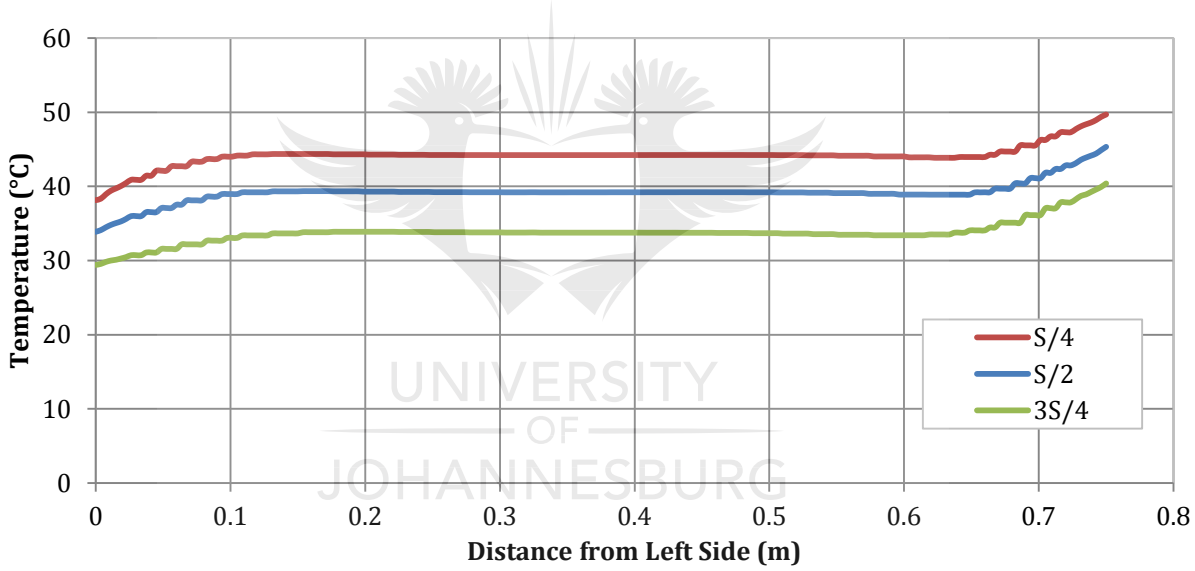

Figure 5.74: Temperature Distribution for ΔT = 70°C (Ra = 1.9 x 10^9)

The velocity distributions through the centre of the cavity (at y/H = 0.5) also exhibit the same trend – a steep velocity increase is noticed adjacent to each wall, with a local maximum reached. A local minimum is reached in the centre of the cavity. Quite a small difference in velocity distribution is noticed between the different opening sizes for each Rayleigh number. The largest noticeable difference is for a Rayleigh number of 2.22 x 10^8, where the velocity is slightly smaller where the maximum is reached near the adiabatic walls. This can be seen in Figure 5.75, Figure 5.76 and Figure 5.77 respectively. The velocity at the maximum adjacent to the right adiabatic wall is also the lowest for the smallest opening size for each Rayleigh number. As expected, the velocity increases with increasing Rayleigh number.

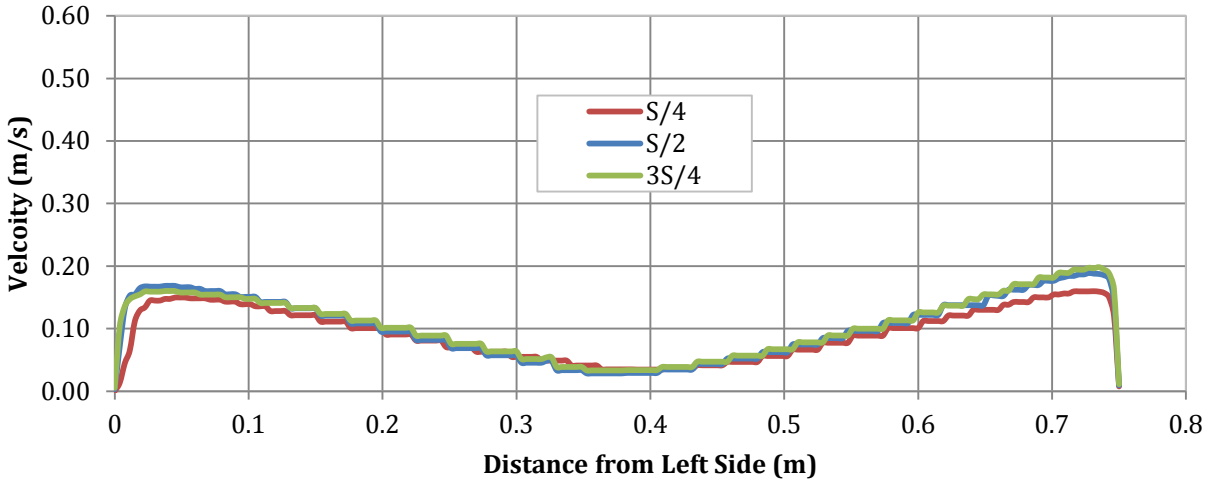

Figure 5.75: Velocity Distribution for ΔT = 5°C (Ra = 2.22 x 10^8)

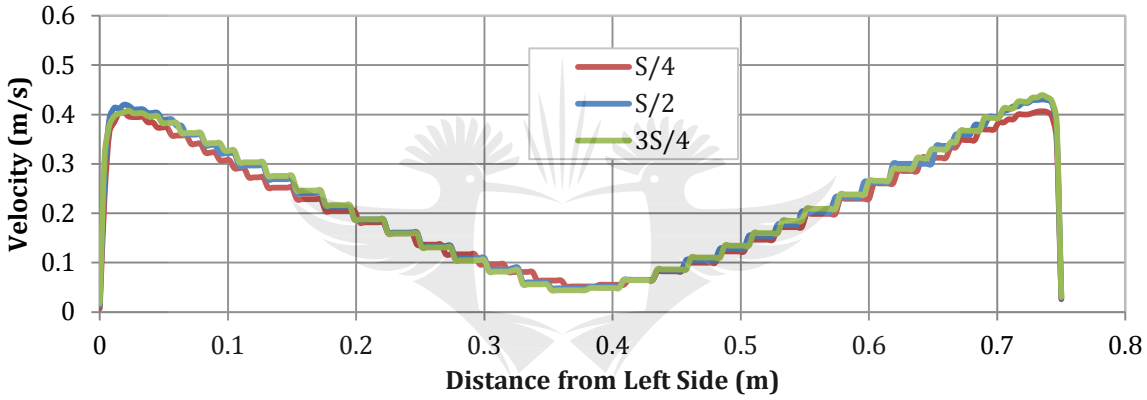

Figure 5.76: Velocity Distribution for ΔT = 40°C (Ra = 1.35 x 10^9)

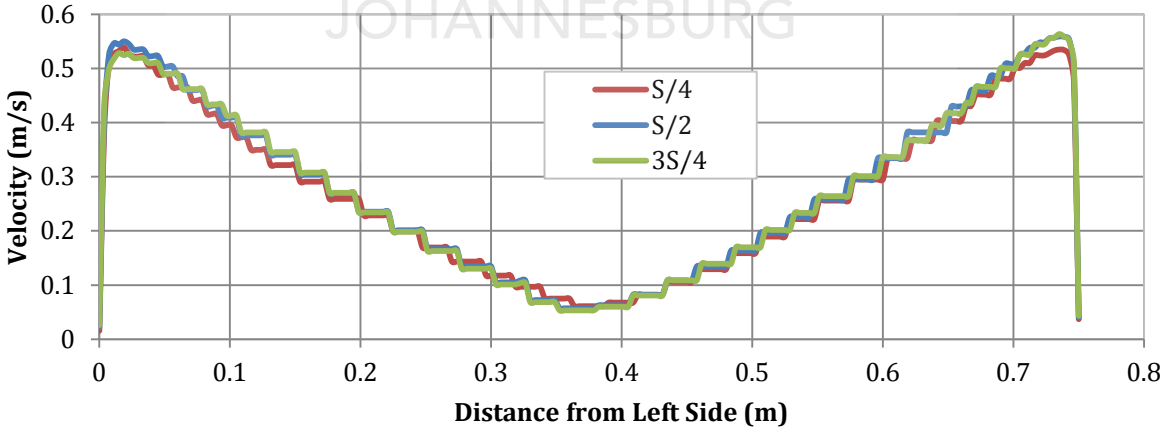

Figure 5.77: Velocity Distribution for ΔT = 70°C (Ra = 1.9 x 10^9)

Figure 5.78 shows the surface averaged Nusselt number for the different opening sizes as a function of Rayleigh number. Overall, the cavity with the largest opening of size 3S/4 exhibits the highest heat transfer, S/2 intermediate, and the lowest heat transfer is for the cavity with

the smallest opening size (S/4). For each opening size, the lowest two Rayleigh numbers (Ra = 2.22 x 10^8 and Ra 4.27 x 10^8), exhibits a slightly higher convective heat transfer compared to the higher numbers (Ra = 7.92 x 10^8 to Ra = 1.9 x 10^9). The last six Rayleigh numbers yield more or less the same Nusselt numbers and convective heat transfer. Therefore it can be concluded that opening size does have an influence on the convective heat transfer in the cavity, depending on the Rayleigh number. The influence is larger for lower Rayleigh numbers.

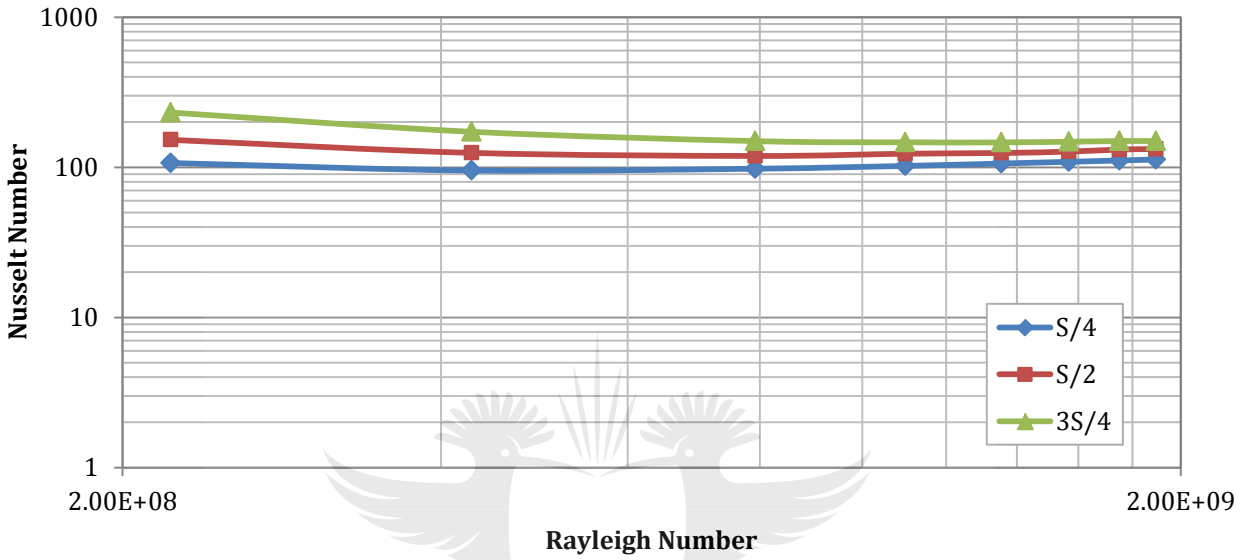

Figure 5.78: Nusselt Number vs Rayleigh for Various Opening Sizes

The curves shown in Figure 5.78 are best fit with a polynomial type series to sufficiently describe the Nusselt-Rayleigh number relationship in the Rayleigh number ranges simulated. The equations for these curves are shown Table 5.13.

Table 5.13: Nusselt-Rayleigh Correlations for Various Opening Sizes

Opening Size	Equation
3S/4	$Nu = -8E-26Ra^3 + 3E-16Ra^2 - 4E-07Ra + 299.5$
S/2	$Nu = -4E-26Ra^3 + 2E-16Ra^2 - 2E-07Ra + 182.33$
S/4	$Nu = -2E-26Ra^3 + 8E-17Ra^2 - 8E-07Ra + 118.6$

5.4.3 Comparison of Roof Ventilator Types

To ascertain whether the type of roof ventilator will have an influence on the heat transfer inside, the numerical greenhouse scale model containing the 25% opening (S/4) was lastly modified to include a flap opened horizontally as shown in Figure 5.79. The mesh parameters,

turbulence parameters and boundary conditions were exactly the same as in the previous section's CFD model.

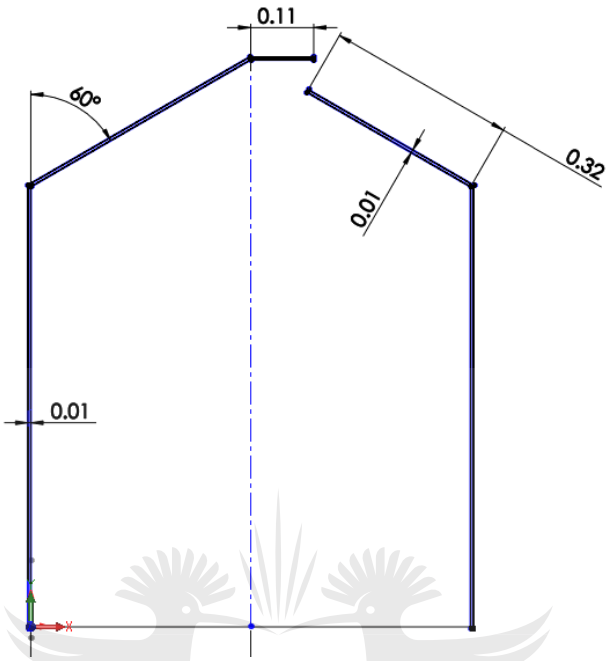

Figure 5.79: Small Flap type ventilator

The average Nusselt numbers on the floor versus Rayleigh number is compared in Figure 5.80. for a roll-up and flap-type ventilator. The same trend was noticed – a slightly increased Nusselt number for the smaller Rayleigh numbers, where as there is little difference between the rest of the Nusselt numbers as the Rayleigh number increases. A slight difference (approximately 17%) in Nusselt number for the two opening types is noticed for the smaller Rayleigh numbers. It can therefore be concluded that for small openings, the type of opening does not seem to have a significant influence on the heat transfer within the cavity.

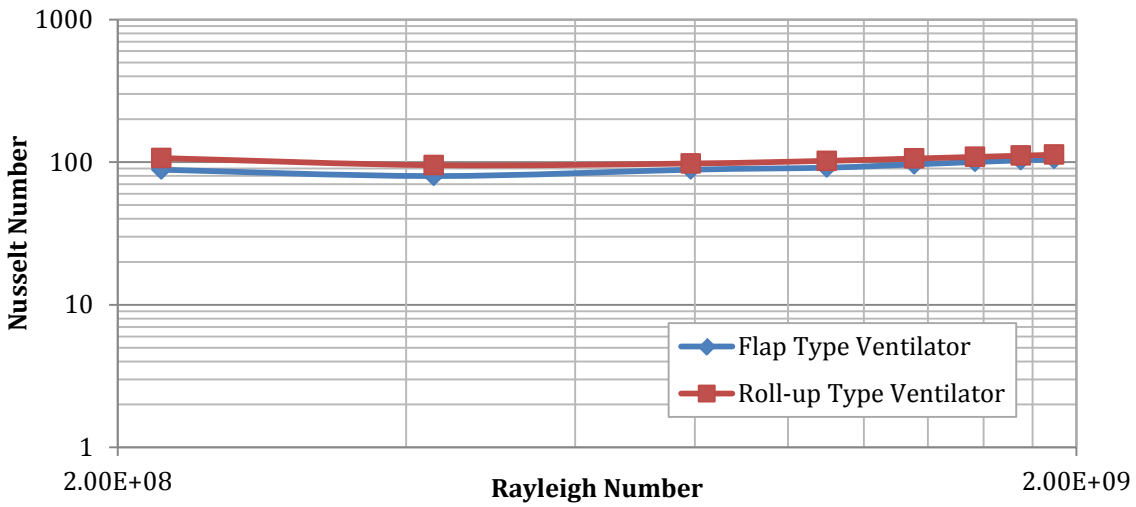

Figure 5.80: Nusselt vs Rayleigh for two ventilator types

5.4.4 Comparison of Closed and Open Cavities

To establish the difference in indoor climate between the closed and ventilated greenhouse, the two cases are compared using the temperature scalar and vector plots as seen in Figure 5.81 and Figure 5.82 for Ra = 1.35 x 10^{9}.

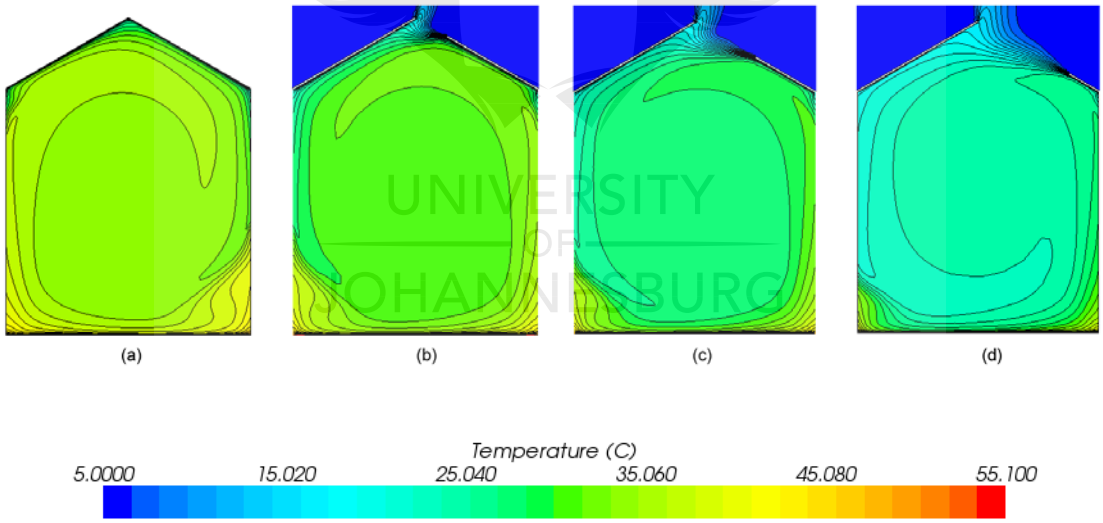

Figure 5.81: Comparison of Temperature Contour Plot (Ra = 1.365 x 10^{9})- Closed Greenhouse (a), S/4 Opening Size (b), S/2 Opening Size (c), 3S/4 Opening Size (d)

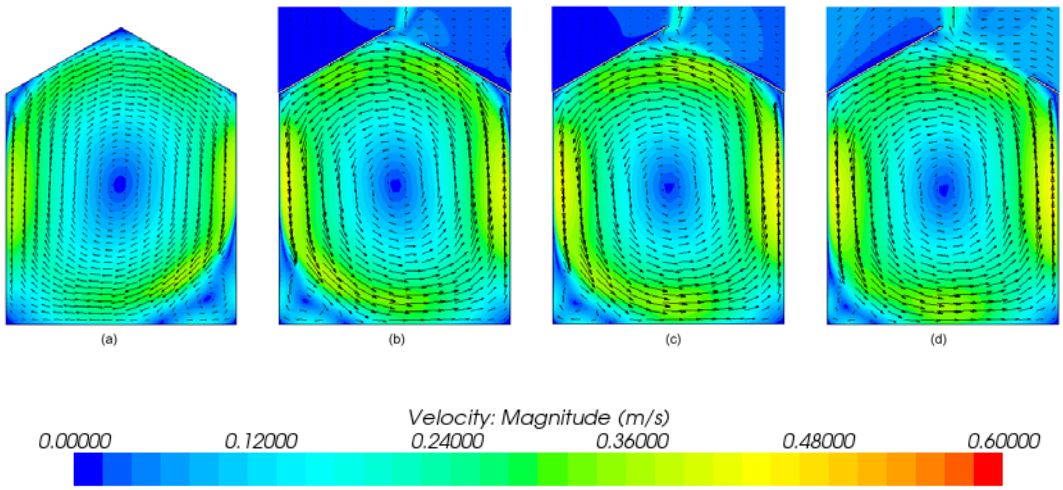

Figure 5.82: Comparison of Vector Plot (Ra = 14.35 x 10^9) - Closed Greenhouse (a), S/4 Opening Size (b), S/2 Opening Size (c), 3S/4 Opening Size (d)

It can be seen from the temperature comparison, that the closed cavity is warmer compared to the open cavities, the largest difference in temperature is noted for the opening size of 3S/4. This is probably due to the influx of cold air from outside the cavity through the roof opening. This is also visible in the comparison between the temperatures along the centre of the cavity (Figure 5.83). The vector plots indicate that the closed cavity forms a clockwise-rotating cell, compared to the counter-clockwise rotating cell observed in the open cavities. This could be due to numerical influences or the driving forces created by the colder outside air moving into and out of the cavity for the open cavity. The velocity vector plot also indicates that the velocities in the cavities are more or less in the same range. From the comparison of the centre distribution of velocities (Figure 5.84), it can be seen that the closed cavity exhibits the lowest velocity (about 0.35m/s) adjacent to the vertical walls, whereas the open cavities have slightly higher velocities (approximately 0.4 m/s at the left wall and 0.43m/s at the right wall). A velocity of 0.05m/s is seen for both the open cavity and all the closed cavities at the centre of the cavity. It can therefore be seen that having a roof ventilator does have an influence on the velocity and temperature distribution inside the cavity.

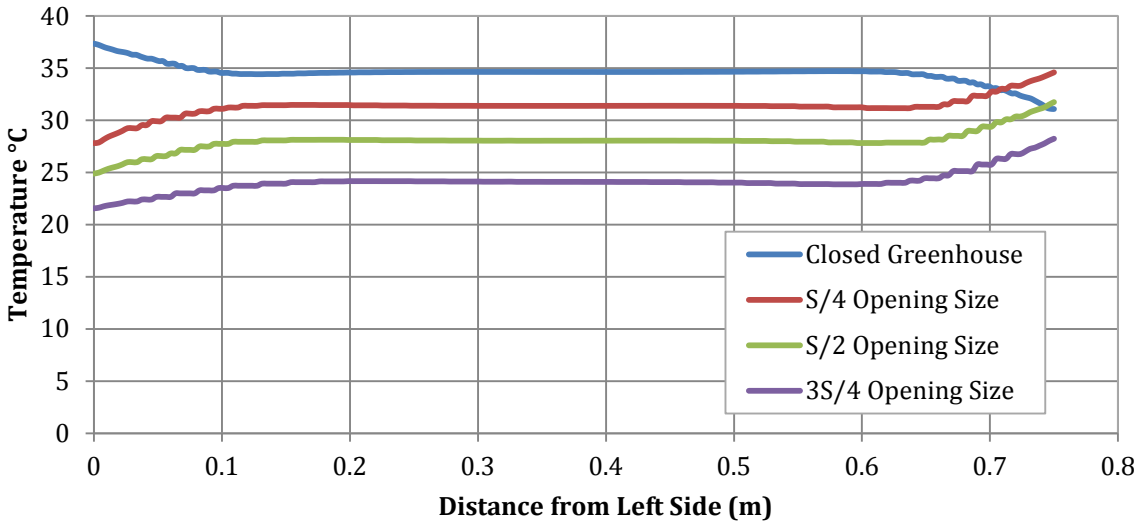

Figure 5.83: Comparison of Centre Temperatures

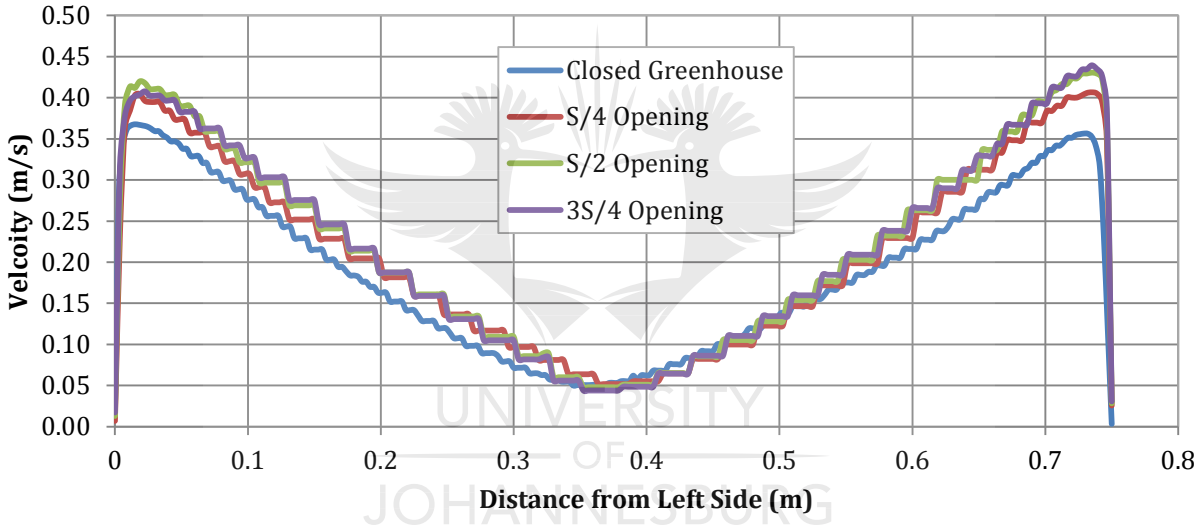

Figure 5.84: Comparison of Centre Velocities

The Nusselt versus Rayleigh number comparison is depicted in Figure 5.85. Overall, the ventilated greenhouse displays a slight decrease in heat transfer with Rayleigh number from the lowest Rayleigh number (Nu = 106.74) to Ra = 4.27 x 10^8 (Nu = 95.15), where after the Rayleigh number increases again to Nu = 112.76 for the highest Rayleigh number. In the closed greenhouse, the heat transfer increases with Rayleigh number. The largest difference is noticed for the lower Rayleigh numbers, where the Nusselt number for the ventilated greenhouse (Ra = 2.22 x 10^8) case is 106.74, whereas the Nusselt number is 44.6 for the closed greenhouse. This is a difference of approximately 58%. For the highest Rayleigh number (Ra = 1.9 x 10^9) there is a difference of 17% in the Nusselt numbers.

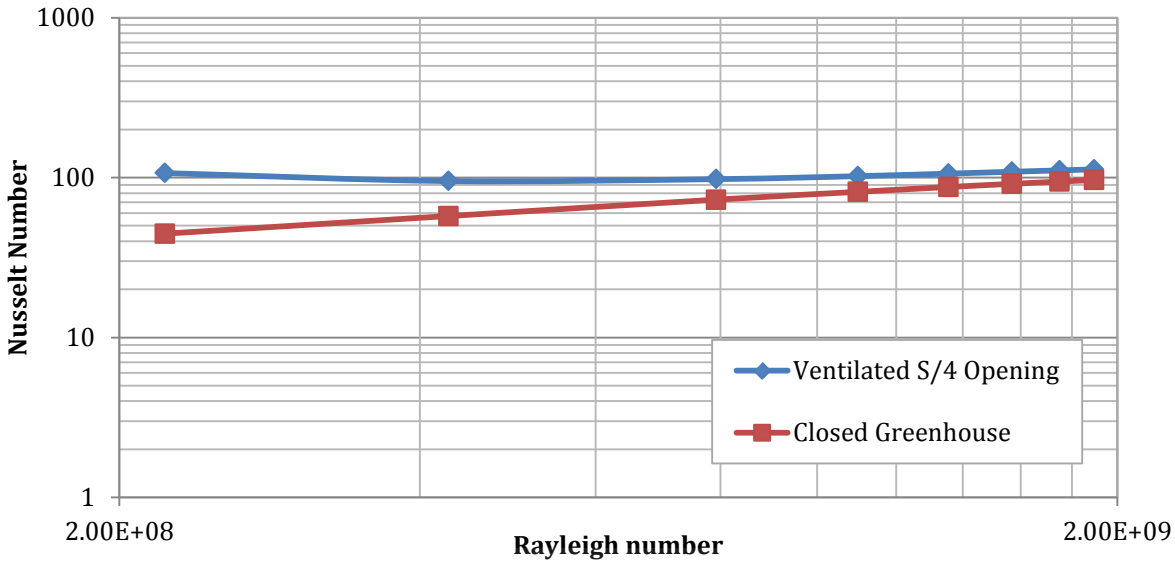

Figure 5.85: Comparison of Nusselt vs Rayleigh for closed and ventilated greenhouse cavity

5.5 Large Two-Dimensional Greenhouse

The numerical results based on using the smaller scale greenhouse of 0.75m, lead to confidence in creating a numerical model for a larger greenhouse. The greenhouse model was scaled up to represent a larger greenhouse similar to the one investigated by Lamrani [3]. Experience gained from the previous numerical simulations of the smaller greenhouse models were used to construct this 2D CFD model. The greenhouse dimensions are shown in Figure 5.86.

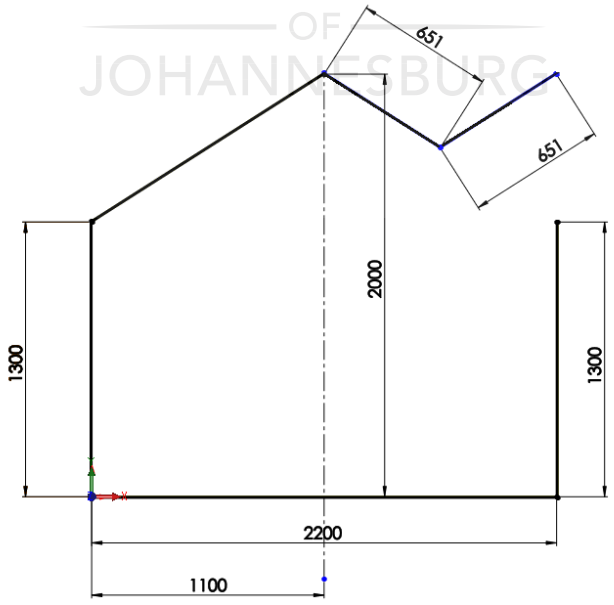

Figure 5.86: Dimensions of Scaled-up Greenhouse [3]

The approach to creating this 2D numerical CFD model was similar to that in the previous section. A large control volume was created around the greenhouse, and the greenhouse walls were created as a gap of 5mm. The mesh around the greenhouse was refined using a volumetric source and is shown in Figure 5.87. The mesh specifications are set out in Table 5.14.

Table 5.14: Mesh settings for scaled-up greenhouse cavity

Property	***Value***
Base Size (m)	0.3
Number of Prism Layers	20
Prism Layer Stretching	1.1
Prism Layer Thickness (m)	0.022
Surface Growth Rate	1.3
Surface Size (Tet/Poly Density)	
Density	1.0
Growth Factor	1.0
Blending Factor	1.0
Volumetric Source	
Size Relative to Base	20

The boundary conditions were specified as discussed in the previous section, and are summarized in Table 5.15, and the turbulence parameters are tabulated in Table 5.16.

Table 5.15: Boundary Conditions for scaled-up greenhouse

Boundary Name	***Boundary Type***
Greenhouse Walls (Inside and Outside)	Wall (no-slip)
Left and Right side of Computational Domain	Velocity Inlet
Top of Computational Domain	Combined Symmetry Plane and Pressure Boundary

Table 5.16: Turbulence parameters for scaled-up greenhouse

Under Relaxation Factor	**0.8**
Convergence Tolerance	0.1
Epsilon	0.0
Turbulent Viscosity (Under Relaxation Factor)	1.0

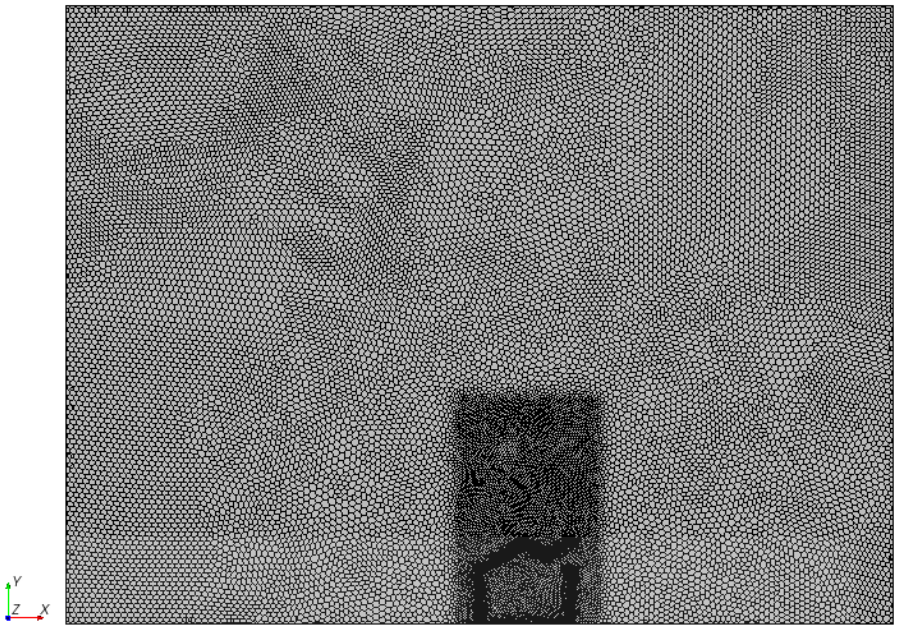

Figure 5.87: Mesh used for Scaled-up model

This case contained an isothermal specified wall and floor. The cavity consisted of a 5mm thick void, and the temperatures were specified on the inner walls of the cavity created by the void. The boundary conditions chosen were also similar to the previous CFD model. The left and right side of the large control volume Figure 5.87) were specified as velocity inlets, with a velocity of 0.004m/s, as the cavity is larger compared to the cavity in the previous section. The top of the control volume was specified as a symmetry plane, with a small section right above the greenhouse specified as a pressure outlet. The temperature of the floor was specified as 62.9°, while the left side of the roof was set to 30.5°C and the right side to 32.5°C respectively to be able to compare qualitatively with Lamrani [3]. The ambient temperature was specified as 18.6°C as measured in the experiment. Flow was assumed to be steady, and the standard k-epsilon low -number turbulence model was activated. Gravity was specified in the negative y-direction. The velocity vector plot of the numerical results can be seen in Figure 5.88 and is compared to the flow pattern observed by Lamrani in [3]. A large single clockwise rotating loop is observed in the CFD results, with maximum velocities present near the floor and left side of the roof. The air moves into the greenhouse at the bottom of the roof vent, moves around the cavity in a clockwise motion, and then exits the cavity at the top of the greenhouse. A small counter-clockwise rotating cell if formed below the flap of the roof ventilator. The overall flow pattern is similar to what was experimentally observed by Lamrani, as can be seen in Figure 5.89.

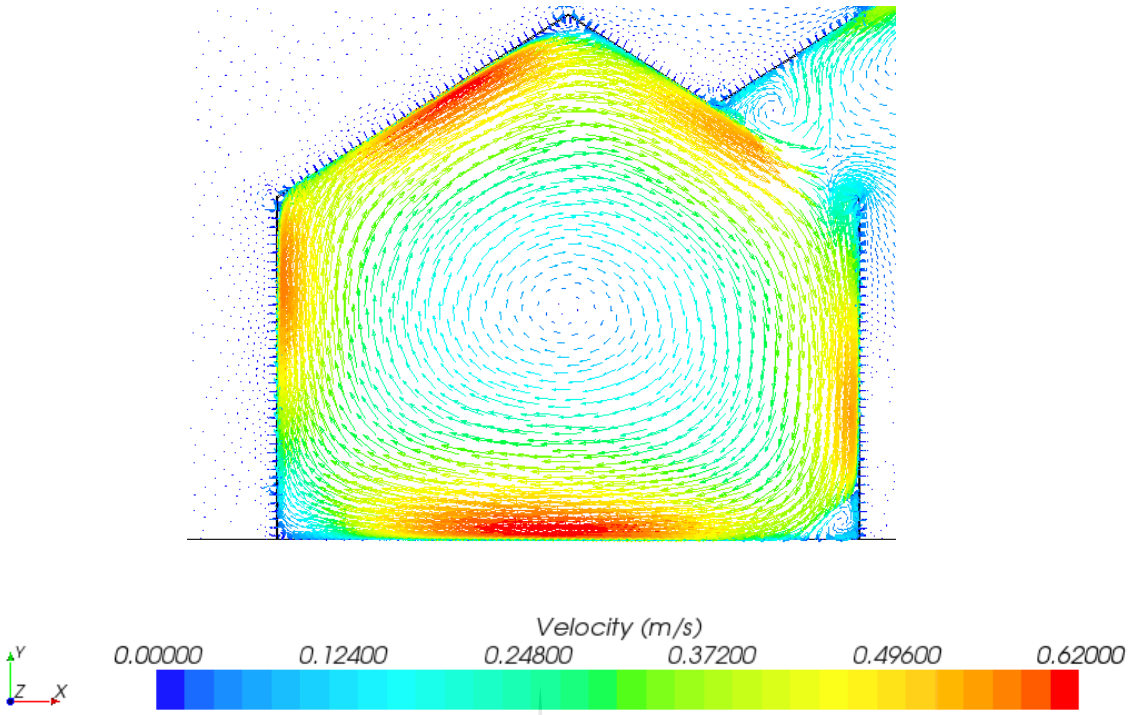

Figure 5.88: Vector Plot of scaled-up greenhouse

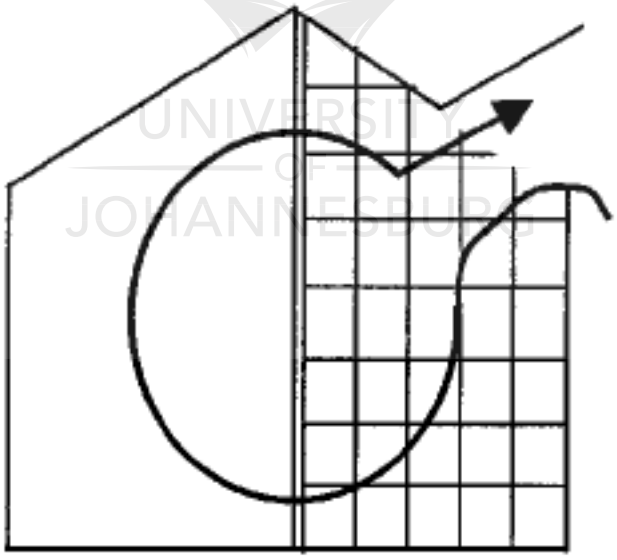

Figure 5.89: Flow pattern observed by Lamrani [3]

Therefore qualitatively the 2D numerical CFD results are similar to those observed by Lamrani, as well as similar to those obtained for the smaller cavity of 0.75m. Thus confidence was again created in the CFD model for modelling a single-span ventilated greenhouse.

5.6 Conclusion

In this chapter the original zero-degree roof angle CFD scale model of the greenhouse was modified to include various design parameters such as roof angles and ventilators. The difference between two and three dimensional models was also investigated. For all the different roof angles of the greenhouse scale model investigated numerically, the flow was dominated by a large, single convective cell, with a smaller rotating cell in one of the bottom corners. For all roof angles it was also found that the Nusselt number distribution on the hot wall (floor) overall increased with Rayleigh number. As the roof angle increased, a more pronounced effect on the temperature distribution at mid-height was noted with increasing Rayleigh number. The overall velocity distribution at mid-height was also found to increase with increasing Rayleigh number. The overall effect of the various roof angles indicated that the average Nusselt number on the hot wall increased with Rayleigh number, but also with roof angle. A power law series was found to best describe the Nusselt-Rayleigh relationships for the range of Rayleigh numbers considered.

When the two- and three-dimensional cases for the cavity containing a 45 degree roof angle was compared, a large convective cell was also noticed in the center of the three-dimensional cavity (z/H =0.5). The temperatures were found to be slightly higher in the three-dimensional compared to the two-dimensional case, and the velocities lower. Nusselt numbers between the two and three-dimensional case however did not compare well between the two cases; the average Nusselt number on the hot floor for the three-dimensional case was significantly lower compared to the Nusselt number for the two-dimensional case.

When different size ventilators were added to the cavity with a 30 degree roof angle, the flow was still characterized by a large, single convective loop, with a smaller rotating loop in the bottom left corner. The largest opening size (3S/4) exhibited the highest heat transfer for all the Rayleigh numbers. As the Rayleigh number increased, an increased influence on the temperature distribution at mid-height with opening size of the cavity was observed. The influence on the velocity with opening size was not as pronounced. A 3rd order polynomial type series curve was found to best describe the behaviour of the curves for the Nusselt-Rayleigh number correlations for the various opening sizes, for the range of Rayleigh numbers considered. When the roof ventilator was changed to a flap-type ventilator, very little change was observed in the curve describing the Nusselt-Rayleigh number behaviour. It can therefore be concluded that the type of roof ventilator does not have a significant influence on the heat transfer within the cavity.

The heat transfer in the closed greenhouse and open greenhouse for an opening size of 4/S has been compared. Overall, the heat transfer decreases slightly with increasing Rayleigh number for the ventilated cavities due to the ingress of cold air from outside. For the closed cavity the heat transfer increases with Rayleigh number The impact of the ventilator seems to be more significant for lower Rayleigh numbers.

Lastly, the cavity was scaled up to represent a larger greenhouse found in the literature. The CFD model was qualitatively successfully validated as a similar flow pattern was observed as in the literature. Therefore confidence was established in using a CFD model to investigate flow inside a larger greenhouse.

The next chapter extends this research study further by focusing on the two-dimensional numerical simulation of a full-scale multi-span greenhouse.

CHAPTER 6

Two-Dimensional Full Scale Simulations for Multi-span Greenhouses

6.1 Chapter Review

The previous chapter addressed natural convection in basic geometries representing single span greenhouse small scale models, with various design alterations such as roof angle and symmetry. A larger scale greenhouse was also successfully validated against data found in the literature. This chapter takes the investigation one step further; the geometry is now altered to represent a multi-span greenhouse consisting of a number of cavities. An initial two-dimensional CFD model of the multi-span greenhouse is validated against data found in the literature by Ould Khaoua [49] for a full-scale four span greenhouse. The first set of simulations is subject to both wind and buoyancy driven flow to compare it to the original greenhouse. The second set of simulations investigates the effect of buoyancy driven flow only. The following research questions are addressed in this chapter:

- Is it possible to create a two-dimensional CFD model of a large, full-scale, multi-span greenhouse, and compare it to results found in the literature?
- Can a CFD model of a full-scale, multi-span greenhouse be used to investigate the differences between a combination of buoyancy and wind driven flow and buoyancy driven flow only?

6.2 Numerical Model

The CFD model in this chapter is based on a greenhouse used in a study by Ould Khaoua [49]. It is a glass four-span greenhouse (width, 4 by 9.60m; length, 68m; eaves height, 3.90m; ridge height, 5.9m). A 2mm plastic partition separates the first two spans from the last two spans. The greenhouse is covered by 4mm thick horticulture glass and has continuous roof vents on both sides of each span (Figure 6.1). During the experimental period, ornamental 0.2m high plants were grown on 0.75m shelves. The length of the shelves were assumed, and the ventilator openings were assumed to be 1.22m wide [29]. The negative y direction in the 2D CFD model

was chosen as the direction of the gravitational constant. The wind was modelled to act in an eastern direction.

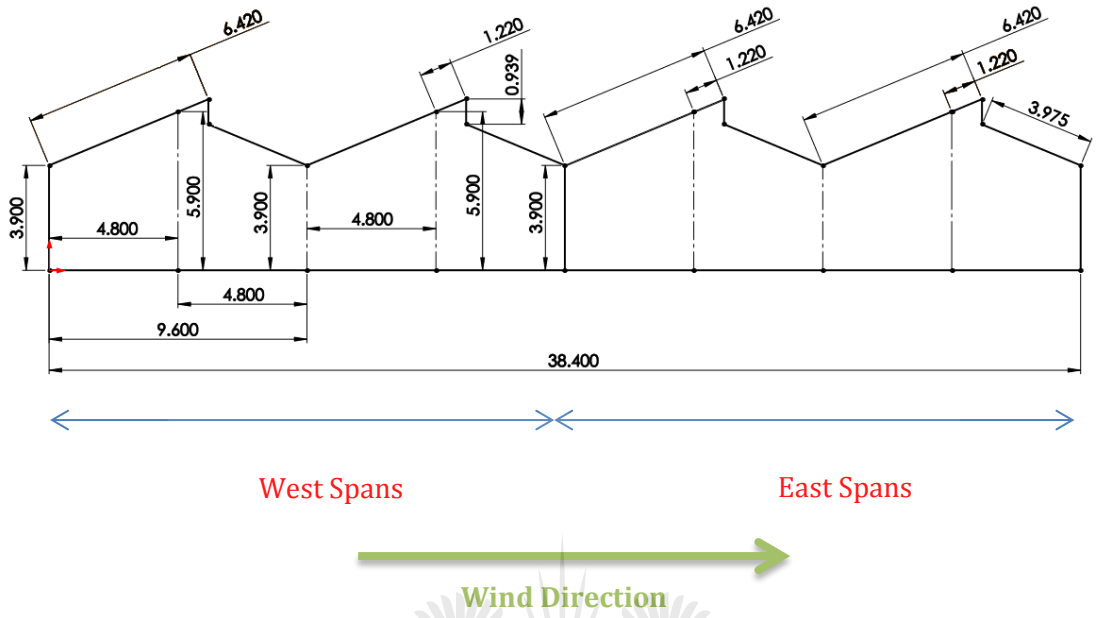

Figure 6.1: Dimensions of Full-Scale Greenhouse

A large computational control volume (250m x 100m x 100m) was created around the greenhouse model to ensure minimal interference from the boundaries on the flow inside the greenhouse and to allow for development and definition of the boundary layer. The wind was modelled to act from left to right in an eastern direction at 1m/s. This was done for comparison purposes with the original validated greenhouse [49]. The outlet of the domain was specified as a porous region, using the mesh extruder in StarCCM+ in order to force the flow out of the domain. This is an artificial boundary created to ensure a positive pressure over the outlet boundary, to avoid recirculating flow developing. As the outlet boundary is far from the region of interest, the effect on the solution was considered negligible. The porous region was 10m, with 10 orthogonal extruded cells, which was extruded from the volume mesh at the outlet boundary.

The solid walls and roof of the greenhouse was modelled using two solid boundaries with a 2mm air gap in-between as shown in Figure 6.2. The implication of this as discussed in previous chapters is that it was assumed in the model that environment did not interact directly through to the greenhouse other than the specified boundary conditions on the inner walls of the greenhouse model.

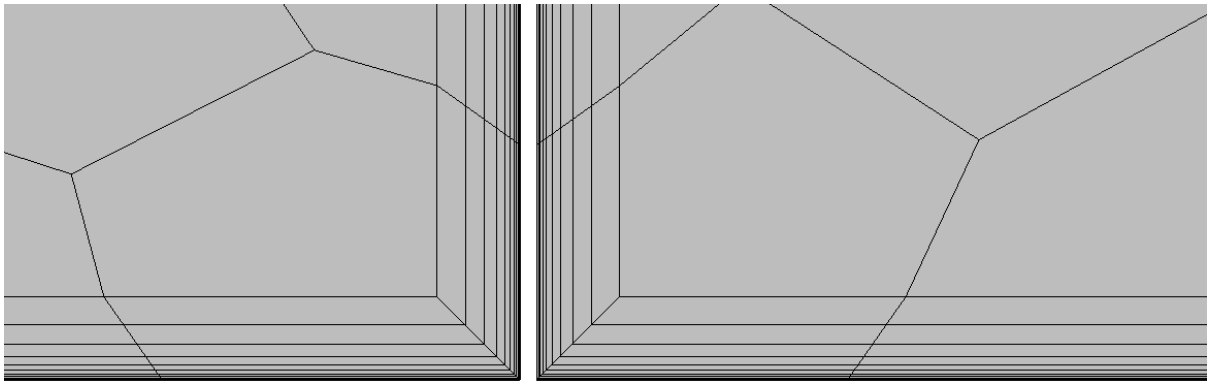

Figure 6.2: Air Gap between Solid Boundaries

Each of the solid boundaries on the inside of the greenhouse was given a constant temperature as shown in Table 6.1. The air properties for the model is summarized in Table 6.2.

Table 6.1: Boundary conditions

Boundary	Type	Unit	Value
Outside Ground	Type	ºC	27.9
Inside Ground	Wall	ºC	27.3
Roof	Wall	ºC	33.6
Plastic Central Partition	Wall	ºC	31.3
Lateral Glass Wall	Wall	ºC	29.1
Reference Velocity	Wall	m/s	1.4
Outside Wind Velocity	Velocity Inlet	m/s	1

Table 6.2: Physics properties

Parameter	Unit	Value
Inlet Air		
Temperature	ºC	22.2
Density	kg/m^3	1.20
Viscosity	kg/m.s	1.51×10^{-5}
Specific Heat	J/kg.K	1005.91
Thermal Conductivity	W/m.K	0.0258
Molecular Weight of Dry Air	kg/kmol	28.9
Gravitational Constant	m/s^2	9.81

The mesh parameters chosen for this model were different to those specified in chapter 5, due to the wind and the large computational domain created around the greenhouse (shown in Figure 6.3). The domain was meshed again using a polyhedral meshing model, together with a boundary layer meshing model.

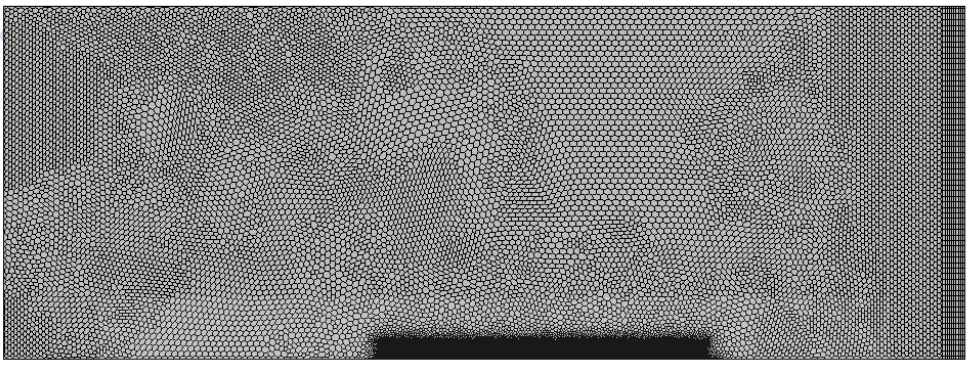

Figure 6.3: Control Volume around Greenhouse

The prism layer model was utilized in the CFD software to ensure adequate modelling of the turbulence in the boundary layer. The prism layer was present on all the wall-type boundaries in the solution domain. Once the three-dimensional mesh had been created, the mesh was converted to a two-dimensional mesh to reduce computational running time. [7] The mesh in the region of the greenhouse was refined to 4% of the chosen base size (visible in Figure 6.4 and Figure 6.5), to ensure sufficient resolution to capture the flow and temperature variations inside the greenhouse cavity. A summary of the mesh parameters is shown in Table 6.3, and the final mesh used in the CFD greenhouse model with the prism layer can be seen in Figure 6.4.

Table 6.3: Mesh Parameters

Property	*Value*
Base Size (m)	3.5
Number of Prism Layers	10
Prism Layer Stretching	1.5
Prism Layer Thickness (m)	0.01
Surface Growth Rate	1.3
Surface Size (Tet/Poly Density)	
Density	1.0
Growth Factor	1.0
Blending Factor	1.0
Volumetric Source	
Size Relative to Base	4

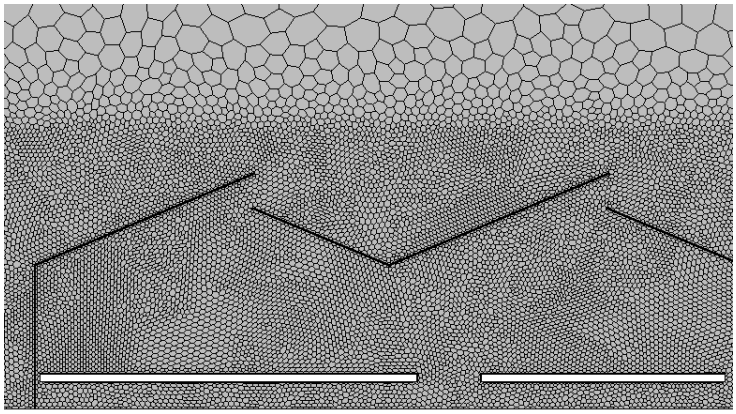

Figure 6.4: Mesh around Greenhouse

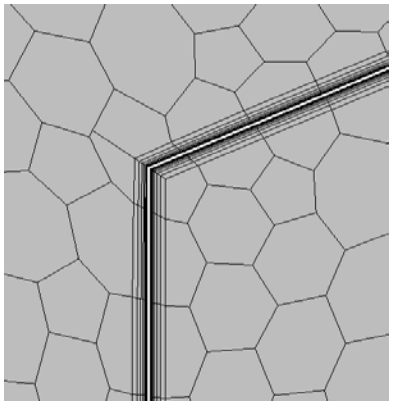

Figure 6.5: Mesh and Prism Layer Mesh

The standard k-epsilon low-Reynolds turbulence model was used for the full-scale simulations. Additional terms have been added in StarCCM+ to account for buoyancy and compressibility effects. In StarCCM+, this approach can be used in conjunction with low-Reynolds number type meshes (y+ must be in the region of 1) or wall-function type meshes (y+ > 30). A scalar contour plot was used in the simulation to monitor the wall y+ values, and since a low-Reynolds number type mesh was used, the y+ value must remain below 1. The turbulence parameters are tabulated in Table 6.4.

Table 6.4: Turbulence Parameters

Under Relaxation Factor	**0.8**
Convergence Tolerance	0.1
Epsilon	0.0
Turbulent Viscosity (Under Relaxation Factor)	1.0

6.3 Results

In order to validate the CFD model of the current greenhouse, the results for the first two spans have been compared to some of the results obtained by Ould Khaoua et al [49]. A scalar plot of the simulated temperature distribution in the first two spans is shown in Figure 6.6. The majority of the greenhouse, especially the first span has a homogenous temperature distribution in the core region above the shelves. The thermal boundary layers are visible adjacent to the glass wall, plastic and roof of the greenhouse. The greenhouse is slightly warmer underneath the shelves compared to the regions above the shelves. The infiltration of cool air from outside can be seen at the second roof ventilator.

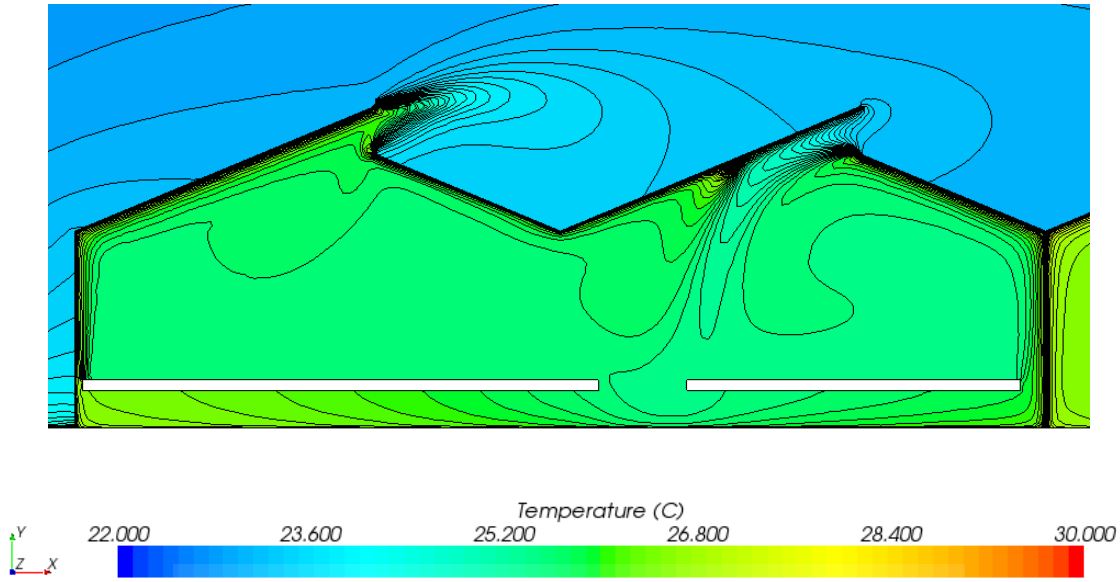

Figure 6.6: Scalar Plot Temperature Distribution inside two West Spans of Greenhouse (Current CFD Study)

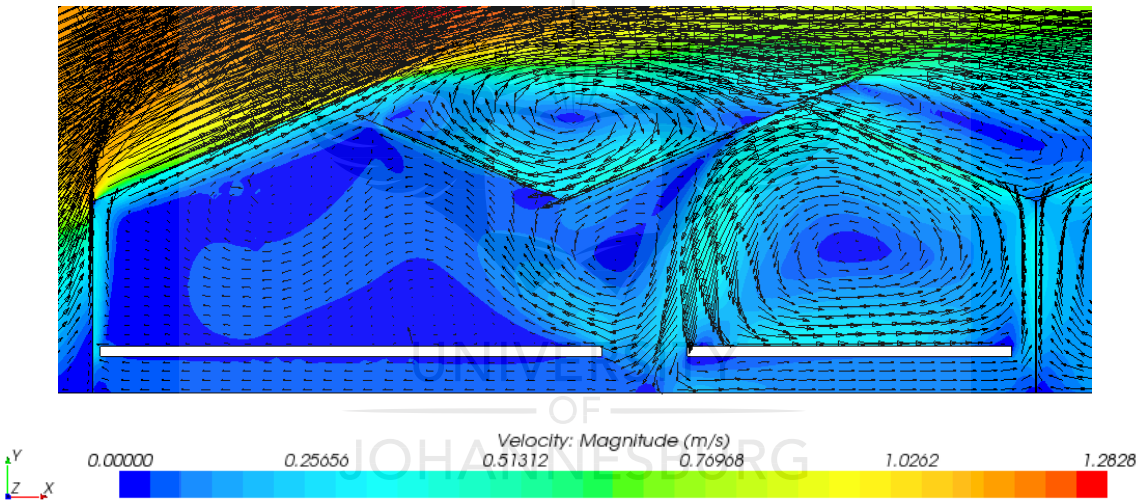

Figure 6.7: Velocity vectors and contours inside two west spans of greenhouse (current CFD study)

The vectors are plotted with the velocity contours in Figure 6.7. The main flow of fresh outside air enters through the second roof ventilator, and splits into two streams just above the shelve height. A large counter clockwise rotating cell is formed above the second shelve, while a smaller clockwise rotating cell forms adjacent to the large cell, forcing some air towards the first span. The air is forced underneath the first shelve by the large rotating cell on the second shelve. This air moves towards the west of the greenhouse, up against the wall and exits the greenhouse at the first ventilator. The rest of the air moves underneath the second shelve towards the east of the greenhouse, up the wall an joins the convective cell above the second shelve. Compared to the second span of the greenhouse, the flow inside the first span is relatively stagnant, with a slow moving clockwise rotating cell above the first shelve. The

majority of the air in the first span leaves the greenhouse through the first ventilator. A higher velocity compared to the core of the first span is noticed near the west wall and roof of the first span. These observations are similar to what was found by the authors in the literature [49].

Figure 6.8 shows the numerical temperature and velocity contour plots obtained by Ould Khaoua et al [49]. Comparing these two contour plots with the contour plots numerically obtained in this study, it can be concluded that a reasonably good comparison was found. Macroscopically, similar flow patterns and flow directions were found in this study, as well as the warmer temperature beneath the shelves. Differences can be attributed to the fact that the length and position of the shelves were assumed, as well as the size of the roof ventilators. It can therefore be concluded that the numerical model is reasonably accurate in terms of flow patterns and direction.

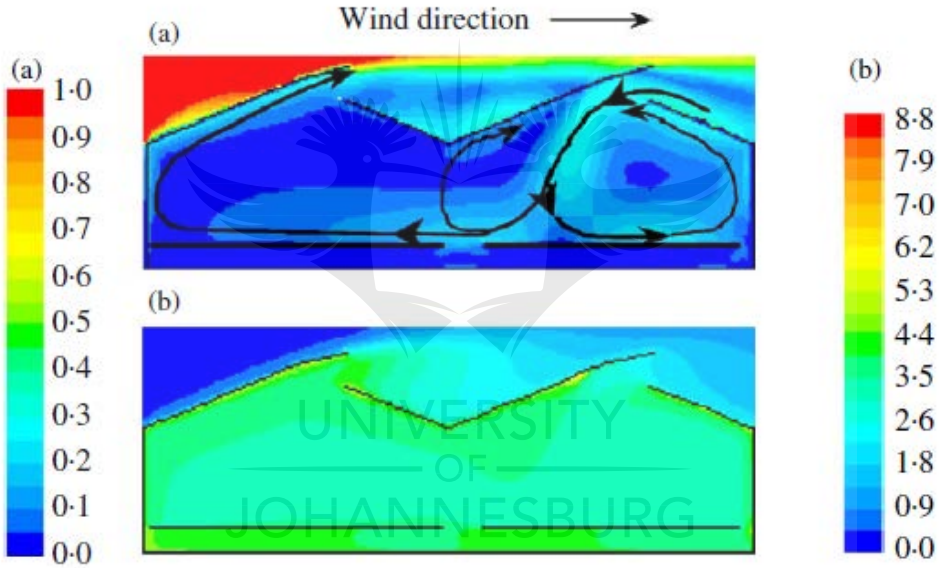

Figure 6.8: CFD results found by Ould Khaoua [49]

For comparison purposes, the temperature difference and velocity difference at plant level (1m) were investigated further using the current CFD models for the multi-span greenhouse. The current temperature difference between the inside and outside of the greenhouse is compared against the numerical results from literature (red blocks) in Figure 6.9 and Figure 6.10. It is evident from Figure 6.10 that the same trend is visible – a constant temperature difference in both the west and east spans, with a slight drop in temperature difference in the right/second spans. Overall the temperature difference is slightly lower compared to the literature. As mentioned before, this can be attributed to certain assumed properties such as the position and length of the shelves. A sudden increase in temperature is also noted adjacent to the walls. This

is due to the line probe used in the CFD program that penetrated the thermal boundary layers next to the wall. This was not necessarily the case in the literature.

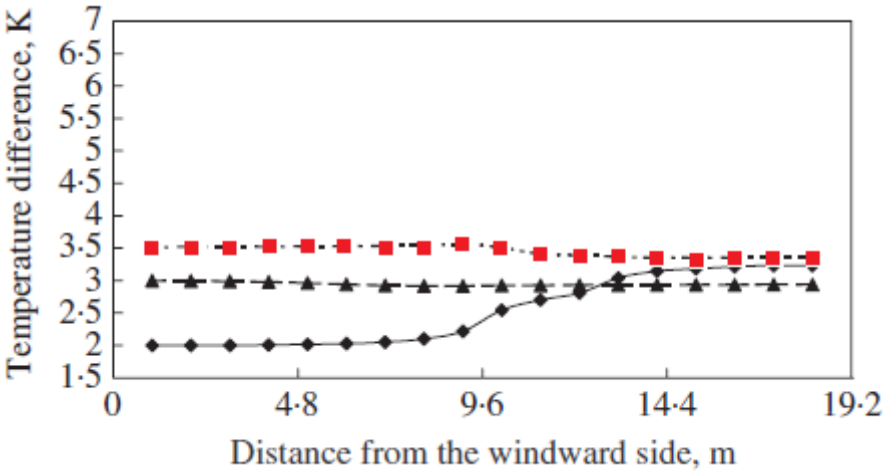

Figure 6.9: Temperature Difference between inside and Outside air, distribution along width at a height of 1m inside the two west spans [49]

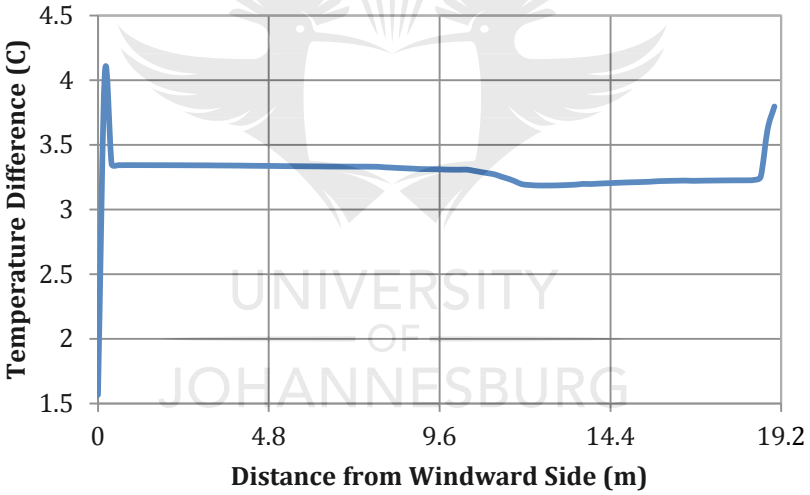

Figure 6.10: Numerical Temperature Difference between inside and Outside air, distribution along width at a height of 1m inside the two west spans ((Current Study)

Figure 6.11 and 6.12 compare the current velocity distribution at 1m height in the greenhouse with the results published in the literature for the two west spans (Refer to Figure 6.1). The numerical results are compared to the curve with the red markers in Figure 6.11. The curve from the numerical results exhibits a similar trend as far as the two peaks are concerned, as they are in almost the same location. The only difference is the velocity distribution in the first span. In the literature a gradual increase is noticed in the velocity from close to zero at the left wall to approximately 0.2m/s. The current numerical results show a sharp increase in velocity adjacent to the next wall, while the flow is stagnant for the first span (first half of two west

spans). A gradual increase is noticed to approximately 0.15m/s at ≈ 12m from the left wall of the greenhouse. These differences are all attributed to the assumed parameters as mentioned before.

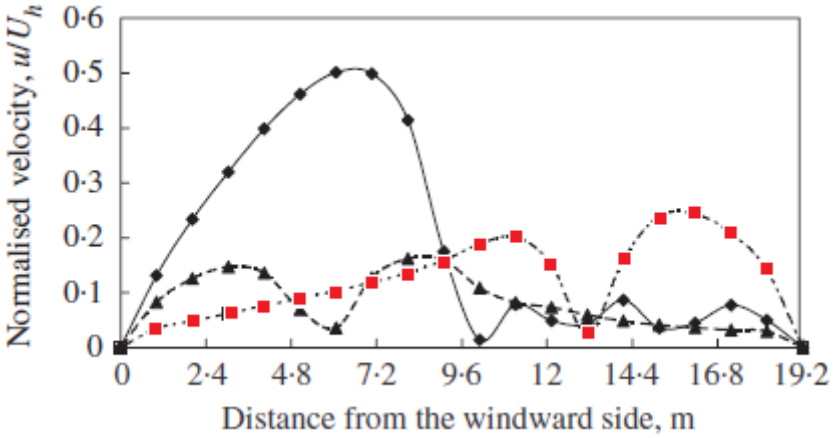

Figure 6.11: Average air velocity normalised by the outside wind speed (u/Uh) along width at a height of 1m inside the two west spans [49]

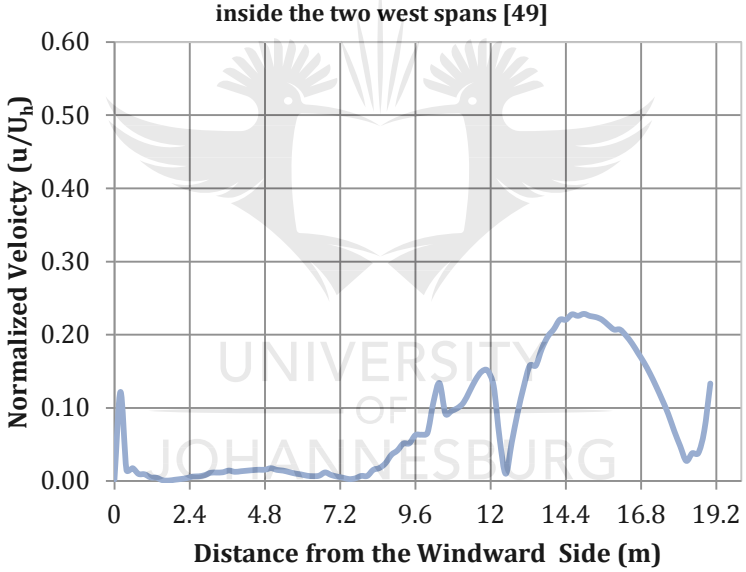

Figure 6.12: Average Numerical Air Velocity Normalised by the Outside Wind Speed (u/Uh) along Width at a Height of 1m inside the two west spans (Current Study)

This section focused on the greenhouse being subjected to both wind and buoyancy driven flow. The next section will investigate the same multi-span greenhouse subjected to buoyancy driven flow only.

6.4 Buoyancy Driven Flow

This section investigates the difference when the greenhouse validated in the previous section is subjected to a combination of wind and buoyancy driven flow, and mainly buoyancy driven flow only. For this case, the wind velocity was specified as close to zero (0.002m/s), and the temperatures was left as stated in the previous section. The temperature contour plots are compared in Figure 6.13 and Figure 6.14, where Figure 6.6 is essentially replicated in Figure 6.13 for comparison purposes with Figure 6.14. It is clearly visible that in general the temperature across the entire two spans is higher for the buoyancy driven case. The temperature below the shelves is also more homogeneous compared to the first case. When the velocity vector plots (Figure 6.15 – replicated from Figure 6.7 for comparison to Figure 6.16) are compared, a difference can immediately be seen in the second span, where the velocity is lower compared to the combination of wind and buoyancy driven case. In the buoyancy driven flow case, the cell in the first span rotates counter-clockwise right above the left shelve at the centre of the shelve. For the combination case, a smaller counter-clockwise cell is formed towards the right side of the first shelve, and a clockwise rotating cell towards the roof on the left side. The velocity of the air exciting the greenhouse from the first ventilator for the buoyancy driven case is also lower compared to the combination case. The velocity underneath the shelves for the buoyancy driven is also lower compared to the combination case, and a small counter-clockwise rotating cell forms right between the shelves on the ground.

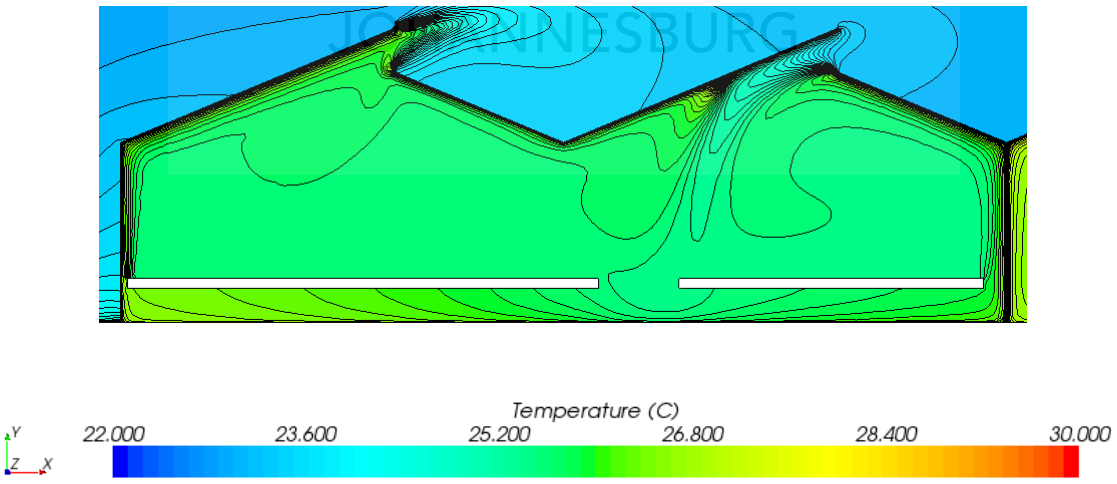

Figure 6.13: Temperature contour plot for a combination of wind and buoyancy driven flow

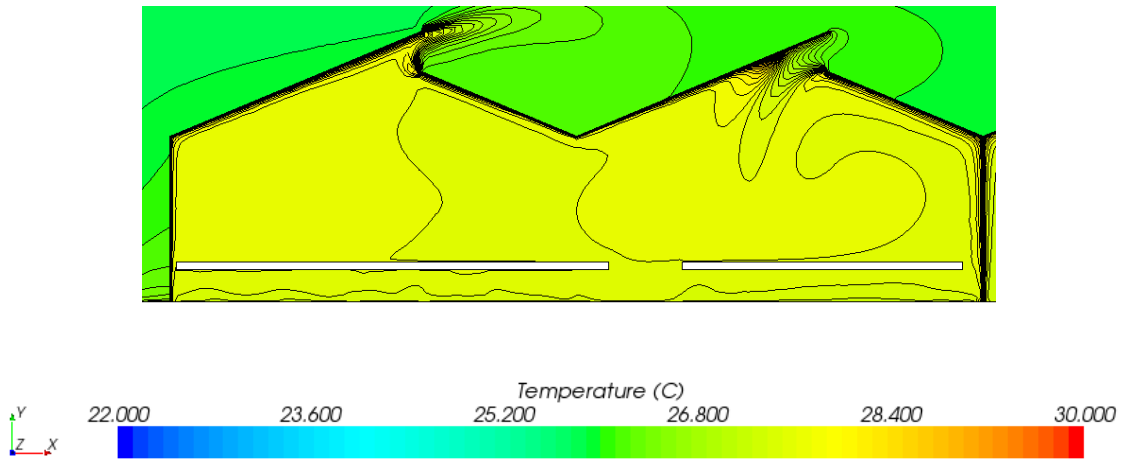

Figure 6.14: Temperature contour plot for buoyancy driven flow only

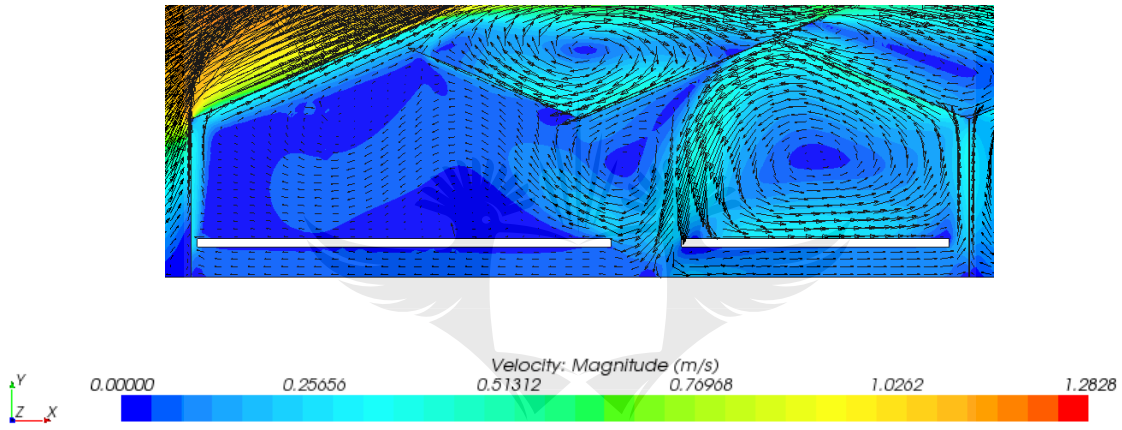

Figure 6.15: Vector and velocity contour plot for a combination of wind and buoyancy driven flow

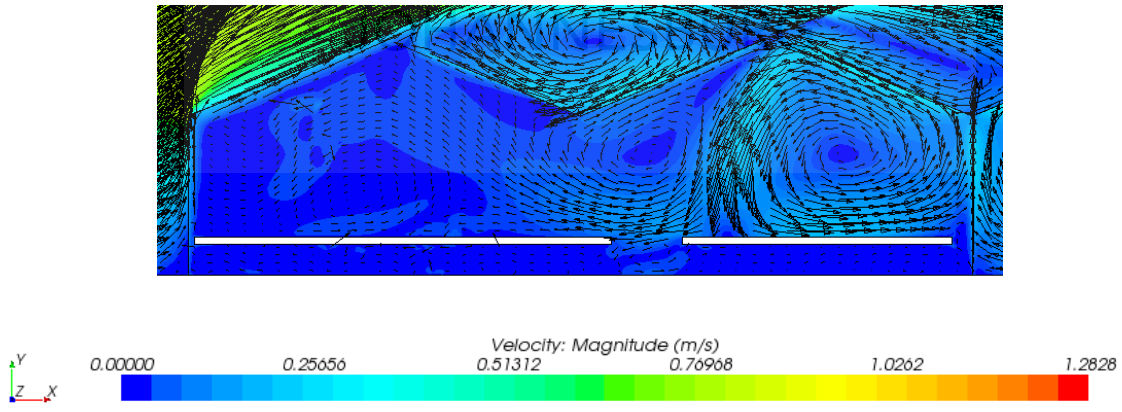

Figure 6.16: Vector and velocity contour plot for buoyancy driven flow only

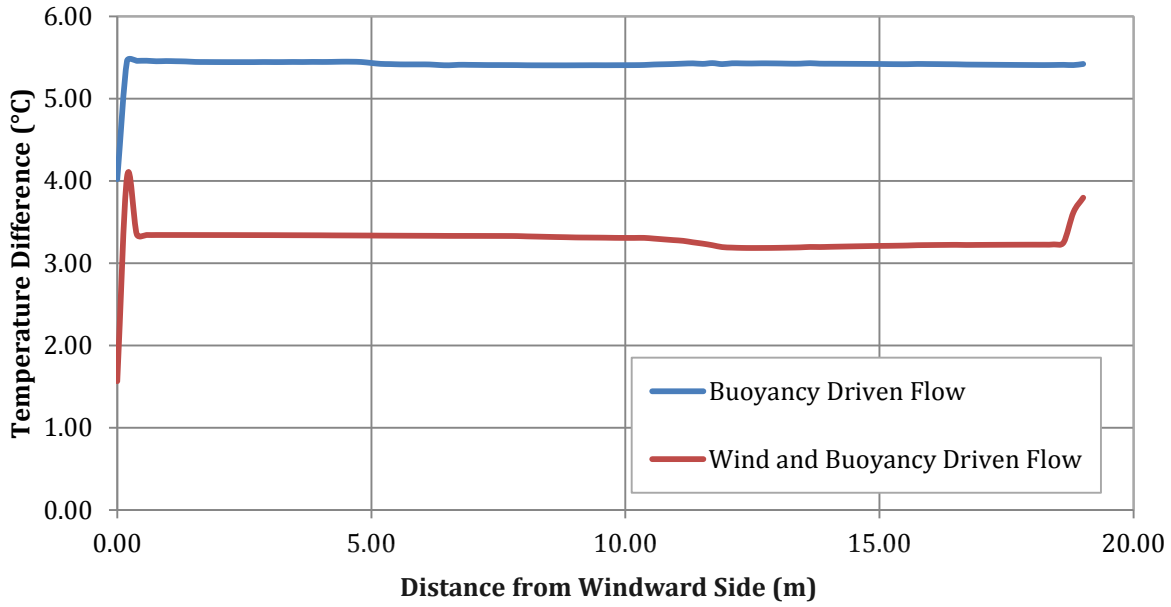

Figure 6.17: Comparison of temperature difference between inside and outside of greenhouse at plant level for buoyancy driven flow and a combination of buoyancy and wind driven flow

The temperature differences between inside and outside at plant level are compared for the two cases in Figure 6.17. For the buoyancy driven flow only case, a temperature difference of approximately 5.5°C is observed throughout the entire cavity. The combination of wind and buoyancy driven flow exhibits a slightly cooler greenhouse, with a temperature difference of about 3.4°C, with a slight drop at 12m to a temperature difference of 3.2°C. The temperature difference becomes larger in the vicinity of the plastic partition at approximately 18.8m, from 3.25°C to 3.79°C due to the high velocity of the air moving up against the plastic partition. The sharp increase in temperature difference adjacent to the left wall for both cases is due to the gap left between the left wall and the bench. Once again, the air has a higher temperature between the bench and the wall in this region for the combination case compared to the buoyancy driven flow only case.

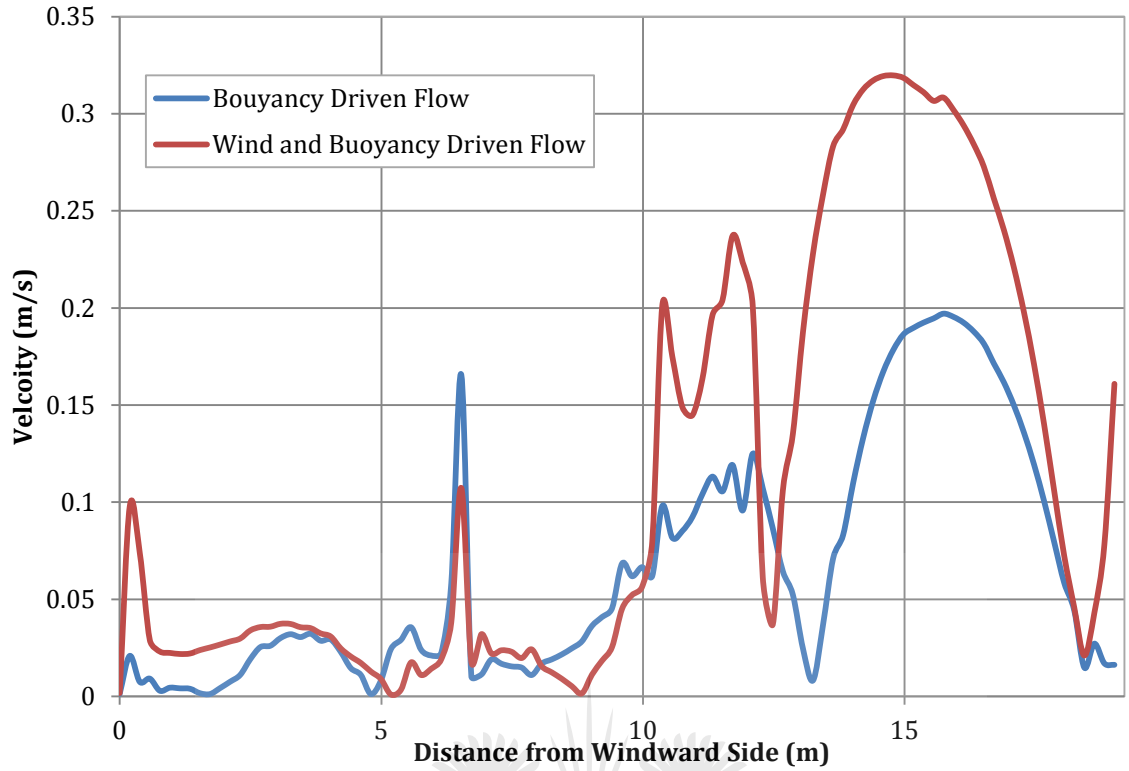

Figure 6.18: Comparison of velocity distribution at plant level for buoyancy driven flow and a combination of buoyancy and wind driven flow

The velocity distribution at plant level is compared for both cases as indicated in Figure 6.18. Generally, the velocity is higher throughout the greenhouse for the combination case compared to the buoyancy driven case. The maximum velocity is reached above the second shelve for both cases. The maximum velocity reached in the combination case is about 0.31m/s, whereas the maximum velocity for the buoyancy driven case is approximately 0.19m/s. The velocity in the first half of the second span (from 10m to 18m) is also higher for the combination case than the buoyancy driven case.

6.5 Conclusion

The objective in this chapter was to obtain confidence in a two-dimensional numerical model of a full-scale greenhouse. This chapter numerically validated a two-dimensional numerical model of a full-scale greenhouse found in the literature [49]. Results show a reasonably good agreement between the velocity and temperature contour plots when the two east spans were compared (Refer to Figure 6.1). The temperature and velocity distributions at a height of 1m were also compared, and found to be reasonably similar, except for small differences such as the in the west spans and near the glass walls. Certain parameters such as the length, position of the shelves and the size of the roof ventilators were all assumed, and could be responsible for the discrepancies between the current and literature results. It is therefore concluded that

confidence has been established in the two-dimensional numerical model developed in this chapter. The model was also used to investigate buoyancy driven flow only which was not presented in the literature [49]. Results showed that the greenhouse is significantly warmer inside when no outside wind was present. An average of 5.4°C temperature difference was noted for buoyancy driven flow only, whereas an average of 3.3°C difference was noted for the combined case. A combination of wind and buoyancy driven flow will be more effective to cool the greenhouse even in a case where only roof ventilators are considered.

The next chapter, Chapter 7 discusses the experimental and numerical validation of a reduced-scale greenhouse.

CHAPTER 7

Experimental and Numerical Validation of a Reduced Scale Greenhouse

7.1 Chapter Review

Some of the previous chapters established the foundations of the experimental work to be conducted in this chapter. A background has been given on reduced scale modelling and visualization techniques. The purpose of this chapter relates to the objective as set out in chapter 1 - to obtain a qualitative comparison of temperature fields and flow patterns against a CFD model using a reduced-scale model of a multi-span greenhouse. The scale model greenhouse will be subject to buoyancy driven flow only. The development of both the reduced-scale experimental greenhouse model and the numerical model is explained in this chapter. The experimental setup and measurement of the relevant parameters will also be presented. This chapter relates to the research question of determining if it is possible to obtain a qualitative comparison of experimental temperature fields and flow patterns against a CFD model using a reduced-scale model of a multi-span greenhouse.

7.2 Full Scale Greenhouse

The greenhouse that will be investigated is based on the same full-scale greenhouse that was used in chapter 6 to validate the two-dimensional model. It is based on a 2500m^2 four -span greenhouse found in the literature [49], which is located near Angers in the west of France. The greenhouse was covered with 4mm thick horticultural glass and equipped with continuous roof vents on both sides of each span. The greenhouse was separated into two compartments by a plastic central partition. Figure 7.1 shows the dimensions of the greenhouse, with the roof vents open toward the leeward side. The total length of the greenhouse was 68m, and the width was 34.8m.

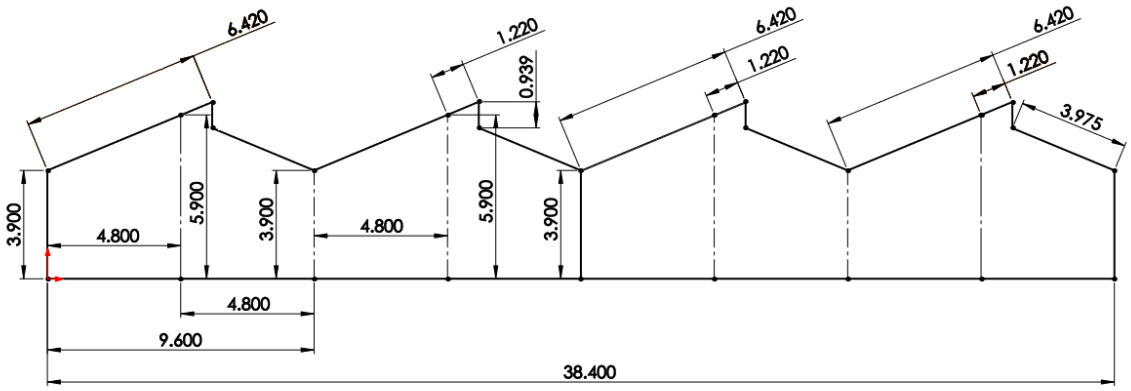

Figure 7.1: Dimensions of Full Scale Greenhouse [49]

7.3 Experimental Setup

7.3.1 Scale Model

The reduced scale experimental model was constructed from 5mm clear acrylic Perspex sheets. Initially the model contained four spans, but due to space limitations in the testing area, only two spans were finally used in the experiments. The panels were cut using a CNC machine, glued together, and mounted on 16mm Medium Density Fibreboard (MDF). To assist with visualization techniques, the MDF board was painted black. The dimensions of the scale model greenhouse (1:32) constructed for this experimental research are shown in Table 7.1.

Table 7.1: Dimensions of Scale Model Greenhouse

Parameter [m]	Full Scale	1/32 Model
Width of one span	9.6	0.3
Total Width	19.2	0.6
Ridge Height:	5.9	0.18
Eaves Height:	3.9	0.12
Length of Greenhouse	34	1.06
Roof Length	3.98	0.12
Roof Vent	1.22	0.04
Side Vents	0.9	0.03
Height of Side Vents from Ground	0.6	0.02

The scale model tested can be seen in Figure 7.2. Each span was equipped with two continuous roof ventilators with the same length as the greenhouse. The vents were constructed to give a maximum opening angle of 45°. The vent mechanism on the front and back of the greenhouse is also visible in Figure 7.3.

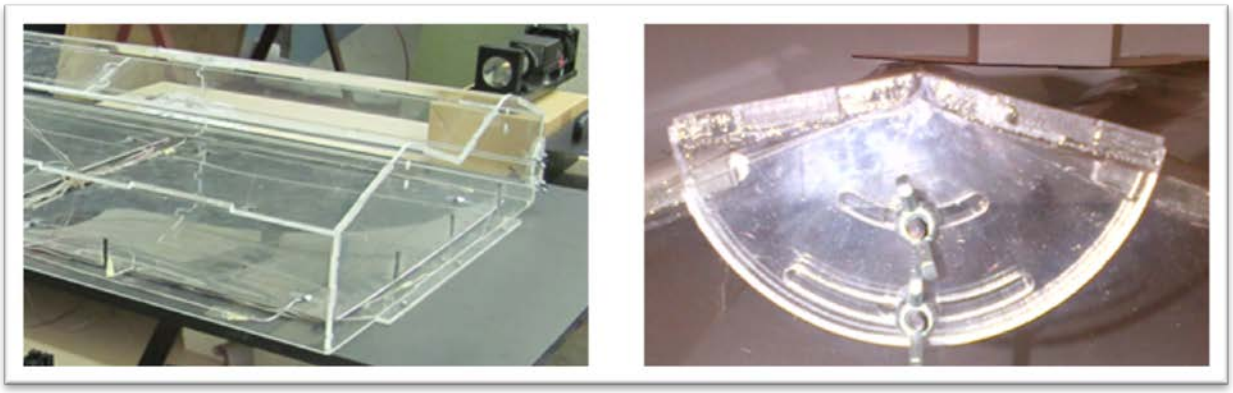

Figure 7.2: Perspex Greenhouse and Ventilator Mechanism

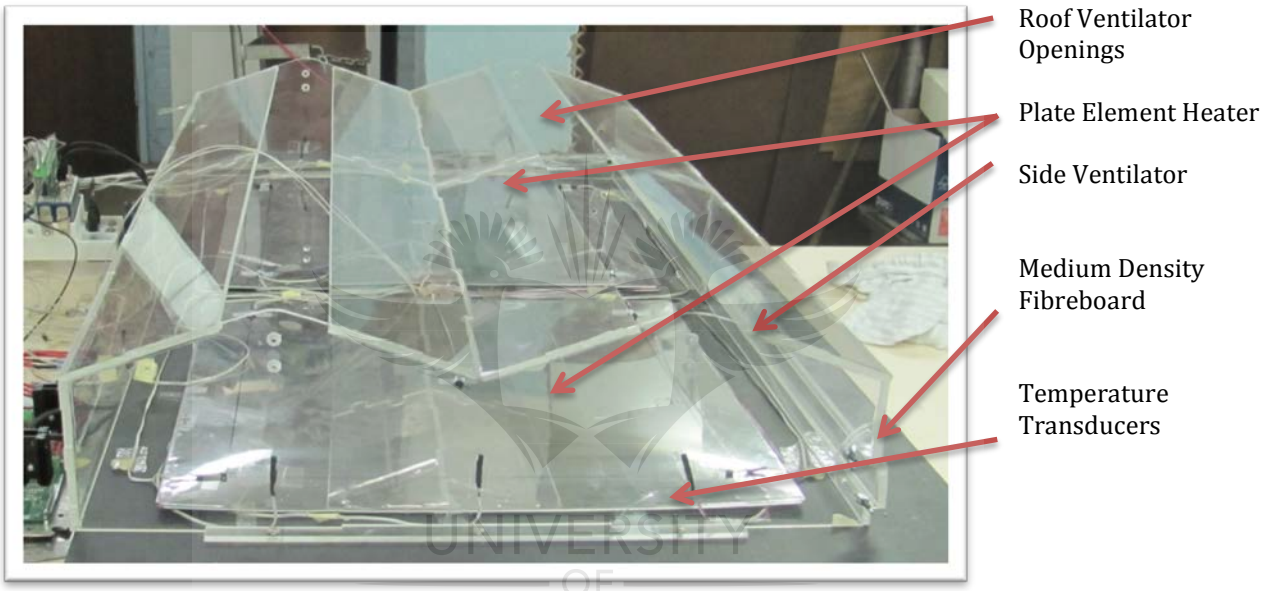

Figure 7.3: Perspex Scale Greenhouse without the Roof Ventilator Flaps

To create buoyancy driven flow, two flat plate heaters of 400W each (500mm x 500mm) were mounted on the floor of the scale model. Temperature measurements were obtained using 2-Terminal IC temperature transducers (Type AD590). These particular temperature sensors were chosen due to their appropriate cost, and their usefulness in remote sensing applications.

A hole was drilled in the centre of the MDF board, between the two plate heaters, which was used to direct all the sensors and power cables of the elements into the model. Five of the temperature sensors were taped with aluminium tape onto each element. The readings from these sensors were used in the control system to control the output of each element. The remaining sensors were taped against the Perspex walls of the greenhouse. One sensor was kept unattached in order to measure the ambient temperature and to obtain the vertical temperature

profile inside the scale model. A summary of all the equipment used in the reduced scale model experiments is shown in Table 7.2. The experiments were performed in a room without windows, to ensure minimal heat gains and a constant ambient temperature.

Table 7.2: Summary of Equipment used in Experiments

Equipment	Type	Function in Experiments
HD Video Camera	JVC Everio	Capturing of Flow Patterns
Software	Labview	Control System for Heaters
Temperature transducers	AD590	Temperature measurement
Laser	Krypton	Light sheet for flow visualization
Plate Element Heaters	Hi-TechElements	Heating of greenhouse floor
Data Acquisition System	Labview	Temperature recordings

7.3.2 Temperature Sensors

The temperature sensors selected for measuring temperatures were temperature transducers, type AD590. This type of temperature transducer is particularly useful in remote sensing applications, as it is relatively insensitive to voltage drops over long lines. Some of the specifications are shown in Table 7.3.

Table 7.3: Temperature Transducer Properties [162]

Temperature Range	**-55 – 150**	**°C**
Calibration error @ 25°C	±0.5	°C
Absolute Error (Over rated Performance Temperature Range)		
Without External Calibration Adjustment	±1.7	°C
With ±25°C Calibration Error Set to Zero	±1.0	°C
Repeatability	±0.1	°C

The temperature transducers were all calibrated by submerging them into transformer oil and measuring the output at two different temperatures. The first measurements were taken at room temperature (24.4°C), and the second set of measurements was taken by heating the oil to an elevated temperature (95.1°C), and capturing the output currents again. The outputs for each set of measurements were transferred to an Excel file. Several readings were recorded per second for each sensor, and the average of these readings was calculated in the Excel spreadsheet for both the minimum and the maximum temperature. The adjustment required to convert the voltages to temperatures were calculated and programmed into the data acquisition

program. This was considered adequate as only temperature differences were used in experiments conducted.

Figure 7.4: Calibration of Temperature Transducers

A total of 32 temperature transducers were used in the scale model. The number used was limited by the data acquisition module. Once calibrated, the temperature transducers were carefully fastened in various locations inside the greenhouse. The layout of the temperature transducers in the greenhouse scale model is shown in Figure 7.5.

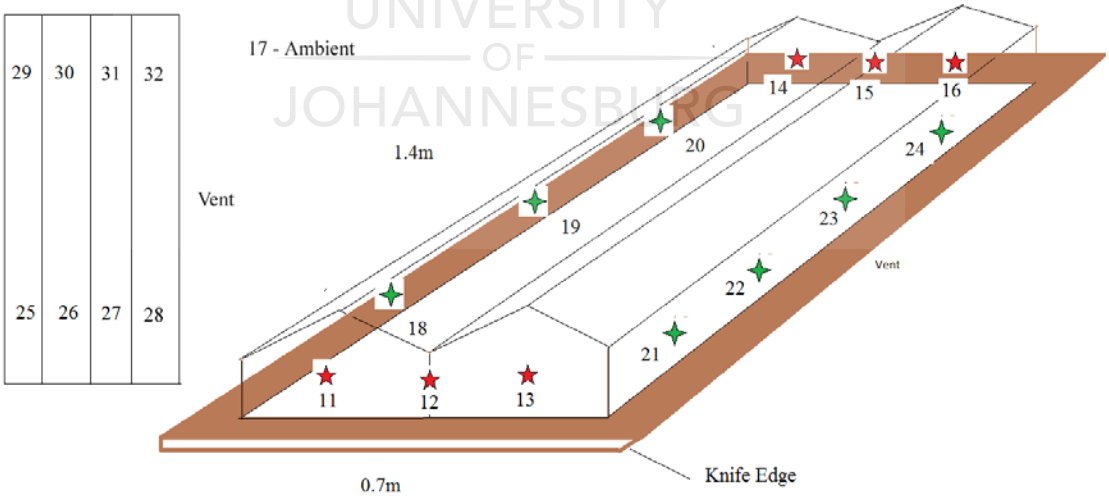

Figure 7.5: Temperature Transducer Positions

7.3.3 Helium Bubble Generator

The helium bubble generator considered for this study is shown in Figure 7.6. This specific model is the SAI Modified Model 5 Console purchased from Sage Action Inc [163]. It generates helium-filled neutrally buoyant bubbles of uniform size for airflow visualization.

Figure 7.6: Helium Bubble Generator System

These bubbles are able to follow streamlines in the flow, and are exceptionally durable. The bubble size can be adjusted, depending on the application and light conditions. The specific weight and rate of generation of the bubbles can also be adjusted. The bubbles are able to trace complicated flow patterns in air without bursting or impacting on objects within the flow field. Conventional lighting can be used to capture the flow patterns. A modulated arch lamp is also available for high-speed flows. The bubbles are manufactured using non-toxic and non-corrosive constituents at room temperature.

This specific model operates using two Plug-in Heads, each driving a "Mini-vortex Filter". The combination of these two components generates the bubbles. The purpose of the mini vortex filter is to remove all the bubbles that are not of the correct size and weight. The plug in head and vortex filter are shown in Figure 7.7.

7.3.4 Control System and Data Acquisition

A program was written by JAD Systems [164] using Labview Software. The program was used to control the temperature of the heaters using pulse width modulation. The software was also combined with a Labview CDAQ data acquisition module to record the temperatures during the tests. Figure 7.8 shows a photo taken of the power supplies for the heaters and the CDAQ data acquisition system.

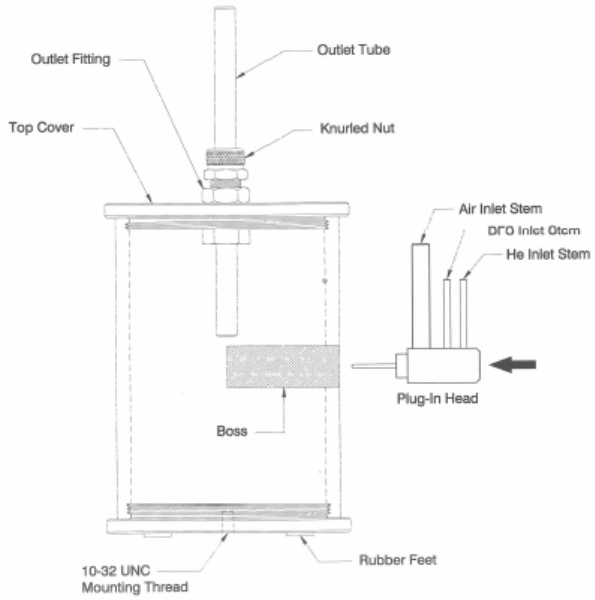

Figure 7.7: Mini Vortex Filter and Plug-in Head [165]

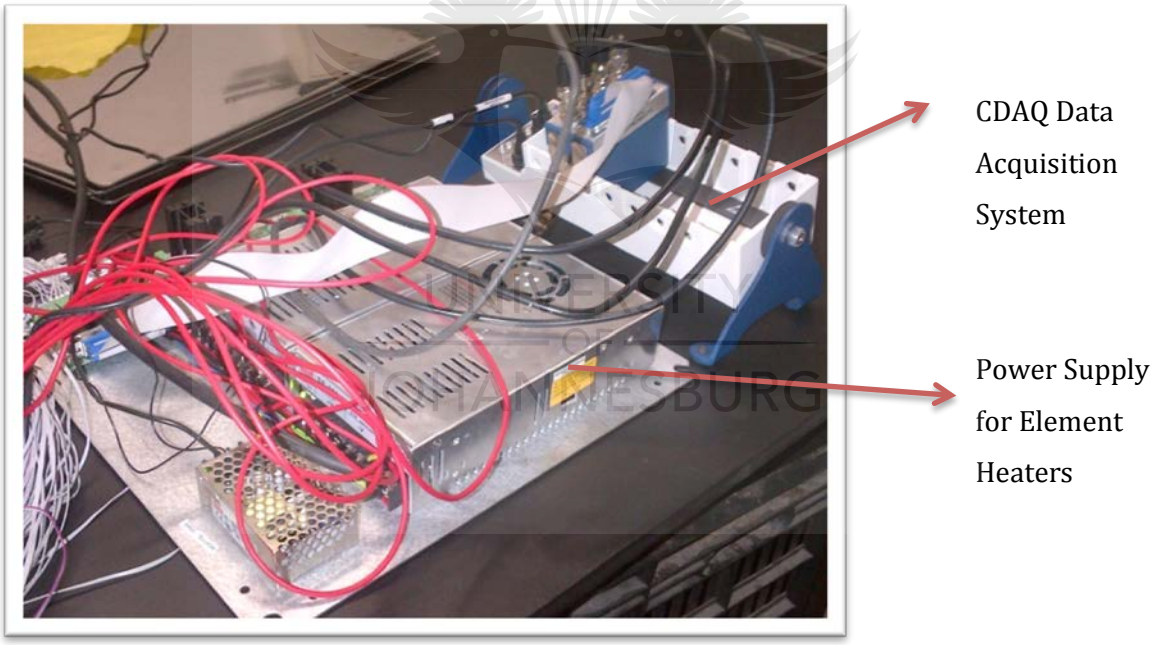

Figure 7.8: CDAQ Data Aqcuisition System and Power Suppy for Element Heaters

7.3.5 Flow Visualization

Several methods were tested in an attempt to visualize the flow patterns inside the scale greenhouse. Initially, neutrally buoyant bubbles were used. The bubbles were produced using the helium bubble generator (SAGE Action Inc). Unfortunately the velocity of the bubbles entering the greenhouse cavity was too high, which influenced the buoyancy generated flow

patterns. Lighting also proved to be problematic. For helium bubble testing to be successful, the environment must be as dark as possible. This was rather difficult to achieve inside the laboratory with the settings used. No definite flow patterns could be identified. Some initial results of the helium bubble generator testing are shown in Figure 7.9. The flow patterns observed was formed by the stream of bubbles entering through the floor of the greenhouse.

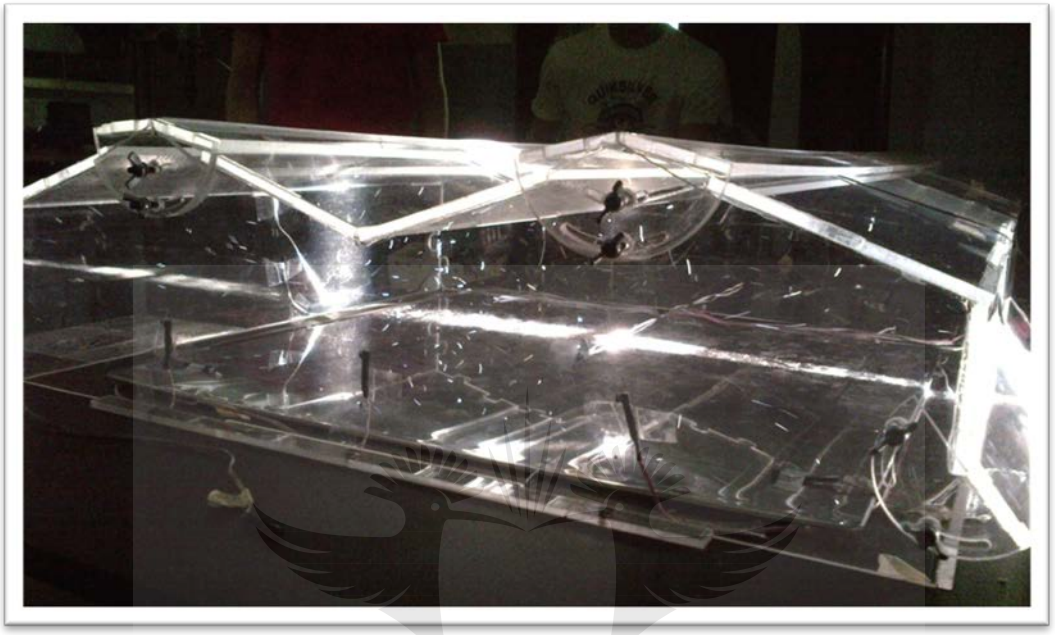

Figure 7.9: Helium Bubble Flow Visualization

A theatre fog machine was also investigated for rendering the flow patterns. This method was also unsuccessful, as the temperature of the fog entering the greenhouse was too high. The fog also dissipated quite quickly, filling the entire greenhouse with a "cloud", after which no definitive flow patterns could be observed. The fog machine attempt is shown in Figure 7.10.

Figure 7.10: Theatre Fog Machine Flow Visualization

The most successful method employed was lighting wicks made of office string, extinguishing the flame, and then using the smoke from the smouldering wicks to visualize the developing flow patterns. Wicks were suspended from the inside of the roof of the greenhouse at several locations. A green 1000 mW laser (Wicked Lasers - Krypton Spyder) with a 45 degree lens was used to illuminate the smoke. It was later found that the suspended wicks were still too hot, and also influenced the flow patterns to some extent. An example of the visualisation obtained using the smoke from the suspended wicks and lasers are shown in Figure 7.11.

Figure 7.11: Smoke from Suspended Wicks Flow Visualization

Another approach was tried to release the smoke inside the scale model through a hole in the bottom of the greenhouse. A large combined wick consisting of several pieces of office string glued onto a piece of wood with a glue gun, were created as shown in Figure 7.14. Several wicks were combined and inserted into a funnel (Figure 7.13), which were positioned underneath the hole containing the wires from the temperature transducers. This method was more effective as

the smoke was allowed to cool down as it enters the greenhouse from below before it reached the laser sheet. This was the chosen method for flow visualization. The entire MDF board was insulated along the bottom using thick sheets of polystyrene to ensure minimal heat loss through the bottom of the greenhouse.

Figure 7.12: Wick used for Smoke Generation

Figure 7.13: Funnel used for inserting smoke

The JVC Everio Full HD camcorder (Model Number GZ-HM445SAS) was used to capture the flow patterns visualized by the smoke. The camera recorded in high-definition, and night mode was found to give the best results in terms of capturing the smoke in low-light conditions.

7.4 Application of Dimensional Analysis and Similitude

The purpose of the reduced scale experimental model was to observe/measure the flow patterns and temperature distribution inside the greenhouse. The results were then used to qualitatively validate a numerical model of the same greenhouse.

In order to meet the geometric similarity requirements, a 1/32 scale replica of the greenhouse was built out of Perspex as discussed in the previous section. A summary of the dimensions of the prototype and scale model are shown in Table 7.1.

The important values used to calculate the dimensionless parameters are summarized in Table 7.4. As already mentioned when evaluating buoyancy-driven flow, the Grashof number is a key parameter to consider. If fluids other than air is used it is imperative to include the Prandtl number in the evaluation through the Rayleigh number (Ra = Gr x Pr).

Table 7.4: Important Definitions used in Calculating Dimensionless Numbers

Reynolds Number	**Hydraulic room diameter [140]**
Grashof Number	Height of Room
ΔT – Temperature Difference	Difference between Average inside and room temperature
Air Properties	Evaluated at Film Temperature
Buoyancy Velocity	Height of room (Ridge Height)

The calculated dimensionless parameters are shown in Table 7.5 for various temperature differences between the inside and outside of the scale model greenhouse. From this table it is seen that the critical Reynolds number based on buoyancy velocity, 2.3×10^3 [140] is exceeded over the entire temperature range (from a difference of 10°C to 80°C between inside and outside). As already mentioned in Chapter 3, research suggests for buoyancy-driven flow it is sufficient to achieve critical values of the Grashof number when air is used as the working fluid as stated by Etheridge for flow in buildings [141]. A critical value of the Grashof number in the range of 10^6 to 10^9 is proposed using the height of the room as characteristic length. The Grashof numbers for all the chosen temperature differences were found to be in this region for the current experiment.

Table 7.5: Dimensionless numbers

Scale Model	1/32		
Ambient Temperature	20	20	20
Temp of Heaters	30	60	100
Film Temperature	25	40	60
G	9.81	9.81	9.81
Beta	0.0033725	0.0032	0.003
Delta T	**10**	**40**	**80**
Height of Ridge (m)	0.18	0.18	0.18
Hydraulic Diameter	0.77	0.77	0.77
Kinematic Viscosity	1.56E-05	1.70E-05	1.89E-05
Buoyancy Velocity	2.44E-01	4.75E-01	6.51E-01
Reynolds Number (based on buoyancy velocity)	1.21E+04	2.16E+04	2.65E+04
Grashof using room height	7.95E+06	2.54E+07	3.84E+07
Prandtl Number	7.13E-01	7.11E-01	7.09E-01
Rayleigh Number	5.67E+06	1.81E+07	2.73E+07

7.5 Experimental Procedure

The scale model experimental greenhouse was investigated for buoyancy driven natural ventilation only. All the results reported in this section were obtained under conditions where steady state was the aim. By adjusting the temperature of the plate heaters, buoyancy driven flow was induced due to the temperature difference inside and outside the scale model. Variations in external or ambient temperature were not accounted for, although it was tested for and found not to vary extensively during the experiment. The following procedure was followed for each of the experiments performed:

7.5.1 Preparation:

- The HD video camera was positioned so as to be at the correct level and tested to ensure the focus was adequate
- A new set of wicks (Figure 7.12) was prepared

7.5.2 Steps:

1) The temperatures of element heaters were set to the required value, and data recording was activated
2) Probe 17 was kept outside the greenhouse to measure the ambient temperature
3) When temperatures on the walls inside the greenhouse has stabilized (probes 11-16 and 18-32 - Figure 7.5), probe 17 was positioned inside the greenhouse
4) The funnel containing the wicks were placed underneath the greenhouse covering the hole at the centre of the greenhouse floor
5) Flow patterns were captured using the video camera, and the time according to the control system was noted
6) Notes were taken of flow patterns inside –direction, position, smaller cells forming in corners
7) Appropriate measurements at 1cm increments were taken inside the greenhouse using probe 17 through the roof ventilator of the greenhouse and recorded.

Numerous cases were investigated experimentally, but to make sure the flow regime falls in the turbulent region, tests for a temperature difference setting of 70 degrees on the plate element heaters will be discussed in more detail here.

7.6 Experimental Results

7.6.1 Flow Visualization

The results for the specific case where the element heater was set to 70°C will be discussed in more detail in this section. The particulars of this test are shown in Table 7.6.

Table 7.6: Test 70°C Details

Ambient Temperature (°C)	**18.6**
Test commenced	09:39
Quasi-steady State reached at	11:06
Video recording at steady state	11:34
Smoke inserted	11:35
Temperature probe inserted	11:51
Test concluded	13:13

Capturing the movement of the smoke graphically was challenging. Initially, the video clip was split into its respective frames. The video camera recorded scenes at 25 frames per second, but

as the video camera was set to night mode, only 2 frames per second was captured. The same frame was repeated for 12/13 frames depending on the sequence. The frames were exported from the video file using the Video to Jpeg converter from Free Studio. Some of the images are shown here, but the movement of the smoke are best viewed in the video clip itself. The video clips are available on request, and can be shared via the internet. The most prominent feature noticed in the clips is perhaps that the flow is turbulent and highly unstable. A few still images taken from the video clip are available in Appendix A.

A sketch showing the observed movement is shown in Figure 7.14. The flow patterns were constantly changing, but an overall trend could be observed. The main flow patterns that was perceived, was that of the flow moving down against the roof at the second roof vent (right side of the cavity), down the wall and towards the centre of the greenhouse along the floor, where it accelerates again upwards towards the ventilator. On the left hand side, there was a slow counter-clockwise cell, mixed with smaller eddies. The air moved down against the right wall, and moved towards the middle of the greenhouse, where it joined the flow from the left side of the greenhouse, and accelerated towards the roof.

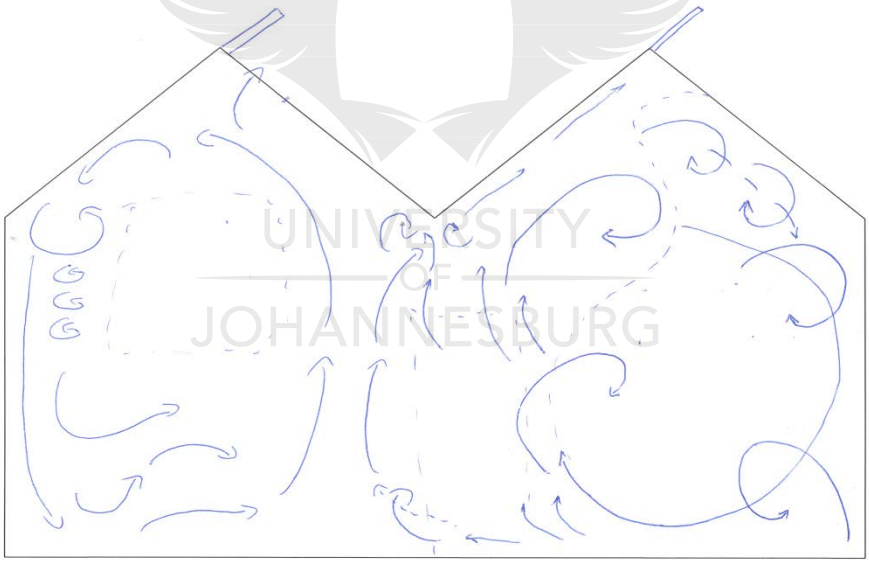

Figure 7.14: Flow Observations (Heaters 70 Degrees)

It was also attempted to deduce the velocity of the air inside the scale greenhouse from the video clips. The following method was followed:

1. A vectorised grid (seen in Figure 7.15) with the dimensions of the greenhouse was produced using *Adobe Illustrator*. The size of each square in the grid was 5mm
2. The video was imported into *Adobe After Effects*, and the grid was superimposed onto the greenhouse

3. The grid points for the corners of the greenhouse were matched to the corresponding points in the video
4. A timer was added to the video
5. The video was re-encoded to include the image, grid and time, and then split into individual frames using *DVDVideoSoft Free Studio.*
6. Identifiable smoke trails were noted in the video clip. The time on the video was used to find the image in the stills
7. The still images were used to map track the motion of the smoke (using the grid) and the time (from the timer)
8. The distances per time step (0.48 and .052 seconds) were recorded along with the location of the smoke trail in the image
9. If the smoke trail moved in the X and Y directions then Pythagoras's Theorem was used to calculate the distance moved

Although this method was not too accurate, it did yield an average velocity of approximately 0.06m/s. This velocity was too low to be measured by the available measuring equipment.

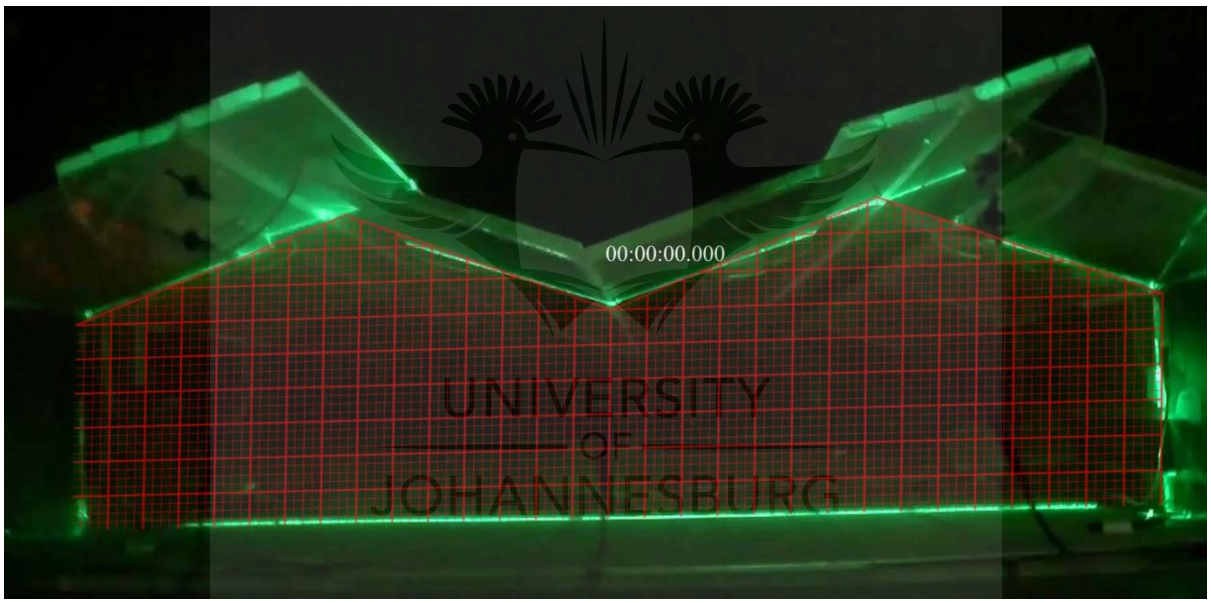

Figure 7.15: Vectorized Grid Superimposed onto Greenhouse in Videoclip Still Images

The three-dimensional effects are clearly visible in a set of frames taken in the longitudinal direction from a test with the heaters set at 40°C. The frames (stills) were extracted using a video to JPEG converter from *FreeStudio,* and exported at 10 frames per second. Figure 7.16 to Figure 7.19 shows consecutive images taken from the video clip, with the camera facing the longitudinal section of the greenhouse. White streaks of smoke are clearly visible as it enters the greenhouse from the funnel at the bottom centre, and then moves in various directions.

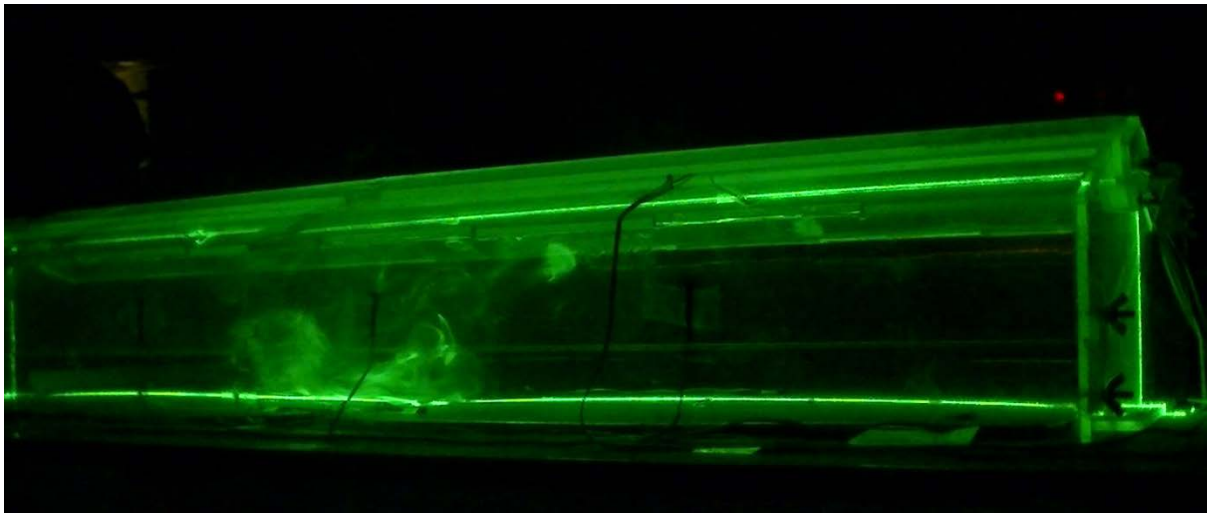

Figure 7.16: Longitudinal View - Frame 6

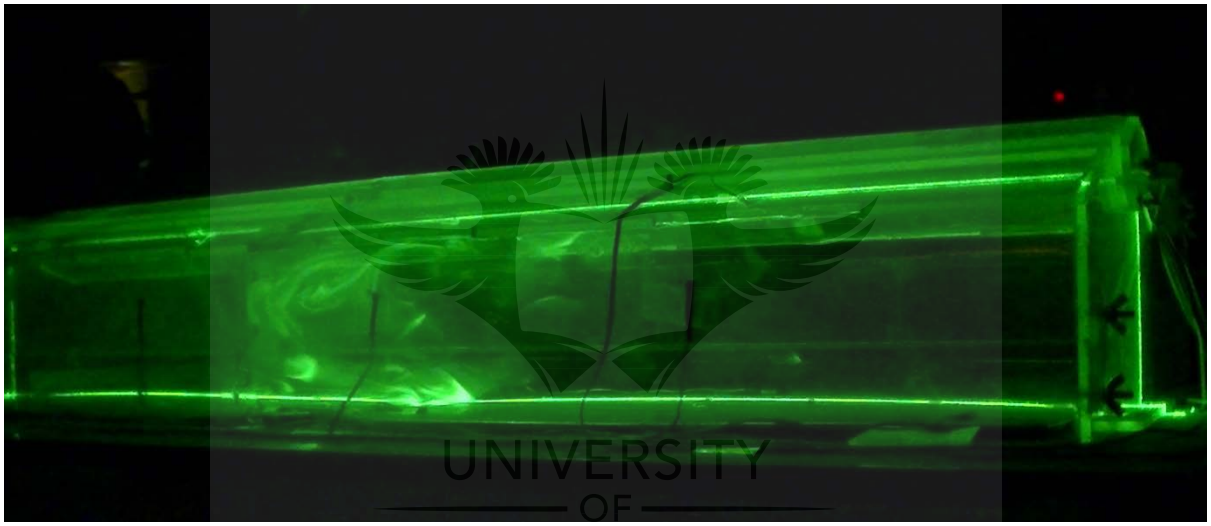

Figure 7.17: Longitudinal View - Frame 7

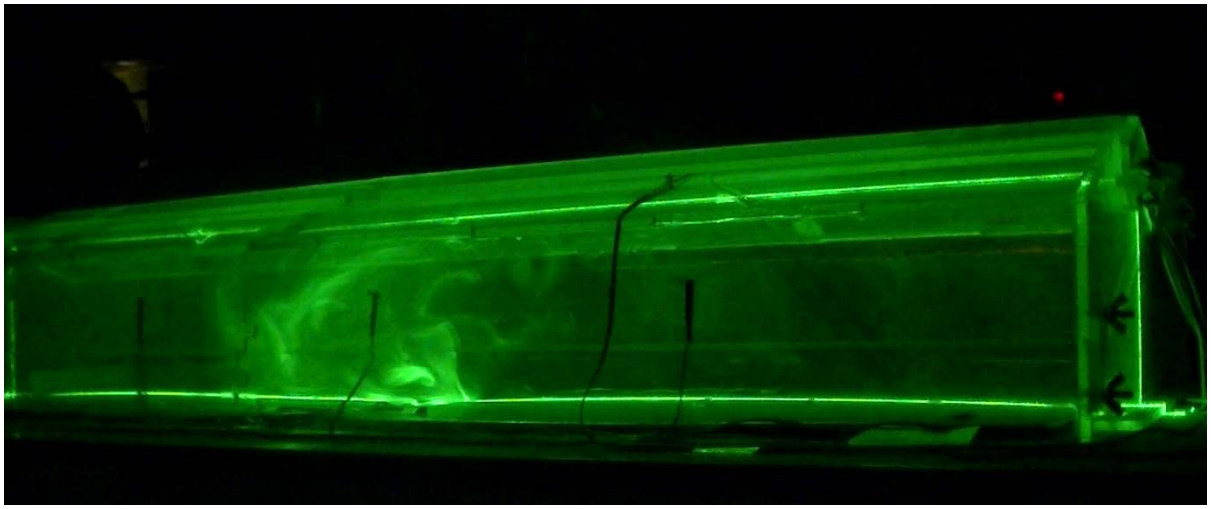

Figure 7.18: Longitudinal View - Frame 8

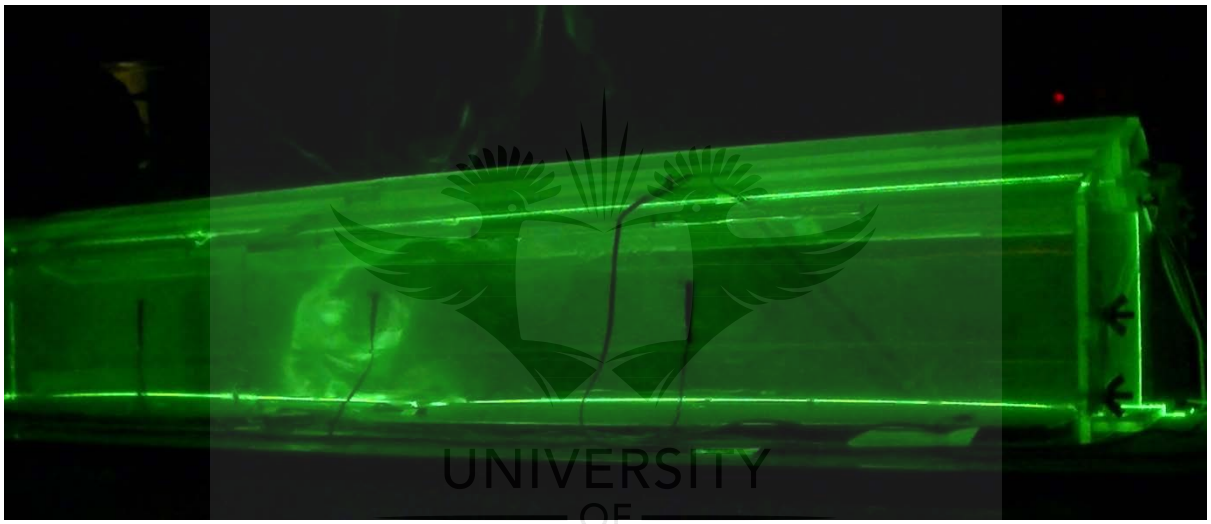

Figure 7.19: Longitudinal View – Frame 9

7.6.2 Temperature

It was noted that the temperature distribution was not uniformly distributed on the plate heaters, therefore the actual temperatures measured for the probes on the heaters is shown in Table 7.7. This was measured once steady state was reached. The probe positions, orientation and measured temperatures are graphically shown in Figure 7.20. The colours seen in this Figure was generated with the CFD software, using the mapped vertex function (this will be explained later). It is can clearly bee seen that for the first heater (in the front of the greenhouse), the temperatures on the close to the front are slightly higher compared to the back. For the second heater (back of greenhouse), the front top corner is hotter compared to the back top corner, and the back top corner are almost 14°C lower compared to the back bottom corner. The centres of the two plates are also at different temperatures; a difference of about 5°C is noticed.

Table 7.7: Temperature probes on element heaters

Probe #	Temperature (°C)	Probe #	Temperature (°C)
1	82.0	6	60.6
2	74.6	7	74.2
3	75.8	8	75.9
4	77.8	9	79.9
5	88.0	10	83.1

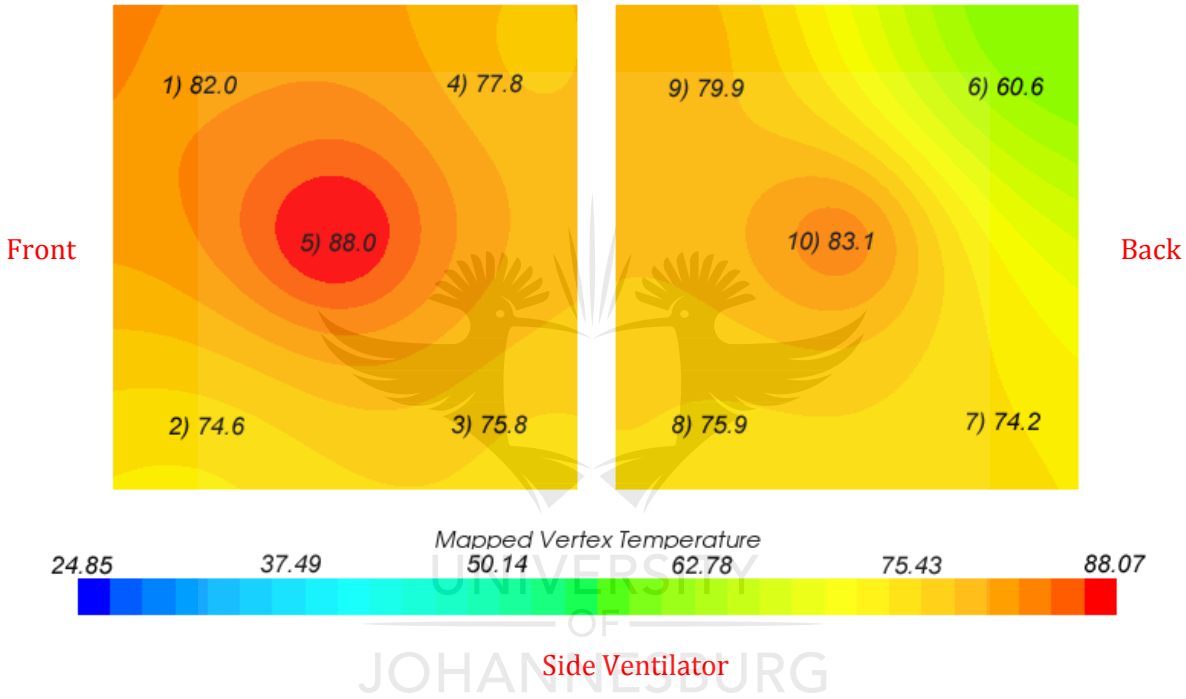

Figure 7.20: Temperature Probe Positions and Measured Temperatures

After the temperatures measured reached steady state, probe number 17 was used to measure the vertical temperature profile at increments of approximately 1cm inside the greenhouse through the roof ventilators. The results for the left and right spans are tabulated in Table 7.8 and graphed in Figure 7.21. There is a clear difference between the two vertical profiles for the right and left side of the reduced scale model greenhouse. The left side shows a decrease from 60°C to 50.7°C in the first 1cm above the plate. A further decrease is noticed to about 47.7°C, after which the temperature remains approximately constant. A small increase in temperature to 50.2°C occurs at 10cm above the plate, and further increases to 52.3°C at 13cm above the plate. The temperature reduces to 47.4 at the roof ventilator entrance. On the right side of the greenhouse, the temperature decreases from 65°C to 46.7°C in the two centimetres above the element heater, after which the temperature remains relatively stable up to the exit at the roof

ventilator, with a slight increase to 47.4°C. The reason for the more stable vertical temperature profile can be attributed to the temperatures on the left side of the heater; the front and back of the heater on the left side has a temperature difference of less than 1°C.

Table 7.8: Vertical Temperature Profiles for 70°C Case

LEFT SPAN			RIGHT SPAN		
Increment	**T (°C)**	**Time**	**Increment**	**T (°C)**	**Time**
On the plate	59.7	11h51-12h00	On the plate	65.1	12h35-12h40
1cm above plate	52.0	12h00-12h05	1cm above plate	50.7	12h40-12h45
2cm	49.7	12h05-12h08	2cm	47.7	12h45-12h49
3cm	49.1	12h08-12h11	3cm	46.5	12h49-12h51
4cm	47.7	12h11-12h13	4cm	46.3	12h51-12h53
5cm	47.9	12h13-12h15	5cm	46.1	12h53-12h55
6cm	47.9	12h15-12h18	6cm	46.3	12h55-12h57
7cm	48.0	12h18-12h20	7cm	46.2	12h57-12h59
8cm	48.3	12h20-12h22	8cm	46.4	12h59-13h01
9cm	48.5	12h22-12h24	9cm	46.4	13h01-13h03
10cm	50.2	12h24-12h26	10cm	46.5	13h03-13h05
11cm	51.6	12h26-12h28	11cm	46.9	13h05-13h07
12cm	52.0	12h28-12h30	12cm	47.2	13h07-13h09
13cm	52.3	12h30-12h32	13cm	47.5	13h09-13h11
At the exit	48.1	12h32-12h34	At the exit	47.4	13h11-13h13

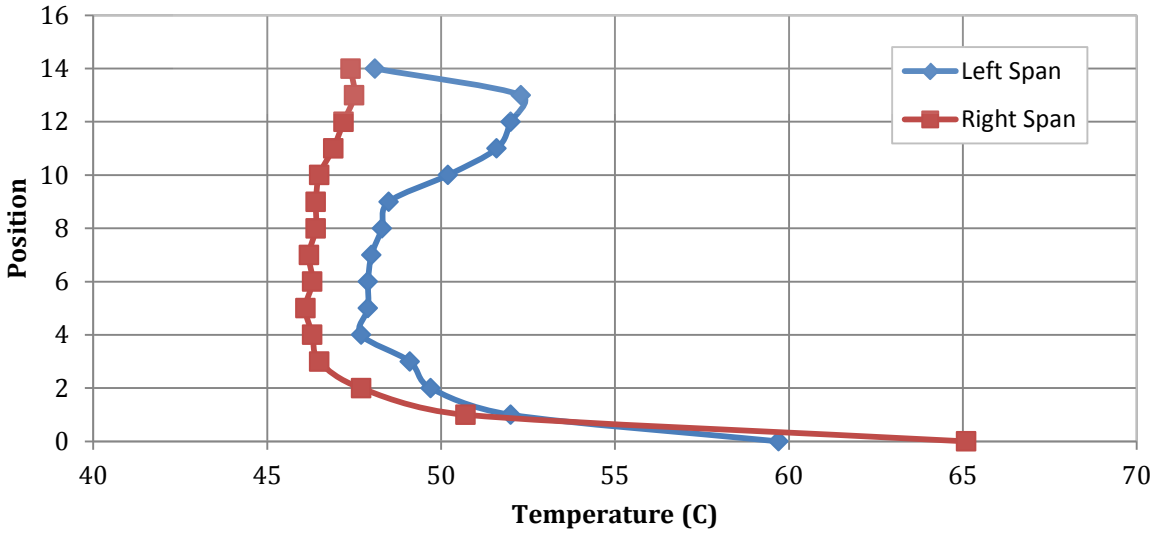

Figure 7.21: Vertical Temperature Profiles for Left and Right Spans

The turbulent nature of the flow is to some extent noticeable in the unsteadiness of the measurements taken by the probes mounted onto the walls of the scale greenhouse. This is shown for a few seconds for a single probe in Figure 7.22. The probes were not exactly stuck right onto the wall, but protruded into the flow by a perhaps millimetre or less. The turbulent temperature measurements translate to turbulent velocity measurements through buoyancy driven flow. A graph containing all the different probe measurements is shown in Appendix B. Movement on a macro scale was also observed to be unsteady. In fact, it was extremely difficult to obtain a complete steady state in the experiments. These results similar to that shown in Figure 7.22 validate in some sense the assumption of the turbulent nature of the flow that was made in the development of the CFD models of the greenhouses in this thesis.

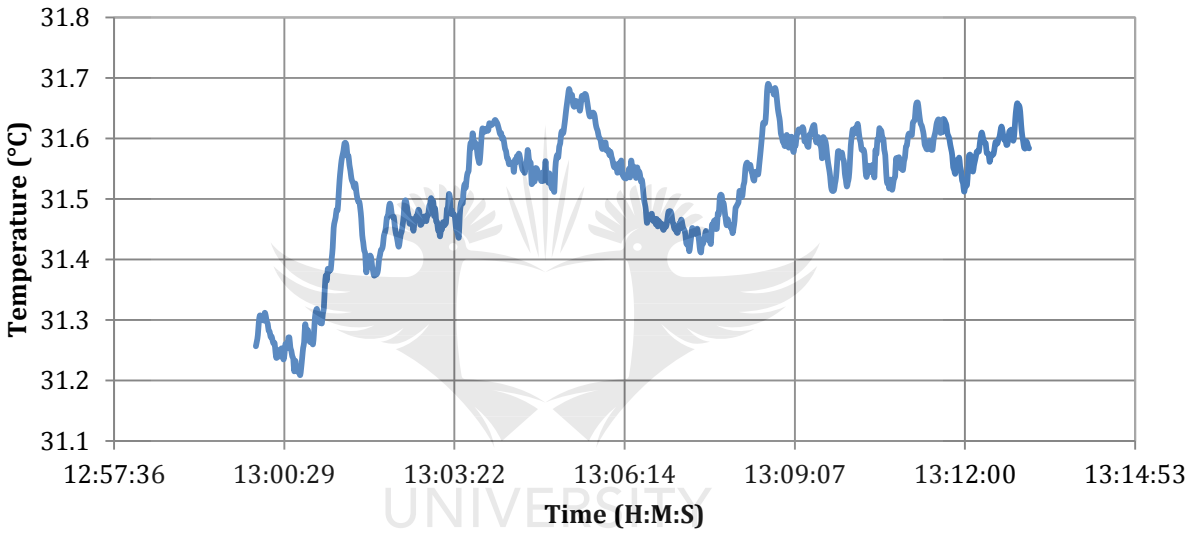

Figure 7.22: Unsteady temperature measurement

7.7 Numerical Model of Scale Model

7.7.1 Numerical Model – Mesh

The scale greenhouse in this numerical CFD model was modelled using a three-dimensional mesh. A large square mesh was created around the greenhouse scale model as shown in Figure 7.23. The mesh properties can be seen in Table 7.9.

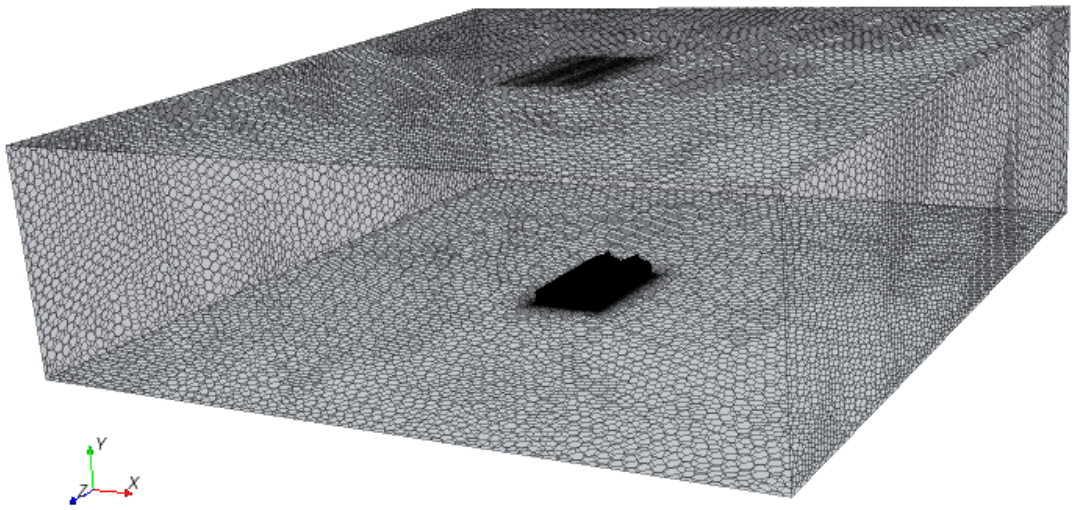

Figure 7.23: Large Control Volume around Scaled Greenhouse

The mesh was refined in several places (using a volumetric source) to ensure adequate capturing of the turbulence and flow patterns inside the cavity, and also the flow exiting the greenhouse through the roof vents. Volumetric controls are used by the software to permit mesh refinement within a user defined region, typically a box or a sphere [132]. One of the volumetric sources can be seen in Figure 7.24. The mesh was also refined adjacent to the solid walls using the prism layer mesher. The prism layer mesh is shown in Figure 7.25, and the mesh layer properties are shown in Table 7.9. A small gap of 1mm was inserted on the wall of the right span, to capture any influx through the side vent not sealing tight. This was done in an effort to simulate some experimental problems noted. The turbulence parameters are shown in Table 7.10.

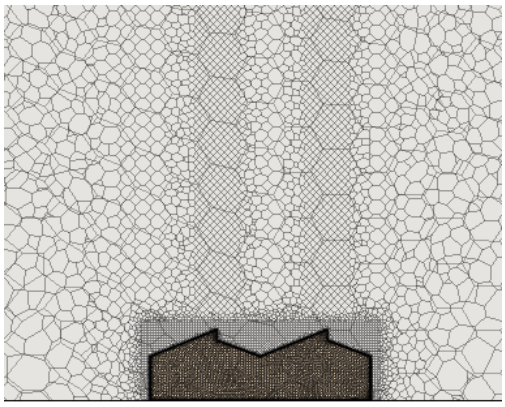

Figure 7.24: Mesh Refinement using a volumetric source

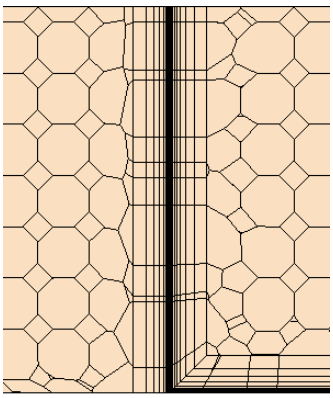

Figure 7.25: Prism Layer Mesh

Table 7.9: Mesh properties

Property	Value
Base Size (m)	0.1
Number of Prism Layers	10
Prism Layer Stretching	1.5
Prism Layer Thickness (m)	0.005
Surface Growth Rate	1.3
Surface Size (Tet/Poly Density)	
Density	1.0
Growth Factor	1.0
Blending Factor	1.0
Surface Size	
Relative Minimum Size	25%
Relative Target Size	100%
Volumetric Source (Relative Size)	
Block 1	7%
Block 2 & 3	20%
Block 4	40%

Table 7.10: Turbulence parameters

Under Relaxation Factor	**0.8**
Convergence Tolerance	0.1
Epsilon	0.0
Turbulent Viscosity (Under Relaxation Factor)	1.0

A total of four volumetric sources (shown in pink) were used to refine the mesh in certain areas, which can be seen in Figure 7.26.

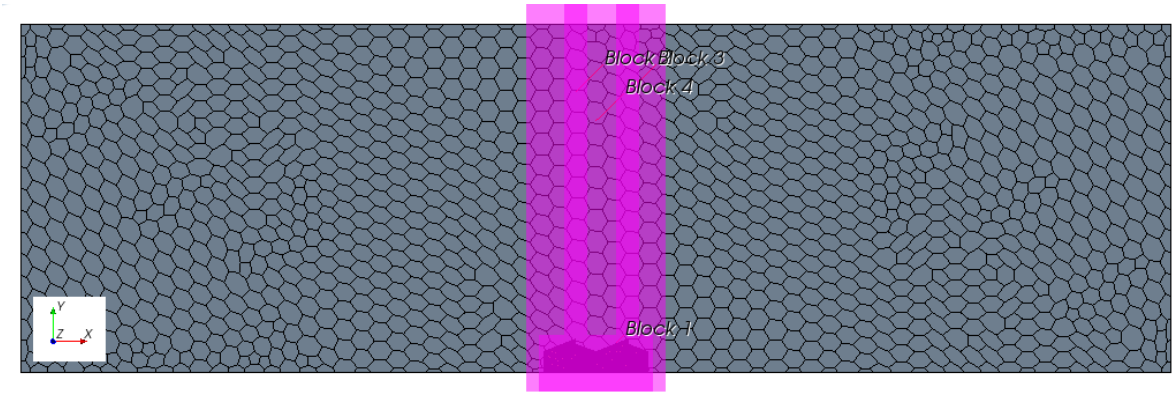

Figure 7.26: Volumetric sources used to refine mesh

7.7.2 Boundary Conditions

All the solid walls of the greenhouse model in this simulation were created as baffles with an effective thermal resistance calculated as shown in Equation 7-1 [132]:

$$\frac{1}{R} = \frac{k}{\Delta x} \qquad 7\text{-}1$$

This is different from previous simulations presented in Chapter 4 to 7 where wall temperatures were present or maintained adiabatic. This current simulation allows a more realistic situation of heat transfer through the walls. The effective thermal resistance was specified for 5mm thick perspex, with a conductivity of 0.19 W/m.K, which yielded an effective thermal resistance of 0.0263m²K/W. The boundary conditions as specified in the CFD model are summarized in Table 7.11. The sides of the large control volume were specified as conducting walls, with a temperature of 18.6°C (ambient temperature) and a heat transfer coefficient of 5000W/m²K. This was done in order ensure the control volume temperature remains constant. If any temperature gradients develop along the walls of the control volume, the heat will be removed.

Table 7.11: Boundary Conditions for Experimental CFD Model

Boundary	Type	Value
Outer Walls of Control Volume	Conducting Walls	5000 W/m²K
Walls of Greenhouse	Baffle Interfaces	N/A
Top of Control Volume	Symmetry Plane	N/A
Small gap in Control Volume above Greenhouse	Pressure Outlet	N/A

Since temperatures were only measured at 5 locations on each element heater, a tabular data mapper was used to specify the temperatures on the mesh of the element heaters in the CFD model. A table was imported with the coordinates and temperature as measured during the experiments. The data mapper function interpolated the temperatures measured at the specific points on the element heaters in the experimental setup, to the target surface of the heaters in the CFD model. The result of the interpolation can be seen in Figure 7.27.

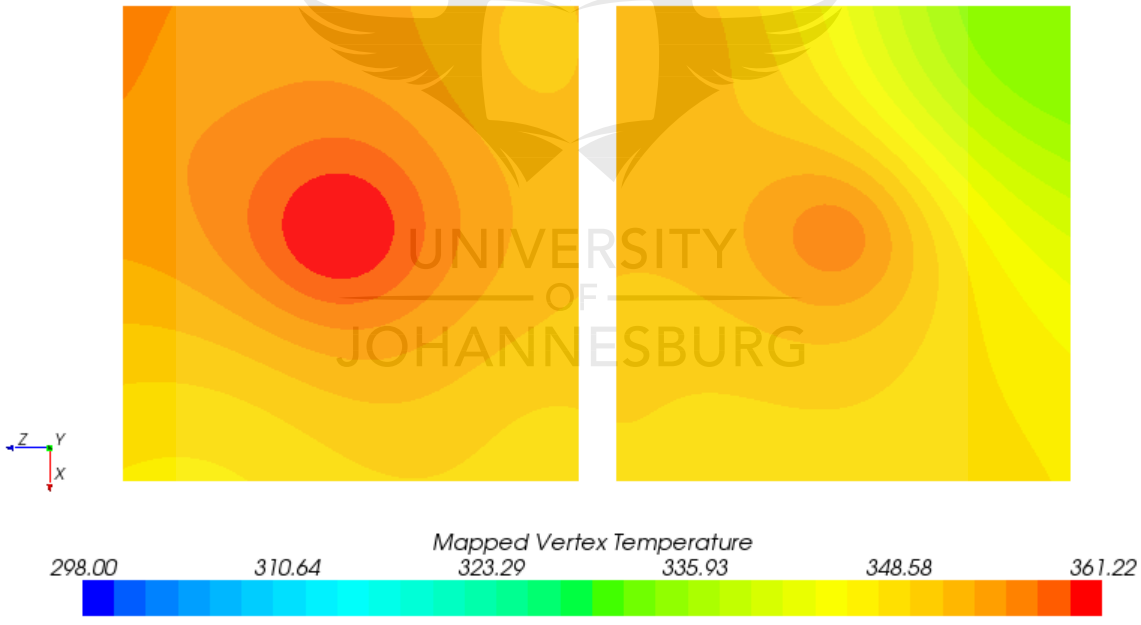

Figure 7.27: Mapped Vertex Temperature on Element Heaters in CFD Model

7.7.3 Physics Setup

The numerical simulation was initialized with the ambient measured temperature in the laboratory. The reference pressure was specified as 82 095 Pa, the reference pressure at a height of 1400m above sea-level where the physical experiment was conducted. The solution was also initialized with the hydrostatic pressure, defined using a user function. This was done

to avoid "sloshing" of the air inside the control volume, which will cause instabilities in the solution. The user function for the hydrostatic pressure was defined as the product of the density, gravitation acceleration and height of the centroid of the cell in the y-direction as shown in the following syntax:

$$0.9799 * 9.81 * \$\$Centroid[1] \quad \text{7-2}$$

The "$$Centroid[1]" syntax is used to reference the local coordinate system. The steady solver was activated, with the standard k-epsilon, low-Reynolds number turbulence model. The low wall Y+ treatment was also chosen. In this case, the coupled flow model together with the coupled energy model was activated. These two models together solve the conservation equations for mass, momentum and energy simultaneously using a time-(or pseudo-time) marching approach. These two models are robust and suitable for flows with dominant source terms, such as buoyancy, particularly high-Rayleigh number natural convection [132]. The air properties were left at the default values in the CFD software.

7.8 Results

The main objective in this chapter was to qualitatively compare the temperatures and flow patterns observed in the experimental setup with the numerical CFD model. The flow patterns were directly observed in during the experiments, with the aid of laser visualization. A plane section was created in the numerical model at a similar place where the laser sheet was placed in the experimental setup. The velocity vector plot is compared with the directly observed flow patterns in Figure 7.14. In general, a good macro or overall comparison was found between the numerical CFD model and the experimental reduced-scale model. Clear similarities can be observed. Two distinct rotating convective cells were noticed in the numerical simulation, the right cell being noticeable larger compared to the left cell. This was also the case in the experiments.

The right cell was rotating clockwise in the experiments, while the left cell rotated counter-clockwise. The left cell was smaller compared to the right cell. This was also visible from the numerical results. Most of the flow in this plane exits the greenhouse at the right roof ventilator, while less exits at the right according to the simulation. This was not noticed in the experiments however. This simulation was run in steady state, therefore the smaller eddies were not visible. It was also extremely difficult, if possible at all, to reach steady state in the experiments. The last section of this chapter deals with the unsteady numerical simulation.

Experimental

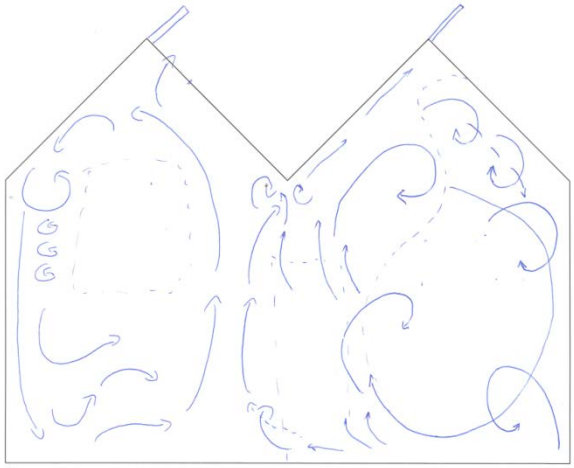

Numerical

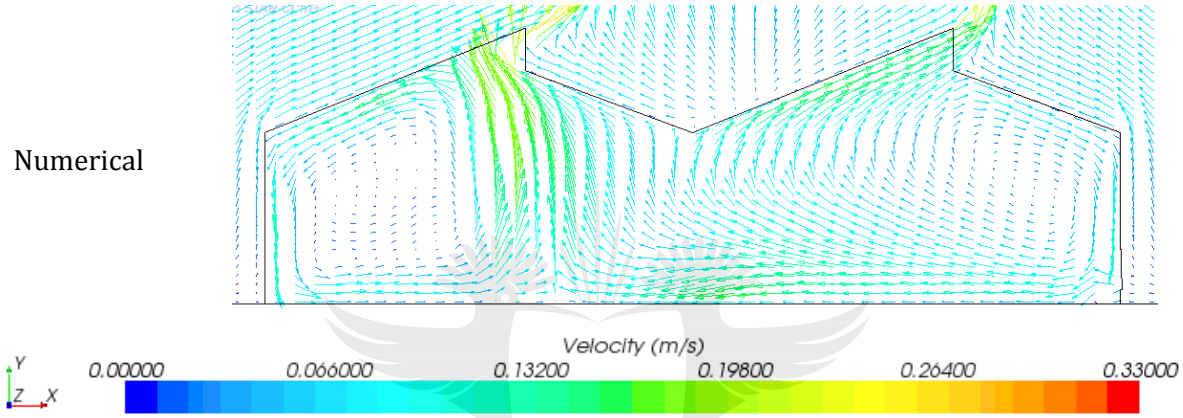

Figure 7.28: Comparison of experimental and numerical flow patterns

Probes were placed at similar locations in the numerical CFD model as where the temperature probes were placed in the experimental setup, and the temperatures were recorded. A comparison of the simulated and measured temperatures is shown in Table 7.12.

Table 7.12: Comparison of experimental and CFD temperatures

Probe #	Exp Temp	CFD Temp	Probe #	Exp Temp	CFD Temp
11	39.10	39.49	**19**	34.67	30
12	41.25	41.9	**20**	30.68	23.65
13	37.67	36.94	**21**	36.51	37.4
14	29.84	19.93	**22**	35.23	33.35
15	30.7	23.24	**23**	33.48	32.94
16	31.38	25.99	**24**	31.52	31.9
18	36.99	39.62			

Most of the values agreed relatively well. There are a few substantial differences though. Probe 14 measured a temperature of 29.84°C in the experiment, while the numerical probe measured 19.93°C. This is a difference of almost 33%. Another discrepancy for example, is probe 15, which measured 30.7°C in the experiment, while the numerical probe yielded 23.24°C. These differences can all be attributed to a number of possible causes. Firstly, the experimental reduced-scale model was not fully sealed at the edges between the MDF board and the Perspex. Secondly, there might have been a slight draft present in the laboratory during the time of the experiment, which was not taken into account in the numerical simulations. Lastly, the temperature distribution on the plate element heaters in the numerical simulation might not have accurately represented the temperature distributions in the experiment. Another factor is that the simulation was run steady state, whereas it was extremely difficult for the experiment to reach fully steady state at any moment during the experiment.

A comparison of the experimental and numerical non-dimensional temperature stratification for the first span and second span at the roof ventilator is shown in Figure 7.29 and Figure 7.30. The non-dimensional temperature was defined as follows in equation 7-2:

$$T^* = \frac{T - T_{amb}}{T_{floor\,\max} - T_{amb}} \qquad \textbf{7-3}$$

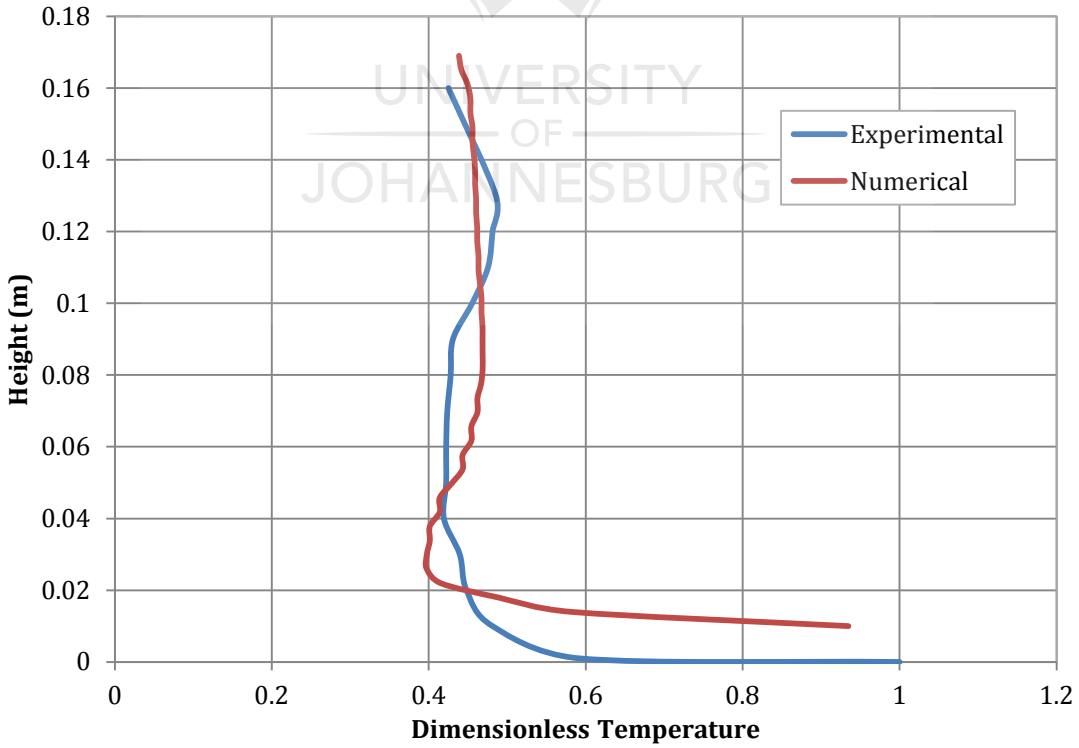

Figure 7.29: Non-dimensional temperature stratification in the left span (Comparison between experimental and numerical results)

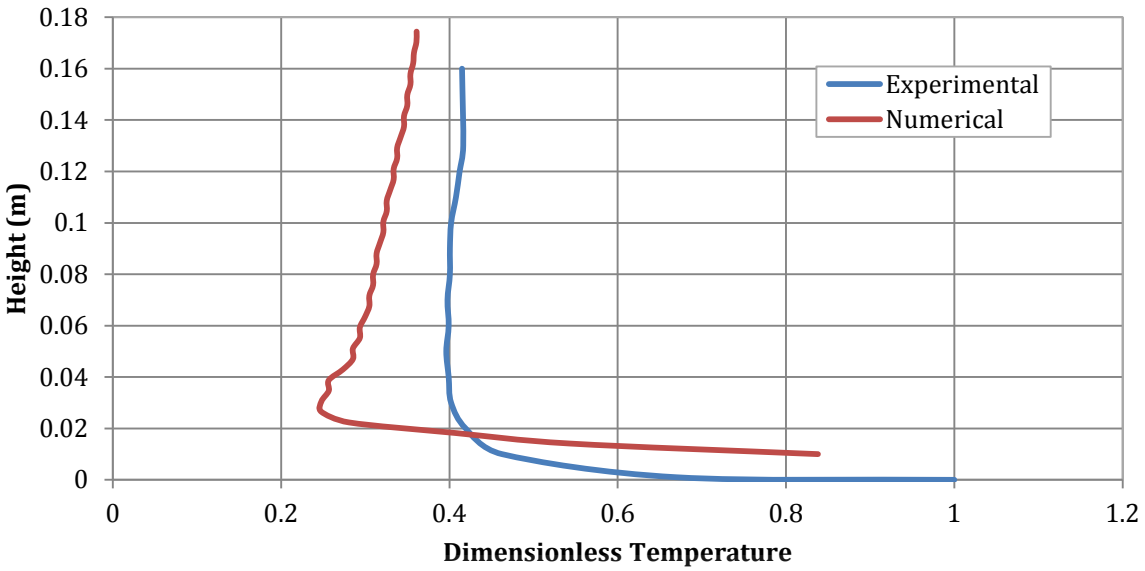

Figure 7.30:Non-dimensional temperature stratification in the right span (Comparison between experimental and numerical results)

Both the numerical and experimental results for the thermal stratification profile indicate a relatively uniform temperature distribution between the floor and the roof, except for the first 20mm, where there quite a sharp drop in temperature can be observed through the floor temperature boundary layer. The difference in the measurements between the experimental and the numerical results could be attributed to inaccuracies with measuring the height within the reduced scale greenhouse. The numerical probe was placed right on top of the plate in the simulation program, whereas the temperature transducer used for measuring the experimental temperatures couldn't be placed exactly on the element heater. In the right span, the same trend is observed – a large drop in temperature during the first 20mm, after which the temperature remains relatively constant up to the roof. A relatively large difference (a maximum difference of 33% is observed) in vertical temperature stratification between the experimental and numerical results was observed from Figure 7.30. The vent in the experimental setup was closed, but still had some small gaps here and there. The vent in the simulation was modelled to be open at 1mm right along the longitudinal wall of the greenhouse. It could be that the air cooled down more in the simulation compared to the experimental results due the gap left by air vent being larger in the numerical simulation than in the experiment itself.

7.9 Unsteady Results

As already mentioned, the experimental results were unsteady to a substantial extent. An indication of the unsteadiness can be seen in some of the still photographs taken in the

longitudinal section of the experimental scale greenhouse. These photographs are also available in Appendix A. The unsteady behaviour was also observed in the numerical CFD simulations. For these simulations, the same model was used as for the steady state results, except now the implicit unsteady solver was activated from the converged steady state solution. To ensure that the time step chosen (0.04s) was sufficient, the convective Courant Number was monitored. The convective Courant Number is used to assist in choosing the time-step for unsteady simulations. It is recommended that for time-accurate simulations, the convective Courant number should 1.0 on average in the region of interest. A value of 1.0 implies that the fluid moves by about one cell per time step. The simulation was run for a total of 23 seconds. The velocity and temperature was numerically monitored at two different points in the flow field, and are shown in Figure 7.31 and Figure 7.32 respectively. The velocity is approximately 0.04m/s at 5 seconds, and increases within 2 seconds to 0.12 m/s for probe 2, whereas the velocity measured by probe 1 is relatively stable. The temperature measured by probe 1 is about 40°C, while the temperature drops from 40°C to almost 25°C in 2 seconds. The positions of the numerical probes are given in Table 7.13.

Table 7.13: Probe coordinates

Probe #	x	y	Z
1	0.149	0.164	0.53
2	0.461	0.144	0.53

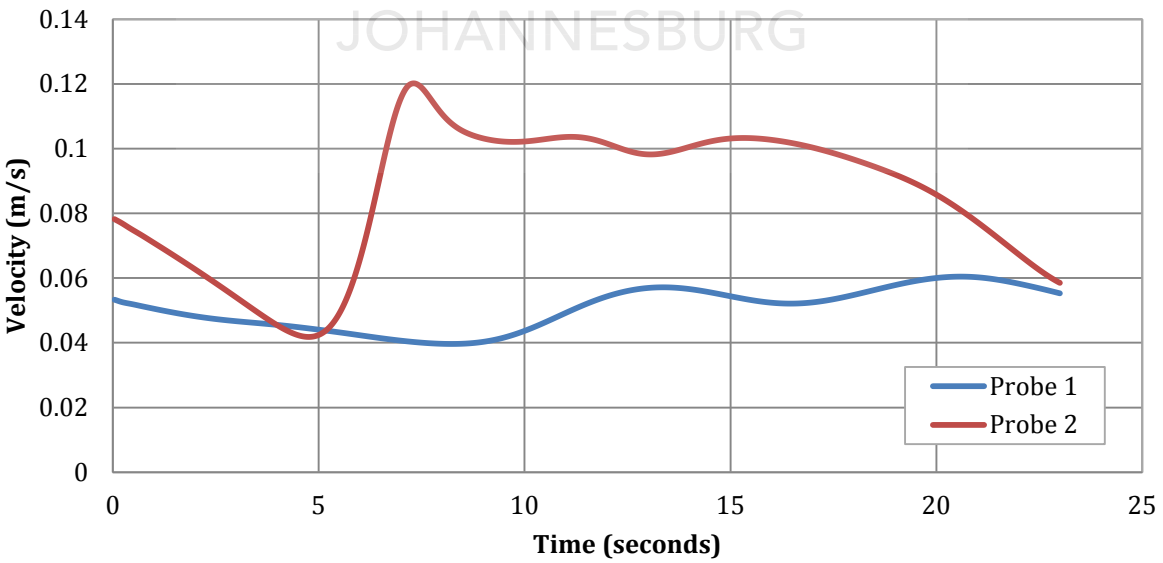

Figure 7.31: Velocity varying with time

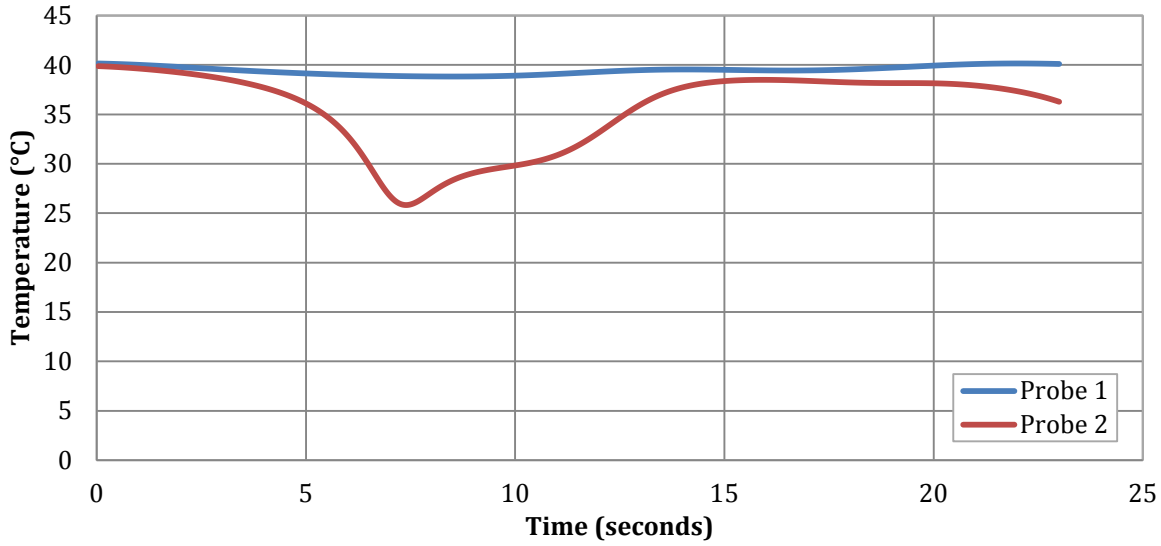

Figure 7.32: Temperature varying with time

The unsteady effects can also be seen in the vector plots plotting the velocity magnitude shown consecutively in Figure 7.33 to Figure 7.36. Figure 7.33 to Figure 7.36 shows a plane section taken longitudinally through the centre of the greenhouse for 0.2s, 4s, 8s and 12s. The most movement is noticed towards the left side (front of greenhouse) where the shape of the convective cell that forms directly in the corner changes with time and becomes smaller.

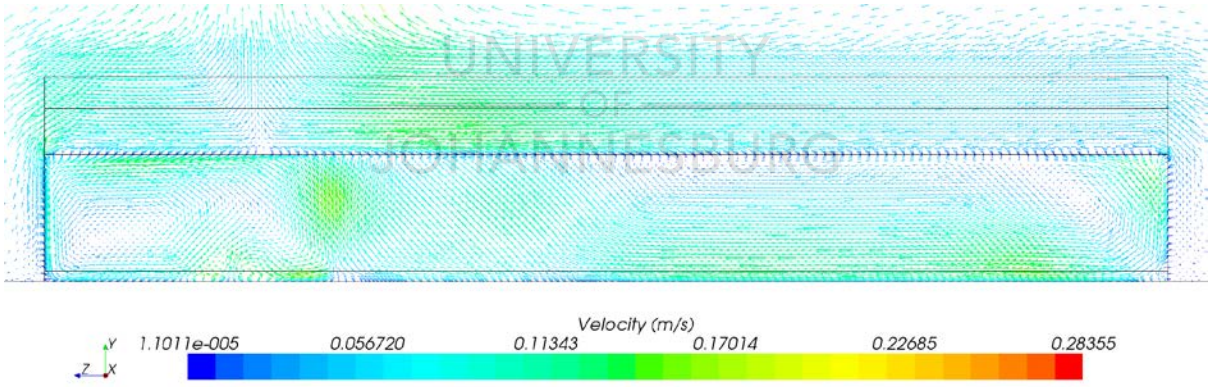

Figure 7.33: Longitudinal velocity vectors at 0.2s

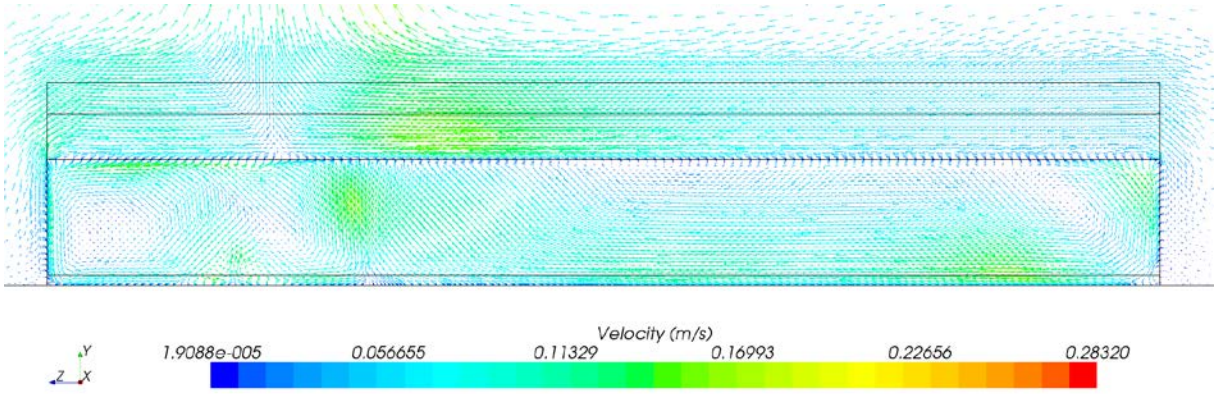

Figure 7.34: Longitudinal velocity vectors at 4s

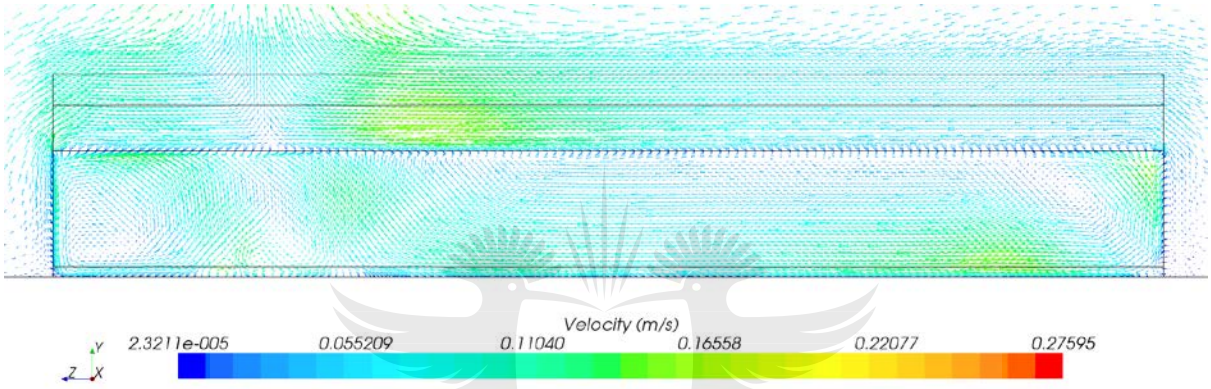

Figure 7.35: Longitudinal velocity vectors at 8s

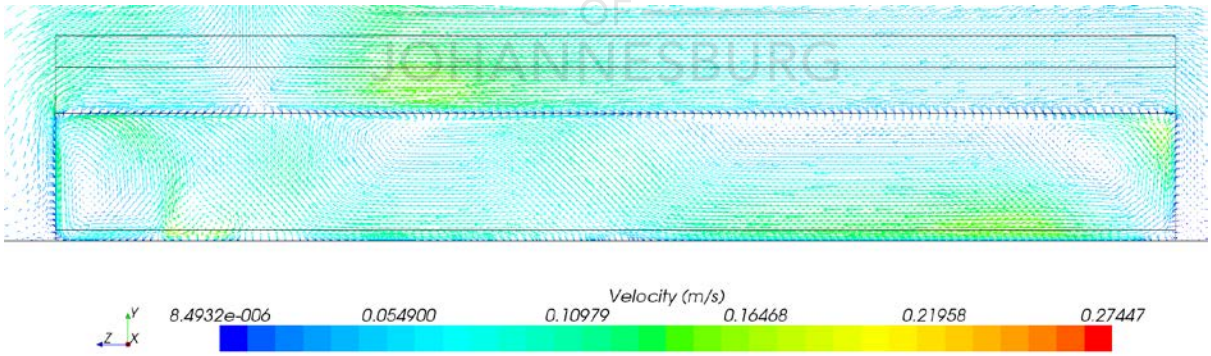

Figure 7.36: Longitudinal velocity vectors at 12s

Figure 7.37 to Figure 7.40 shows a cross-sectional view of the vectors (same location as the laser in the experimental setup) for 0.2s,4s,8s and 12s respectively. In this case the most noticeable movement is once again a change in the convective cell in the left corner.

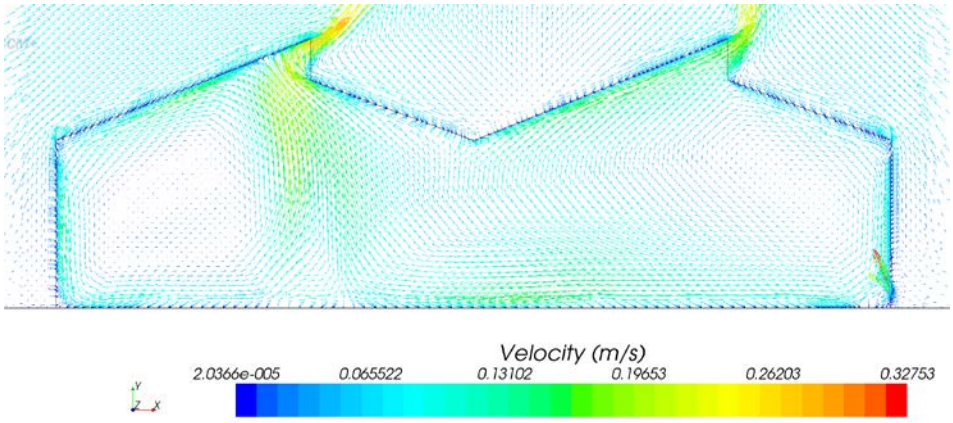

Figure 7.37: Cross-sectional velocity vectors at 0.2s

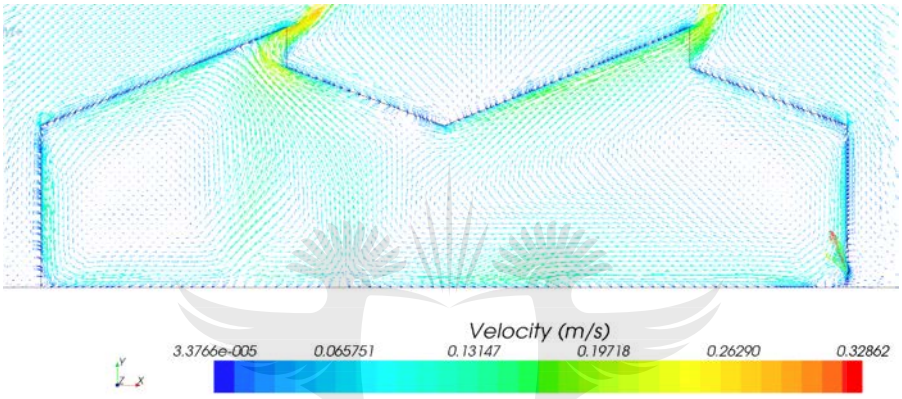

Figure 7.38: Cross-sectional velocity vectors at 4s

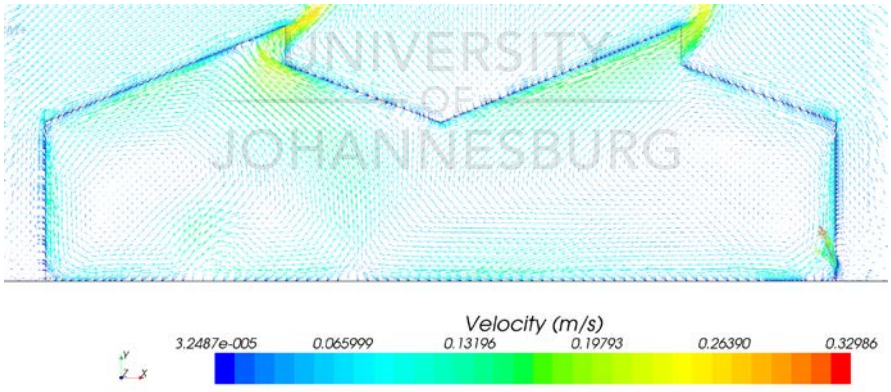

Figure 7.39: Cross-sectional velocity vectors at 8s

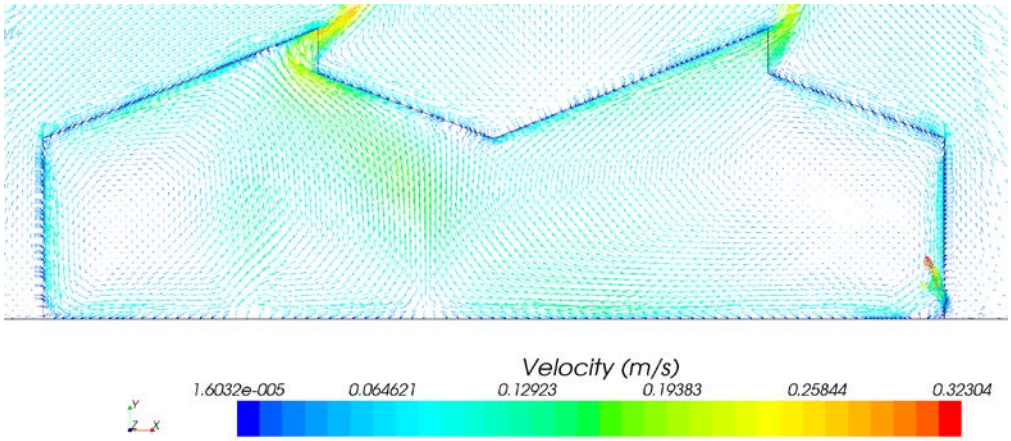

Figure 7.40: Cross-sectional velocity vectors at 12s

7.10 Conclusion

The objective of this chapter was to build a reduced-scale model of a full-scale multi-span greenhouse and validate in some sense a similar reduced scale numerical greenhouse model. Flow patterns were directly experimentally observed and visualized using a green laser and smoke. The experimental results proved to be turbulent and unsteady, as could be seen from the photographs and the temperature measurements taken on the walls and in the flow near the walls. This was also noticed in the CFD results. However, the model was successfully validated qualitatively, as similar flow patterns and temperatures were observed in both the experimental tests and the CFD model for the quasi-steady state as well as transient simulations. Therefore a reduced-scale model can be used with adequate confidence to investigate flow patterns for buoyancy driven flow in the greenhouse application.

The next chapter in this thesis investigates the flow inside a full-scale greenhouse containing bench arrangements.

CHAPTER 8

Numerical simulation of Full-Scale Greenhouse Containing Plant Benches

8.1 Chapter Review

The previous chapters established the foundations of natural convection in a cavity similar to a single span greenhouse with a zero degree roof angle (Chapter 4) and a greenhouse with various roof angles (Chapter 5). Chapter 5 also investigated a ventilated single span greenhouse cavity. Chapter 6 focused on validating a numerical model of a full-scale greenhouse, while Chapter 7 experimentally validated a two-dimensional numerical model of a reduced-scale greenhouse, thereby establishing confidence in the numerical CFD models of greenhouses used. The last chapter of this thesis is dedicated to the numerical simulation of a complex three-dimensional greenhouse, with various bench arrangements. This chapter relates to the research question of determining whether a full scale three-dimensional numerical model can be used to determine the effect of various ventilator configurations and bench arrangements on the indoor climate of the full scale greenhouse.

As already mentioned in Chapter 2 – greenhouse plant benches have several advantages when compared to cultivating crops directly in the soil. Additionally, several layouts or designs of bench arrangements are available, each with its own advantages. Popular bench arrangements used commonly in greenhouses include longitudinal and peninsular arrangements (Figure 8.1). The peninsular design allows for segregation of various species, whereas routine tasks such as watering is easier on longitudinally placed benches [166]. It is recommended for efficiency that the bench-to-aisle ratio not exceed 1/3 to 1/4 of the total greenhouse area [167]. The presence of a crop and plant benches usually has a negative effect on ventilation, as they exert a drag force and induce a momentum loss in the airflow [168]. Bench space efficiency (percentage) is defined as follows in equation (8-1) [166]:

$$BSE = \frac{\text{number of benches} \times \text{length of each bench} \times \text{width of bench}}{\text{greenhouse dimensions}\left(\text{width} \times \text{length}\right)} \times 100 \qquad 8\text{-}1$$

If the bench space efficiency is calculated for both the peninsular and longitudinal layout, it is usually found that the peninsular design allows for more growing area [166].

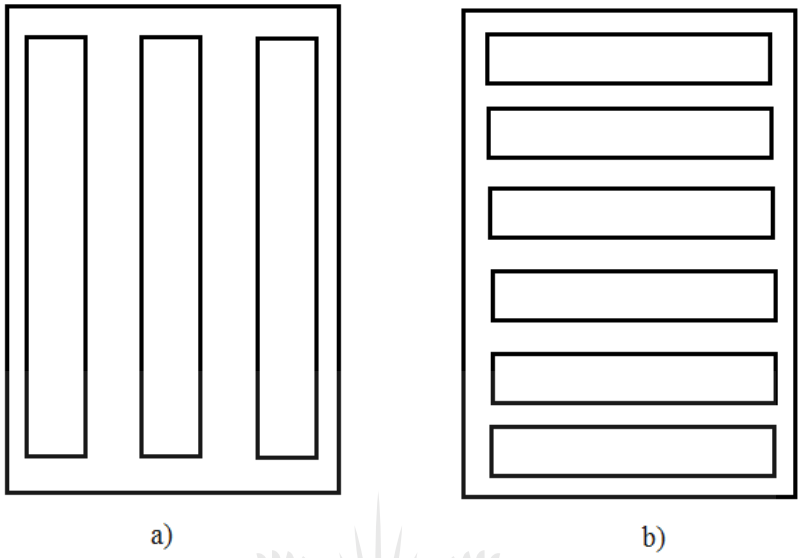

Figure 8.1: a) Longitudinal Arranged Benches b) Peninsular Arranged Benches [15]

8.2 Numerical Model of a Full Scale Greenhouse containing Plant Benches

The full-scale greenhouse CFD model validated previously in Chapter 6 is now modified to include bench arrangements. The greenhouse was filled with 12 peninsular placed benches (7.5m × 0.9m) equal to a bench space efficiency of 42% (using eq. 8-1).The greenhouse in the CFD model was only 20m in length and contained 2 spans of 9.6m each. The origin was chosen as the bottom left corner, at the back of the greenhouse as shown in Figure 2.

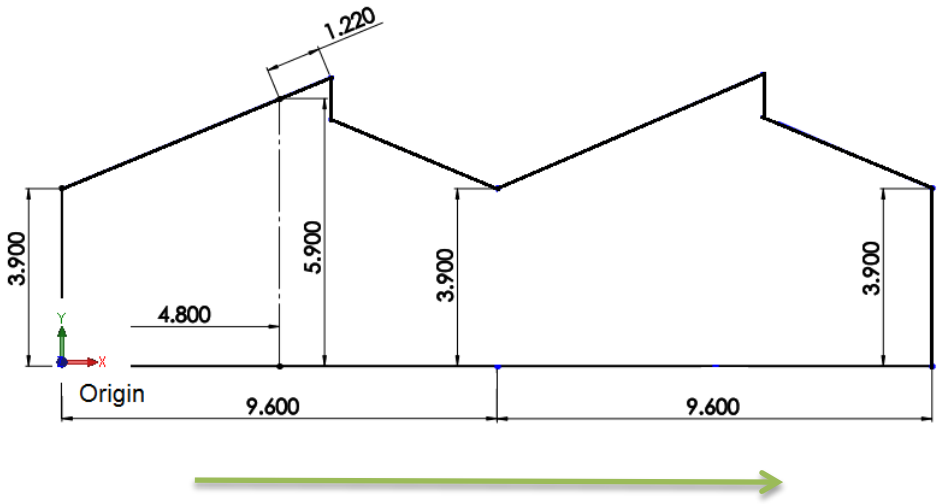

Figure 8.2: Greenhouse Dimensions and Origin used in the CFD model

A large computational control volume (250m x 100m x 100m) was created around the greenhouse to ensure minimal interference from the boundaries on the flow inside the greenhouse and to allow for development and definition of the boundary layer (Refer to Figure 8.3). The negative y-direction was chosen as the direction of the gravitational constant for all the greenhouse models in this paper. The wind was modelled to act from left to right in an eastern direction at 1m/s. This was done for comparison purposes with the original validated greenhouse [49]. The boundaries are summarized in Table 8.1, and the input values in Table 8.2.

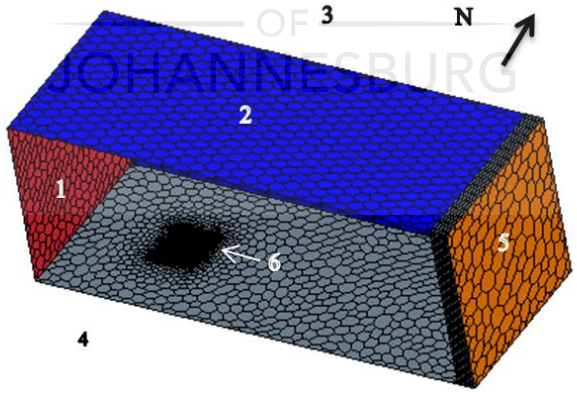

Figure 8.3: Boundaries and control volume around greenhouse

Table 8.1: Boundary conditions

Nr	Boundary Name	Boundary Type
1	Inlet	Velocity Inlet
2,3,4	Top, front, back	Symmetry Plane
5	Outlet	Pressure Outlet
6	Glass Walls	Baffle Interfaces

Table 8.2: Input values for CFD simulations

Parameter	Unit	Value
Inlet Air		
Temperature	ºC	22.2
Velocity	m/s	1
Outside Ground	ºC	27.9
Inside Ground	ºC	27.3
Effective Thermal Resistance (Baffles)	W/m^2	0.00286

The outlet of the domain was specified as a porous region, using the mesh extruder in StarCCM+ in order to force the flow out of the domain. This is an artificial boundary created to ensure a positive pressure over the outlet boundary, to avoid recirculating flow developing. As the outlet boundary is far from the region of interest, the effect on the solution was considered negligible. The porous region was 10m, with 10 orthogonal extruded cells, which were extruded from the volume mesh at the outlet boundary. Three volumetric controls were used to refine the mesh. The first volumetric control refined the mesh around the entire greenhouse and extended towards the back to accurately capture recirculating flow. Three smaller volumetric controls were applied to the region around the plant benches, and around the ventilators in developing the greenhouse model in the CFD software. The relative sizes and refined regions are shown in Figure 8.4 and Table 8.3.

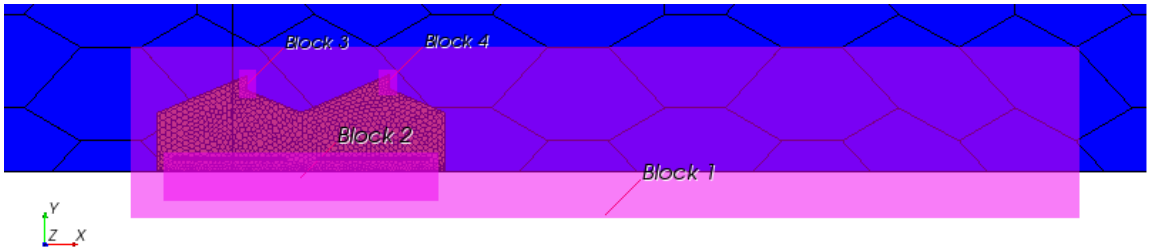

Figure 8.4: Volumetric controls applied around greenhouse

Table 8.3: Volumetric controls applied to greenhouse CFD model

Volumetric Control	Specified Area	% Relative of Base Size
Block 1	Entire Greenhouse	2.5 (0.375m)
Block 2	Benches	0.5 (0.075m)
Block 3	Ventilator 1	1.5 (0.225m)
Block 4	Ventilator 2	1.5 (0.225m)

A meshed 3D model of a leeward-facing (ventilators) greenhouse containing longitudinal plant benches is shown in Figure 8.5. The glass walls of the greenhouse were modelled as baffle interfaces with an effective thermal resistance. A baffle interface physically represents one or more thin sheets of impermeable, conducting materials in a fluid, with a minimal thickness [90]. The prism layer model was activated, and after monitoring the solution, 20 orthogonal prismatic cells with a combined thickness of 100mm was selected. A summary of the mesh parameters are shown in Table 8.4. After careful consideration, taking running time and convergence into account it was decided to use a base size 15m for all the simulations.

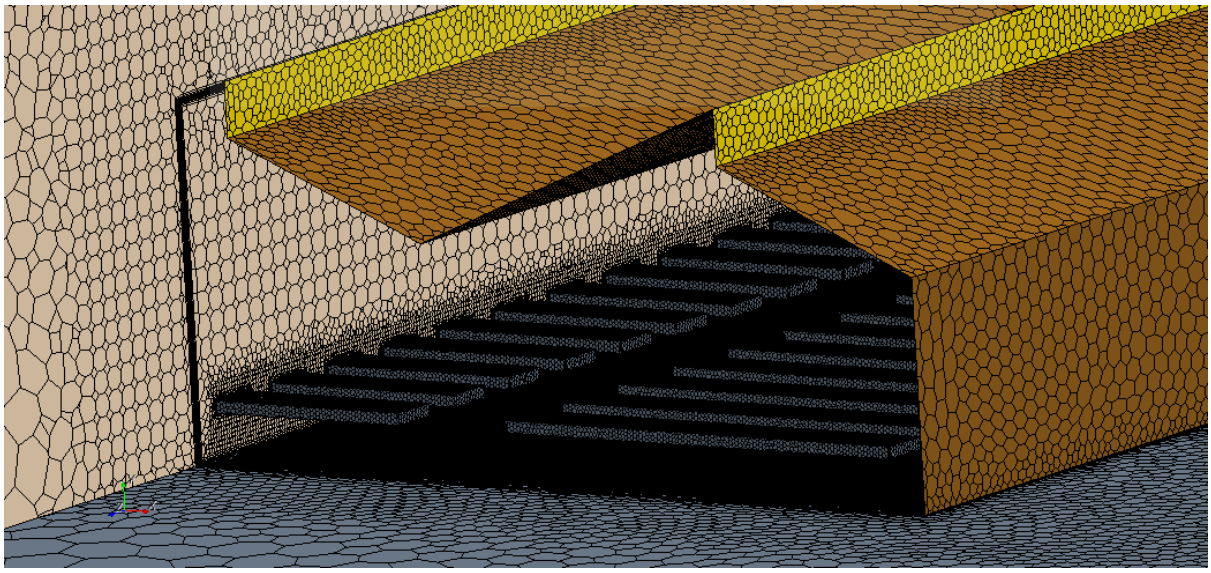

Figure 8.5: Greenhouse with Polyhedral Mesh

Table 8.4: Mesh Parameters for 3D Full-scale Greenhouse

Property	Value
Base Size (m)	15m
Number of Prism Layers	20
Prism Layer Stretching	1.5
Prism Layer Thickness (m)	0.1
Surface Growth Rate	1.3
Surface Size (Tet/Poly Density)	
Density	1.0
Growth Factor	1.0
Blending Factor	1.0
Local Custom Surface Size	
Relative Minimum Size	25% of Base Size
Relative Target Size	100% of Base Size

Previous studies confirmed the turbulent nature for both inner and outer flow of greenhouses [28] and also confirmed in the experiments reported on in Chapter 7. As computational hardware was limited, the realizable *k*-epsilon model was implemented developed by Shih et al [169] and combined with the two-layer approach. All the simulations were solved with the steady solver. The wind was modelled as 1m/s in an easterly direction as in the original case investigated by Ould Khaoa [49]. The input boundary conditions and other parameter values from [49] used in each simulation are shown in Table 8.5, and the turbulence parameters in Table 8.6.

Table 8.5: Properties for CFD Simulations

Parameter	Unit	Value
Inlet Air:		
Temperature	ºC	22.2
Density	kg/m^3	1.20
Viscosity	kg/m.s	1.51×10^{-5}
Specific Heat	J/kg.K	1005.91
Thermal Conductivity	W/m.K	0.0258
Molecular Weight of Dry Air	kg/kmol	28.9
Isothermal Boundaries:		
Outside Ground	ºC	27.9
Inside Ground	ºC	27.3
Effective Thermal Resistance	W/m^2	0.00286

Table 8.6: Turbulence Parameters

Under Relaxation Factor	0.8
Convergence Tolerance	0.1
Epsilon	0.0
Turbulent Viscosity (Under Relaxation Factor)	1.0

The simulation was run using the steady state solver, and gravity was modelled in the negative y-direction. To keep the simulation from diverging immediately, gravity was gradually introduced by ramping it up from 0 to 9.81 over 100 iterations. The following field function was developed and used in the CFD software:

($Iteration<100)?(-9.81*$Iteration/100):-9.81

8.3 Results

Figure 8.6 shows the numerical simulated velocity and temperature at plant level for a leeward facing greenhouse containing peninsular arranged plant benches. The velocity distribution is noticeably heterogeneous throughout, with parts in the first span, and next to the right wall with low velocity. A few stagnant regions with low velocities and high temperatures are visible, especially throughout greenhouse, especially towards the right side of the greenhouse. A cooler region is noticed at the left back side of the greenhouse as well, as this region contains slightly higher velocities. The temperature and velocity distribution at three different intervals; 5.005m,10m and 15m (measured from the back of the greenhouse) is shown in Figure 8.7. It is observed that the temperature and velocity distribution at the three sections vary considerably. Temperatures are generally hotter towards the right side of the greenhouse for all three sections. A high velocity adjacent to the roof in the second span is also noticed. For the 5.005m section, there is also a stream of air moving at a high velocity underneat h the second shelve.

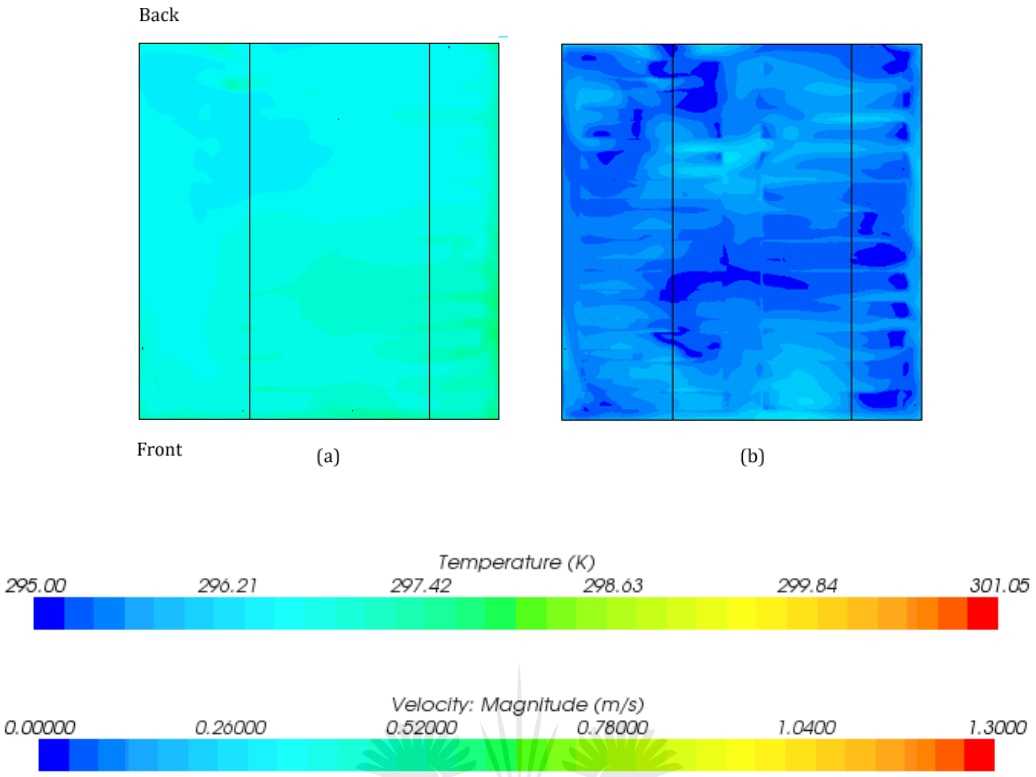

Figure 8.6: Temperature (a) and velocity distribution (b) at plant level for peninsular benches

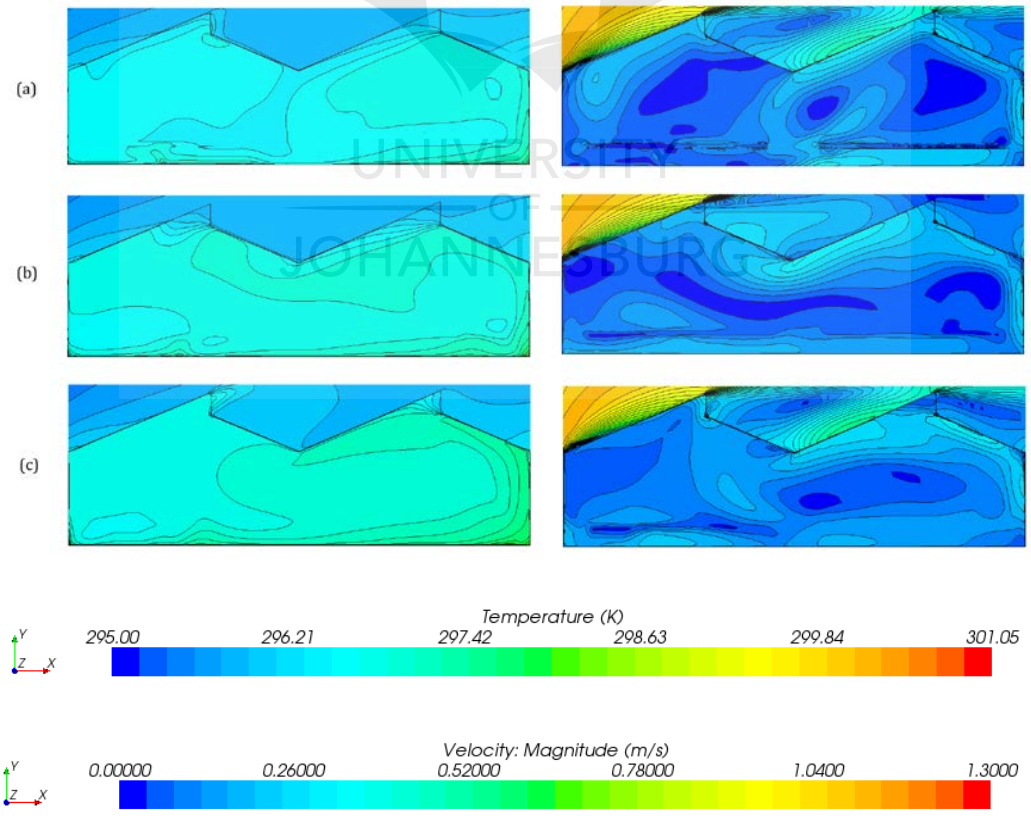

Figure 8.7: Temperature and velocity contour plots at a)5m, b), 10m and c)15m from the back of the greenhouse

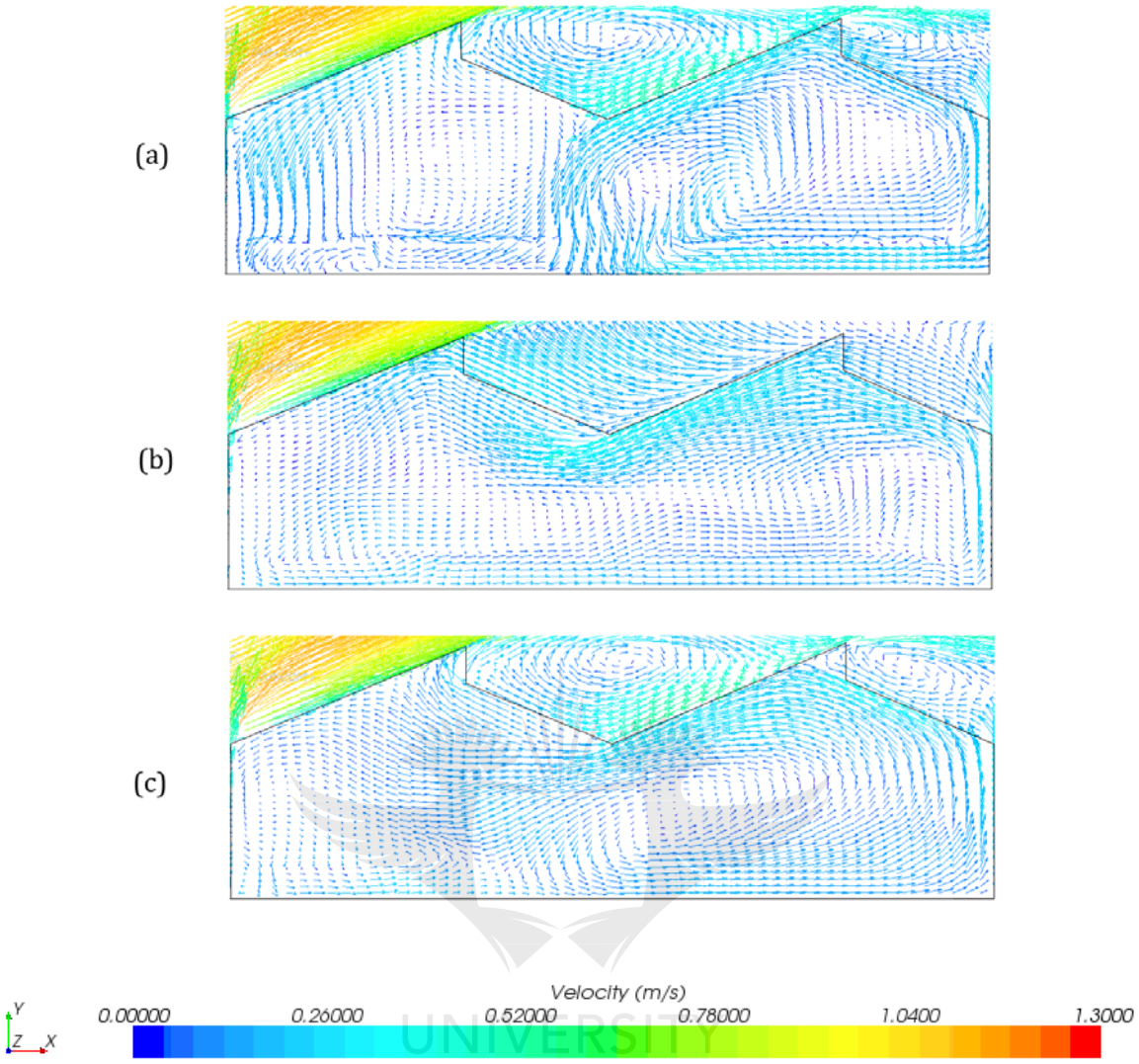

Figure 8.8: Velocity vector plots at a) 5m, b), 10m and c)15m from the back of the greenhouse

At the first plane, 5.005m from the back (Figure 8.8a), the air is sucked into the greenhouse through the second roof ventilator. A large counter-clockwise cell is formed as most of the flow moves down towards the floor in the center of the greenhouse, and towards the right underneath the shelve. The flow moves up again against the right wall. Some of the flow entering through the second roof ventilator moves towards the left of the greenhouse as it drops to the floor. The air moves slowly towards the left of the wall of the greenhouse underneath the shelve. A small counter-rotating cell is formed underneath the first shelve. Air can also be seen leaving the greenhouse through the first roof ventilator. There are some cells visible rotating above the first shelve, but the direction is difficult to discern, as the flow is three-dimensional.

At the centre plane of the greenhouse – 10m from the back (Figure 8.8b) air is mostly drawn into the greenhouse at both roof ventilators. The air from the second ventilator moves adjacent to the roof towards and down the left wall, where it moves underneath the shelves towards the right wall. In this plane a large counter-clockwise rotating cell is basically formed, with some smaller cells present in the middle of the greenhouse.

Very little air enters the greenhouse in the last plane – 15m from the back Figure 8.8c). A large counter-clockwise rotating cell forms in the second span, with smaller cells rotating in the first span. Most of the flow moves out of the two roof ventilators.

Contour plots taken in the longitudinal section of the greenhouse are shown in Figure 8.9 at three different sections (4.8m,9.6m and14.4m) measured from the left of the greenhouse. As can be seen from these plots, the indoor climate varies considerably throughout the greenhouse. Some stagnant regions are noticed, especially in the 15m plane, with high velocities against the roof.

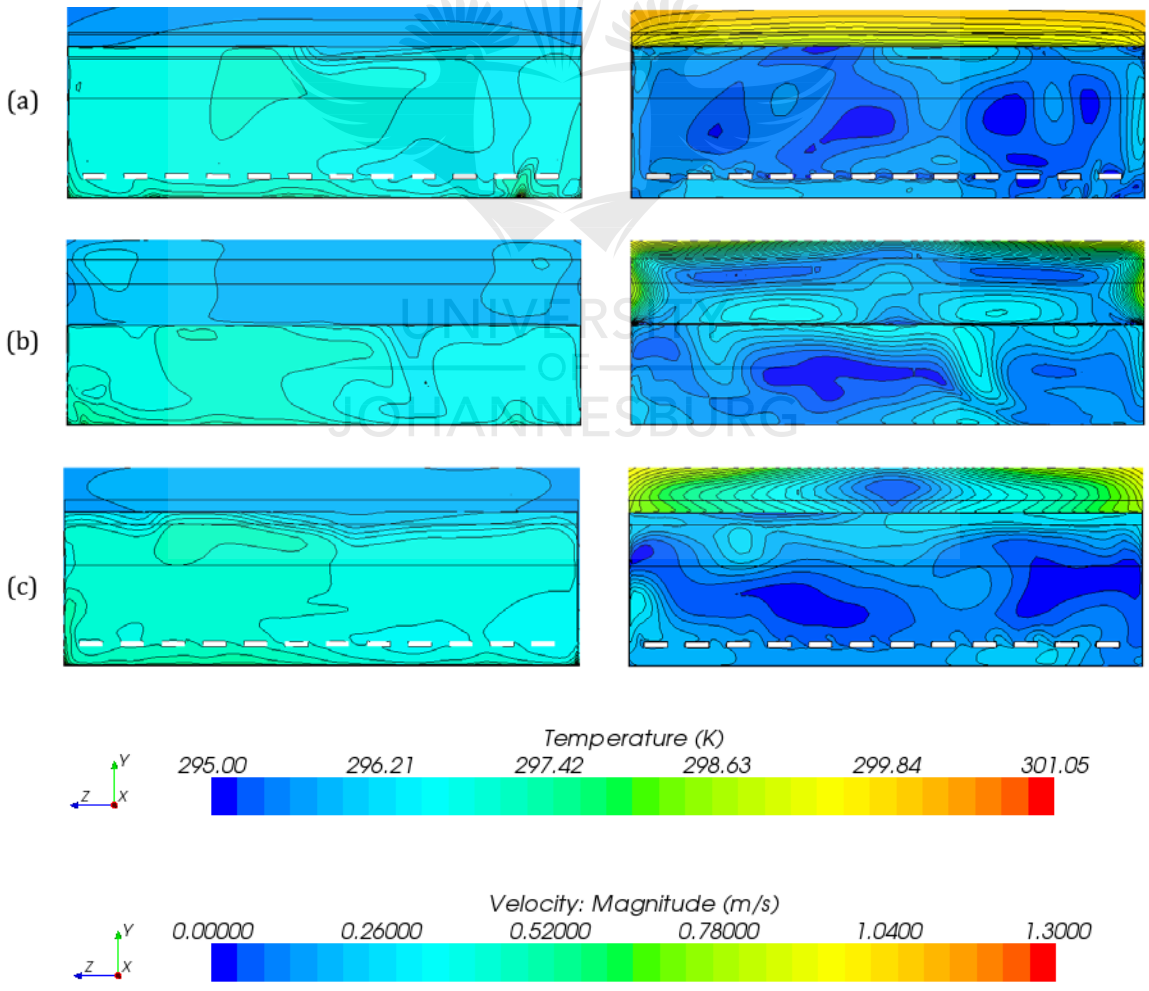

Figure 8.9: Temperature and velocity contour plots at a) 4.8m b) 9.6m and c) 14.4m from left of greenhouse

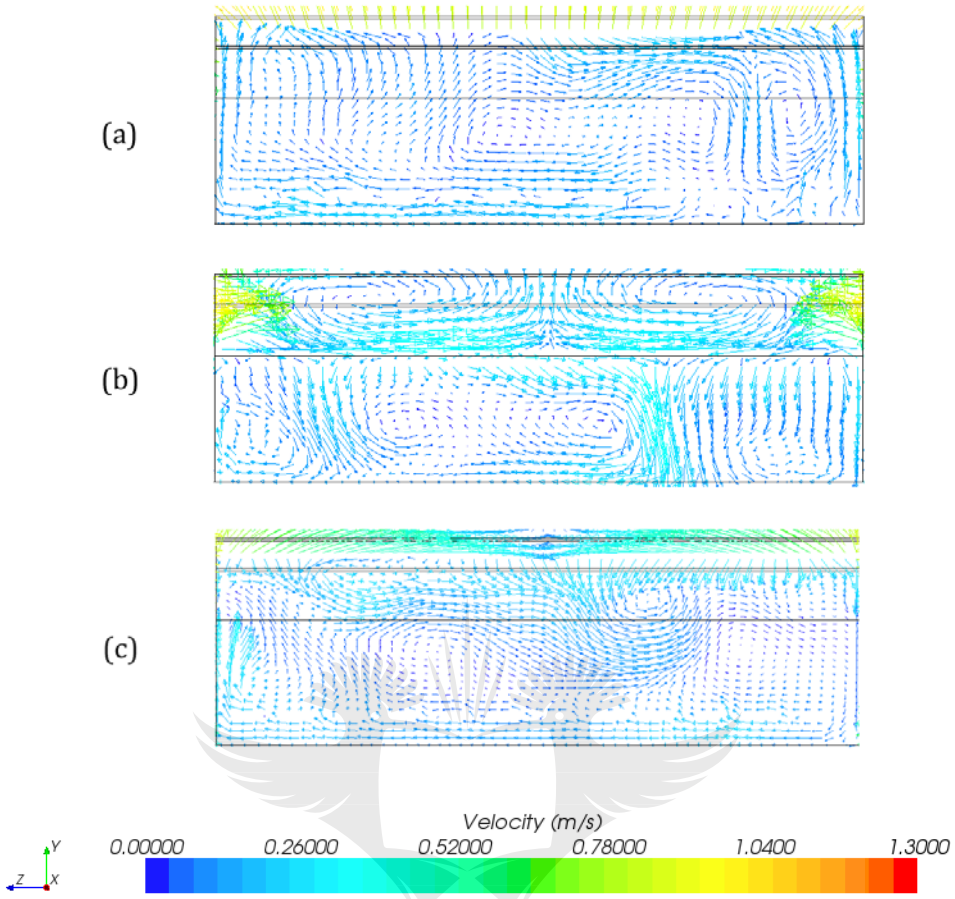

Figure 8.10: Velocity vector plots for a) 4.8m b) 9.6m and c) 14.4m from the left of the greenhouse

From Figure 8.10 the vector plots indicate that the velocity distribution at longitudinal sections throughout the greenhouse is heterogeneous. Various small convective cells are noticed, as well as stagnation regions, but also regions with high velocity (for example in the 9.6m section)

The temperature difference at plant level (1m) between the inside and the outside of the greenhouse is plotted for the three transverse sections (5m,10m and 15m from the back) in Figure 8.11. The greenhouse is generally warmer towards the front, and there is a temperature increase in temperature adjacent to the right wall for all three sections. A maximum temperature difference of 2.3°C is noticed adjacent to the right wall at the 15m section.

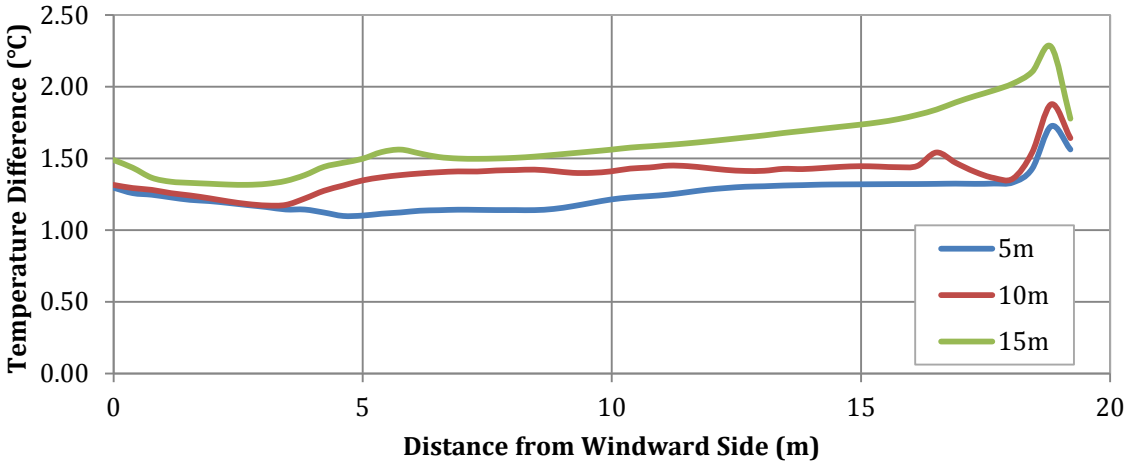

Figure 8.11: Temperature difference at plant level between inside and outside of greenhouse for 5m,10m and 15m planes

The velocity distribution at plant level is shown in Figure 8.12 for the three transverse sections. The distribution is noticeably heterogeneous throughout, and varies from a minimum of 0.04 m/s in the 5m section, to a maximum of 0.2 m/s also in the 5m section. A sharp increase in velocity can be seen for each section adjacent to the right wall.

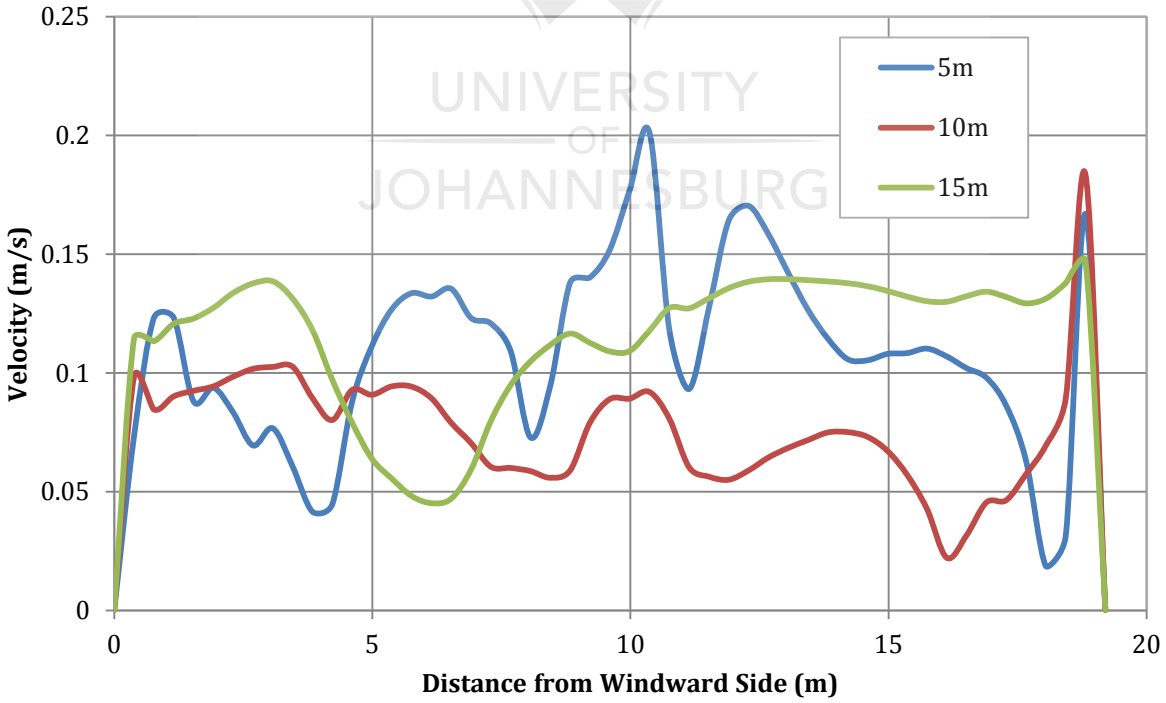

Figure 8.12: Velocity distribution at plant level for 5m,10m and 15m planes

If the temperature distribution at plant level in the longitudinal direction is investigated, in general it can be seen that the greenhouse is warmer at the back compared to the front for all three sections (Figure 8.13). Figure 8.14 shows the velocity at plant level for the three longitudinal sections. The velocity distribution is largely heterogeneous, with velocities varying considerably especially towards the left (4.8m) and right (14.4m) of the greenhouse. The velocity distribution in the centre plane (9.6m) does not exhibit a variation to the same extent.

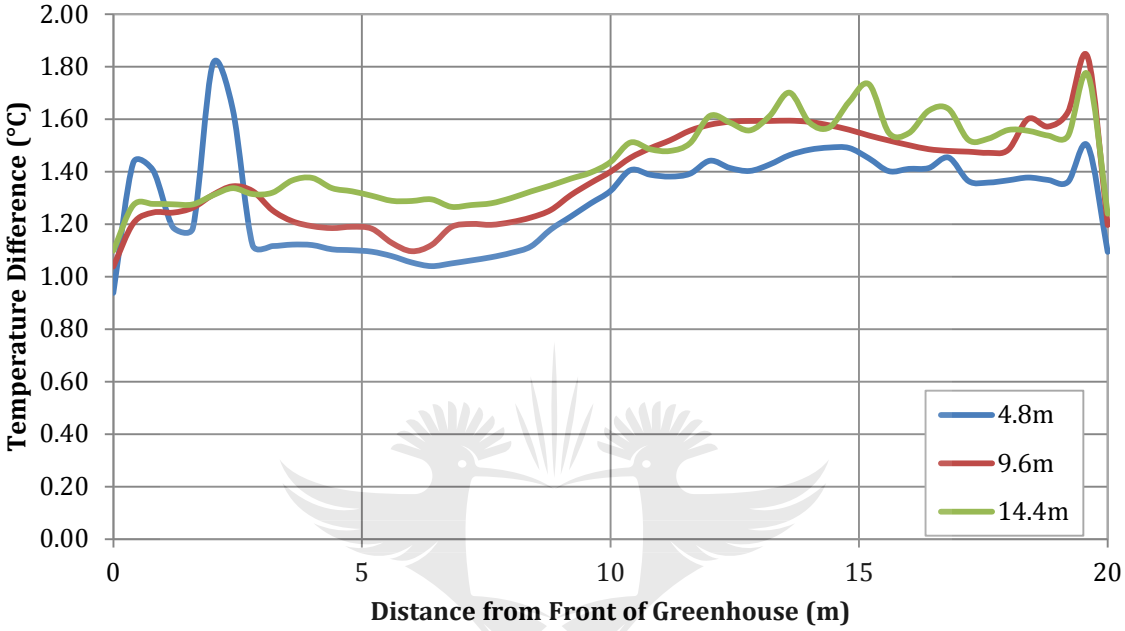

Figure 8.13: Temperature difference between inside and outside of greenhouse at plant level (Longitudinal sections)

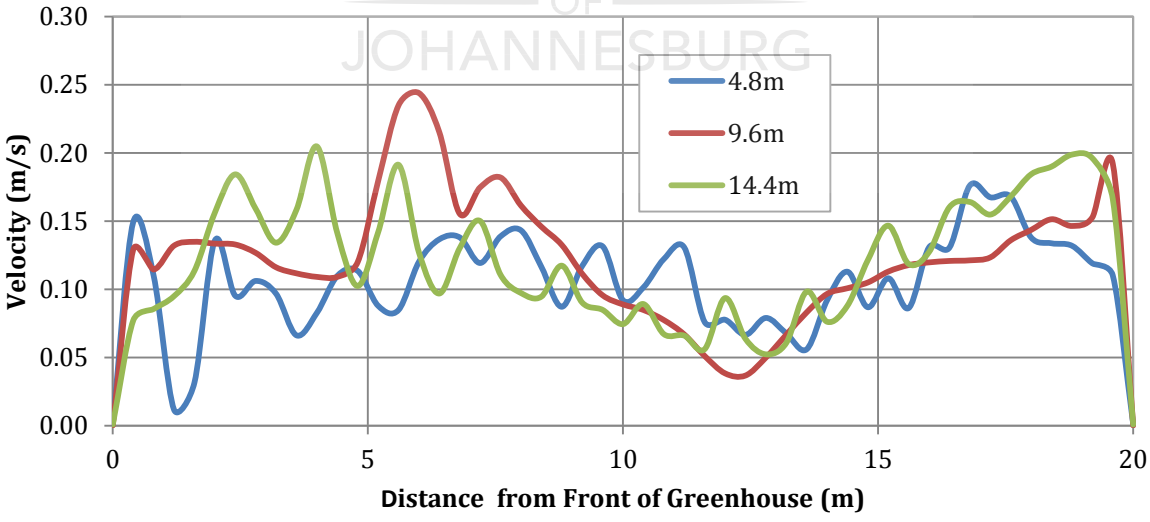

Figure 8.14: Velocity distribution at plant level (Longitudinal sections)

8.4 Comparison with 2D Case

A preliminary comparison of the 2D and 3D cases for the temperature difference between the inside and outside of the greenhouse is shown in Figure 8.15. In general the two-dimensional CFD model indicates that the greenhouse is on average 3.3°C warmer than the outside of the greenhouse. The three-dimensional model indicates a maximum average temperature difference of 1.6°C for the 15m section. Therefore the two-dimensional CFD model could possibly over predict the temperature difference between inside and outside. The velocity distribution at plant level is compared in Figure 8.16. The two-dimensional model under predicts the velocity distribution in the first span, and over predicts the velocity in the second span.

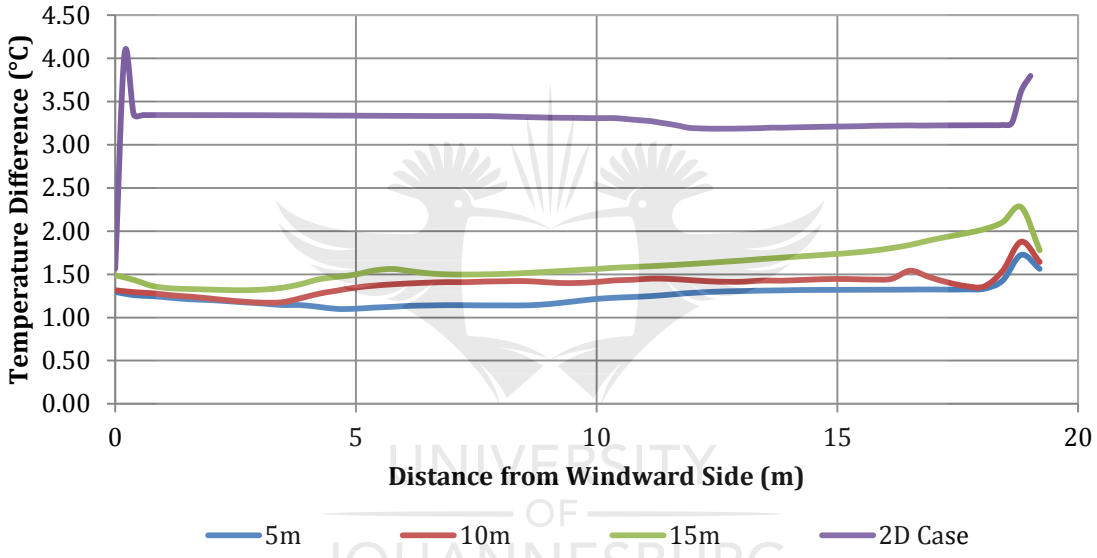

Figure 8.15: Comparison of 2D and 3D temperature distribution

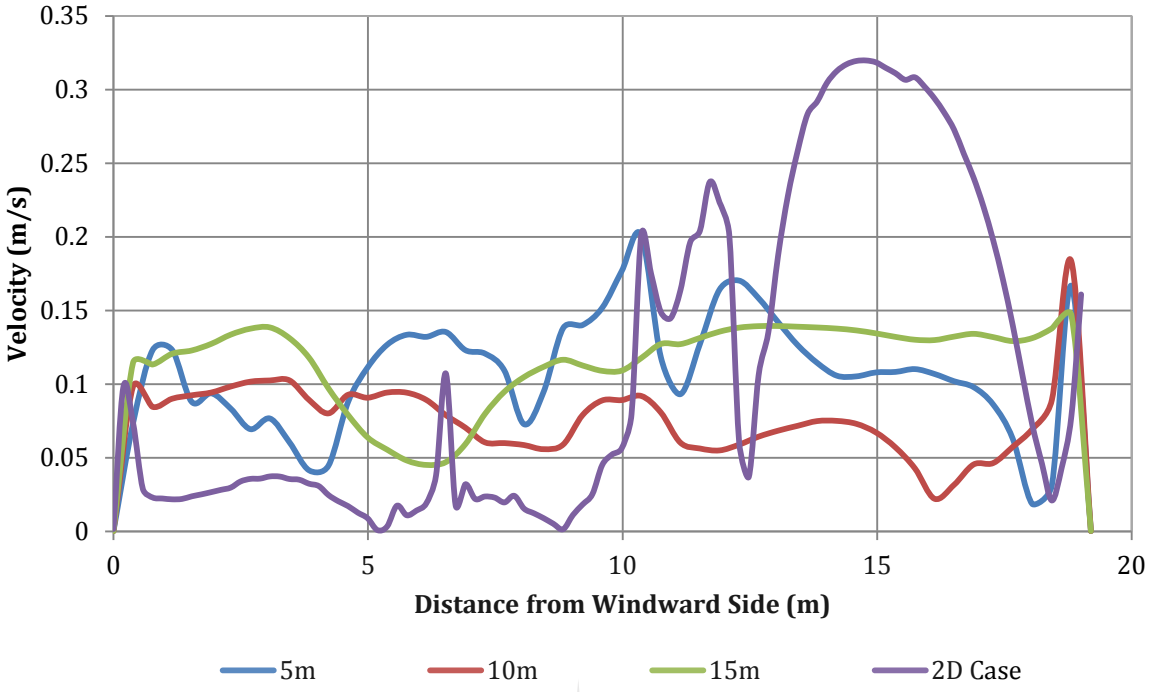

Figure 8.16: Comparison of 2D and 3D velocity distribution at plant level

8.5 Conclusion

The objective of this chapter was to develop a three-dimensional CFD model to investigate the flow inside a multi-span greenhouse containing peninsular placed plant benches. The model was based on a greenhouse found in the literature. The two-dimensional case was successfully validated in Chapter 6, and modified in this chapter to include peninsular arranged benches. The model was also three-dimensional in this chapter. Overall, it was found that the microclimate at plant level was significantly influenced by the presence of the plant benches. Temperature and velocity distributions at plant level varied considerably throughout the length as well as the width of the greenhouse. The flow was found to be three-dimensional, and moves into and out of the greenhouse at different places throughout the length of the greenhouse. It was also found that the front of the greenhouse was generally warmer compared to the rest of the greenhouse environment. A comparison between the two- and three-dimensional case yielded significant differences. It can be concluded that care has to be taken when approximating the flow inside a greenhouse with a two-dimensional model.

In the last chapter, Chapter 9, the work done in this research study is summarized and concluded, and recommendations for future research are made.

CHAPTER 9

Conclusions

9.1 Chapter Review

This chapter discusses and summarizes the research done in this thesis. Conclusions are drawn and recommendations are made for possible future work related to CFD and greenhouses.

9.2 Summary

The objective of this research study was to evaluate multi-dimensional heat transfer effects in greenhouses. The investigation commenced by conducting research on the available literature . Different greenhouse designs were discussed, as well as the various parameters influencing the indoor climate of greenhouses. The influence of crop presence was investigated, and whether the number of spans of a greenhouse will have an influence on the indoor climate. Lastly the influence on indoor climate of plant benches were investigated. Different numerical methodologies were briefly investigated to ascertain which numerical methodology could be used to investigate the flow inside greenhouses. Computational Fluid Dynamics based on the Finite Volume Method was the method of choice. The numerical CFD work conducted in this research study was based on results using the commercially available CFD code, StarCCM+. The program and method used in this research proved useful in investigating the flow inside greenhouse cavities, and establishes a useful tool for industry to assess and improve the performance of greenhouses.

Several numerical models were created and successfully validated against data found in the literature. The numerical results in Chapters 4, 5 and 6 established confidence in the numerical models to further conduct parametric studies containing various design parameters. The numerical work in this research study commenced by investigating the heat transfer in a cavity representing a simple, single-span, zero degree greenhouse (square). This greenhouse CFD model was evaluated against data found in the literature. The numerical CFD model was then used to investigate and compare the thermal performance between a two-dimensional and three dimensional square greenhouse. The subsequent numerical models focused on

determining the effect of geometrical design alterations on a single span greenhouse. This model was also modified to investigate the differences between two- and three-dimensional single span greenhouses with nonzero roof angles. The influence of the size of a roll-up roof ventilator was also studied, as well as the whether the type of roof ventilator has an effect on the flow inside the greenhouse model. The small scale numerical greenhouse was used to construct a numerical model of a larger greenhouse and the results validated qualitatively. An initial two-dimensional CFD model of a multi-span greenhouse was validated against data found in the literature. This validated numerical model was then modified to a three-dimensional numerical model containing plant benches placed in an peninsular arrangement.

9.3 Conclusions and Research Contributions

In conclusion the following research contributions adding to the body of knowledge on design and simulation for greenhouses were made during the course of this thesis:

The literature review formed a critical part of the thesis by identifying potential areas that require more detailed investigation. The complexity of buoyancy driven flow was again highlighted, and it was found that reduced-scale models of buildings such as greenhouses can be utilized to obtain flow patterns and microclimate information inside the buildings. The literature review also indicated that there are very few published literature regarding natural convection in structures similar to greenhouses. The literature review also revealed a number of important articles that was used in this research study to validate the current novel CFD models for greenhouses.

A brief but relevant overview of CFD and the experimental background applicable to the research in this thesis was given in Chapter 3. The most important dimensionless numbers were identified, namely the Reynolds, Grashof and Rayleigh numbers proved useful in characterising the important distinguishing heat transfer effects in the greenhouse models.

Various cavities corresponding to basic structures often found in greenhouses were studied and presented in a novel manner to highlight the thermal effects in these structures in a logical and progressive manner. In chapter 4, a greenhouse with a zero-degree roof angle was validated against data published in the literature. A two-dimensional CFD model using the standard k-epsilon low-Reynolds number turbulence model was created; a reasonably good comparison was found, and the following additional Nusselt-Rayleigh relationship was deduced for the specific Rayleigh number ranges simulated:

$$Nu = 0.0589 Ra^{0.3422} \quad \text{9-1}$$

In order to validate a three-dimensional model of a zero degree roof greenhouse, a further three-dimensional CFD model was developed and once again compared to results published in the literature. A reasonably good comparison was also found for the three-dimensional cavity, the difference found when compared to the literature [117] was calculated to be 5.04%. To compare a two and three dimensional model of a greenhouse with a zero degree roof similar to the initial two-dimensional validated CFD model, another three-dimensional model heated from below and cooled from above was developed. Similar CFD parameters were used as in the validated cases. Small differences between the two and three dimensional cases was found. A difference of 1.8% in surface averaged Nusselt number was found for the two cases. It was also concluded that the numerical models in this chapter could be used to further investigate the influence of geometric design changes on the thermal performance of the cavity. All these CFD model results for the greenhouses add to the current body of knowledge on thermal effects in greenhouse design and simulation.

Chapter 5 was concerned with exploratory design effects in a single-span greenhouse model. The initial validated two-dimensional model in Chapter 4 was modified to include a pitched roof at different angles (10, 30,45 and 60 degrees respectively). Overall it was found that the effect of roof angle for all Rayleigh numbers was to increase the average heat transfer on the hot wall. Additional Nusselt-Rayleigh relationships that best fit the curves were deduced and are shown inTable 9.1. These relationships also add to the body of knowledge for greenhouse design and simulation in the simulated range of Rayleigh numbers.

Table 9.1: Nusselt-Rayleigh number relationships for pitched roof single-span greenhouse

Roof Angle	Nusselt-Rayleigh Relationship
10°	$Nu = 0.0646Ra^{0.3381}$
30°	$Nu = 0.0436Ra^{0.3613}$
45°	$Nu = 0.0405Ra^{0.3699}$
60°	$Nu = 0.061Ra^{0.3556}$

The differences between two and three-dimensional single-span greenhouses were also explored. The temperature and velocity contours at a plane section in the middle of the greenhouse (z/H = 0.5) were investigated and showed a significant differences for both the temperature and velocity contour plots. A distinctive clockwise rotating cell were noticed in the two-dimensional case, but were not as clear in the three-dimensional case, as the flow patterns

formed in three dimensions. It was noted that the front of the cavity was at a higher temperature compared to the back of the cavity. From velocity plots an increase in velocity in the top corner at the back of the cavity was noticeable. The average Nusselt number for the floor of the three-dimensional cavity was found to be 67.25, while for the two-dimensional case the average Nusselt number on the floor was 97.25.

The same single-span greenhouse model used initially in Chapter 5 was modified to include a roof ventilator of different sizes. The overall Nusselt number distribution on the floor of the cavity followed a similar trend for all the Rayleigh numbers, but was found to increase with increase in opening size. It was concluded that opening size have an influence on the convective heat transfer in the cavity, depending on the Rayleigh number. The influence was found to be larger for lower Rayleigh numbers. A polynomial type series was used to describe the Nusselt-Rayleigh number relationship, shown in Table 9.2. This also adds to the body of knowledge on design and simulation for greenhouses in the simulated range of Rayleigh numbers.

Table 9.2: Nusselt-Rayleigh number relationships for ventilated single-span greenhouse

Opening Size	Equation
3S/4	$Nu = -8E-26Ra^3 + 3E-16Ra^2 - 4E-07Ra + 299.5$
S/2	$Nu = -4E-26Ra^3 + 2E-16Ra^2 - 2E-07Ra + 182.33$
S/4	$Nu = -2E-26Ra^3 + 8E-17Ra^2 - 8E-07Ra + 118.6$

The difference in roof ventilator types were also investigated. The novel results obtained in this investigation indicated that the type of opening (roll-up or flap type) does have a limited influence on the heat transfer in the cavity, especially at lower Rayleigh numbers. The convective heat transfer in closed and ventilated cavities were compared for a specific Rayleigh number. For the ventilated cavity, heat transfer was found to decrease from the smallest Rayleigh number to Ra = 4.27 x 10^8, and increase again for the higher Rayleigh numbers. The closed cavity showed an increase in heat transfer for all Rayleigh numbers. The last numerical model investigated in chapter 5 was that of a scaled-up model which represented a larger greenhouse similar to the greenhouse investigated in the literature. The results were validated qualitatively and found to be similar, as the flow patterns observed were similar. Therefore confidence was established in the CFD model for modelling a single-span ventilated greenhouse.

A numerical model of a full-scale greenhouse was created and validated in chapter 6 again adding to the body of knowledge on greenhouse design in a novel manner. Reasonably good agreement was found between the velocity and temperature contour plots when the first two

spans (west spans) were compared. The temperature and velocity distribution at plant level were also compared, and the results were found to agree well with those published in the literature. Small discrepancies were found, and attributed to assumed properties of the greenhouse. Confidence was therefore established in the CFD model, and it can be concluded that a two-dimensional CFD model can be successfully used to investigate elements of the indoor climate of a full-scale multi-span greenhouse. The model was also used to investigate buoyancy driven flow only. The CFD simulation results obtained showed that the greenhouse is significantly warmer inside when no outside wind was present, and that a combination of wind and buoyancy driven flow will be more effective to cool the greenhouse.

In Chapter 7, a reduced-scale model of a large two-dimensional multi-span greenhouse was constructed and successfully validated using CFD. Various flow visualization techniques were tested, and the final method chosen was smoke and a laser sheet. The flow visualization method was used to illuminate the flow patterns, and the flow patterns were recorded by direct observation, as well as with a video camera. A numerical model was constructed using CFD, and the flow patterns observed in the experiments were similar to those observed in the simulations. The temperatures measured numerically correlated mostly with those measured experimentally, although some differences were noticed. The experiments were noticeably unsteady, and the unsteady nature of the flow was also noted in the numerical simulations. Video clips were taken, and used to calculate an average velocity of 0.06m/s inside the greenhouse. It can therefore be concluded that a reduced-scale model can be used to investigate flow patterns in a multi-span greenhouse, and that a CFD model of the reduced-scale greenhouse should also yield useful results.

Chapter 8 was dedicated to investigating a full-scale, multi-span greenhouse containing peninsular arranged plant benches. Overall, it was found that the microclimate at plant level was significantly influenced by the presence of plant benches, as temperature and velocity distributions varied quite considerably at plant level. When the two-dimensional case was compared to the three-dimensional case, significant differences were noted. These results are important to consider when planning further CFD research on greenhouse design.

9.4 Main Conclusions: In Reflection

In summary and reflecting on the research roadmap presented in the introduction to this thesis the following main conclusions can be drawn from this research study:

- Both two and three-dimensional CFD models can be used successfully to evaluate the heat transfer in cavities representing a single span greenhouses and multi-span

greenhouses albeit reflecting on different issues. The CFD models presented in this study can be used to evaluate reduced-scale or full-scale models

- Multi-dimensional heat transfer effects were noticed in all the cavities investigated. Therefor care has to be taken when investigating flow inside greenhouses using two-dimensional CFD models. The research purpose of the simulation always has to be taken into consideration
- Additional Nusselt-Rayleigh number relationships for specific Rayleigh number ranges were deduced for single-span pitched roof greenhouses, and can be useful for greenhouse designers
- The addition of a ventilator to the roof of a single-span greenhouse does have an influence on the heat transfer inside the cavity
- The type of ventilator does not have a significant influence on the heat transfer inside the cavity
- Nusselt-Rayleigh relationships have been established for closed and ventilated single-span greenhouses. These relationship can be useful for designer when evaluating thermal characteristics of single-span greenhouses
- It is possible to investigate the flow inside a full-scale greenhouse using a reduced scale greenhouse as long as the Grashof numbers fall in the turbulent regime for both models.
- Experimental results are highly turbulent and unsteady
- A three-dimensional CFD model based on a reduced-scale model can be used to further investigate flow patterns inside a full-scale greenhouse
- The presence of plant benches, particularly peninsular arranged plant benches has a significant influence on the indoor climate at plant level inside a multi-span greenhouse.

9.5 Recommendations for Future Research

The following topics can be addressed in future to advance the work done in this thesis:

- The effect of adding partitions to the greenhouse on the indoor climate. This is often used to create different climates for different plant species
- The influence of wind direction in three-dimensions on the microclimate inside the greenhouse containing plant benches.
- Model the glass walls of the three-dimensional CFD models as a solid instead of baffles, to further investigate multidimensional heat transfer through the greenhouse walls as well.

- The effect of the crop can be included together with the bench layouts. The plants in this study were ignored as they were small with a low transpiration rate, but can be represented by porous baffles in the CFD model.

Bibliography

[1] M. Djevic and A. Dimitrijevic, "Greenhouse Energy Consumption and Energy Efficiency".

[2] S. Wang and J. Deltour, "Theoretical Study of Natural Ventilation flux in a Single Span Greenhouse," *Biotech.Agron.Soc.Environ,* vol. 5, no. 4, pp. 256-263, 1998.

[3] M. A. Lamrani, T. Boulard, J. C. Roy and A. Jaffrin, "Airflows and Temperature Patterns induced in a Confined Greenhouse," *Journal of Agricultural Engineering Research,* vol. 78, no. 1, pp. 75-88, 2001.

[4] T. Basak, S. Roy and A. R. Balakrishnan, "Effects of thermal boundary conditions on natural Convection Flows within a Sqaure Cavity," *International Journal of Heat and Mass Transfer,* vol. 49, pp. pp 4525-4535, 2006.

[5] S. Kruger and L. Pretorius, "The Effect of Internal Obstructions in Naturally Ventilated Greenhouse Applications," in *5th International Conference on Heat Transfer, Fluid Mechanics and Thermodynamics*, Sun City, South Africa, 2007.

[6] S. Kruger and L. Pretorius, "The Effect of Various Inlet Boundary Conditions On the Indoor Climate of A Four Span Naturally Ventilated Greenhouse," in *Sixth South African Conference on Computational and Applied Mechanics (SACAM)*, Cape Town, South Africa, 2008.

[7] S. Kruger and L. Pretorius, "Comparison of Indoor Climate In Detached And Multi-Span Greenhouses," in *6th International Conference on Heat Transfer, Fluid Mechanics and Thermodynamics*, Pretoria, South Africa, 2008.

[8] L. Pretorius, S. J. Benade and S. Kruger, "Technology Forecasting: The Case of Computational Fluid Dynamics (CFD)," in *4th IEEE International Conference on Management of Innovation and Technology*, Bangkok, Thailand, 2008.

[9] S. Kruger and L. Pretorius, "Comparison Of The Indoor Climate In Multi-Span And Detached Greenhouses With Various Ventilator Configurations," in *ASME International*

Mechanical Engineering Congress and Exposition, Boston, USA, 2008.

[10] S. Kruger and L. Pretorius , "An Assessment of Different Boundary Conditions in a Naturally Ventilated Venlo-Type Greenhouse," in *Proceedings of the International Heat Transfer Conference, IHTC14*, Washington DC, USA, 2010.

[11] S. Kruger and L. Pretorius , "The Effect Of Time-Varying Wind Direction on the Indoor Climate of a Naturally Ventilated Greenhouse," in *ASME International Mechanical Engineering Congress and Exposition*, Vancouver, Canada, 2010.

[12] S. Kruger and L. Pretorius, "The Effect of Bench Arrangements on The Indoor Climate of Naturally Ventilated Greenhouses," in *8th International Conference on Heat Transfer, Fluid Mechanics and Thermodynamics*, Pointe Aux Piments, Mauritius, 2011.

[13] S. Kruger and L. Pretorius, "Numerical Investigation of Natural Convection in a Mono-Span Greenhouse," in *ASME 11th Biennial Conference On Engineering Systems Design And Analysis,* , Nantes, France, 2012.

[14] S. Kruger and L. Pretorius, "Analysis of Natural Convection in a Mono-Span Naturally Ventilated Greenhouse," in *Eigth South African Conference on Computational and Applied Mechanics (SACAM)*, Johannesburg, South Africa, 2012.

[15] S. Kruger and L. Pretorius , "The Effect Of Bench Arrangments on the Natural Ventilation of A Multispan Greenhouse," in *ASME International Mechanical Engineering Congress and Exposition, November*, San Diego, USA, 2013.

[16] S. Kruger and L. Pretorius, "The effect of vertical and horizontal partitions on natural convection in a heated enclosure," in *ASME 2013 Summer Heat Transfer Conference*, Minneapolis, USA, 2013.

[17] S. Kruger and L. Pretorius , "Effect Of Boundary Conditions and Ventilator Size on the Natural Convection in A Naturally Ventilated Greenhouse," in *International Heat Transfer Conference, IHTC15*, Kyoto, Japan, 2014.

[18] S. Kruger and L. Pretorius, "Comparison of the Indoor Climate in multi-span and detached greenhouses with various ventilator configurations," in *IMECE2008*, Boston, Massachusetts, USA, 2008.

[19] H. S. Paris and J. Janick, "What the Roman Emperor Tiberius Grew in his Greenhouse," in *Proceedings of the IXth EUCARPIA meeting on genetics and breeding*, Avignon, 2008.

[20] M. H. Jensen and A. j. Malter, Protected Agriculture - A Global Review, Washington DC: The International Bank for Reconstruction and Development, 1995.

[21] ASHRAE, "Fundamentals," in *2005 ASHRAE Fundamentals Handbook*, Atlanta, ASHRAE, 2005.

[22] D. L. Critten and B. j. Bailey, "A review of greenhouse engineering developments during the 1990's," *Agricultural and Forest Meteorology,* vol. 112, pp. 1-22, 2002.

[23] T. Boulard , S. Wang and R. Haxaire, "Mean and Turbulent Air Flows and Microclimatic patterns in an empty greenhouse tunnel," *Agricultural and Forest Meteorology,* vol. 100, pp. 169-181, 2000.

[24] T. Norton, D. Sun, J. Grant, R. Fallon and V. Dodd, "Applications of Computational Fluid Dynamics (CFD) in the Modelling and Design of Ventilation Systems in the Agricultural Industry: A Review," *Bioresource Technology,* vol. 98, pp. 2386-2414, 2007.

[25] A. Mistriotis, T. De Jong, M. J. M. Wagemans and G. P. A. Bot, "Computational Fluid Dynamics (CFD) as a tool for the Analysis of Ventilation and Indoor Climate in Agrigultural Buildings," *Netherlands Journal of Agricultural Science,* vol. 45, pp. pp 81-96, 1997.

[26] S. Wang, T. Boulard and R. Haxaire, "Air speed profiles in a naturally ventilated greenhouse with a tamato crop," *Agricultural and Forest Meteorology,* vol. 96, pp. pp 181-188, 1999.

[27] E. J. Baeza, J. J. Perez-Parra, J. I. Montero, B. J. Bailey, J. C. Lopez and J. C. Gazquez, "Analysis of the role of sidewall venta on buoyance-driven natural ventilation in parral-type greenhouse with and without insect Screens using Computational Fluid Dynamics," *Biosystems Engineering,* vol. 104, pp. pp 86-96, 2009.

[28] T. Boulard , S. Wang and R. Haxaire , "Mean and Turbulent air flows and microclimatic patterns in an empty greenhouse tunnel," *Agricualtural and Forest Meteorology,* vol. 100, p. 169 – 181, 2000.

[29] J. Boodley, The Commercial Greenhosue, New York: Delmar Publishers, 1998.

[30] E. Shilo, M. Teitel, Y. Mahrer and T. Boulard, "Airflow patterns and heat fluxes in roof-ventilated multi-span greenhouse with insect-proof screens," *Agricultural and Forest Meteorology,* vol. 122, pp. pp 3-20, 2004.

[31] "Greenhouse Types and Structures," [Online]. Available: http://faculty.yc.edu/ycfaculty/ags250/week04/greenhouse_types_and_structures/Greenhouse_types_and_structures_print.html. [Accessed 21 08 2013].

[32] M. Brugger, J. Montero, E. Baezz and J. Perez-Parra, "Computational Fluid Dynamic Modeling to Improve the Design of the Spanish Parral Style Greenhouse," *Acta Horticulturae,* vol. 361, 2005.

[33] T. Bartzanas, T. Boulard and C. Kittas , "Effect of Vent Arrangement on Windward Ventilation of a Tunnel Greenhouse," *Biosystems Engineering,* vol. 2, pp. pp 479-490, 2004.

[34] P. E. Bournet, S. A. Ould Khaoua and T. Boulard, "Numerical prediction of the effect of vent arrangements on the ventilation and energy transfer in a multi-span glasshouse using a bi-band radiation model," *Biosystems Engineering,* vol. 98, no. 2, pp. pp 224-234, 2007.

[35] M. Teitel, M. Barak and Y. Zhao, "Ventilation of a Greenhouse with Continuous Roof and Side Vents," *Acta Horticulturae,* vol. 719, 2006.

[36] S. Kruger and L. Pretorius, "The Effect Of Ventilator Configurations In Naturally Ventilated Greenhouse Applications," in *Proceedings of the 10th UK National Heat Transfer Conference*, Edinburgh, Scotland, UK, 2007.

[37] F. D. Molina-Aiz, D. L. Valera, A. A. Pena, A. J. Alvarez and J. A. Gil, "Analysis of the Effect of Rollup Vent Arrangement and Wind Speed on Almería-type Greenhouse Ventilation Performance Using Computational Fluid Dynamics," *Acta Horticulturae,* vol. 719, 2006.

[38] F. D. Molina-Aiz, D. L. Valera, A. A. Peña and J. A. Gil, "Optimisation of Almería-type Greenhouse Ventilation Performance with Computational Fluid DynamicsOptimisation of Almería-type Greenhouse Ventilation Performance with Computational Fluid Dynamics," *Acta Horticulturae (ISHS),* vol. 691, 2005.

[39] C. Kittas and T. Bartzanas, "Greenhouse Microclimate and Dehumidification effectiveness

under different ventilator configurations," *Building and Environment,* 2006.

[40] T. Boulard, C. Kittas and P. Feuilloley, "Natural Ventilation Performance of Six Greenhouse and Tunnel Types," *Journal of Agricultural Engineering Research,* vol. 67, p. 249 – 266, 1997.

[41] E. J. Baeza, J. Perez-Parra and J. I. Montero, "Effect of Ventilator Size on Natural Ventilation in Parral Greenhouse by Means of CFD Simulations," *Acta Hort,* vol. 691, 2005.

[42] C. Kittas, T. Boulard, M. Mermier and G. Papadakis, "Wind Induced Air Exchange Rates in a Greenhouse Tunnel with Continuous Side Openings," *Journalf of Agricultural Engineering Research,* vol. 65, pp. pp 37-49, 1996.

[43] P. E. Bournet and T. Boulard, "Effect of ventilator configuration on the distributed climate of greenhouses:A review of experimental and CFD studies," *Computers and Electronics in Agriculture,* vol. 74, pp. pp 195 - 217, 2010.

[44] F. J. Baptista, B. J. Bailey, J. M. Randall and J. F. Meneses, "Greenhouse Ventilation Rate: Theory and Measurement with Tracer Ga Techniquess," *Journal of Agricultural Engineering Research,* vol. 72, pp. pp 636 - 374, 1999.

[45] N. Chandrawanshi, S. D. Upadhyaya, P. S. Nayak, S. Paroha and A. B. Tiwari, "Growth and Yield Quality Parameter of Phyllanthus Amarus as Affected by Moisture and Temperature Stress Factors," *JOURNAL OF STRESS PHYSIOLOGY & BIOCHEMISTRY,* vol. 9, no. 2, 2013.

[46] M. Barbora and L. Ales, "Influence of Temperature and Light Conditions on Germination, Growth and Conidiation of Oidium neolycopersici," *J Phytopathol,* vol. 158, pp. 616-627, 2010.

[47] Y. Zhao, M. Teitel and M. Barak, "Vertical Temperature and Humidity Gradients in a Naturally Ventilated Greenhouses," *Journal of Agricultural Engineering Research,* vol. 78, no. 4, pp. pp 431-436, 2001.

[48] S. Sase, T. Takakura and M. Nara, "Wind Tunnel Testing on Airflow and Temperature Distribution of a Naturally Ventilated Greenhouse," *Acta Horticulturae,Energy in Protected Cultivation,* vol. 148, 1984.

[49] S. Ould Khaoua, P. Bournet, C. Migeon and G. Chasseriaux, "Analysis of Greenhouse Ventilation Efficiency based on Computational Fluid Dynamics," *Biosystems Engineering,*

pp. 83-98, 2006.

[50] H. Fatnassi, T. Boulard, C. Poncet and R. Suay-Cortes, "3D CFD Modelling and Validation of the Distributed Climate in a Full-Scale Multi-span Plastic House," *Acta Horticulturae,* vol. 893, 2011.

[51] K. Popovski, "Greenhouse Climate Factors," *GHC Bulletin,* January 1997.

[52] W. Vandre, "Controlling the Greenhouse Environment," University of Alaska Fairbanks Cooperative Extenstion Service, Fairbanks, 2013.

[53] W, S. Wang and J. Deltour, "Lee-side Ventilation-induced Air Movement in a Large-scale Multi-span Greenhouse," *Journal of Agricultural Engineering Research,* vol. 74, pp. 103-110, 1999.

[54] M. Teitel, G. Ziskind, O. Liran, V. Dubovsky and R. Letan, "Effect of wind Direction on greenhouse ventilation rate, airflow patterns and temperature distributions," *Biosystems Engineering,* pp. pp 1-19, 2008.

[55] T. Boulard, G. Papadakis, C. Kittas and M. Mermier, "Air flow and associated sensible heat exchanges in a naturally ventilated greenhouse," *Agricultual and Forest Meteorology,* vol. 88, pp. pp 111-119, 1997.

[56] J. C. Roy, T. Boulard, C. Kittas and S. Wang, "Convective and Ventilation Transfers in Greenhouses, Part 1: the Greenhouse considered as a Perfectly Stirred Tank," *Biosystems Engineering,* vol. 83, no. 1, pp. pp 1 - 20, 2002.

[57] E. Shilo, M. Teitel, Y. Mahrer and T Boulard, "Air-flow patterns and heat fluxes in roof-ventilated multi-span greenhouse with insect-proof screens," *Agricultural and Forest Meteorology,* vol. 122, pp. pp 3 - 20, 2004.

[58] H. Fatnassi, T. Boulard and J. Lagier, "Simple Indirect Estimation of Ventilation and Crop Transpiration Rates in a Greenhouse," *Biosystems Engineering ,* vol. 88, no. 4, pp. pp 467 - 478, 2004.

[59] N. Katsoulas, T. Bartzanas, T. Boulard, M. Mermier and C. Kittas, "Effect of Vent Openings and Insect Screens on Greenhouse Ventilation," *Biosystems Engineering,* vol. 93, no. 4, pp. pp 427 - 436 , 2006.

[60] A. Kichah, P. E. Bournet, C. Migeon and T. Boulard, "Measurement and CFD simulation of microclimate characteristics and transpiration of an Impatiens pot plant crop in a greenhouse," *Biosystems Engineering,* vol. 112, pp. pp 22 - 34, 2012.

[61] G. Papadakis, A. Frangoudakis and S. Kyritsis, "Mixed,Forced and Free Convection Heat Transfer at the Greenhouse Cover," *Journal of Agricultural Engineering Research,* vol. 51, pp. 191-205, 1992.

[62] C. Kittas, B. Draoui and T. Boulard, "Quantification of the ventilation of a greenhouse with a Roof Opening," *Agricultural and Forest Meteorology,* vol. 77, pp. pp 95 -111, 1995.

[63] J. A. Businger, "De invloed van raamstanden op de ventilatie van Kassen (The influence of window openings on the ventilation of greenhouses," *Meded. Dir. Tuinbouw (Neth.),* 1954.

[64] J. I. Montero, A. Anton, R. Kamaruddin and B. J. Bailey, "Analysis of Thermally Driven Ventilation in Tunnel Greenhouses using small scale models," *Journal of Agricultural Engineering Research,* vol. 79, no. 2, pp. pp 213 - 222, 2001.

[65] J. Oca, J. I. Montero, A. Anton and D. Crespo, "A Method for Studying Natural Ventilation by Thermal Effects in a Tunnel Greenhouse using Laboratory Scale Models," *Journal of Agricultural Engineering Research,* vol. 72, pp. 93-104, 1999.

[66] T. Boulard, R. Haxaire, M. A. Lamrani, J. C. Roy and A. Jaffrin, "Characterization and Modelling of the Air Fluxes induced by Natural Ventilation in a Greenhouse," *Journal of Agricultural Engineering Research,* vol. 74, pp. pp 135 - 144, 1999.

[67] P. Munoz, J. I. Monterp, A. Anton and F. Giuffrida, "Effect of Insect-proof Screens and Roof Openings on Greenhouse Ventilation," *Journal of Agricultural Engineering Research,* vol. 73, pp. pp 171 - 178, 1999.

[68] G. Gan, "Simulation of buoyancy-driven natural ventilation of buildings—Impact of computational domain," *Energy and Buildings,* vol. 42, pp. pp 1290-1300, 2010.

[69] G. P. Bot, Greenhouse Climate - from Physical Processes to a Dynamic Model, Wagengin, 1983.

[70] N. Tadj, T. Bartzanas, B. Draoui, G. Theodoridis and C. Kittas, "Convective Heat Transfer in a Tunnel cultivated Greenhouse," *International Journal of Applied Engineering Research,*

vol. 3, no. 9, pp. 1161-1168, 2008.

[71] A. Mistriotis, C. Arcidiacono, P. Picuno and G. Scarascia-Mugnozza, "Computational analysis of ventilation in greenhouses at zero- and low-wind-speeds," *Agricultural and Forest Meteorology,* vol. 88, no. 121-135, 1997.

[72] J. B. Campen and G. P. A. Bot, "Determination of Greenhouse-specific Aspects of Ventilation using Three-dimensional Computational Fluid Dynamics," *Biosystems Engineering,* vol. 84, no. 1, pp. pp 69-77, 2003.

[73] A. Shklyar and A. Arbel, "Numerical model of the three-dimensional Isothermal flow patterns and mass fluxes in a pitch-roof Greenhouse," *Journal of Wind Engineering and Industrial Aerodynamics,* vol. 92, pp. 1039-1059, 2004.

[74] R. Haxaire, T. Boulard and M. Mermier, "Greenhouse Natural Ventilation by Wind Forces," *Acta Horticulturae,* vol. 534, pp. pp 31 - 40, 2000.

[75] H. Majdoubi, T. Boulard, H. Fatnassi and L. Bouirden, "Airflow and microclimate patterns in a one-hectare Canary type greenhouse:An experimental and CFD assisted study," *Agricultural and Forest Meteorology,* vol. 149, pp. pp 1050-1062, 2009.

[76] I. B. Lee, S. W. Hong, H. S. Hwang and I. H. Seo, "Study on Ventilation Efficiencies of Naturally Ventilated Multi-Span Greenhouses in Korea," *Acta Horticulturae,* vol. 719, 2006.

[77] T. Boulard, J. C. Roy, H. Fatnassia, A. Kichah and I. B. Lee, "Computer fluid dynamics prediction of climate and fungal spore transfer in a rose Greenhouse," *Computers and Electronics in Agriculture,* vol. 74, pp. pp 280-292, 2010.

[78] X. Wang, J. Luo and X. Li, "CFD Based Study of Heterogeneous Microclimate in a Typical Chinese Greenhouse in Central China," *Journal of Integrative Agriculture,* vol. 12, no. 5, pp. pp 914-923, 2013.

[79] A. Mistriotis, G. P. A. Bot, P. Picuno and G. Scarascia-Mugnozza, "Analysis of the efficiency of greenhouse ventilation using computational fluid dynamics," *Agricultural and Forest Meteorology,* vol. 85, pp. pp 217-228, 1997.

[80] M. A. Schnelle and J. M. Dole, "Division of Agricultural Sciences and Natural Resources," [Online]. Available: http://pods.dasnr.okstate.edu/docushare/dsweb/Get/Document-

1287/HLA-6703web.pdf. [Accessed 1 April 2011].

[81] L. Jacobsen and O. F. Nielsen, "Modelling Airflow Rate through Perforated Benches in Greenhouses," *CIGR Journal of Scientific Research and Development,* vol. 6, 2004.

[82] V. Sethi and R. K. Dubey, "Optimal space utilization of a greenhouse using multi-rack tray system:Thermal modeling and experimental validation," *Energy Conversion and Management,* vol. 49, pp. pp 2890 - 2899, 2008.

[83] S. Reichrath, F. Ferioli and T. W. Davies, "A Simple Computational Fluid Dynamics (CFD) Model of a Tomato Glasshouse," *Acta Horticulturae,* vol. 534, 2000.

[84] F. D. Molina-Aiz, D. L. Valera and A. J. Álvarez, "Measurement and simulation of climate inside Almería-type greenhouses using computational fluid dynamics," *Forest Meteorology,* vol. 125, pp. pp 33 - 51, 2004.

[85] S. Reichrath and T. W. Davies, "Computational Fluid Dynamics Simulations and validation of the Pressure Distribution on the roof of a Commercial Multi-span Venlo-type Greenhouse," *Journal of Wind Engineering and Industrial Aerodynamics,* vol. 90, pp. pp 139 - 149, 2002.

[86] I. B. Lee, S. W. Hong, H. S. Hwang and I. H. Seo, "Study on Ventilation Efficiencies of Naturally Ventilated Multi-Span Greenhouses in Korea," *Acta Horticulturae,* vol. 719, 2006.

[87] K. J. Hsieh and F. S. Lien, "Numerical modeling of buoyancy-driven turbulent flows in enclosures," *International Journal of Heat and Fluid Flow,* vol. 25, pp. pp 659 - 670, 2004.

[88] J. C. Roy and T. Boulard, "CFD Prediction of the Natural Ventilation in a Tunnel-Type Greenhouse: Influence of Wind Direction and Sensibility to Turbulence Models," *Acta Horticulturae,* vol. 691, 2005.

[89] R. Nebbali, J. C. Roy, T. Boulard and S. Makhlouf, "Comparison of the Accuracy of Different CFD Turbulence Models for the Prediction of the Climatic Parameters in a Tunnel Greenhouse," *Acta Horticulturae,* vol. 719, 2006.

[90] CD-Adapco, StarCCM+ User Manual, 6.02 ed., CD-Adapco, 2011.

[91] A. Bejan and A. D. Krauss, "Natural Convection," in *Heat Transfer Handbook*, John Wiley

and Sons, 2003.

[92] T. Boulard, C. Kittas, J. C. Roy and S. Wang, "Convective and Ventilation Transfers in Greenhouses, Part 2 - Determination of the Distributed Greenhouse Climate," *Biosystems Engineering ,* vol. 83, no. 2, pp. pp 129 - 147, 2002.

[93] M. Sathiyamoorthy, T. Basak, S. Roy and I. Pop, "Steady natural convection flows in a square cavity with linearly heated side wall(s)," *International Journal of Heat and Mass Transfer,* vol. 50, pp. pp 766-775, 2007.

[94] W. Wu, D. Ewing and C. Y. Ching, "The effect of the top and bottom wall temperatures on the laminar natural convection in an air-filled square cavity," *International Journal of Heat and Mass Transfer,* vol. 49, pp. pp 1999-2008, 2006.

[95] H. N. Dixit and V. Babu, "Simulation of high Rayleigh number natural convection in a square cavity using the lattice Boltzmann method," *International Journal of Heat and Mass Transfer,* vol. 49, pp. pp 727-739, 2006.

[96] F. Ampofo and T. G. Karayiannis, "Experimental benchmark data for turbulent natural convection in an air filled square cavity," *International Journal of Heat and Mass Transfer,* vol. 46, pp. pp 3551-3572, 2003.

[97] J. Salat, S. Xin, P. Joubert, A. Sergent, F. Penot and P. Le Quere, "Experimental and numerical investigation of turbulent natural convection in a large air-filled cavity," *International Journal of Heat and Fluid Flow,* vol. 25, pp. pp 824 - 832, 2004.

[98] A. Bairi, "Nusselt–Rayleigh correlations for design of industrial elements: Experimental and numerical investigation of natural convection in tilted square air filled enclosures," *Energy Conversion and Management,* vol. 49, pp. 771 - 782, 2008.

[99] J. Rasoul and P. Prinos, "Natural Convection in an inclined enclosure," *International Journal of Numerical Methods for Heat and Fluid Flow,* vol. 7, no. 5, pp. pp 438 - 478, 1997.

[100] W. H. Leong, K. G. T. Hollands and A. P. Brunger, "On a physically!realizable benchmark problem in internal natural convection," *International Journal of Heat and Mass Transfer,* vol. 41, pp. pp 3817 - 3828, 1998.

[101] D. W. Crunkleton and T. J. Anderson, "A numerical study of flow and thermal fields in tilted Rayleigh–Bénard convection," *International Communications in Heat and Mass*

Transfer, vol. 33, pp. pp 24 - 29, 2006.

[102] J. T. Lir and T. F. Lin, "Visualization of roll patterns in Rayleigh–Bénard convection of air in a rectangular shallow cavity," *International Journal of Heat and Mass Transfer,* vol. 44, pp. pp 2889-2902, 2001.

[103] A. Bairi, N. Laraqi and J. M. Garcia de Maria, "Numerical and experimental study of natural convection in tilted parallelepipedic cavities for large Rayleigh numbers," *Experimental Thermal and Fluid Science,* vol. 31, pp. pp 309 - 324, 20075.

[104] M. Corcione, "Effects of the thermal boundary conditions at the sidewalls upon natural convection in rectangular enclosures heated from below and cooled from above," *International Journal of Thermal Sciences,* vol. 42, pp. pp 199-208, 2003.

[105] F. S. Zaman, T. S. Turja and M. Molla, "Buoyancy Driven Natural Convection Flow in an Enclosure with Two Discrete Heating from below," *Procedia Engineering,* vol. 56, pp. pp 104 - 111, 2013.

[106] S. A. Said, M. A. Habib and M. A. Khan, "Turbulent Natural Convecion Flow in Paritioned Enclosures," *Computers and Fluids,* vol. 26, no. 6, pp. pp 541 - 563, 1997.

[107] E. Bilgen and A. Muftuoglu, "Natural convection in an open square cavity with slots," *International Communications in Heat and Mass Transfer,* vol. 35, pp. pp 896 - 900, 2008.

[108] E. Bilgen and H. Oztop, "Natural convection heat transfer in partially open inclined square cavities," *International Journal of Heat and Mass Transfer,* vol. 48, pp. pp 1470 - 1479, 2005.

[109] E. Fontana, A. da Silva and V. C. Mariani, "Natural convection in a partially open square cavity with internal heat source: An analysis of the opening mass flow," *International Journal of Heat and Mass Transfer,* vol. 54, p. 1369–1386, 2011.

[110] M. Prakash, S. B. Kedare and J. K. Nayak, "Numerical study of natural convection loss from open cavities," *International Journal of Thermal Sciences,* vol. 51, pp. 23 - 30, 2012.

[111] K. Vafai and J. Ettefagh, "Thermal and Fluid Flow Instabilities in buoyancy-driven flows in open-ended cavities," *International Journal of Heat and Mass Transfer,* vol. 33, no. 10, pp. pp 2329-2344, 1990.

[112] O. Polat and E. Bilgen, "Laminar natural convection in inclined open shallow cavities," *International Journal of Thermal Sciences,* vol. 41, pp. pp 360 - 368, 2002.

[113] S. K. S. Boetcher and E. M. Sparrow, "Buoyancy-induced flow in an open-ended cavity: Assessment of a similarity solution and of numerical simulation models," *International Journal of Heat and Mass Transfer,* vol. 52, pp. pp 3850 - 3856, 2009.

[114] E. Ntibarufata, M. Hasnaoui, ,. E. Bilgen and P. Vasseur, "Natural Convection in Partitioned Enclosures with Localized Heating," *International Journal of Numerical Methods for Heat & Fluid Flow,* vol. 3, no. 2, pp. pp 133-143, 1993.

[115] A. Alamiri, K. Khanafer and I. Pop, "Buoyancy-induced flow and heat transfer in a partially divided square enclosure," *International Journal of Heat and Mass Transfer,* vol. 52, pp. pp 3818-3828, 2009.

[116] F. Ampofo, "Turbulent natural convection of air in a non-partitioned or partitioned cavity with differentially heated vertical and conducting horizontal walls," *Experimental Thermal and Fluid Science,* vol. 29, pp. pp 137 - 157, 2005.

[117] N. A. Kurecki and O. Ozcan, "An experimental and Numerical Study of Laminar Natural Convection in a differentially-heated Cubical Enclosure," *Journal of Therrmal Science and Technology,* vol. 32, no. 1, pp. 1-8, 2012.

[118] A. W. Date, Introduction to Computational Fluid Dynamics, New York: Cambridge University Press, 2005.

[119] J. Blazek, Computational Fluid Dynamics: Principles and Applications, Elsevier, 2005.

[120] M. M. Nasr-Azadani and E. Meiburg, "Turbidity currents interacting with three-dimensional seafloor topography," *Journal of Fluid Mechanics,* vol. 745, pp. 409-443, 2014.

[121] CD-Adapco, "CD-Adapco," [Online]. Available: http://www.cd-adapco.com. [Accessed 9 October 2014].

[122] J. Blazek, Computational Fluid Dynamics: Principles and Applications, Oxford: Elsevier, 2001.

[123] H. K. Versteeg and W. Malalasekera, An introduction to Computational Fluid Dynamics, The Finite Volume Method,2nd Ed, England: Pearson Prentice Hall, 2007.

[124] J. D. Anderson, Computational fluid dynamics. The basics with applications, New York: McGraww-Hill, 1995.

[125] P. W. McDonald, "The Computation of Transonic Flow through Two-Dimensional Gas Turbine Cascades," in *ASME*, 1971.

[126] E. Dick, Introduction to Finite Element Methods in Computational Fluid Dynamics, Berlin Heidelberg: Springer-Verlag, 2009.

[127] M. J. Turner, R. W. Clough, H. C. Martin and L. P. Topp, "Stiffness and Deflection of Complex Structures," *Journal of the Aeronautical Society,* vol. 23, p. 805, 1956.

[128] S. V. Patankar and D. B. Spalding, "A calculation procedure for heat, mass and momentum transfer in three-dimensional parabolic flows," *Int. J . Heat AIass Transfer,* vol. 15, pp. 1787-1806, 1972.

[129] S. V. Patankar and D. B. Spalding, "A Calculation procedure for Heat, Masas and Momentum Transfer in Three-dimensional Parabolic Flows," *International Journal of Mass Transfer,* vol. 15, p. 1787, 1972.

[130] S. V. Patankar and D. B. Spalding, "A Calculation Procedure for Heat Mass and Momentum transfer in Three-Dimensional Parabolic Flows," *Int J. Heat and Mass Transfer,* vol. 15, p. pp1787, 1971.

[131] S. V. Patankar, Numerical Fluid Flow and Heat Transfer, New York: Hemisphere, 1980.

[132] CD-Adapco, "StarCCM+ User Guide," CD-Adapco, 2012.

[133] I. B. Celik, "Introductory Turbulence Modeling - Lecture Notes," West Virginia University, Morgantown, West Virginia, 1999.

[134] P. K. Kundu and I. M. Cohen, Fluid Mechanics, 3rd ed., California: Elsevier, 2004.

[135] L. Davisdon , "An Introduction to Turbulence Models," CHALMERS UNIVERSITY OF TECHNOLOGY, Goteborg, Sweden, 2011.

[136] P. J.-Y. Yu, "Course Notes: ESS 55: Earth's Atmosphere," [Online]. Available: http://www.ess.uci.edu/~yu/class/ess228/lecture.4.vorticity.all.pdf. [Accessed 28 April 2015].

[137] B. E. Launder and B. Spalding, "The Numerical Computation of Turbulent Flows," *Methods Appl Mech Eng,* vol. 3, pp. 269-289, 1974.

[138] R. A. Henkes, F. F. van der Vlugt and C. J. Hogendoorn, "Natural Convection flow in a square cavity calculated with low-Reynolds-number turbulence models," *International Journal of Heat and Mass Transfer,* vol. 2, pp. 377-388, 1991.

[139] D. C. Wilcox, Turbulence Modelling for CFD, Glendale: DCW Industries, 1994.

[140] C. E. Walker, Methodology for the evaluation of natural ventilation in buildings using a reduced-scale air model - PhD Thesis, Boston: Massachusetts Institute of Technology, 2006.

[141] D. Etheridge, "Natural Ventilation in Buildings - Theory, Measurement and Design," John Wiley & Sons Ltd, 2012.

[142] M. S. Imbabi, "A General Procedure for the Small-scale Modelling of Buildings," *International Journal of Energy Research,* vol. 14, pp. 311-321, 1990.

[143] H. Awbi, Ventilation of Buildings, London: Spon Press, 2003.

[144] D. J. Nevrala, Modelling of Air Movement in Rooms. PhD Thesis, UK: Cranfield Institute of Technology, 1979.

[145] F. P. Incropera and D. P. De Witt, Introduction to Heat Transfer, Singapore: Wiley, 1990.

[146] P. H. Oosthuizen and D. Naylor, An Introduction to Convective Heat Transfer Analysis, Singapore: WCB/McGraw-Hill, 1999.

[147] K. Richards, M. Schatzmann and B. Leitl, "Wind tunnel experiments modelling the thermal effects within the vicinity of a single block building with leeward wall heating," *Journal of Wind Engineering and Industrial Aerodynamics,* vol. 94, pp. pp 621-636, 2006.

[148] D. Etheridge and M. Sandberg, Building Venilation - Theory and Measurement, New York: John Wiley & Sons, 1996.

[149] K. Hagstrom, Influence of Kinetic Energy Sources and Internal Obstructions on Room Air Conditioning Strategy, Efficiency of Ventilation and Room Velocity Conditions, Helsinki: Helsinki University, 2002.

[150] B. Metais and E. R. G. Eckert, "Forced,mixed and free convection regimes," *Trans ASME, Journal of Heat Transfer,* 1964.

[151] A. J. Smits and T. T. Lim, Flow Visualization - Techniques and Examples, London: Imperial College Press, 2000.

[152] C. Tropea, A. L. Yarin and J. F. Foss, Springer Handbook of Experimental Fluid Mechanics, Berlin: Springer-Verlag, 2007.

[153] R. W. Hale, P. Tan and D. E. Ordway, "Experimental Investigation of Several Neutrally-Buoyant Bubble Generators for Aerodynamic Flow Visualization," *Naval Research Reviews,* pp. 19-24, June 1971.

[154] SAGE Action Inc, "Bubble Generator Systems," Sage Action Inc, [Online]. Available: www.sageaction.com. [Accessed 25 09 2013].

[155] S. A. Inc, "Sage Action Inc Bubble Generator Systems," [Online]. [Accessed 9 October 2014].

[156] N. A. Kurekci and O. Ozcan, "An Experimental and Numerical Study of Laminar Natural Convection in a Differentially-heated Cubical Enxlosure," *Journal of Thermal Science and Technology,* vol. 32, no. 1, pp. 1-8, 2012.

[157] M. Aounallah, Y. Addad and S. Benhamadouche, "Numerical investigation of turbulent natural convection in an inclined square cavity with a hot wavy wall," *International Journal of Heat and Mass Transfer,* vol. 50, pp. pp 1683-1693, 2007.

[158] R. A. Henkes, F. F. van der Vlugt and C. J. Hogendoorn, "Natural Convection flow in a square cavity calculated with low-Reynolds-number turbulence models," *International Journal of Heat and Mass Transfer,* vol. 2, pp. 377-388, 1991.

[159] H. S. Dol and K. Hanjalic, "Computational study of turbulent natural convection in a side-heated near-cubic enclosure at a high Rayleigh number," *International Journal of Heat and Mass Transfer,* vol. 44, pp. 2323-2344, 2001.

[160] E. Bilgen, "Natural convection in cavities with a thin fin on the hot wall," *International Journal of Heat and Mass Transfer,* vol. 48, pp. 3493-3505, 2005.

[161] A. Baïri , E. Zarco-Pernia and J. M. García de Maria, "A review on natural convection in

enclosures for engineering applications. The particular case of the parallelogrammic diode cavity," *Applied Thermal Engineering,* pp. pp 304 - 322, 2014.

[162] Analog Devices, "2-Terminal IC Temperature Transducer," Analog Devices, Norwood, 2009.

[163] S. A. Inc, "Bubble Generator Systems - Air Flow Visualization and Measurement," Sage Action Inc, [Online]. Available: http://www.sageaction.com/. [Accessed 29 11 2014].

[164] J. Systems, "JAD Systems," [Online]. Available: www.jadsys.co.za. [Accessed 7 10 2014].

[165] S. A. Inc, Bubble Generator Systems - Manual, New York: Sage Action Inc, 2011.

[166] M. A. Schnelle and J. M. Dole, "Greenhouse Floors and Benches - OSU Fact Sheets," [Online]. Available: http://osufacts.okstate.edu. [Accessed 15 January 2013].

[167] J. N. Walker and G. A. Duncan, "Greenhouse Benches," [Online]. Available: http://www.bae.uky.edu/publications/aens.asp. [Accessed 18 April 2013].

[168] F. D. Molina-Aiz, D. L. Valera, A. J. Alvarez and A. Madueno, "A Wind Tunnel Study of Airflow through Horticultural Crops: Determination of the Drag Coefficient," *Biosystems engineering,* vol. 93, no. 4, 2006.

[169] T. Shih, W. W. Liou, A. Shabbir, Z. Yang and J. Zhu, "A New k-epsilon Eddy Viscosity Model for High Reynolds Number Turbulent Flows - Model Development and Validation," *NASA,* 1994.

[170] J. W. Worley, "Hobby Greenhouses," [Online]. Available: http://www.caes.uga.edu/Publications/pubDetail.cfm?pk_ID=6071. [Accessed 21 08 2013].

[171] I. S. Walker and D. J. Wilson, "Evaluating models for superposition of wind and stack effect in air infiltration," *Building and Environment,* vol. 28, no. 2, pp. 201-210, 1993.

[172] L. Vandaele and P. Wouters, *Modeling Ventilation: basic mechanisms,* Liege, Belgium, 1994.

[173] A. S. Thom, "Momentum absorption by vegetation," *Quarterly Journal of the Royal Meteorological Society,* vol. 97, pp. 414-428, 1971.

[174] M. Teitel, O. Liran, J. Tanny and M. Barak, "Wind driven ventilation of a mono-span greenhouse with a rose crop and continuous screened side vents and its effect on flow patterns and microclimate," *Biosystems Engineering,* vol. 101, pp. 111-122, 2008.

[175] M. Teitel and J. Tanny, "Natural ventilation of greenhouses: experiments and model," *Agricultural and Forest Meteorology,* vol. 96, pp. pp 59-70, 1999.

[176] H. Tantau, "Energy saving potential of greenhouse climate control," *Mathematics and Computers in Simulation,* pp. 93-101, 1998.

[177] T. Shih, W. W. Liou, A. Shabbit, Z. Zang and J. Zhu, "A New k-epsilon Eddy Viscosity Model for High Reynolds Number Turbulent Flows," NASA, 1994.

[178] M. H. Sherman and D. T. Grimsrud, "Infiltration-pressurization correlation: simplified physical modeling," *Trans. ASHRAE,* vol. 86, pp. 778-807, 1980.

[179] F. Salisbury and C. Ross, Plant Physiology, Belmont, CA: Wadsworth Publishing, 1992.

[180] M. Saleem, S. Asghar and M. A. Hossain, "Natural Convection flow in an open rectangular cavity with cold sidewalls and constant volume heat source," *Proceedings of the Institution of Mechanical Engineers, Part C: Journal of Mechanical Engineering Science,* vol. 225, 2011.

[181] J. C. Roy and T. Boulard, "CFD Prediction of the Natural Ventilation in a Tunnel-Type Greenhouse: Influence of Wind Direction and Sensibility to Turbulence Models," *Acta Hort 691,* 2005.

[182] S. Reichrath and T. W. Davies, "Computational fluid dynamics simulations and validation of the pressure distribution on the roof of a commercial multi-span Venlo-type Greenhouse," *Journal of Wind Engineering and Industrial Aerodynamics,* vol. 90, pp. 139-149, 2002.

[183] J. M. Randall and R. Patal, "Thermally Induced Ventilation of Livestock Transporters," *Journal of Agricultural Engineering Research,* vol. 57, pp. 99-107, 1994.

[184] M. Prakash, S. B. Kedare and J. K. Nayak, "Numerical study of natural convection loss from open cavities," *International Journal of Thermal Sciences,* vol. 51, pp. pp 23-30, 2012.

[185] G. Papadakis, M. Mermier, F. Meneses and T. Boulard, "Measurement and Analysis of Air Exchange Rates in a Greenhouse with Continuous roof and side openings," *Journal of*

Agricultural Engineering Research, pp. 219-228, 1996.

[186] J. Pallares, F. X. Grau and F. Giralt, "Flow transitions in laminar Rayleigh–Bénard convection in a cubical cavity at moderate Rayleigh numbers," *International Journal of Heat and Mass Transfer,* vol. 42, pp. 753-769, 1999.

[187] N. Ouertatani, N. Ben Cheikh, B. Ben Beya and T. Lili, "Numerical simulation of two-dimensional Rayleigh–Bénard convection in an enclosure," *C. R. Mecanique,* vol. 336, pp. 464-470, 2008.

[188] A. M. Omer, "Energy use and environmental impacts: A general review," *Journal of Renewable and Sustainable Energy,* vol. 1, 2009.

[189] L. Okushima, S. Sase and M. Nara, "A support system for natural ventilation design of greenhouses based on computational aerodynamics," *Acta Hortic,* vol. 284, pp. 129-136, 1989.

[190] F. D. Molina-Aiz, D. L. VAlera, A. J. Alvarez and A. Madueno, "A Wind Tunnel Study of Airflow through Horticultural Crops: Determination of the Drag Coefficient," *Biosystems Engineering,* vol. 93, no. 4, pp. 447 - 457, 2006.

[191] A. Mistriotis, C. Arcidiacono C, P. Picuno, G. P. Bot and G. Scarascia-Mugnozza, "Computational Analysis of Ventilation in Greenhouses at zero- and low-wind-speeds," *Agricultural and Forest Meteorology,* vol. 88, pp. pp 121-135, 1997.

[192] A. Mistriotis, G. P. A. Bot, P. Picuno and G. Scarascia-Mugnozza, "Analysis of the efficiency of greenhouse ventilation using computational fluid dynamics," *Agricultural and Forest Meteorology,* vol. 85, pp. 217 - 228, 1997.

[193] M. M. Teitel, G. Ziskind, O. Lirana and V. Dubovsk, "Effect of wind direction on greenhouse ventilation rate,airflow patterns and temperature distributions," *Biostystems Engineering,* 2008.

[194] P. Liu , H. Lin and J. Chou, "Evaluation of buoyancy-driven ventilation in atrium buildings using computational fluid dynamics and reduced-scale air model," *Building and Environment,* vol. 44, pp. 1970-1979, 2009.

[195] J. T. Lir and T. F. Lin, "Visualization of roll patterns in Rayleigh–Bénard convection of air in a rectangular shallow cavity," *International Journal of Heat and Mass Transfer,* vol. 44, pp.

2889-2902, 2001.

[196] P. F. Linden, "The Fluid Mechanics of Natural Ventilation," *Annual Review of Fluid Mechanics,* vol. 31, 1999.

[197] C. Lei and J. C. Patterson, "Unsteady natural convection in a triangular enclosure induced by absorption of radiation," *Journal of Fluid Mechanics,* vol. 460, pp. 181-209, 2002.

[198] I.-B. Lee, *Fluid dynamic simulation and validation of a naturally ventilated multispan greenhouse,* Ohio State University, 1998.

[199] I. B. Lee, S. W. Hong, H. S. Hwang and I. H. Seo, "Study on Ventilation Efficiencies of Naturally Ventilated Multi-Span Greenhouses in Korea," *Proc. IS on Greenhouse Cooling, Acta Hort 719,* 2006.

[200] T. Larsen, *Natural Ventilation Driven by Wind and Temperature Difference,* Aalborg University, 2006.

[201] S. Kruger and L. Pretorius, "Analysis of Natural Convection in a Mono-span Naturally Ventilated Greenhouse," in *Eigth South African Conference on Computiational and Applied Mechanics (SACAM 2012)*, Johannesburg, 2012.

[202] Kruger, S. Kruger, L. Pretorius and R. Laubscher, asdfasdfadsf, Jhb: Wiley, 2006.

[203] T. Kozai and S. Sase, "A Simulation of natural ventilation for a multi-span greenhouse," *Acta Horticultarae,* vol. 87, pp. 339-349, 1978.

[204] L. Khezzar, D. Siginer and I. Vinogradov, "Natural convection in inclined two dimensional rectangular cavities," *Heat and Mass Transfer,* vol. 48, pp. pp 227 - 239, 2012.

[205] N. Khan, Y. Su and S. B. Riffat, "A review on wind driven ventilation techniques," *Energy and Buildings,* vol. 40, pp. 1586-1604, 2008.

[206] I. Impron, S. Hemming and G. P. Bot, "Effects of cover properties, ventilation rate, and crop leaf area on tropical greenhouse climate," *Biosystems Engineering,* vol. 99, pp. pp 553 - 564, 2008.

[207] J. Hanan, Greenhouses - Advanced Technology for protected horticulture, USA: CRC Press LLC, 1998.

[208] C. P. Groth, "Lecture Notes - Aer1310," 2010. [Online]. Available: http://utias.utoronto.ca/~groth/aer1310/Lecture_Notes/1_Intro_Turbulent_Flows.pdf. [Accessed 30 09 2013].

[209] J. E. Emswiler, "The natural zone in ventilation," *ASHVE Trans,* vol. 32, p. pp 59–74., 1962.

[210] M. Djevic and A. Dimitrijevic, "Energy consumption for different greenhouse constructions," *Energy,* pp. 1325-1331, 2009.

[211] T. De Jong, Natural Ventilation of Large Multi-span Greenhouses, Wageningen: Agrictultural University Wageningen, 1990.

[212] C. o. A. U. o. A. Cooperative Extension, "Arizona Master Gardener Manual," 1998. [Online]. Available: http://ag.arizona.edu/pubs/garden/mg/index.html. [Accessed 23 08 2013].

[213] M. Brugger, J. Montero, E. Baezz and J. Perez-Parra, "Computational Fluid Dynamic Modeling to Improve the Design of the Spanish Parral Style Greenhouse," *Acta Horticulturae 691,* 2005.

[214] J. M. Bruce, "Natural Ventilation - its role and application in the bio-climate System," *Farm Buildings R & D Stud,* vol. 8, pp. 1-8, 1977.

[215] T. Boulard and B. Draoui, "Natural ventilation of a greenhouse with continuous roof vents: measurements and data Analysis," *Journal of Agricultural Engineering Research,* pp. 27-36, 1995.

[216] T. Boulard and W. S , "Experimental and numerical studies on the heterogeneity of crop transpiration in a plastic tunnel," *Computers and Electronics in Agriculture.*

[217] T. Boulard, R. Haxaire, M. A. Lamrani, J. C. Roy and A. Jaffrin, "Characterization and Modelling of the Air Fluxes induced by Natural Ventilation in a Greenhouse," *Journal of Agricultural Engineering Research,* vol. 74, pp. pp 135-144, 1999.

[218] G. Bot, "Developments in Indoor Sustainable plant production with Emphasis on Energy Saving," *Computers and Electronics in Agriculture,* pp. 151-165, 2001.

[219] F. J. Baptista, B. J. Bailey, J. M. Randall and J. F. Meneses, "Greenhouse Ventilation Rate: Theory and Measurement with Tracer Gas Techniques," *Journal of Agricultural Engineering Research,* vol. 72, pp. pp 363 - 374, 1999.

[220] N. Banaeian, M. Omid and H. Ahmadi, "Energy and economic analysis of greenhouse strawberry production in Tehran Province of Iran," *Energy Conversion and Management,* vol. 52, pp. 1020-1025, 2011.

[221] A. Bairi, E. Zarco-Pernia and J. M. Garcia de Maria, "A review on natural convection in enclosures for engineering applications. The particular case of the parallelogrammic diode cavity," *Applied Thermal Engineering,* vol. 63, pp. 304-322, 2014.

[222] ASHRAE, 2003 ASHRAE HVAC Applications SI Edition, Atlanta: American Society of Heating, Ventilation and Air Conditioning Engineers, 2001.

[223] U. o. Arizona, 1998. [Online]. Available: http://ag.arizona.edu/pubs/garden/mg/vegetable/temperature.html.

[224] M. Aounallah, Y. Addad and S. Benhamadouche, "Numerical investigation of turbulent natural convection in an inclined square cavity with a hot wavy wall," *International Journal of Heat and Mass Transfer,* vol. 50, pp. 1683-1693, 2007.

[225] F. Ampofo and T. G. Karayiannis, "Experimental benchmark data for turbulent natural convection in an air filled square cavity," *International Journal of Heat and Mass Transfer,* vol. 46, pp. pp 3551-3572, 2003.

[226] "Measurement and CFD simulation of microclimate characteristics and transpiration of an Impatiens pot plant crop in a greenhouse," *Biosystems Engineering,* vol. 112, pp. 22-34, 2012.

[227] "Experimental and Numerical Investigation of Convective Heat Transfer in a Tunnel Greenhouse," *International Review of Mechanical Engineering (I.RE.M.E),* vol. 2, no. 6, November 2008.

[228] "American Nursery Man," [Online]. Available: http://www.amerinursery.com/article-9348.aspx.

[229] C. Tropea, A. L. Yarin and J. F. Foss, Springer Handbook of Experimental Fluid Mechanics, Heidelberg: Springer, 2007.

[230] W. P. Jones and B. E. Launder, "The Prediction of Laminarization with a Two-Equation Model of Turbulence," *Int J or Heat and Mass Transfer,* vol. 15, pp. 30-314, 1972.

[231] S. Kruger and L. Pretorius, "The Effect of Internal Obstructions in Naturally Ventilated Greenhouse Applications," in *Proceedings of the 5th International Conference on Heat Transfer, Fluid Mechanics and Thermodynamics* , Sun City, 2007.

[232] J. W. Boodley, The Commercial Greenhouse, New York: Delmar Publishers, 1998.

[233] A. Mistriotis, T. De Jong, M. J. M. Wagemans and G. P. A. Bot, "Computational Fluid Dynamics (CFD) as a tool for the Analysis of Ventilation and Indoor Microclimate in Agricultural Buildings," *Netherlands Journal of Agricultural Science,* vol. 45, pp. 81-96, 1997.

[234] L. Okushima, S. Sase and M. Nara, "A Support System for Nat Vent Design of Greenhouses Based on Computational Aerodynamics," *Modelling in Protected Cultivation, Acta Horticulturae,* vol. 248, 1989.

[235] P. Bournet and T. Boulard, "Effect of ventilator configuration on the distributed climate of greenhouses: A review of experimental and CFD studies," *Computers and Electronics in Agriculture,* vol. 74, pp. 195-217, 2010.

[236] M. Teitel, G. Ziskind, O. Liran, V. Dubovsky and R. Letan, "Effect of Wind Direction on Greenhouse Ventilation Rate,airflow Patterns and Temperature Distributions," *Biosystems Engineering,* pp. 1-19, 2008.

[237] I. H. Shames, Mechanics of Fluids, New York: McGraww-Hill, 2003.

[238] S. V. Patankar, Numerical Heat Transfer and Fluid, Washington: Hemisphere, 1980.

[239] S. Sase, "The Effect of Plant Arrangement on Airflow Characteristics in a Naturally Ventilated Glasshouse," *Acta Hoirticulturae - Energy Saving in Protected Cultivation,* vol. 245, pp. 429-435, 1989.

[240] S. Reichrath and T. W. Davies, "Computational Fluid Dynamics Simulations and validation of the Pressure Distribution on the roof of a Commercial Multi-span Venlo-type Greenhouse," *Journal of Wind Engineering and Industrial Aerodynamics* , vol. 90, pp. 139-149, 2002.

[241] W. P. Jones and B. E. Launder, "The Prediction of Laminarization with a Two-Equation Model of Turbulence," *International Journal of Heat and Mass Transfer,* vol. 15, pp. pp 301-

314, 1972.

[242] S. A. Ould Khaoua, P. E. Bournet, C. Migeon, T. Boulard and G. Chasseriaux, "Analysis of Greenhouse Ventilation Efficiency based on Computational Fluid Dynamics," *Biossystems Engineering,* vol. 95, pp. 83-98, 2006.

Appendix A

Flow Visualization Results

The next series of cross-sectional photographs in Figure A.1 were taken from the videoclip at 1 second intervals for the heaters set to 70°C. Figure A.2 shows longitudinal photograpsh of another case with the all the vents closed, the heaters was set to 40°C.

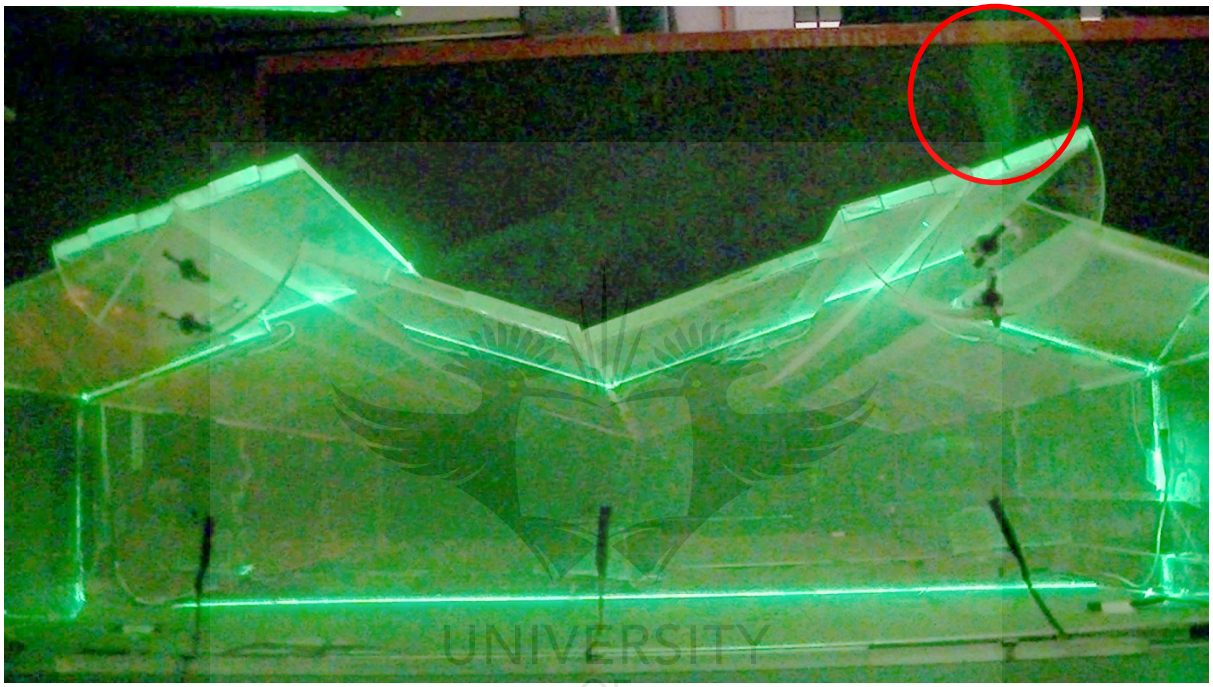

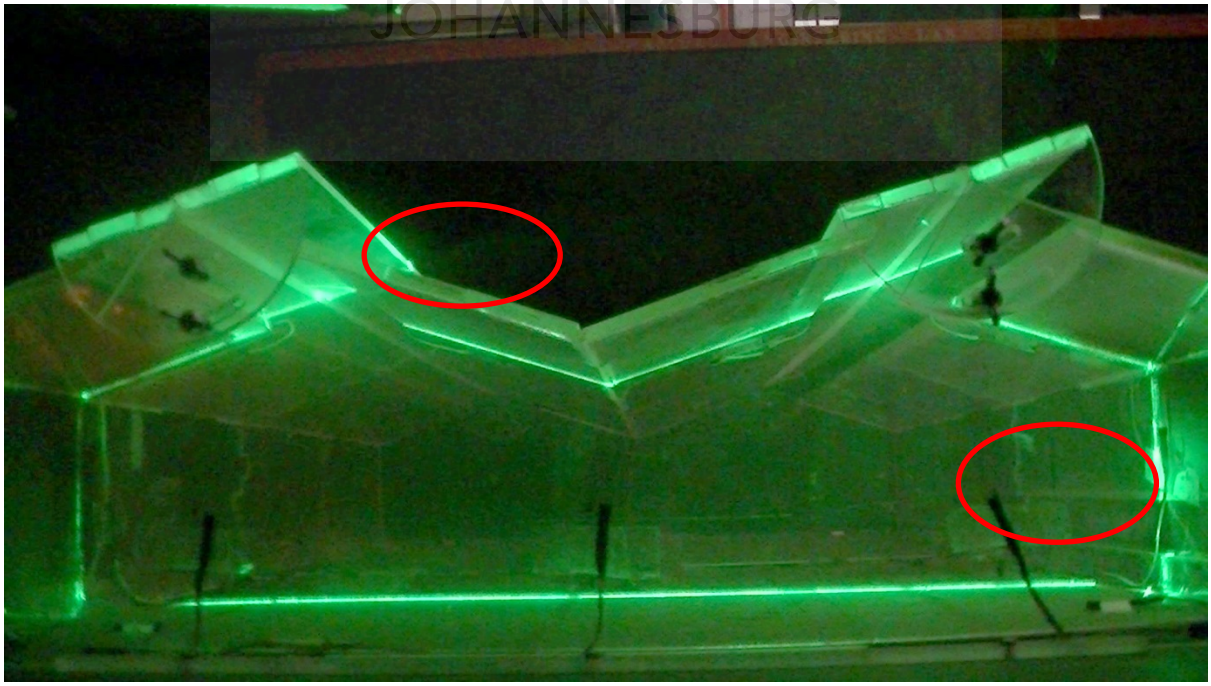

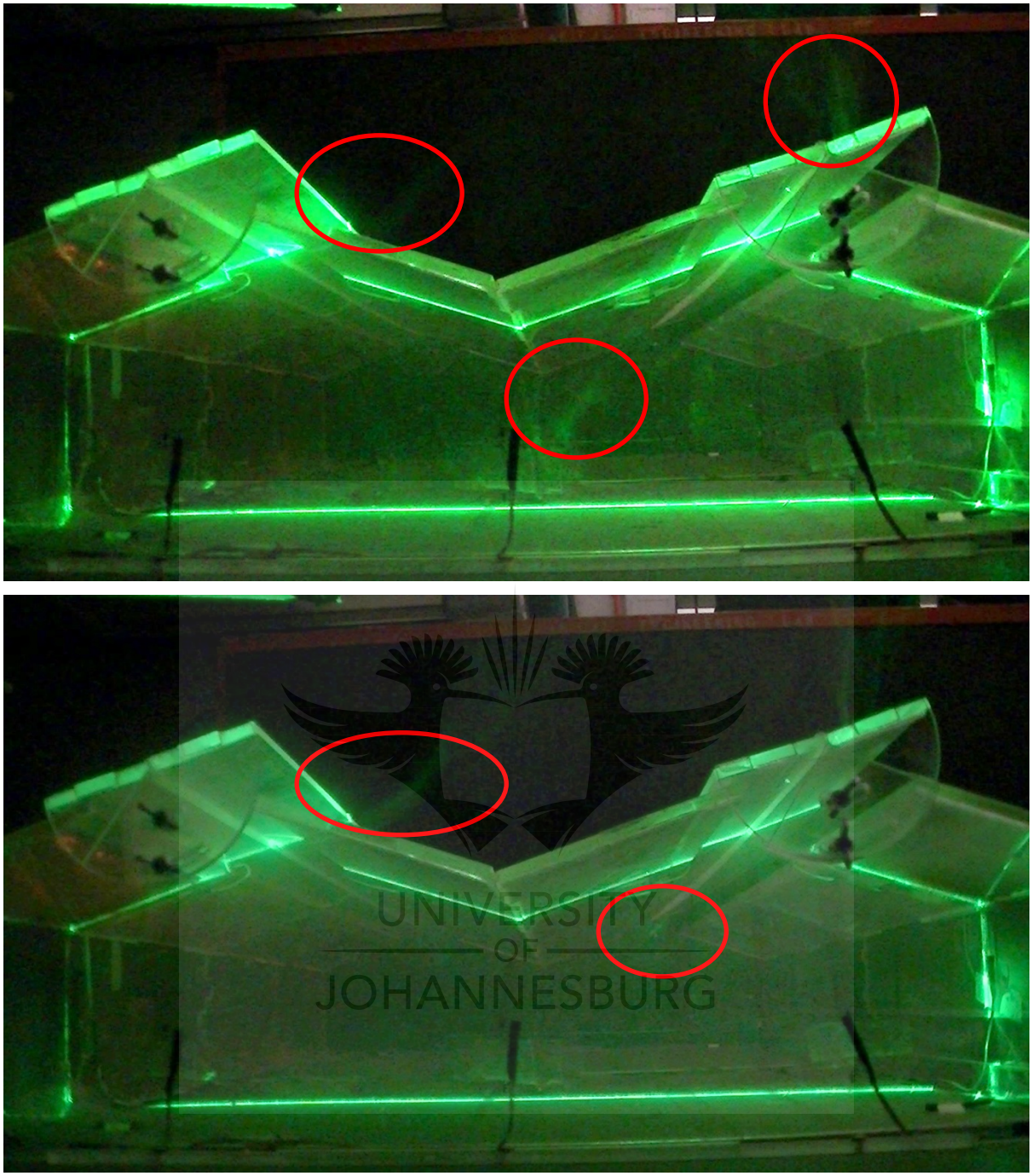

Figure A-1: Consecutive Images showing Smoke and Plumes (Heaters = 70°C)

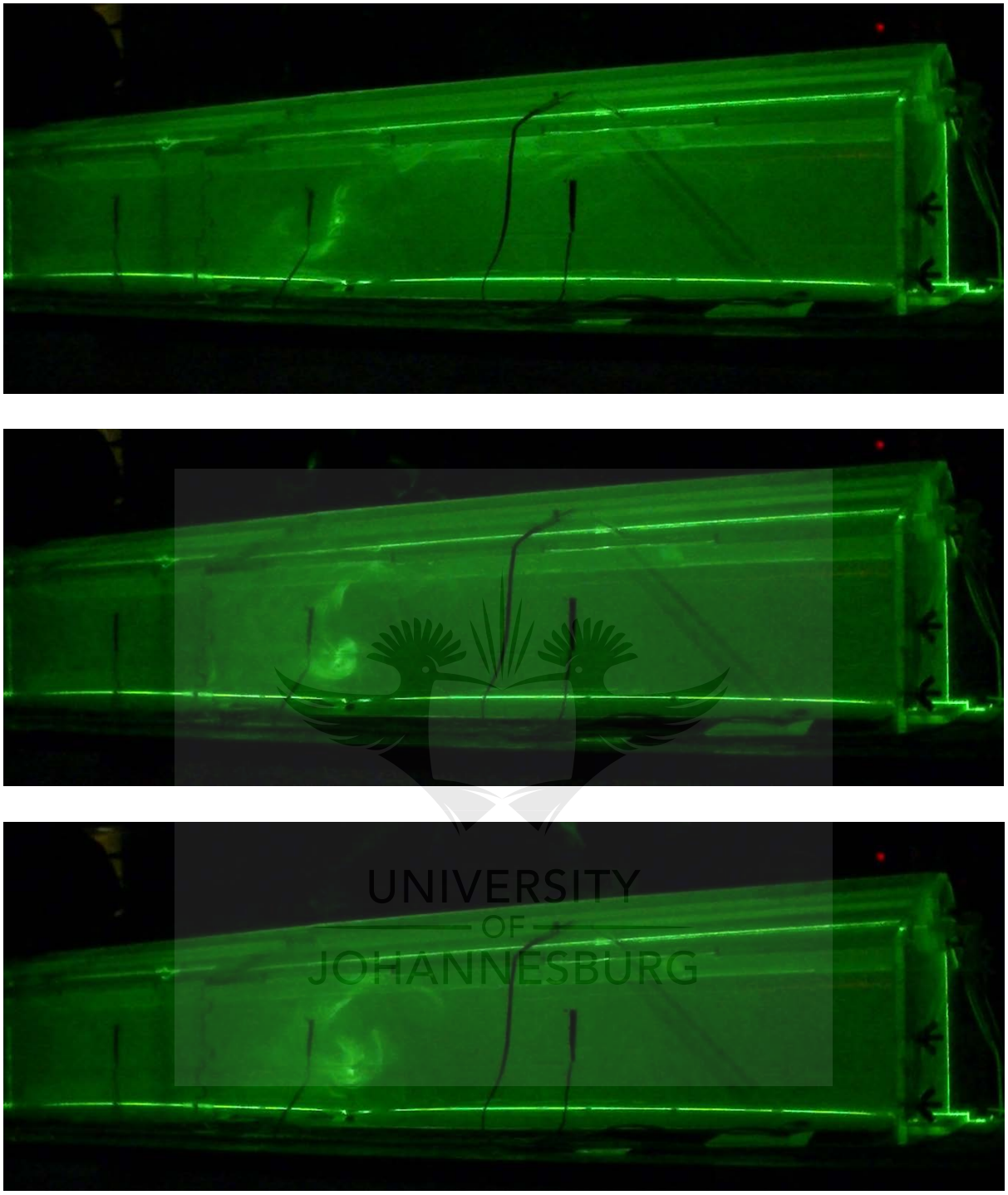

Figure A.2: Consecutive Longitudinal Images showing Smoke and Plumes (Heaters = 40°C

Appendix B

Temperature Measurements

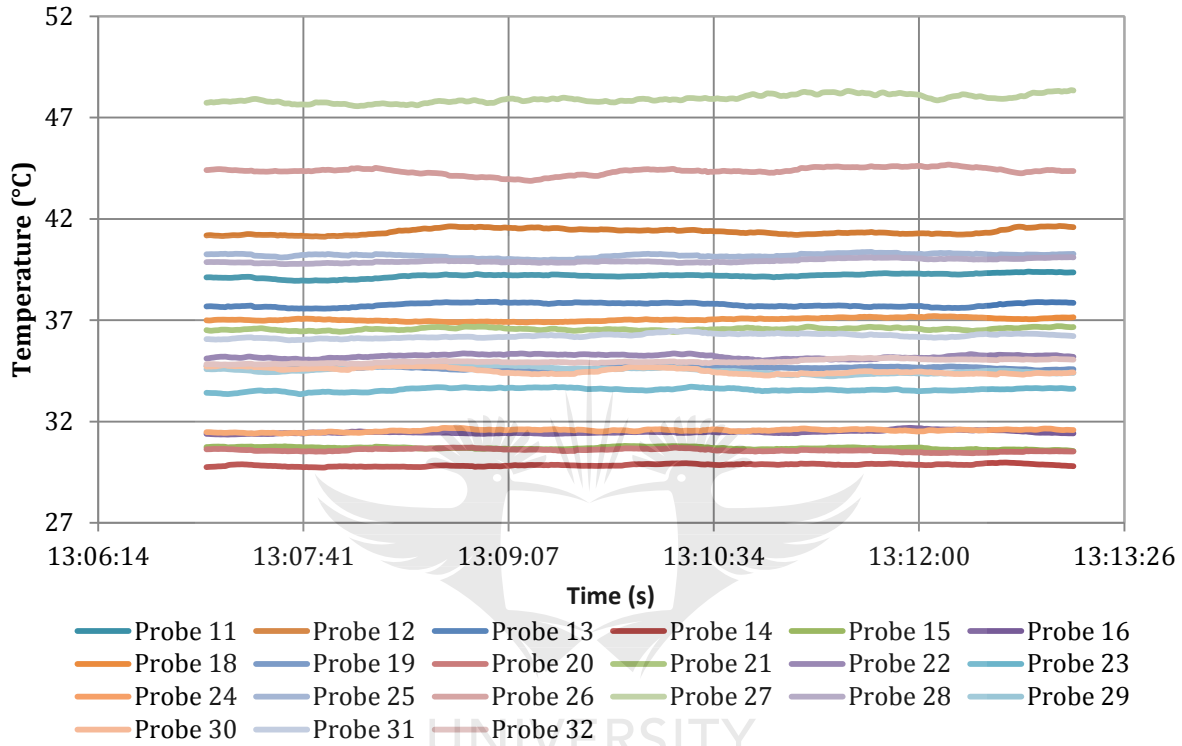

Figure B.1: Temperature measurements during experiment